

Macrocyclic Tetraaza Gold Complexes: Synthesis, Spectroscopy, Theoretical Studies

Dissertation zur Erlangung des Grades eines
Doctor rerum naturalium (Dr. rer. nat.)

des Fachbereichs 09
Chemie, Pharmazie, Geographie und Geowissenschaften
der Johannes Gutenberg-Universität Mainz
im Promotionsfach Chemie

vorgelegt von

Lukas Paul Sorge

geboren in Arnsberg.

Mainz, 2024

This thesis was written in the period from May 2019 to June 2024 at the Department of Chemistry of the Johannes Gutenberg University Mainz under the supervision of [REDACTED].

“I, Lukas Paul Sorge, hereby declare that I wrote the dissertation submitted without any unauthorized external assistance and used only sources acknowledged in the work. All textual passages which are appropriated verbatim or paraphrased from published and unpublished texts as well as all information obtained from oral sources are duly indicated and listed in accordance with bibliographical rules. In carrying out this research, I complied with the rules of standard scientific practice as formulated in the statutes of Johannes Gutenberg University Mainz to insure standard scientific practice.”

Mainz, 13th of June 2024

Dean

[REDACTED]

First reviewer

[REDACTED]

Second reviewer

[REDACTED]

Date of the oral exam

Abstract

The spectroscopic and structural signature of the oxidation state +II of gold in mononuclear systems has remained unclear for a long time due to inadequate strategies for the molecular stabilization. Strong relativistic effects promote the dimerization or disproportionation into the oxidation states +I and +III, resulting in high requirements for the ligand design. The limited spectroscopic and structural insights have relied on gas-phase studies of *in situ* generated, on compartmented gold(II) complexes in a zeolite supercage or chelating thioether ligands. Extensive theoretical studies were conducted on gold-xenon or gold-fluoride complexes exclusively isolated at low temperatures. However, gold(II), trapped in the rigid macrocyclic square-planar tetraaza coordination environment of the tetraphenylporphyrinato ligand (TPP²⁻) exhibits an extraordinary high stability. This facilitated the isolation of the mononuclear (tetraphenylporphyrinato)gold(II) complex Au^{II}(TPP) and comprehensive spectroscopic and structural studies on the divalence of gold, as well as investigations of its reactivity.

This work deals with the potential utilization of a 14-membered tetraaza bis(β -diiminato) macrocycle for the molecular stabilization of gold(II). This macrocycle adopts the same local coordination environment as porphyrins, with a more accessible synthesis. Moreover, due to the redox-innocent nature of the ligand, the reduction of the gold(III) precursor complex should be exclusively metal-centered. The equilibrium between different valence isomers, as detected for Au^{II}(TPP), should be of no significance.

The quasi-reversible gold-centered two-electron reduction of [Au^{III}L]⁺ is strongly cathodically shifted compared to the [Au(TPP)]⁺ complex and becomes irreversible upon further reduction. NMR and absorption spectroscopic studies of the reaction solution of the gold(III) complex with one equivalent potassium graphite as reducing agent reveal the disproportionation of gold(II) into gold(I) and gold(III). While this equilibrium is reversible for Au^{II}(TPP), due to a ligand-centered second reduction, accompanied by only slight changes of the complex geometry, the monoanionic bis(β -diiminato)gold(I) complex [Au^IL]⁺ (d¹⁰ electron configuration) bears a strongly distorted geometry with nearly linear coordination of the genuine gold(I) ion. The subsequent disproportionation into gold(0) and gold(III), under release of the pro-ligand, is irreversible.

The isolation of Au^{II}(TPP) has facilitated instructive insights into the spectroscopic and electronic nature of mononuclear gold(II) complexes. For insights into the electronic and geometric properties of binuclear gold complexes without direct gold-gold bond, a novel bis(porphyrinato)gold(III) complex

Abstract

$[\text{Au}_2(\text{DPD})][\text{PF}_6]_2$ is synthesized. In a "Pacman"-like complex geometry, two gold(III) porphyrins are rigidly connected in a cofacial manner through a dibenzofuran bridge. This provides high lateral stability towards both porphyrin subunits, alongside with a high axial flexibility. The minor bathochromic shift of the Soret band compared to the mono(porphyrinato)gold(III) complex indicates a small excitonic interaction between both porphyrin subunits. The absorption spectra of the twofold chemically reduced bis(porphyrinato)gold(III) complex features a slightly intensity-reduced Soret band and bathochromically shifted Q bands indicating gold centered reductions. The broad absorption bands of low intensity at longer wavelengths could be assigned to weak gold-to-gold transitions. The one- and twofold chemical reduction of the bis(porphyrinato)gold(III) complex yields indistinguishable EPR spectra of the intensity ratio 1:2. The electrochemical data suggest a high thermodynamic stability of the neutral gold(II)/gold(II) complex, whereas the mixed-valent gold(II)/gold(III) species is prone to disproportionation. The binuclear $[\text{Au}_2(\text{DPD})][\text{PF}_6]_2$ and monomeric (octaethylporphyrinato) gold(III) complexes exhibit weak phosphorescence with lifetimes in the nanosecond range at room temperature and in the microsecond range in frozen solution at low temperatures.

Structurally, macrocyclic corroles only differ from porphyrins by the absence of a methine bridge and charge. In contrast to the (porphyrinato)gold(III) complexes, which exhibit metal-centered reductions, the coordination of the corrolato ligand to gold(III) leads to a ligand-centered reduction, as reported by several groups. This is attributed to the comparatively high-energy of the $5d_{x^2-y^2}$ orbital of gold situated in the small tetraaza cavity of the corrolato ligand. A comprehensive theoretical study deploying density functional theory (DFT) methods is conducted for a systematic screening of the impact of electron-donating (aryl)substituents at different positions of the corrole scaffold on the energy of the ligand-centered π -type lowest unoccupied molecular orbitals (LUMO). An energetic raising of the ligand-centered LUMOs should make a metal-centered localization of the spin density more likely. The spin density onto the gold atom of the DFT geometry optimized structures remains unaffected independent from the electron-donating strength and position of the substituents. The spin density is exclusively delocalized over the corrolato ligand and resides mainly onto the *meso*- and β -carbon atoms. The implementation of bulky substituents involves strong *out-of-plane* distortions of the corrole macrocycle which are mainly dominated by the domed, waving x and ruffled modes. The substitution of at least one of the methine groups with an oxygen or sulfur atom results in a spin redistribution with involvement of the gold center, indicating that the gold center could be involved in redox-processes of such a complex. This is attributed to the larger tetraaza cavity upon introduction of the larger sulfur atoms leading to a weaker destabilization $5d_{x^2-y^2}$ orbital not as a consequence of the energetic alignment of the corrole-centered lowest-unoccupied molecular orbitals to the gold-centered molecular orbitals.

Kurzzusammenfassung

Die spektroskopische und strukturelle Signatur der Oxidationsstufe +II von Gold blieb aufgrund unzureichender Strategien für die molekulare Stabilisierung unklar. Starke relativistische Effekte begünstigen die Dimerisierung oder Disproportionierung in die Oxidationsstufen + I und + III und stellen daher hohe Anforderungen an das Ligandendesign. Die begrenzten spektroskopischen und strukturellen Einsichten basierten daher unter anderem auf Gasphasen-Experimenten an *in situ* erzeugten oder anhand von Gold(II)-Komplexen, die in den Poren von Zeoliten voneinander isoliert waren. Umfangreiche theoretische Arbeiten wurden an den bei ausschließlich tiefen Temperaturen isolierten Gold-Xenon oder Gold-Fluorid-Komplexen durchgeführt. Jedoch zeigt Gold(II), eingebettet in die rigide makrozyklische Tetraaza Umgebung des Tetraphenylporphyrinato Liganden TPP²⁻ eine außerordentlich hohe Stabilität. Dies ermöglichte sowohl die Isolation des mononuklearen (Tetraphenylporphyrinato)gold(II)-Komplexes Au^{II}(TPP) als auch umfangreiche spektroskopische und strukturelle Studien zur Divalenz des Goldes sowie erste Einblicke in die Reaktivität.

Hierauf basierend wird in dieser Arbeit die potentielle Verwendung des 14-gliedrigen Tetraaza Bis(β -diiminato) Makrozyklus für eine molekulare Stabilisierung von Gold(II) untersucht. Dieser Makrozyklus verfügt über dieselbe lokale Koordinationsumgebung wie Porphyrine, ist allerdings leichter synthetisch zugänglich. Darüberhinaus sollte der redox-unschuldige Charakter des Liganden eine ausschließlich Gold-zentrierte Reduktion begünstigen. Das Gleichgewicht zwischen zwei Valenzisomeren, wie es bei Au^{II}(TPP) vorliegt, sollte hier nicht von Bedeutung sein.

Die quasi-reversible erste Gold-zentrierte zwei-Elektronen-Reduktion Bis(β -diiminato)gold(III) ist gegenüber Au^{II}(TPP) stark kathodisch verschoben und wird irreversibel sobald die weitere Gold-zentrierte Reduktion adressiert werden. NMR- und Absorptions-spektroskopische Untersuchungen der Reaktionslösung des Gold(III)-Komplexes mit einem Äquivalent KC₈ als Reduktionsmittel ergaben die Disproportionierung der zunächst gebildeten Gold(I) Spezies nach Gold(I) und Gold(III). Während dieses Gleichgewicht für Au^{II}(TPP) aufgrund einer Liganden-zentrierten zweiten Reduktion, die nur mit geringfügigen Veränderungen der Komplexgeometrie einhergeht, reversibel verläuft, zeigt der monoanionische bis(β -diiminato)gold(I) (d¹⁰ Elektronenkonfiguration) eine stark verzerrte Geometrie mit annähernd linearer Koordination des Gold(I) Ions. Die nachfolgende Disproportionierung in Gold(0) und Gold(III), unter Freisetzung des Pro-Liganden, ist irreversibel.

Die Isolation von Au^{II}(TPP) ermöglichte umfangreiche Einsichten in die spektroskopische und elektronische Natur eines mononuklearen Gold(II)-Komplexes. Für derartige Einblicke in binukleare

Kurzzusammenfassung

Gold-Komplexe ohne eine Gold-Gold-Bindung wird der cofaciale Bis(porphyrinato)gold(III)-Komplex dargestellt. In dieser „Pacman“-artigen Komplexgeometrie werden zwei Gold(III)-Porphyrine rigide über eine Dibenzofuran-Brücke miteinander verbunden. Diese verleiht den beiden (Porphyrinato)gold(III) Untereinheiten eine hohe laterale Stabilität zueinander, während die axiale Flexibilität erhalten bleibt.

Die geringe bathochrome Verschiebung der Soret-Bande des Bis(porphyrinato)gold(III)-Komplexes, verglichen mit dem monomeren (Porphyrinato)gold(III)-Komplex indiziert eine schwache exzitonische Wechselwirkung zwischen beiden Porphyrin Untereinheiten. Die Absorptionsspektrum der zweifach chemisch reduzierten Bis(porphyrinato)gold(III)-Komplexe zeigt Intensitäts-reduzierte Soret und geringfügig bathochrom verschobene Soret Bande. Dies deutet auf Gold-zentrierte Reduktionen ohne Beteiligung des Liganden hin. Die breiten, intensitätsschwachen Absorptionsbanden bei längeren Wellenlängen können mithilfe von TDDFT Gold-zu-Gold-Übergängen zugeordnet werden. Die ein- und zweifache Reduktion des Bis(porphyrinato)gold(III)-Komplexes führt zu ununterscheidbaren EPR Spektren in einem Intensitätsverhältnis von 1:2. Die elektrochemischen Daten indizieren eine hohe thermodynamische Stabilität der neutralen Gold(II)/Gold(II) Verbindung hin, während die gemischt-valente Spezies Disproportionierung unterliegt. Sowohl der binukleare als auch mononukleare Gold(III)-Komplex zeigen Phosphoreszenz geringer Intensität mit Lebenszeiten im Nanosekunden-Bereich bei Raumtemperatur und im Mikrosekunden-Bereich in gefrorener Lösung bei tiefen Temperaturen.

Der Makrozyklus der Corrole unterscheidet sich strukturell von Porphyrinen lediglich durch die Abwesenheit einer Methinbrücke. Im Gegensatz zu den (Porphyrinato)gold(III)-Komplexen dokumentieren eine Vielzahl von Studien eine Liganden-zentrierte Ein-Elektronen-Reduktion der (Corrolato)gold(III)-Komplexe. Dies wird dem vergleichsweise energetisch hochliegenden $5d_{x^2-y^2}$ Orbital des Goldes zugeschrieben, welches sich in der kleineren Tetraaza Koordinationsumgebung befindet.

In einer umfangreichen theoretischen Studie unter Anwendung von Methoden der Dichtefunktionaltheorie (DFT) wird der Einfluss von elektronenschiebenden Substituenten an verschiedenen Positionen des Corrol-Grundkörpers auf die Energie der Liganden-zentrierten LUMOs durchgeführt. Eine energetische Angleichung zum $5d_{x^2-y^2}$ Orbital des Goldes sollte eine mehrheitlich Gold-zentrierte Spindichte begünstigen.

Die Spindichte auf dem Goldatom der Geometrie-optimierten Strukturen bleibt unbeeinflusst von der Stärke und Position der elektronenschiebenden Substituenten. Die Spindichte ist ausschließlich auf dem Corrol-Liganden delokalisiert, mehrheitlich auf den Kohlenstoffatomen der *meso*- und β -Positionen. Die

Implementierung von sterisch anspruchsvollen Liganden induziert starke *out-of-plane* Verzerrungen des Corrolato-Liganden, die hauptsächlich von den *dom*-, *wav x*- und *ruf*-Moden bestimmt werden. Die Substitution von mindestens einer der Methingruppen gegen ein Sauerstoff oder Schwefelatom führt schließlich zu einer Spindichteverteilung unter Einbezug des Gold-Zentrums. Dies ist allerdings nicht auf die energetische Destabilisierung der Liganden-zentrierten LUMOs zurückzuführen, sondern eine Konsequenz aus der Vergrößerung der Tetraaza Bindungstasche und der damit einhergehenden energetischen Stabilisierung des $5d_{x^2-y^2}$ Orbitals des Goldes.

Contents

Abstract	I
Kurzzusammenfassung	III
Contents	VII
Abbreviations	IX
1 Introduction.....	1
1.1 Porphyrins – Remarkable Allrounder.....	2
1.1.1 Structure and Photophysical Properties.....	3
1.1.2 Performance on the Highest Level – Porphyrins in Nature	12
1.1.3 Backstage – Chemical Synthesis of Porphyrins	15
1.1.4 Onstage – Pacman Complexes in Action.....	21
1.1.5 Beyond Porphyrins – The Macrocyclic Tetraaza beta-Diiminato Ligand.....	26
1.2 An Incipient Success Story – Gold in its Oxidation State +II.....	27
1.2.1 The Origin of Relativistic Effects.....	28
1.2.2 Pseudo- and Binuclear Gold(II) Complexes.....	30
1.2.3 Transient Gold(II) Complexes.....	31
1.2.4 Suggested Gold(II) Complexes.....	33
1.2.5 Affirmed Gold(II) Complexes.....	35
1.3 Fundamentals of Electron Transfer.....	41
1.3.1 Marcus Theory of Electron Transfer	41
1.3.2 Marcus-Hush Theory and Robin-Day Classification	43
2 Motivation and Aim of the Work	47
3 Results and Discussion.....	49
3.1 14-Membered Macrocyclic beta-Diiminato Gold(II) – A New Member for the Gold(II) Complex Family?.....	51
3.2 Face-to-Face Gold Porphyrins.....	59

Contents

3.3	Pushing Molecular Orbitals to Higher Energy – A DFT Study on the Spin Distribution in Gold Corrole Complexes	71
3.3.1	Introduction.....	71
3.3.2	Results and Discussion.....	75
3.3.3	Conclusion	87
4	Summary and Outlook.....	89
5	References	97
6	Appendix	107
6.1	Supporting Information to 3.1: 14-Membered Macrocyclic beta-Diiminato Gold(II) – A New Member for the Gold(II) Complex Family?	107
6.2	Supporting Information to 3.2: Face-to-Face Gold Porphyrins	147
6.3	Supporting Information to 3.3: Pushing Molecular Orbitals to Higher Energy – A DFT Study on the Spin Distribution in Gold Corrole Complexes	224
7	Acknowledgements	245
8	Curriculum Vitae	247
8.1	List of Publications.....	249
8.2	Conference Contributions.....	250

Abbreviations

δ	chemical shift [ppm]
ϵ	molar absorption coefficient [$M^{-1} \text{ cm}^{-1}$]
λ	wavelength in nm or reorganization energy
τ	lifetime
$\tilde{\nu}$	wavenumber [cm^{-1}]
A	amplitude
Ar	aryl(substituent)
BET	back electron transfer
COSY	correlated spectroscopy
CV	cyclic voltammetry
DFT	density functional theory
$E_{1/2}$	half wave potential
EPR	electron paramagnetic resonance
ESI	electron spray ionisation
ET	electron transfer
eV	electron volt
g	gram
G	Gauss
g	g value (EPR)
h	hour
H₂L	5,7,12,14-tetramethyl-1,4,8,11-tetraazacyclotetradeca-5,7,12,14-tetraene
H₄(DPD)	4,6-Bis[(5-(2,3,15,17-tetraethyl-3,7,12,18-tetramethylporphyrinyl)]dibenzofuran
H₄(DPX)	4,6-Bis[(5-(2,3,15,17-tetraethyl-3,7,12,18-tetramethylporphyrinyl)]dimethylxanthene
HOMO	highest occupied molecular orbital
HMBC	heteronuclear multiple bond correlation (NMR)
HSQC	heteronuclear single quantum coherence (NMR)
IC	internal conversion

Abbreviations

IR	infrared
ISC	intersystem crossing
IVCT	intervalence charge transfer
$^{\circ}J$	coupling constant [Hz] or excitonic coupling [cm^{-1}]
k	rate constant
K	Kelvin
L	ligand
LUMO	lowest unoccupied molecular orbital
m	milli (10^{-3})
MC	metal-centered
Me	methyl
MS	mass spectrometry
m/z	mass-to-charge ratio
NIR	near-infrared
nm	nanometer
NMR	nuclear magnetic resonance
n.r.	non-radiative
ns	nanosecond
P	porphyrin
PET	photoinduced electron transfer
Ph	phenyl
ppm	parts per million
SWV	square wave voltammetry
T	temperature
H₃TPC	5,10,15-triphenylcorrol
H₂TPP	5,10,15,20-tetraphenylporphyrin
UV	ultraviolet
VIS	visible
VR	vibrational relaxation

1 Introduction

The macrocyclic porphyrin ligand, its derivatives and corresponding metalloporphyrins are extensively distributed in nature and of outstanding importance for many crucial photophysical and biological processes.¹ The iron-containing heme is involved as prosthetic group in hemoglobin and myoglobin in the binding and transport of oxygen in the bloodstream and storage in the muscle tissues, respectively.¹⁻³ Cytochromes, as a part of the inner mitochondrial membrane, enable the electron transport inside the respiratory chain, as well as the ultimate reduction of oxygen to water.¹ Chlorophylls, coordinated to magnesium, are located in the chloroplasts of plants and play an outstanding role in the process of photosynthesis by capturing the light energy from the sun and subsequent energy transfer and charge separation.^{1,4,5} Vitamin B₁₂ (cobalamin) is the most famous representative of a corrole comprising biomolecule and involved in the DNA synthesis and the metabolism of fatty acids or amino acids.^{1,6}

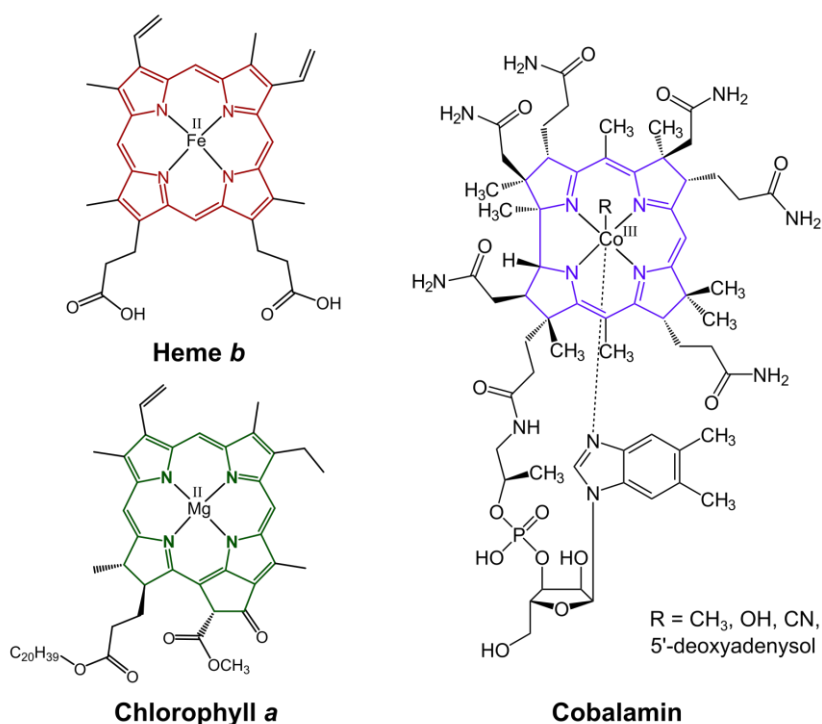


Figure 1.1 Molecular structures of representative biomolecules containing the porphyrin or corrole scaffold.¹⁻⁶

Since the first synthesis of porphine by Hans Fischer in 1936, porphyrins and corroles as well as their corresponding metal complexes have become indispensable in modern chemical research and related disciplines.⁷ Synthetic metalloporphyrins have found entrance into molecular biomimetic compounds, biocatalysis, organic photovoltaic cells, bioimaging, near-infrared dyes, molecular wires, supramolecular chemistry, sensing or medicine (Figure 1.2). This series of applications is not intended to be exhaustive.⁸

CHAPTER 1 | Introduction

The metal complex portfolio of the parent corrolato ligand is less extensive, however, it contains some intriguing applicabilities in the field of catalysis, solar cells, sensing or medicine (Figure 1.2).⁹

Found in living organisms		Synthetic cofacial bis(porphyrins)												
Naturally occurring		Relevant in this study												
Porphines														
1	2	3	4	5	6	7	8	9	10	11	12	13	14	15
Li												B	C	
Na	Mg											Al	Si	P
K	Ca	Sc	Ti	V	Cr	Mn	Fe	Co	Ni	Cu	Zn	Ga	Ge	As
Rb	Sr	Y	Zr	Nb	Mo	Tc	Ru	Rh	Pd	Ag	Cd	In	Sn	Sb
Cs	Ba	Ln	Hf	Ta	W	Os	Ir	Pt	Au	Hg		Tl	Pb	Bi
Corroles														
1	2	3	4	5	6	7	8	9	10	11	12	13	14	15
Li												B	C	
Na	Mg											Al	Si	P
K	Ca	Sc	Ti	V	Cr	Mn	Fe	Co	Ni	Cu	Zn	Ga	Ge	As
Rb	Sr	Y	Zr	Nb	Mo	Tc	Ru	Rh	Pd	Ag	Cd	In	Sn	Sb
Cs	Ba	Ln	Hf	Ta	W	Os	Ir	Pt	Au	Hg		Tl	Pb	Bi

Figure 1.2 Excerpt of the periodic table displaying the elements with known synthetic porphyrinato or corrolato complexes.^{9,10}

In the course of its evolution, nature has given rise to many porphyrin- and corrole-based highly functionalized enzymes that have enabled life on earth. Modern science has embraced these natural models, extensively studied and brought forth many artificial systems for various applications or for a better understanding of the mechanistics of their natural paragons. The appropriate insights into the fundamental structural and photophysical properties of porphyrins and their synthetic accessibilty, in special regard to this work, are discussed in the following sections.

1.1 Porphyrins – Remarkable Allrounder

Sections 1.1.1 and 1.1.2 address the structure and unique photophysical properties of (metallo)porphyrins and present examples of naturally-occurring porphyrins. The chemical approach to synthetic monomeric porphyrins (1.1.3) and prominent examples of synthetic molecular binuclear bis(porphyrin) complexes imitating the redox-active center of biologic enzymes are discussed in section 1.1.4.

Due to their exclusive experimental relevance for this work, the further photophysical considerations largely refer to the porphyrinoid macrocycle and its metal complexes. The origin of the characteristic absorption spectra or macrocyclic distortions in (metallo)porphyrins is also generally valid for the corrole complexes.

1.1.1 Structure and Photophysical Properties

The cyclic arrangement of four pyrrole units connected via four methine bridges forms the porphine's scaffold – the simplest representative of the porphyrin family. The porphine tetraaza macrocycle can be formally converted to corrole by the removal of one methine bridge (Figure 1.3). This apparently marginal change in the structural formula is accompanied by significant changes in the geometry, electronic properties and charge.⁹

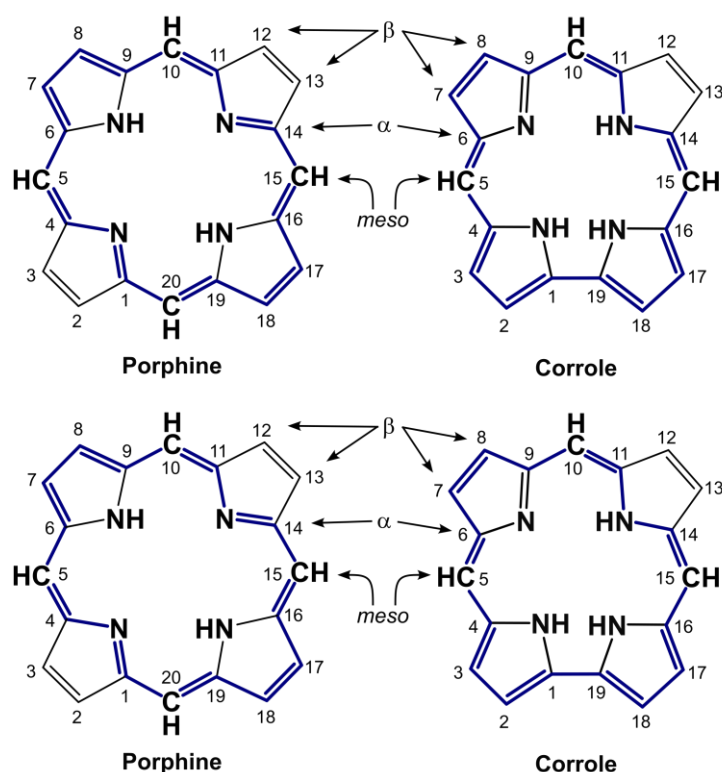


Figure 1.3 Molecular structures of the porphine and corrole macrocycles with IUPAC nomenclature and visualization of the aromatic aza[18]annulene system (indicated in blue).^{11,12}

Both almost planar and rigid macrocyclic ligands exhibit an inner 16-membered diaza[18]annulene ring of 18 π electrons, therefore satisfying Hückel's rule for aromaticity.¹² The nearly flat macrocycle exhibits notable thermal stability, as evidenced by the occurrence of porphyrin complexes in sediments of unrefined mineral oil.^{1,13}

The Brønsted amphoteric character of porphyrins and corroles is reflected in the formation of the protonated and deprotonated porphyrinato $[H_4P]^{2+}$ or $[P]^{2-}$ and corrolato ligands $[H_4C]^+$ or $[C]^{3-}$, respectively.¹⁴ Corroles act as stronger Brønsted acids and weaker corresponding Brønsted bases compared with their porphyrin counterparts, which is attributed to the smaller cavity size of corroles compared with porphyrins. This induces a stronger electrostatic repulsion between the inner NH protons. Therefore, the loss of one of these protons attends a steric relief.^{9,14}

The trianionic and therefore high σ -donating nature of the corrolato ligand is reflected in the affinity to stabilize high-valent metals, such as chromium(V),^{15,16} chromium(IV), manganese(V),^{17,18} iron(IV),^{19,20} cobalt(III),^{21,22} copper(III),^{23–25} copper(IV),^{9,26} silver(III)^{25,27–29} or gold(III).^{30–40}

The proton exchange between the inner nitrogen atoms is fast at room temperature – compared with the ^1H NMR timescale. This is reflected in only one NH proton resonance.⁴¹

Due to the aromaticity of the diaza[18]annulene an external magnetic field induces a strong ring current that covers the entire molecule. The secondary magnetic field – induced by this ring current – is opposed to the external field within the perimeter and aligned outside of the perimeter. Hence, the chemical shift of the ^1H resonance of the inner NH protons typically lies in the negative range. The exact value depends on the extent of the induced ring current, which is influenced by geometric distortions of the diaza[18]annulene. The absence of this very characteristic resonance is a reliable indicator for the coordination of a metal ion to the porphyrin.^{12,42}

(Metallo)porphyrins, regardless of whether isolated or covalently linked to another molecule or complex, can be easily detected via absorption spectroscopy. This is due to the specific number and shape of absorption bands of very high molar absorption coefficients of about $10^5 \text{ M}^{-1} \text{ cm}^{-1}$. In particular, these include the high-intense Soret band (B band) near the UV region, as well as up to four less-intense Q bands in the visible part of the electromagnetic spectrum (Figure 1.4).^{43,44}

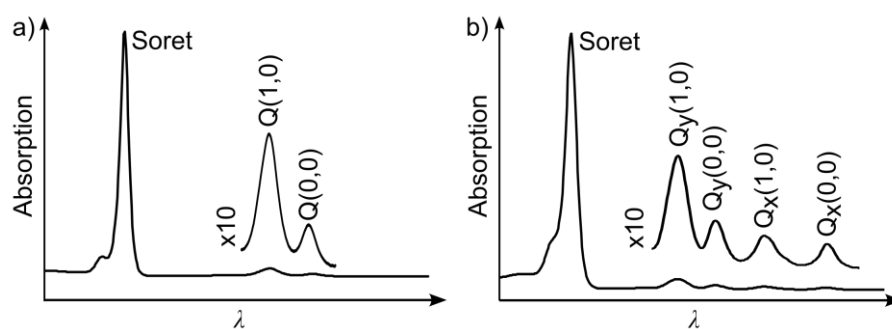


Figure 1.4 UV/Vis absorption spectra of a) Zn(TPP) and b) H_2TPP in THF at room temperature and detonation of the absorption bands according to Gouterman's four orbital model.^{43,44}

The energetic position and number of these absorption bands are sensitively influenced by the electronic properties of the substituents at the porphyrin's scaffold and the associated induced electronic and geometric distortions in the porphyrinoid macrocycle. Not only the presence of a metal ion in the center of the porphyrin, but also the intrinsic electronic properties, such as the electron configuration or orbital energies, leave a distinct signature in the absorption spectra.^{43–45}

The explanation for the unique shape of these absorption spectra of (metallo)porphyrins has been provided by Martin Gouterman.^{43–45} Accordingly, the absorption bands in a D_{4h} -symmetrical metalloporphyrin, are attributed to π - π^* transitions between the two porphyrin-centered highest

molecular orbitals (HOMO–1 and HOMO) and the two lowest unoccupied molecular orbitals (LUMO and LUMO+1). The HOMO–1 and HOMO feature a_{2u} and a_{1u} symmetry, whereas the LUMO and LUMO+1 have e_g symmetry (Figure 1.5). For the extension of this model on symmetry-reduced free-base porphyrins (D_{2h}), Gouterman introduced the more general descriptions b_1/b_2 and c_1/c_2 for the HOMOs and LUMOs, respectively. Since the *meso*-positions feature the highest atomic orbital coefficients, the energy level of the frontier molecular orbitals can be most strongly influenced by the introduction of electron-donating or -withdrawing ligands at these positions. However, steric effects and the concomitantly induced porphyrin's geometric distortions must also be taken into account (Figure 1.11).

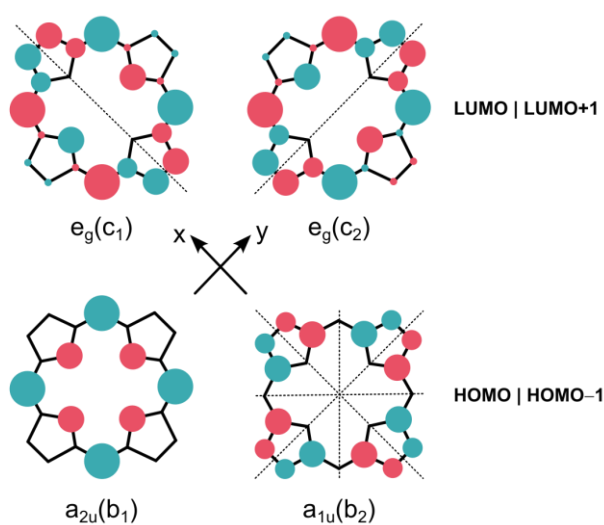


Figure 1.5 Shape, including symmetry description, of the frontier molecular π orbitals of porphine relevant to the Gouterman's four orbital model.^{43,44}

Assuming two energetically degenerate HOMOs (b_1 and b_2) and two degenerate LUMOs (c_1 and c_2) there are four possible transitions leading to two excited states of x-polarization, $^1(a_{1u}e_g(y))$ and $^1(a_{2u}e_g(x))$, and two of y-polarization, $^1(a_{1u}e_g(x))$ and $^1(a_{2u}e_g(y))$. The similar energies and symmetries of these excited states facilitate a mixing resulting in a high energy transition with parallel transition dipole moments, reflected in the B band, and two transitions with anti-parallel transition dipole moments, reflected in the Q bands. Vibronic progression entails the increase of numbers of the detected Q bands (Figure 1.6). The Q bands are labeled with two numbers set in parentheses: The first denotes the excited vibronic state whereas the second number denotes the respective electronic ground state.^{43,44} The Soret band is a highly sensitive indicator of whether an (electro)chemical reduction in a metalloporphyrin is metal- or ligand-centered. A metal-centered reduction is usually escorted only by a slight energetic shift and a reduced intensity of the Soret band, whereas the ligand-centered reduction entails the full disappearance of the Soret band.⁴⁶

The reduced local symmetry of free-base porphyrins (D_{2h}) compared with metalloporphyrins due to the presence of two NH protons along the x-axis, stabilizes the molecular orbital c_2 energetically compared to c_1 (Figure 1.6). The electronic transitions involving excited states with x- and y polarization are no longer degenerate. This leads to the separation of the B- and Q-bands into B_x/B_y and Q_x/Q_y , respectively, accompanied by vibronic progression. The polarization of the transitions is indicated by the index x or y.^{43,44,47}

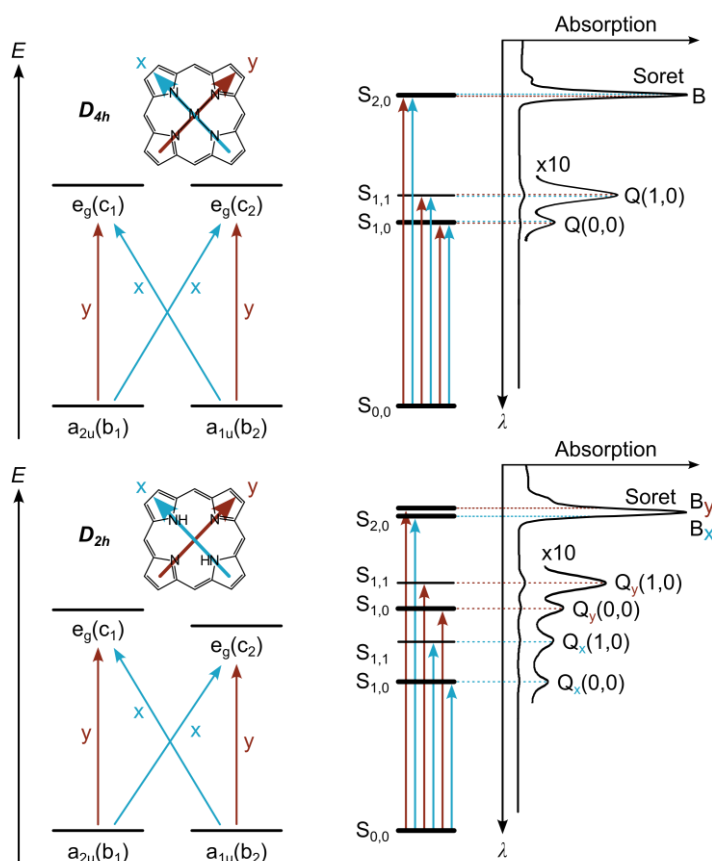


Figure 1.6 Relative energies of the frontier molecular orbitals for a porphyrin with local D_{4h} or D_{2h} symmetry and possible electronic transitions of different polarizations (x or y). Electronic transitions responsible for the characteristic absorption spectra of porphyrins.^{43,44,47}

The electron configuration and atomic orbital energy levels of the accommodated metal ion influence the corresponding absorption spectra and metalloporphyrins are further subdivided into *normal*, *hypso* and *hyper* porphyrins.⁴⁸

Normal-type absorption spectra are obtained for metalloporphyrins coordinating metals with d^0 - or d^{10} electron configuration (magnesium(II) or zinc(II)). Due to only weak interactions between the metal's atomic orbital and the porphyrin's frontier molecular orbitals the Soret- and Q-bands are marginally shifted.⁴⁸

1.1 | Porphyrins – Remarkable Allrounder

The absorption spectra of *hyper* porphyrins are characterized by intense charge transfer bands in the UV region. Outstanding examples are the absorption spectra of the porphyrinato complexes of chromium(III), manganese(III) or iron(III). The vacant d_{xz} - and d_{yz} -orbitals of e_g symmetry facilitate a porphyrin-to-metal charge transfer arising from the π -type a_{1u} - and a_{2u} molecular orbitals. Another class of *hyper* spectra includes porphyrinato complexes of main group elements such as tin(IV), lead(II) or arsenic(II) arising from transitions between the metal's np_z orbital to the π -type e_g orbitals of the porphyrin.⁴⁸

Completing, *hypso* absorption spectra are obtained for metalloporphyrins with d^6 to d^9 electron configuration, such as rhodium(II), nickel(II), palladium(II), copper(II) or gold(III).⁴⁹ The mixing of the filled $e_g(d_{xz,yz})$ metal orbitals with the $e_g^*(\pi)$ molecular orbitals of the porphyrinato ligand leads to the increase of the HOMO-LUMO energy gap (E_{hypso}) and the blue shift of the Soret band compared with the free-base porphyrin (Figure 1.7).⁴⁸

Based on computational studies by Ghosh and co-workers, the blue-shift of the Soret band can additionally be explained by the energetic lowering of the porphyrin's HOMO of a_{2u} symmetry arising from the interaction with the more electronegative metals such as palladium(II), platinum(II) or gold(III) compared with the closed-shell zinc(II) ion (Figure 1.5). In contrast to zinc(II) porphyrins, the higher atomic orbital coefficients at the nitrogen s atomic orbitals result in a lower energy of the porphyrin-centered a_{2u} molecular orbitals leading to a hypsochromic shift of the Soret band compared with free-base porphyrins.⁵⁰

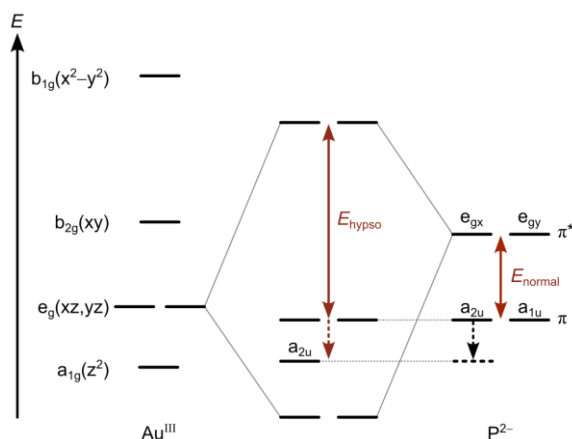


Figure 1.7 Illustration of the interaction between the gold(III) atomic orbitals ($e_g d_{xz,yz}$) and porphyrin-centered molecular orbitals (e_g, π^*) and energetic destabilization of the a_{2u} HOMO.⁵⁰⁻⁵²

The excitation of (metallo)porphyrins to the Soret band leads to the population of the S_2 state followed by fast internal conversion (IC) to the S_1 state. Weak fluorescence arising from the S_2 state has only been reported for some metal porphyrins with lifetimes in the lower picosecond range whereas the competing IC process in free-base porphyrins is dominant resulting in fluorescence or non-radiative deactivations

from the S_1 state.⁵³ However, the relatively high energy gap between the S_2 and S_1 state (approx. 6700 cm^{-1}) decelerates the IC process and, additionally, the high intensity of the $S_0 \rightarrow S_2$ transition facilitates a high radiation rate constant for the $S_2 \rightarrow S_1$ transition.⁵³

The emission spectrum of (tetraphenylporphyrinato)zinc(II) Zn(TPP) at room temperature is dominated by two bands which can be assigned to the transitions from the $S_{1,0}$ state to the first excited vibrational state $S_{0,1}$ and vibrational ground state $S_{0,0}$ of the electronic ground state. The emission bands are denoted according to the Gouterman's four orbital model with $Q(1,0)$ and $Q(0,0)$, respectively. Fluorescence quantum yield amounts to 3.3% in toluene at room temperature and 3.0% in frozen solution at 77 K.⁵³

A further radiative deactivation pathway is given by the spin-forbidden, isoenergetic intersystem-crossing (ISC) to the triplet state T_1 , vibronic relaxation followed phosphorescence ($T(1,0)$ and $T(0,0)$). The lifetime of Zn(TPP) was determined as $\tau_p = 25.5\text{ ms}$ ($\phi_p = 1.2\%$) at 77 K and 1.2 ms at room temperature, ascertained by transient absorption spectroscopy (Figure 1.8).⁵³

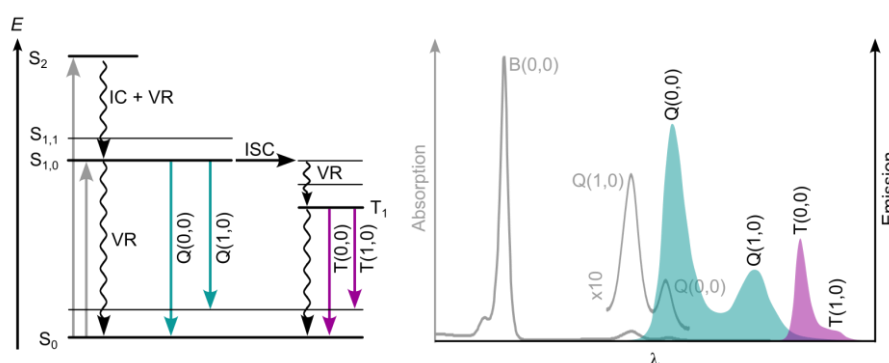


Figure 1.8 Jablonski diagram with selected excitation and relaxation pathways and typical photoluminescence spectrum of a representative (metallo)porphyrin.⁵³

Gold(III) porphyrins are used as electron acceptors in donor-chromophore dyads for the investigation of photoinduced electron transfer^{54–56} (section 1.2.3) or triplet-triplet energy transfer with different chromophores. The lowest excited singlet state S_1 has been reported to be very short-lived (240 fs), and the triplet states are typically the starting point for subsequent photophysical processes. Albinsson and co-workers studied the photophysical properties of two different *meso*-aryl- β -alkyl gold(III) porphyrins by steady-state and time-resolved absorption and emission spectroscopy dependent on the temperature (Figure 1.9). To prevent any bimolecular processes the gold(III) porphyrins were immobilized in a solid matrix of poly(ethylmethacrylate) (Figure 1.9).⁵⁷

The studied gold(III) porphyrins exhibited phosphorescence at low temperatures with quantum yields of 4% and 8% at 4 K, whereas above 200 K no phosphorescence has been detectable.⁵⁷

The excitation to the Q-band (518 and 524 nm, respectively) is followed the optically forbidden $^1\text{LMCT}$ resulting in a “dark state” with a lifetime of 20 to 50 ns in rigidified media. This state acts as gate for the

triplet states T_{1A} and T_{1B} , respectively, which are populated and depopulated independently from each other at temperatures lower than 200 K with lifetimes of 143 and 21 μs for $[\text{Au}(\text{P1})]^+$ and 150 and 30 μs for $[\text{Au}(\text{P2})]^+$. Based on TDDFT calculations, these two triplet states can be assigned to the transitions $(a_{2u})^2(a_{1u})^1 \rightarrow (e_{gx})^1(e_{gy})^0$ or $(e_{gx})^0(e_{gy})^1$ (B_{1u}) and $(a_{2u})^1(a_{1u})^2 \rightarrow (e_{gx})^1(e_{gy})^0$ or $(e_{gx})^0(e_{gy})^1$ (B_{1u}), respectively.⁵⁷

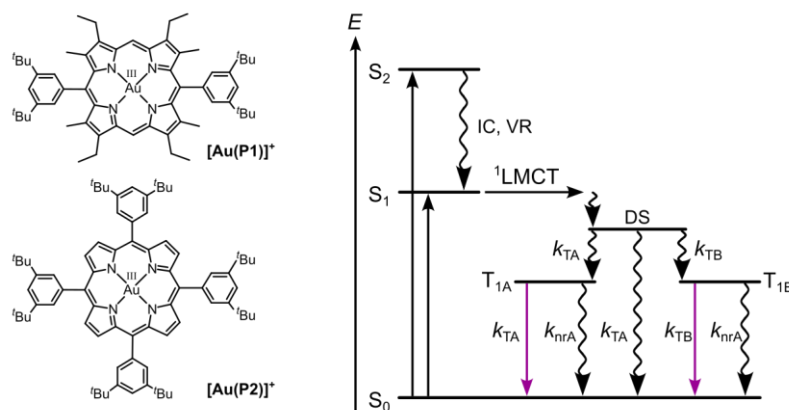


Figure 1.9 Molecular structure of the relevant gold(III) porphyrin complexes $[\text{Au}(\text{P1})]^+$ and $[\text{Au}(\text{P1})]^+$ and Jablonski diagram with the relevant excitation and relaxation pathways. DS = “dark state”.⁵⁷

A molecule can absorb a photon of the energy with a wavelength that correspond to the energy gap between the electronic ground state and excited state. Therefore, the electric field vector E of the electromagnetic wave must interact with the electric transition dipole moment of the molecule. The absorption is – simply spoken – accompanied by the redistribution of electron density leading to an electron density distribution that differs from that in the electronic ground state. The resulting instantaneous electric transition dipole moment μ is determined by the electron displacement and the magnitude is proportional to the intensity of the transition. If two or more molecules are located in close spatial proximity, the individual electronic transitions cannot be treated independently from each other. The electronic transitions are delocalized over the entire assembly of the molecules via the so-called excitonic coupling mediated by Coulomb interaction.^{53,58}

The excess of excitonic coupling J depends on the magnitude and mutual orientation of the individual electric transition dipole moments μ_1 and μ_2 , respectively, and the center-to-center distance r between them (equation 1).⁵⁸

$$J = \frac{\mu_1 \mu_2}{r^3} [\cos(\phi) - 3 \cos^2(\alpha)] \quad (1)$$

In case of the excitonic coupling of two energetically degenerate electronic states a set of two non-degenerate excited states is formed, which can be described by the linear combination of the individual

excited states of each molecule. The parallel (collinear) arrangement (head-to-tail) with a slip angle of $\phi = 0^\circ$ between the electric dipole moments and a fixed center-to-center distance r lead to a negative exciton coupling energy J and a high-energy out-of-phase ($\mu_{\text{sum}} = 0$) and a low-energy in-phase coupling ($\mu_{\text{sum}} \neq 0$) of the individual electric dipole moments. The transition to the higher electronic state is forbidden whereas the transition to the low-energy state is allowed. The maximum of the absorption band displays a hypsochromic shift compared to the absorption band of the individual chromophores. These types of aggregates are called J-type, named after its discoverer Edward Jelley.⁵⁹ Upon increasing slip angle, the excitonic energy difference $2J$ is reduced. At a slip angle of 54.7° ($1 - 3 \cos^2(\alpha) = 0$) the excitonic coupling amounts to zero and the changes in the absorption spectrum are only due to van-der-Waals interactions (E_{vdW}) since both excitonic states are energetically degenerate. For a sandwich-type alignment ($\alpha = 90^\circ$) of the electric transition dipole moments of the individual chromophores the exciton energy $2J$ is positive. The high-energy in-phase coupling is allowed, whereas the low-energy out-of-phase coupling is forbidden. These H-type called aggregates exhibit a hypsochromic shift of the maximum of the absorption band and typically a strong quenching of luminescence, since the excitation to the high-energy exciton state is followed by internal conversion to the low-energy non-emissive dark state.⁵⁸ A rotation angle $0^\circ < \phi < 90^\circ$ (oblique orientation) between both electric transition dipole moments will lead to a splitting of the exciton states and the transition to the low- and high-energy states are allowed. The sum transition dipole moment is different from zero resulting to a hypsochromic and bathochromic shift of the absorption band compared with the individual chromophores. For a rotation angle $\phi \neq 0^\circ$ the exciton energy splitting $2J$ amounts to zero leading to two degenerate exciton state and a single absorption band.⁵⁸

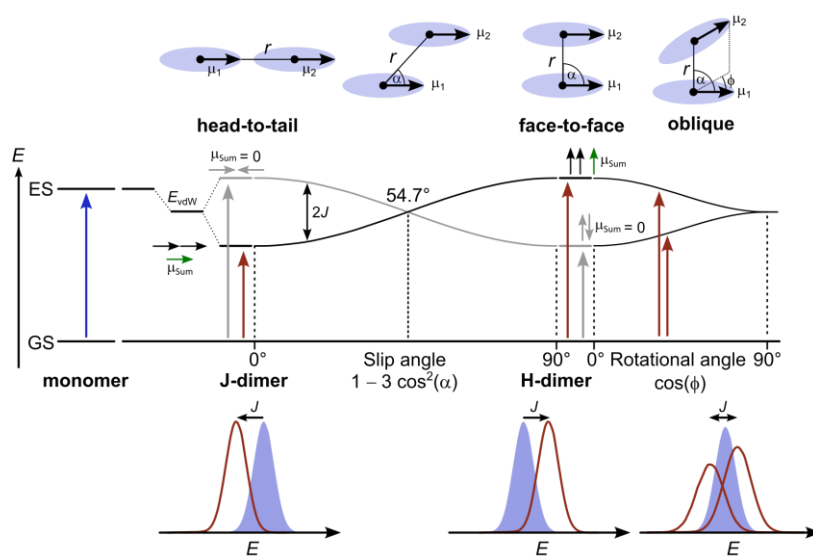


Figure 1.10 Energy diagram for two excitonically coupled electric transition dipole moments μ_1 and μ_2 dependent on the center-to-center distance r and mutual orientation defined by the slip angle α and rotational angle ϕ and changes in absorption spectra due to excitonic coupling J .^{51,58}

The unsubstituted macrocycles of porphine and its mate corrole exhibit almost geometric planarity. Inter- and intramolecular effects, including bulky substituents at the *meso*- and/or β -positions, metalation, axial ligands or crystal effects, can induce strong macrocyclic distortions (see: Figure 1.12). The axial coordination of oxygen to the high spin iron(II) center in deoxyhemoglobin and subsequent release from oxyhemoglobin in the muscle tissues is accompanied by a strong conformational change of the porphyrin (Fe-protoporphyrin IX) in both cases.⁶⁰

For a quantitative description and classification of the conformational distortions of (metallo)porphyrins, Shelnutz established the normal-coordinate structural decomposition (NSD) method.⁶¹ The intramolecular degrees of freedom for a n -atom molecule is given by $3n - 6$. Considering the 24-atom macrocycle of porphyrin the total number of degrees of freedom amount to 66 modes, which are further subdivided into 21 ($24 - 3$) *out-of-plane* (OOP) and 45 ($2 \cdot 23 - 3$) *in-plane* (IP) modes. The D_{4h} point group features four *out-of-plane* distortions (Figure 1.11) and each of them corresponds to a conformation mode. Besides the irreducible representations B_{1u} , B_{2u} , A_{2u} , $E_g(x)$, $E_g(y)$ and A_{1u} , the more descriptive terms saddling (sad), ruffling (ruf), domed (dom), waving x (wav x), waving (wav y) and propelling (pro) have become established (Figure 1.11). A frequently used illustrative description of the conformational distortions is the plot of the deviation of each carbon atom the porphyrin's macrocycle backbone from the mean plane, given in Å, as a function of the atom position. Therefore, the porphyrin is formally opened, as illustrated for the B_{1u} (saddling) distortion, between a *meso*- and α -carbon atom and the resulting chain is suspended like on a string.⁶¹ The NSD method can also be applied for the quantitative description of geometric distortions of the corrole macrocycle. While the illustrative, porphyrin-adapted descriptions of the distortions are conserved, the lower symmetry of the corrole macrocycle must be taken into account. The loss of the mirror plane perpendicular to the z -axis implicated a loss of the indexed symmetry elements of the inversion symmetry "g" and "u". The irreducible representations are adjusted to B_1 (doming, ruffling and waving x), A_2 (saddling, waving y and propelling).^{61,62}

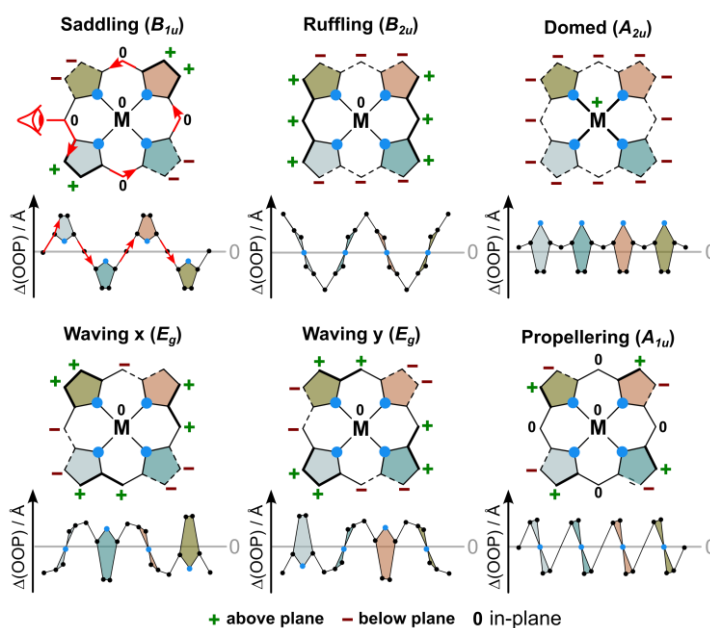


Figure 1.11 Out-of-plane (OOP) distortions of porphyrins extracted from normal-coordinate decomposition (NSD) method with trivial names and symmetry denotation.^{60–62}

1.1.2 Performance on the Highest Level – Porphyrins in Nature

The outstanding importance of porphyrins and their metal complexes for natural processes, including light-harvesting, energy transfer and charge separation in the photosynthesis, the oxygen transport in the blood stream and the storage in the muscle tissues, as well as the final consumption of oxygen in the mitochondria of eukaryotes, has resulted in several Nobel Prizes awarded to scientists, who have contributed to the research on the structure and functionality of porphyrin containing enzymes. Hans Fischer has been awarded “for his researches into the constitution of haemin and chlorophyll”,⁶³ Max Perutz and John Kendrew for “their studies on the structure of hemoglobin and myoglobin”⁶⁴ or Robert Woodward for the natural product “synthesis of chlorophyll or vitamin B₁₂”,⁶⁴ to mention but a few.

In this section, the structural and photophysical properties of (metallo)porphyrins, introduced in section 1.1.1, will come to light based on selected examples from nature and with special respect to this work, namely redox-activity, structural flexibility as well as energy transfer and electron transport (Figure 1.12).

A The cytochrome P450 enzyme, located in the endoplasmatic reticulum of cells and mainly found in the liver, catalyses the oxygenation of inert organic substances. This includes the monooxygenation of fatty acids, amino acids or hormones. However, in the absence of aliphatic chains, the enzyme catalyzes the epoxidation of benzene or benzo[a]pyrene to the carcinogenic epoxide derivatives.^{1,65}

The reaction center of cytochrome P450 consists of a heme-containing prosthetic group (protoporphyrin IX). The low-spin iron(III) center is axially tied to the enzyme by a cysteine thiolate ligand and weakly coordinated by a water molecule on the opposite side. The next steps involves the

1.1 I Porphyrins – Remarkable Allrounder

coordination of the substrate (RH), loss of water and the change of the electron configuration of iron(III) from low-spin to high-spin involving a pronounced *out-of-plane* distortion of the porphyrin with a dominating A_{2u} (dom) mode (see: section 1.1.1). In the further course of the catalytic cycle, iron formally adopts the oxidation state +5. However, the non-innocent nature of the porphyrin ligand prevents the formation of this high-valent oxidation state by the donation of one electron for the twofold reduction of the hydroperoxyl HOO^- at this step of the catalysis. The remained positive charge is distributed and therefore stabilized on the porphyrin macrocycle, whereas the high charge of iron(IV) is stabilized by the π -donating thiolato ligand. In the following step the oxygen is transferred on the substrate RH (“rebound”) yielding both the monooxygenated product and cytochrome P450 in its resting state.¹

B The tetrameric hemoglobin and monomeric myoglobin are further prominent representatives for heme-containing enzymes. They share the same prosthetic group as cytochrome P450, however the iron center features a high-spin d^6 electron configuration. The iron(II) center is axially coordinated by a proximal histidine and slightly dislocated by 400 pm above the significantly domed (A_{2u}) porphyrin’s mean plane. The histidine assisted coordination of oxygen to the iron(II) center invokes the change of the electron configuration from high-spin to low-spin, the oxidation to iron(III) under superoxide formation and the decrease of the ionic radius from 78 to 61 pm. The contracted low-spin iron(II) center perfectly fits into the macrocyclic plane. The accompanied local geometric changes induces in all further hemoglobin subunits structural changes further increasing the affinity to bind oxygen (cooperative effect).¹

C The light-harvesting complex (LHC) of the photosynthesis apparatus consists, besides carotenoids, of the magnesium(II) coordinating chlorophylls nestling in the thylakoid membrane of chloroplasts and cyanobacteria. The molar absorption coefficients (up to $5 \cdot 10^5 \text{ M}^{-1} \text{ cm}^{-1}$) over a broad range of the electromagnetic spectrum enable the effective absorption of the diffuse sunlight, and concomitantly an immediate energy transfer, which can be described by the Förster mechanism, to the reaction center.⁶⁶ This requires a well-defined mutual spatial orientation and distance of the chlorophylls. This is ensured by the aliphatic phytyl side-chain anchored in the thylakoid membrane. The reaction center consists of two chlorophyll units arranged cofacially to each other, whose collective energy level is lower than each individual energy level due to excitonic interactions (Figure 1.7, right). The high negative charge in the reaction center is used for the reduction of NADP^+ to NADPH, which is essential for the synthesis of glucose. The high positive charge left behind in photosystem II is used for the oxidation of water to oxygen under the catalytic influence on the manganese- and calcium-containing oxygen evolving complex (OEC).^{1,67}

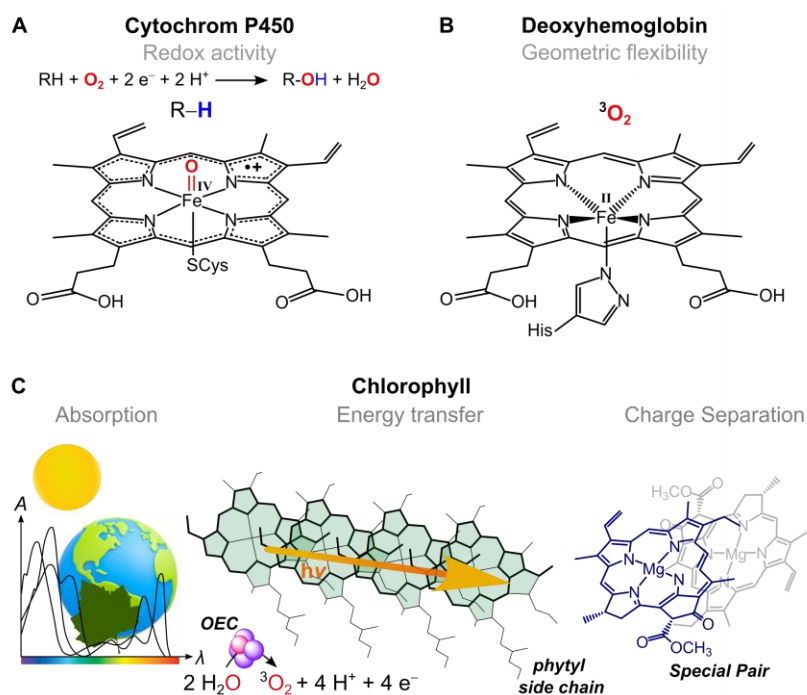


Figure 1.12 Selected geometric and electronic features of metalloporphyrins involved in fundamental biochemical or physical processes in nature and discussed in these subsections (A-C).^{1-3,65,67}

The cytochrome c oxidase is located in the inner mitochondrial membrane and catalyses the four proton four electron reduction of oxygen to water. It can be therefore seen as the counterpart of the oxygen-evolving complex and constitutes one of the most prominent natural representatives of two redox-active metal centers working in concert for the activation of a small molecule. The entire complex consists of 14 subunits and is equipped with a tailored ensemble of cytochromes and copper centers ensuring the rapid electron transfer to the reaction center.¹

The catalytically active reaction center consists of iron(II), appearing as cytochrome a_3 , and a copper(I) center at a distance of 4.5 Å. The iron(II) center of cytochrome a_3 features a high-spin d^6 electron configuration and a total spin of $S = 2$, which is the ideal coordination site for triplet oxygen. The diamagnetic copper(I) center features a d^{10} electron configuration and is coordinated by three histidines, while one coordination site remains available for oxygen. The oxygen is incrementally reduced in a cooperative redox-active reaction by both the iron center and the copper center. The coordination of triplet oxygen to the h.s. iron(II), leading to l.s. iron(III), is followed by a concerted twofold reduction of oxygen to the bridging (hydro)peroxo ligand and regeneration of the tyrosine radical anion to the tyrosinate. The unhampered entry of several protons in the further course of the catalytic cycle initiates the subsequent oxidation to water.^{1,68,69}

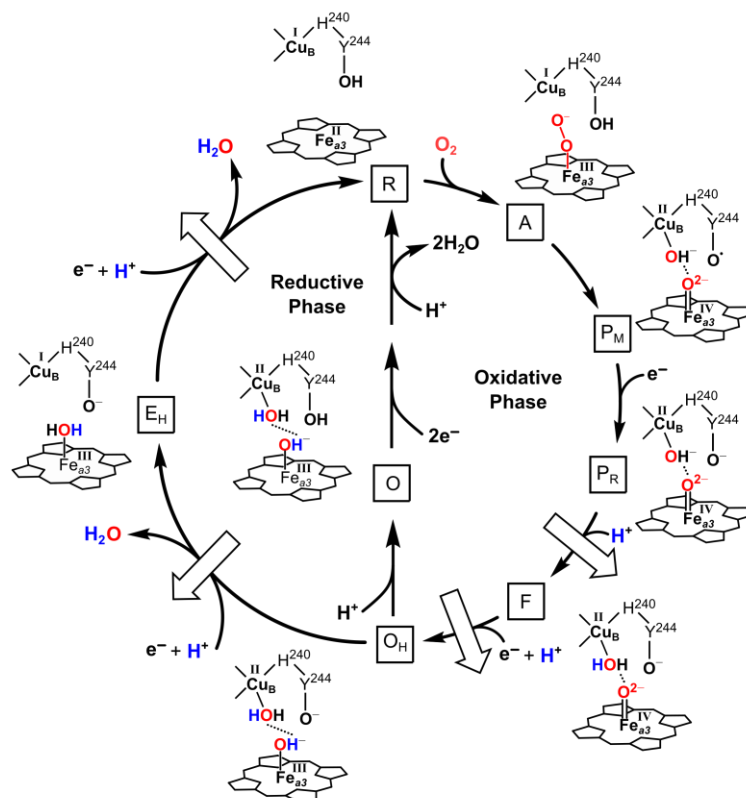


Figure 1.13 Catalytic cycle of the cytochrome c oxidase.⁶⁸

The targeted metabolism of oxygen to water requires a large integral membrane enzyme consisting of 13 subunits. The cytochrome c oxidase, as well as the photosynthetic apparatus along with the “special pair” are impressive examples for the collaboration of metalloporphyrins in nature.

The following section will outline different strategies for the chemical synthesis of mono- and bis(porphyrins).

1.1.3 Backstage – Chemical Synthesis of Porphyrins

The first synthesis of porphine by Hans Fischer in 1936 merely required one step – the reaction of pyrrole-2-carboxaldehyde in boiling formic acid in the presence of ethanol. The author’s note that only 17 mg of porphine were obtained from 30 g of the starting material – this corresponds to a yield of less than 1 percent – already gave an indication of the low yields typically associated with the porphyrin synthesis. The author’s further note that a “resinous, black mass” was formed as main product – not suitable for analyses – gave a first indication of the nature of the formed by-products: The desired cyclic assembly of four pyrrole units in a condensation reaction is competing with the continuous linear condensation.⁷

In the following decades, further important foundations have been laid for a conceptual porphyrin ligand design, and ongoing research has by no means stopped. Among these foundations are, from a historical

CHAPTER 1 | Introduction

perspective, the syntheses of heme *b* by Hans Fischer, as well as the first total syntheses of chlorophyll *a* and vitamin B₁₂ by the groups of Woodward and Eschenmoser, respectively.⁷⁰

The research groups of McDonald and Lindsey predominantly focused on symmetrically and asymmetrically *meso*-aryl functionalized porphyrins (section 1.1.1) based on the targeted linkage of pre-functionalized dipyrromethanes bearing the latter *meso* aryl-substituents. The simplest representative of the *meso* aryl-substituted porphyrin is the *S*₄ symmetric 5,10,15,20-tetraphenylporphyrin H₂TPP. The first syntheses was accomplished by Rothmund and Adler-Longo by the reaction of pyrrole and benzaldehyde in the presence of propionic acid. Lindsey further optimized this procedure by the use of Lewis acids like BF₃ · Et₂O or trifluoroacetic acid as Brønsted acid for the initial formation of the reduced porphyrinogen and subsequent oxidation with 1,4-benzoquinones.^{71–73}

(*Meso*-tetraarylporphyrinato)metal complexes bearing asymmetric substituents patterns are valuable as sensitizer or electron acceptor in artificial photosynthesis systems. The electronic finetuning of the acceptor or donor units allows direct influence on the rates of forward- and backward electron transfer and the lifetime of the charge-shifted state.^{8,54–56}

The synthesis of free-base β -substituted porphyrins (Figure 1.14) requires a different strategy than that of *meso*-tetraarylporphyrins. For the further discussion in the context of this work, the β -alkylsubstituted porphyrins are subdivided into four types (A-D).⁷⁴

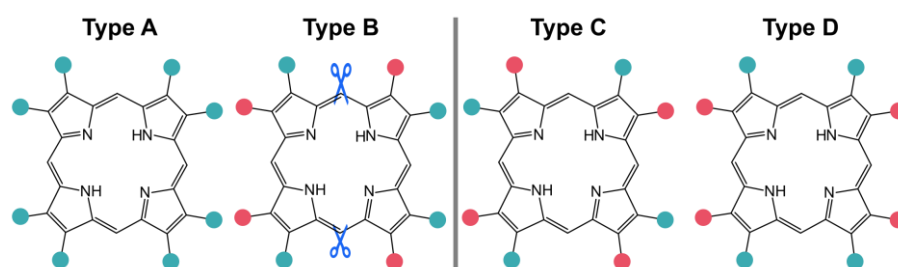


Figure 1.14 Different types (A-D) of free-base β -alkyl-substituted porphyrins.⁷⁴

The construction of these porphyrins is carried out by the use of pyrrolic building blocks bearing already the alkyl substituents at the positions 3 and 4 (pre-functionalization).⁷⁵

The symmetric eightfold β -substituted 2,3,7,8,12,13,17,18-octaethylporphyrin H₂OEP (type A) holds a similar significance in academic research and industry as H₂TPP and appears as the simplest β -octaalkylporphyrin. The required 3,4-dialkylsubstituted pyrrole is constructed by a [3+2]-cycloaddition reaction (Barton-Zard) between ethyl isocyanoacetate and 3-nitro-hex-3-ene under basic conditions (Figure 1.15). The subsequent reduction of the ethylcarboxylate functional group to hydroxymethyl fits the pyrrole for the cyclisation yielding the corresponding porphyrinogen, which is then oxidized to H₂OEP – air is typically sufficient. One of the fundamental differences in the syntheses of *meso*-tetraaryl-

1.1 | Porphyrins – Remarkable Allrounder

substituted and β -substituted porphyrins is the origin of the *meso*-carbon atom. In the first case it is provided by the benzaldehyde, while in the second case it is provided by the pyrrole.^{74,76,77}

The creation of unsymmetrically β -substituted porphyrins in the style of their natural prototype heme *b* (Figure 1.1) is the supreme discipline of the porphyrin synthesis. Type B porphyrins require a more sophisticated synthesis strategy than those of type A (Figure 1.14). From the retrosynthetic perspective, the porphyrin is built up out of two mirror-symmetrical halves – the left and the right part – if the β -substituents are not taken into account. The methine bridges between both parts are formally broken in their center leading to two dipyrromethane building blocks bearing the opposite substituent pattern. The dipyrromethane modules are derived from the corresponding pyrrole building blocks, which are synthetically accessible from commercially available educts (Figure 1.15).^{74,76–79}

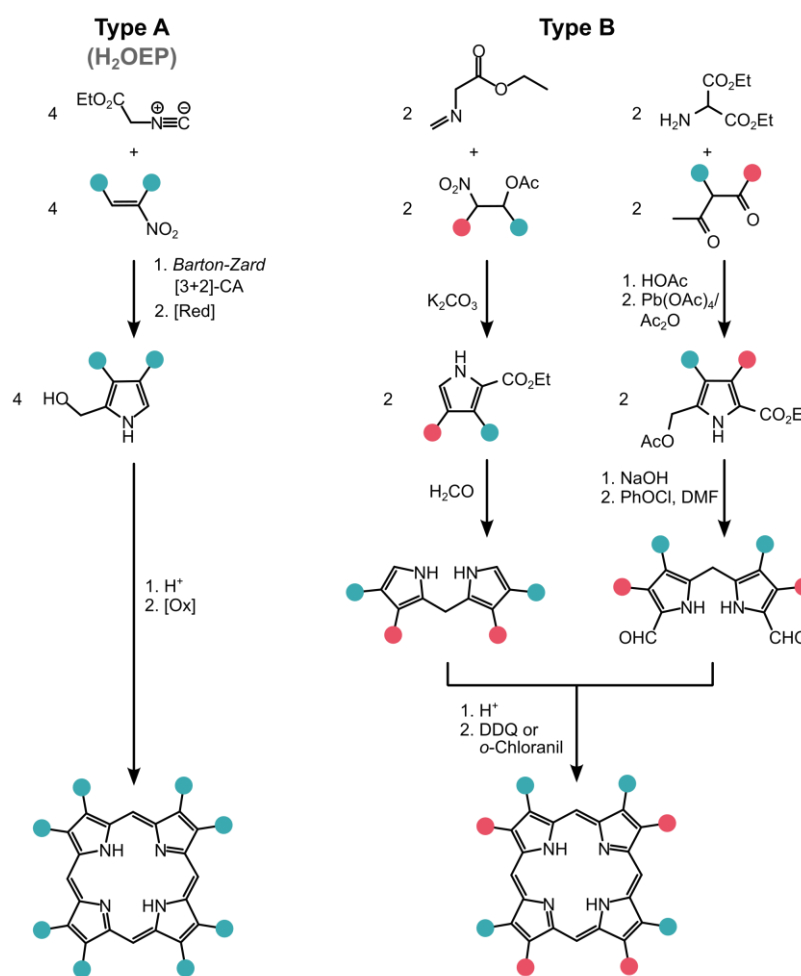


Figure 1.15 Scheme for the synthesis of type A (H₂OEP) and type B free-base porphyrins.^{74,76–80}

The attachment of two type B β -alkyl-substituted monoporphyryns to a dibenzofuran or comparable spacer for the cofacial mutual assembly of two monoporphyryn subunits requires a modified synthesis strategy (Figure 1.16). The first branch involves the regioselective dilithiation of dibenzofuran at the positions 4 and 6. The formylation of these positions is achieved by dimethylformamid followed by

hydrolysis according to the Vilsmeier-Haack procedure. Each of these carbon atoms of the formyl groups serves as anchor point for the porphyrin. The second branch contains the Barton-Zard built up of the pyrrole units bearing an unsubstituted position 2. The ethylester group at position 5 ensures the targeted C-C coupling between C⁴ and C⁶ of the dibenzofuran spacer and the C² carbon atom of the pyrrole. The third branch entails the construction of the appropriate dipyrromethane. The building blocks of the three paths are now ready for the final 2+2 McDonald condensation. For this, both reactants are suspended in methanol or THF under the exclusion of light and oxygen. The dropwise addition of *p*-toluenesulfonic acid or trifluoroacetic acid over several hours yields the highly reactive dipyrromethane-dicarbonyl, which further reacts with the dibenzofuran-bridged dipyrromethanes obtained from branches 1 and 2. Subsequent oxidation of the porphyrinogen, applying DDQ (2,3-dichloro-5,6-dicyano-1,4-benzoquinone) or *o*-chloranil, affords the free-base cofacial bis(porphyrin) in yields usually ranging between 15 and 20%. The competition between the cyclization and oligomerization is highly sensitive to the concentration of acid, dipyrromethane building blocks and reaction time. Chang and Lindsey have optimized these reaction conditions in their pioneering studies. However, there is no generally valid recipe for the construction of porphyrins of all types. Each new synthesis requires an adjustment of the reaction parameters.^{71,74,81}

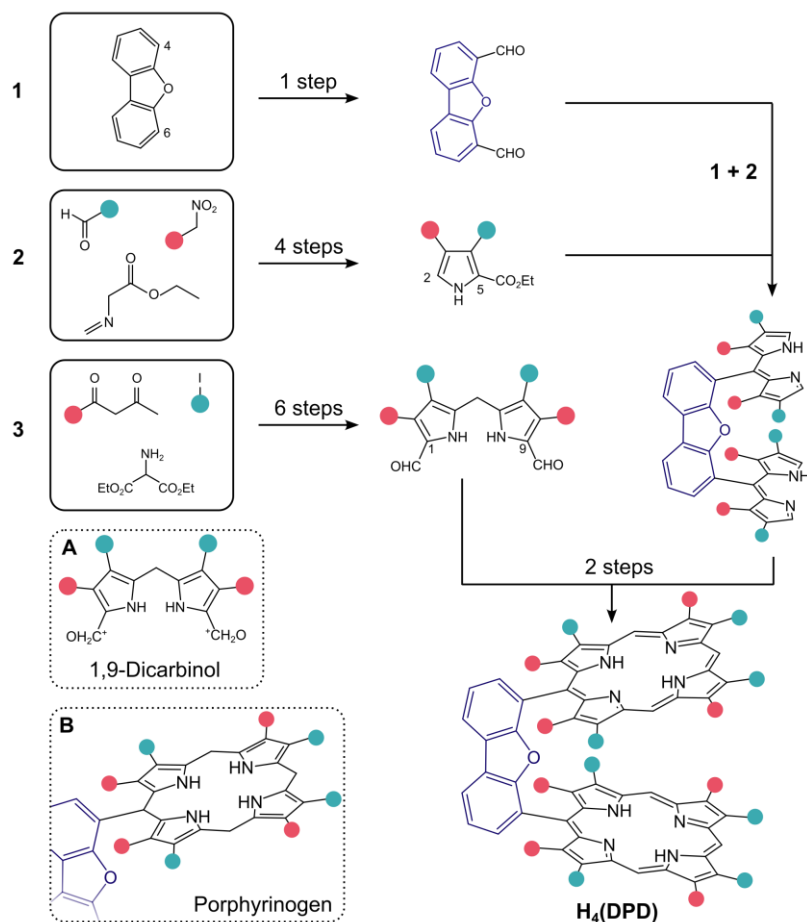


Figure 1.16 Scheme for the synthesis of the free-base cofacial bis(porphyrin) H₄DPD including the molecular formulas of the intermediate 1,9-dicarbonyl and porphyrinogen.⁸¹

1.1 | Porphyrins – Remarkable Allrounder

This type of cofacial molecular porphyrin arrangement opened the door for versatile applications such as the cooperative binuclear redox-mediated transformation of a substrate or the study of the energy transfer between both porphyrin subunits analogous to their natural prototypes (section 1.1.2).^{52,82,83} Depending on the requirements, given by the potential applications, conceptional porphyrin- and spacer design allows the targeted fine-tuning of the overall geometric, electronic and photophysical properties of the “Pacman”-like bis(porphyrins). This is achieved by the choice of the spacer (length, lateral and axial flexibility), number, kind and positions of the substituents at the porphyrin subunits, as well as by the selection of the metal center (Figure 1.17). Typical spacer of high lateral and axial rigidity are dimethylxanthene, anthracene, dibenzofuran or dibenzothiofuran, typical representatives of flexible spacers are ethane and ethene. The attachment of bulky substituents at the *meso*-positions trans to the spacer can induce a more open form of the bis(porphyrin) due to steric hindrance. This geometric change can have an effect on the selectivity of a catalysed reaction as presented below (section 1.1.4).⁸³ Both the energy of the orbitals and the electron configuration of the coordinated metal affect the energy of the frontier molecular orbitals of the porphyrin subunits (section 1.1.1).

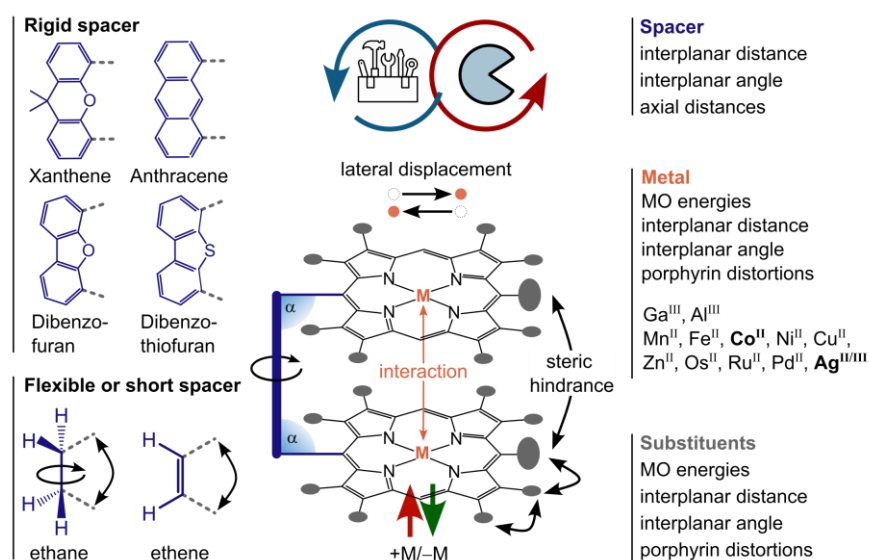


Figure 1.17 Illustration of the geometric and electronic influences of the different building blocks on the overall complex geometry and representative rigid and flexible spacer.

The groups of Nocera and Guillard synthesized, independently of each other, cofacial palladium(II) bis(porphyrin) complexes and the free-base bis(porphyrins), each of them either anchored by a dibenzofuran- or xanthene spacer (Figure 1.18). The palladium complexes Pd₂(DPD) and Pd₂(DPX) show phosphorescence, whereas the free-base bis(porphyrins) H₄(DPD) and H₄(DPX) exhibit fluorescence. Nocera’s group additionally synthesized the corresponding (monoporphyrinato) palladium(II) complexes for comparison reasons.^{52,81,82}

The Soret band of Pd₂(DPX) is blue-shifted compared with the comparative (monoporphyrinato)palladium(II) complex (386 and 397 nm), demonstrating excitonic coupling

between both (porphyrin)palladium(II) subunits. This effect is less pronounced in Pd₂(DPD) due to the larger bite angle and only visible in a slight blue-shift of the Q bands (from 515 and 648 nm to 511 and 546 nm) while the Soret band remains unaffected in its energetic position (391 nm) compared with the monomeric (porphyrinato)palladium(II) complex.⁸²

The excitation of the Pd₂(DPD) or Pd₂(DPX) complexes in the Q-band region initially populates the singlet excited state (¹[Pd₂(DPD)] and ¹[Pd₂(DPX)]) followed by effective fast intersystem crossing (ISC), arising from the heavy palladium(II) ion, which induces a strong spin-orbit coupling and therefore weakens the spin-selection rule, to the triplet state ³[Pd₂(DPD)] and ³[Pd₂(DPX)], respectively. The triplet-excited states of the complexes have two deactivation pathways available: The slow radiative phosphorescence pathway with typical lifetimes in the microsecond region or the fast non-radiative pathway due to geometric distortions with typical rates between $k_{nr} = 10^{11}$ and 10^{14} s^{-1} . The Pd₂(DPX) complex features a Pd-Pd distance of 3.97 Å and an interplanar angle of 3.9° in the solid state. This enforces the Pd₂(DPX) complex a more rigid geometry with pronounced electronic interaction between both porphyrins.

The Pd₂(DPD) complex features a significantly larger Pd-Pd distance of 6.81 Å and a bite angle of 11.0° resulting in an overall more flexible geometry. The constrained geometry of Pd₂(DPX) promotes the radiative phosphorescence pathway while in the case of the geometrically more flexible Pd₂(DPD) complex the non-radiative pathway becomes prevalent. This is reflected in the lower phosphorescence quantum yields ($\Phi_p = 0.0046$) and lifetimes ($\tau_p = 18.2(2) \mu\text{s}$) of the Pd₂(DPD) complex compared with the Pd₂(DPX) complex ($\Phi_p = 0.029$ and $102(3) \mu\text{s}$).⁸² The free-base porphyrins H₄(DPD) and H₄(DPX) do not undergo efficient ISC due to the absence of a heavy atom. The excitation of these bis(porphyrins) in the Q-band region populates the respective singlet excited states followed by fast radiative fluorescence or even faster non-radiative processes in case of strong geometric distortions. For this set of bis(porphyrins), the fluorescence lifetime and quantum yield decrease with larger bite angle from $\tau_F = 0.004 \mu\text{s}$ to $\tau_F = 0.0013 \mu\text{s}$ and from $\Phi_F = 0.045$ to $\Phi_F = 0.011$. This can be ascribed to the larger flexibility of the porphyrin subunits in case of H₄(DPD) than for H₄(DPX), which facilitates more efficient non-radiative deactivation pathway.⁵²

The group of Nocera showed, based on the exploratory work by Knyukshto, that the phosphorescence lifetimes of the cofacial palladium(II) bis(porphyrins) complexes are predominantly affected by the extent of the torsional flexibility around the C^{meso}-C^{aryl} bond motion in the triplet excited state and not simply by interplanar interactions.^{82,84,85} The monomeric (*meso*-monophenyletioporphyrinato)-palladium(II) complex Pd(PhEtio) exhibited a significantly reduced phosphorescence lifetime and quantum yield at room temperature compared with (etioporphyrinato)palladium(II) ($\tau_p = 1.14 \mu\text{s}$ to $\tau_p = 321 \mu\text{s}$ and from $\Phi_p = 0.000723$ to $\Phi_p = 0.0064$, respectively). The phenyl substituent induces

strong *out-of-plane* distortions, dominated by saddling, resulting in a reduced T_1-S_0 energy gap facilitating more non-radiative deactivation pathways (energy gap law).^{52,53,82}

The fundamental difference between both systems are the time scales of the relevant photophysical processes upon photoexcitation. The phosphorescence is slow due to its spin-forbidden nature. Therefore, the less distorted geometry in the excited state due to a higher complex rigidity facilitates a more effective radiative deactivation pathway as given in the more-closed $\text{Pd}_2(\text{DPD})$ complex. In contrast, the more open form of the free-base bis(porphyrin) $\text{H}_4(\text{DPD})$ displays a higher geometric flexibility, which is reflected in the lower fluorescence lifetimes compared with $\text{H}_4(\text{DPX})$.^{52,81,83}

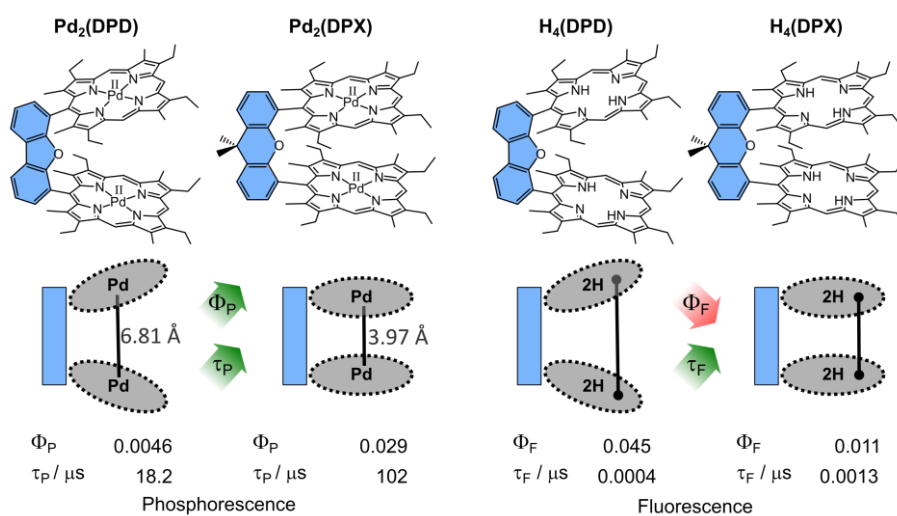


Figure 1.18 Influence of the interplanar angle of xanthene- and dibenzofuran-bridged palladium(II) and free-base bis(porphyrins) on the luminescence quantum yield Φ_P/Φ_F and lifetimes τ_P/τ_F , respectively, at room temperature.^{52,82}

1.1.4 Onstage – Pacman Complexes in Action

The group of Nocera synthesized dibenzofuran- and dimethylxanthene-bridged cofacial bis(β -octaethylporphyrinato)cobalt(II) complexes bearing different bulky aryl-substituents at the *meso*-position trans to the spacer (Figure 1.19). The binuclear cobalt(II) complexes are capable of the catalysis of the four-proton-four-electron reduction of oxygen to water under the involvement of the cobalt centers analogous to their natural $\text{Cu}^I/\text{Fe}^{\text{II}}$ -containing prototype cytochrome c oxidase (Figure 1.26).

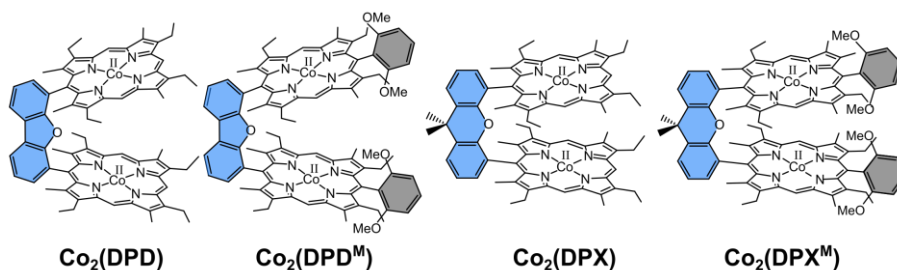


Figure 1.19 Molecular structures of cofacial bis(porphyrinato)cobalt(II) complexes used as catalysts for the proton-coupled oxygen reduction.^{83,86}

CHAPTER 1 | Introduction

The spacers ensure the cofacial mutual presentation of the porphyrin subunits associated with a high lateral rigidity. The bulky 2,6-dimethylphenyl substituents induce a larger interplanar angle due to steric hindrance compared with the unsubstituted complexes and could inhibit the just-in-time-delivery of four protons instead of two as required for the formation of water instead of hydrogen peroxide. The Co^{II}-Co^{II}-distance of the Co₂(DPX) complex in the solid state (4.582 Å) falls within the same range as the Cu^I/Fe^{II} distance of the cytochrome c oxidase (4.5 Å), whereas the Co^{II}-Co^{II} distance in Co₂(DPD) amounts to 8.624 Å.⁸⁶

The μ¹-μ¹ end-on coordination of oxygen to the cobalt-centers, subsequent ground state activation and reduction requires a proximal orientation of the two cobalt(II) centers. At the same time, this type of coordination claims a high geometric flexibility from the porphyrin subunits – no insurmountable obstacle as demonstrated by the numerous examples of porphyrinoid gymnastics of their natural counterparts (Figure 1.11 and section 1.1.2).

The effect of the spacer on the collaborative redox properties is nicely reflected in the electrochemical data. The more open cobalt(II) complex Co₂(DPD) exhibits a single Co^{II}/Co^{III} two-electron oxidation wave at +0.33 V whereas the closed form Co₂(DPX) shows two separate Co^{II}/Co^{III} one-electron oxidations at +0.28 V and +0.17 V vs. Ag/AgCl, respectively. Hence, the dibenzofuran spacer imposes the cobalt centers in Co₂(DPD) a larger spatial distance compared with the xanthene spacer in Co₂(DPX) preventing them from interfering electronically with each other. The oxidation potentials of the *meso*-aryl-substituted complexes Co₂(DPD^M) and Co₂(DPX^M) are only marginally shifted (Figure 1.19). The selectivity for the catalytic reduction of oxygen to water should be therefore only influenced by the *meso*-substituents regulated proton delivery and not by the redox competence of the cobalt centers. The Co₂(DPD) complex featured a selectivity of 80%, the Co₂(DPX) complex of 72% for the reduction of oxygen to water. The selectivity was lower for the *meso*-substituted complexes Co₂(DPD^M) and Co₂(DPX^M), featuring selectivities of 46% and 52%, respectively. The attachment of the bulky-*meso*-substituents eventuated in a reduced selectivity for the reduction to water.⁸³

Nocera and co-workers proposed a catalytic cycle for the activation of the oxygen bond and subsequent stepwise reduction to H₂O or H₂O₂. According to that, the dicationic Co^{III}/Co^{III} complex does not exhibit catalytic activity, whereas the monocationic Co^{II}/Co^{III} and neutral Co^{II}/Co^{II} complexes are able to bind oxygen (state 1). Based on EPR studies the [Co^{II}Co^{III}(O₂)(bisorphyrin)]⁺ complex (state 2) forms the beginning of the catalytic cycle. The delivery of protons to this highly basic reaction core implies a multielectron transport avoiding the one-electron reduction under the initial formation of [Co^{III}(O₂)Co^{II}(bisorphyrin)] (state 2a) and subsequent release of H₂O₂ under the formation of the [Co^{III}Co^{III}(bisorphyrin)]. In case of the *meso*-aryl-substituted cobalt complexes Co₂(DPD^M) and

$\text{Co}_2(\text{DPX}^{\text{M}})$, the high basicity of the $[\text{Co}^{\text{II}}\text{Co}^{\text{III}}(\text{O}_2)(\text{bisporphyrin})]^+$ intermediate cannot be addressed due to the inhibited proton transfer – the production of H_2O_2 is favoured.⁸³

For an unrestrained proton delivery – as given in the unsubstituted complexes $\text{Co}_2(\text{DPD}^{\text{M}})$ and $\text{Co}_2(\text{DPX}^{\text{M}})$, the following oxygen bond cleavage is achieved by the protonation (state 3) and ensuing concerted two electron reduction under the formation of the mixed-valent $[\text{Co}^{\text{III}}(\text{OH})\text{Co}^{\text{IV}}(\text{O})(\text{bisporphyrin})]$ complex (state 4). This intermediate is similar to the $\text{Fe}^{\text{IV}}\text{-oxo}/\text{Cu}^{\text{II}}\text{-hydroxido } \text{P}_{\text{R}}$ state in the catalytic cycle of the cytochrome c oxidase (Figure 1.13). Since the stability of this Co^{IV} intermediate has not been conclusively determined, a direct twofold reduction to $[\text{Co}^{\text{III}}(\text{OH})\text{Co}^{\text{III}}(\text{OH})(\text{bisporphyrin})]$ is also conceivable (state 5). The double protonation forms the desired product H_2O under the regeneration of the catalyst in its resting state $\text{Co}_2(\text{bisporphyrin})$.⁸³

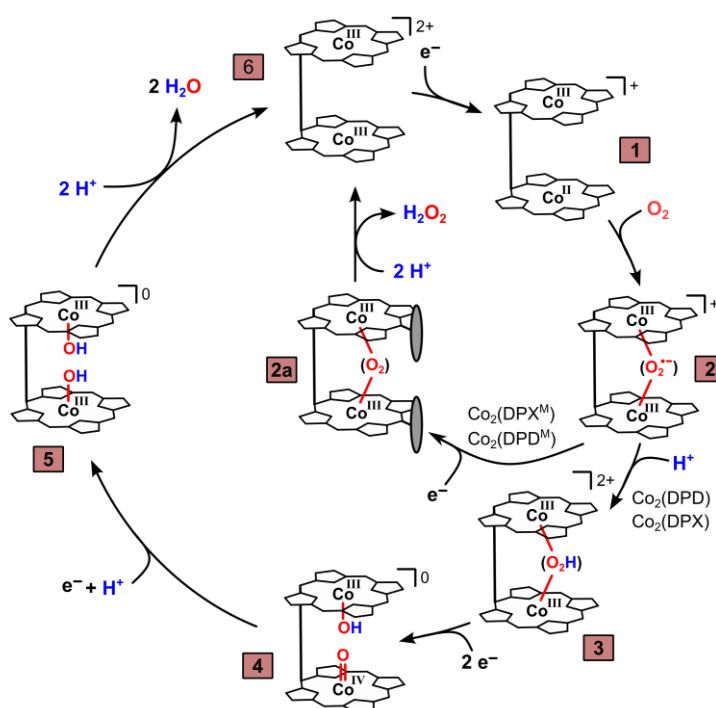


Figure 1.20 Catalytic cycle of a cofacial bis(porphyrinato)cobalt(III) complex for the reduction of oxygen to water.⁸³

As demonstrated above, the catalytic applicability of bis(porphyrinato) metal complexes requires a proximal presentation of the two-metals centers to the substrate and a spacious porphyrin cavity with unhindered access for the substrate and further reaction equivalents like protons. This is exclusively guaranteed by rigid spacers like dibenzofuran or xanthene.

However, highly flexible bridging units, such as ethane or ethene, fundamentally change the geometric and electronic properties of the free-base bis(porphyrins) and their corresponding metal complexes. The

CHAPTER 1 | Introduction

following complexes demonstrate the significant influence of metallophilic interactions on the overarching complex geometry when using flexible bridges.

The type A ethane-bridged free-base bis(porphyrins) are obtained by a McMurry coupling between two *meso*-formyl-octaethylporphyrins or Stille cross coupling reaction between the *meso*-halide-octaethylporphyrin and the 1,2-bis(trialkylstannyl)ethene.^{80,87} The ethane bridged bis(porphyrins) are synthesized in a condensation reaction between two *meso*-hydroxymethyl-octaethylporphyrins. The metallation was accomplished by the corresponding silver acetate salt.⁸⁸ The electrochemical characterization of the ethene-bridge silver(II) bis(porphyrin) unveiled a strong electronic communication between both silver(II) centers due to the presence of two Ag^{II}/Ag^{III} one-electron-oxidation waves (+0.20 V and +0.40 V vs. Ag/AgCl). The absorption spectra neither showed any silver-to-porphyrin charge transfer bands nor a decrease of the intensity of the Soret bands. Both indicators for an oxidation under the exclusion of the porphyrin ligand. In the solid state the silver-silver-distances become smaller upon one- and twofold oxidation from 3.611 Å to 3.534 Å in the mixed-valent complex and finally to 3.463 Å. The lateral shift remains nearly unaffected in the mixed-valent Ag^{II}/Ag^{III} complex (1.42 Å and 1.41 Å), but it is reduced to 1.07 Å in the Ag^{III}/Ag^{III} complex. The parent ethane-bridged complex exhibits a significantly larger Ag^{II}/Ag^{II} distance of 5.824 Å, which is reduced to 3.463 Å in the Ag^{III}/Ag^{III} complex (3.659 Å for Ag^{II}/Ag^{III}). The lateral shift is reduced from 4.82 Å to 4.82 Å and finally to 0.96 Å.⁸⁹⁻⁹¹

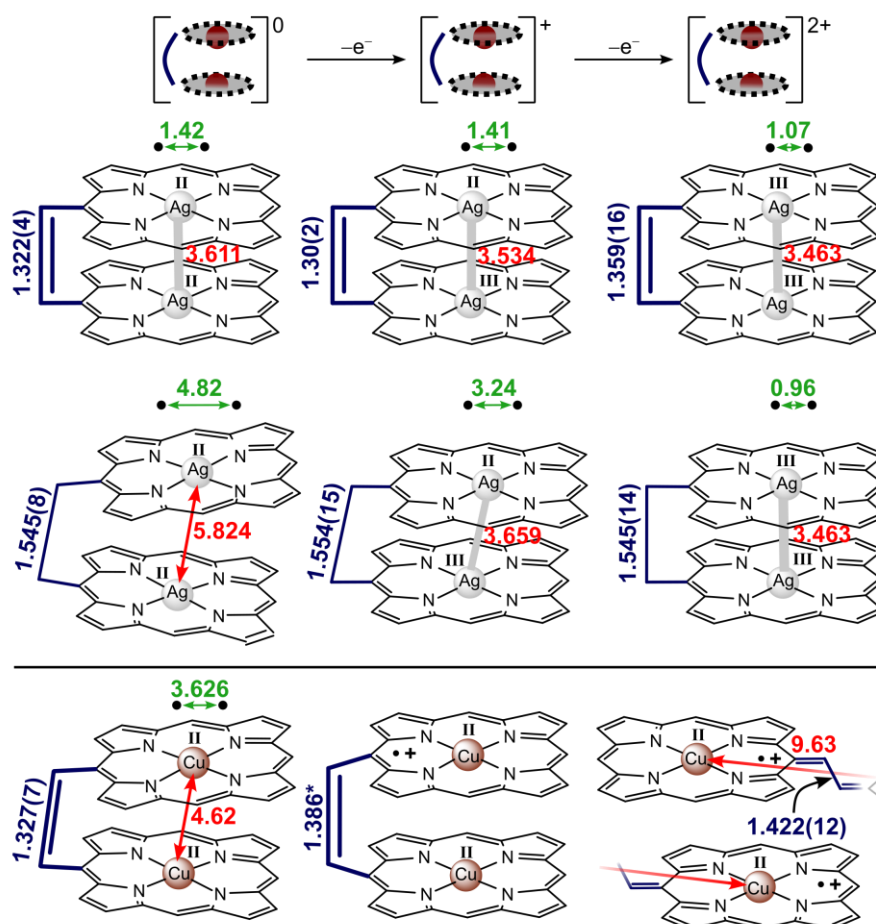


Figure 1.21 Schematic representation of the effect of metallophilic interactions on the overall structure of binuclear bis(porphyrinato)silver and copper complexes in different oxidation states dependent on the respective anchor unit. Ethyl groups and hydrogen atoms omitted for clarity reasons. Distances obtained from X-ray diffraction analyses.^{90–93}

This comparative study demonstrated the effect of argentophilic interactions between two silver-centers in different oxidation states. In both cases, the silver centers move closer to each other upon each oxidation step. The face-to-face presentation of the two porphyrins would support a larger distance between both porphyrin subunits. This effect is compensated by the strong argentophilic interactions between the silver centers. Indeed, both the free-base bisporphyrin and corresponding bis(porphyrinato) metal complexes with clearly ligand-centered oxidations prefer a stabilization in the anti conformation, as exemplarily shown for the copper(II)⁹² complex and described in the literature for the binuclear cobalt(II)^{94,95}, iron(II)^{89,96} and zinc(II)⁹⁷ complexes.

In summary, the synthesis of cofacial “Pacman”-type bis(porphyrin) complexes is accompanied with a high synthetic effort. Beginning with the first synthesis of porphine in 1936 the syntheses strategies have been continually refined over the decades thanks to the pioneering research by many chemists resulting

CHAPTER 1 | Introduction

in free-base porphyrins and their metal complexes with tailored geometric and electronic properties. As demonstrated in selected application examples above, the effort is worthwhile.

1.1.5 Beyond Porphyrins – The Macrocyclic Tetraaza beta-Diiminato Ligand

Metal complexes of the 14-membered macrocyclic ligand 5,7,12,14-tetramethyl-1,4,8,11-tetraazacyclotetradeca-5,7,12,14-tetraenato (L^{2-}) are sparsely described in the literature (Figure 1.22). The ligand synthesis and its first coordination to the 3d transition metals iron(II), cobalt(II) or zinc(II) was published in 1971.⁹⁸ Until today, only 16 publications have been added, discussing just the synthesis and a few fundamental spectroscopic or structural properties of the iron(II)^{98–101}, cobalt(II)¹⁰², nickel(II)^{98,103–106}, copper(II)^{101,102,104,105,107–109}, zinc(II)⁹⁸, palladium(II)¹¹⁰, or, with special regard to this work, gold(III)^{111–116} complex of the L^{2-} ligand. Over the same time period, more than 450 articles have been published about metal complexes only of monomer β -ethyl substituted porphyrinato ligands in the context of catalysis, chromophores, or medical applications.

The synthesis of the metal complex $[M(L)][X]$ is achieved through a formally fourfold condensation reaction between acetylacetone and ethane-1,2-diamine, yielding the neutral H_2L ligand, and subsequent metallation.^{98,99,101,105,107,110} The alternative approach is the synthesis of the bis(ethane-1,2-diamine) metal complex $[M(en)_2][X]_n$ and the downstream double condensation with two equivalents of acetylacetone in slightly alkaline aqueous solution.^{102,103,106,110}

The porphyrin's smaller sibling H_2L shares the same local tetraaza coordination environment, but differs significantly in its electronic and geometric properties.

Firstly, the clear redox-innocent ligand imposes metal-centered redox processes on the complex. The ability of the porphyrin ligand either to accommodate or to provide an electron, for example in the context of a (natural) catalytic cycle, is not bestowed on the H_2L ligand (section 1.1.2).

Secondly, the absorption spectrum is dominated by a single band in the UV region, making it appear colorless to the human eye.⁹⁹

1.2 I An Incipient Success Story – Gold in its Oxidation State +II

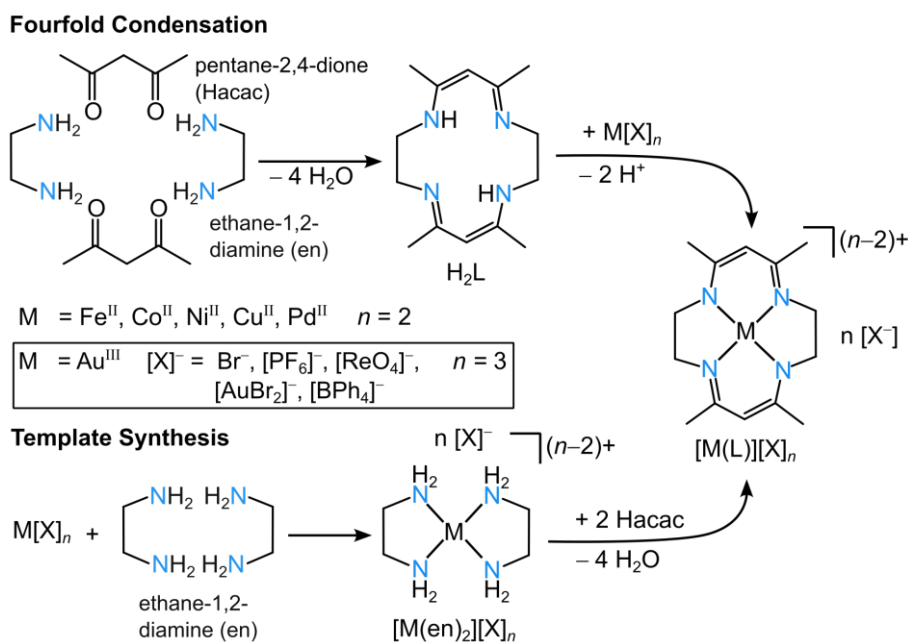


Figure 1.22 Scheme of the synthesis of metal complexes of the 14-membered macrocyclic ligand L^{2-} via fourfold condensation or template synthesis.^{98–110,112,114,117–123}

The group of Mironov reported the mixed-valent $[\text{Au}^{\text{III}}\text{L}][\text{Au}^{\text{I}}\text{Br}_2]$ complex featuring relatively short $\text{Au}^{\text{III}}\text{-Au}^{\text{I}}$ distances of 3.964(6) Å in the solid state indicating aurophilic interactions between the anion and cation.¹¹⁴

The gold-nitrogen distances range between 1.981(3) and 1.986(3) Å in the solid state and are therefore slightly shorter than the corresponding distances in $[\text{Au}^{\text{III}}(\text{TPP})][\text{ClO}_4]$ (2.032(5) - 2.033(5) Å). This indicates a larger overlap between the ligand- and the gold-centered $5d_{x^2-y^2}$ orbital resulting in a stronger energetic destabilization.¹²⁴

1.2 An Incipient Success Story – Gold in its Oxidation State +II

The preceding section has paid tribute to the unique photophysical properties of porphyrins and their significance for biological and physical processes in nature. The modern science recreates the nature's control centers in simplified systems – both for a better understanding of the functions of their natural models and for various applications in catalysis, technology, medicine or fundamental research.

This section is a gathering of the allrounder porphyrin and gold in its oxidation state +II. For this purpose, many strategies have been adopted over the past decades. After a short introduction into the relativistic effects, these approaches will be compiled, the insights from the failures classified and, ultimately, brought together in the synthesis, isolation and characterization of the first mononuclear gold(II) complex.

1.2.1 The Origin of Relativistic Effects

The yellow brightness of gold, the liquid aggregate state of mercury or metallophilic interactions originate from strong relativistic effects in heavy elements attributable to high atomic numbers.^{125,126}

Higher nuclear charges induce a stronger electrostatic attraction of the nucleus to the electrons, followed by the increase of the velocity v_e and mass m_e of the core-proximal electrons. This involves the decrease of the radii of all s and p shells (direct relativistic effect), since the Bohr radius a is inversely proportional to the electron mass m_e (equation 2).¹²⁶

$$a \sim \frac{1}{m_e} \quad (2)$$

The decrease of the radii of the inner s and p orbitals result in a reduced effective nuclear charge and the expansion and energetic destabilization of the diffuse d- and f orbitals (indirect relativistic effect). The ratio between the relativistic and the non-relativistic Bohr radius a_R and a_0 , respectively, decreases with increasing electron velocity v_e or electron mass m_e (equation 3).¹²⁶

$$\frac{a_R}{a_0} = \sqrt{1 - \left(\frac{v_e}{c}\right)^2} \quad (3)$$

The influence of the relativistic effects on the contraction of the diffuse 6s orbital for elements $Z < 55$ is less than 5%. Elements with higher atomic number and successively filled 4f orbitals feature stronger 6s shell contractions resulting in the local minimum at ${}_{78}\text{Pt}$, ${}_{79}\text{Au}$ and ${}_{80}\text{Hg}$, forming the “relativistic triad”. Similarly strong relativistic contractions of the 6s orbitals are not reached until fermium (Figure 1.23b).¹²⁷

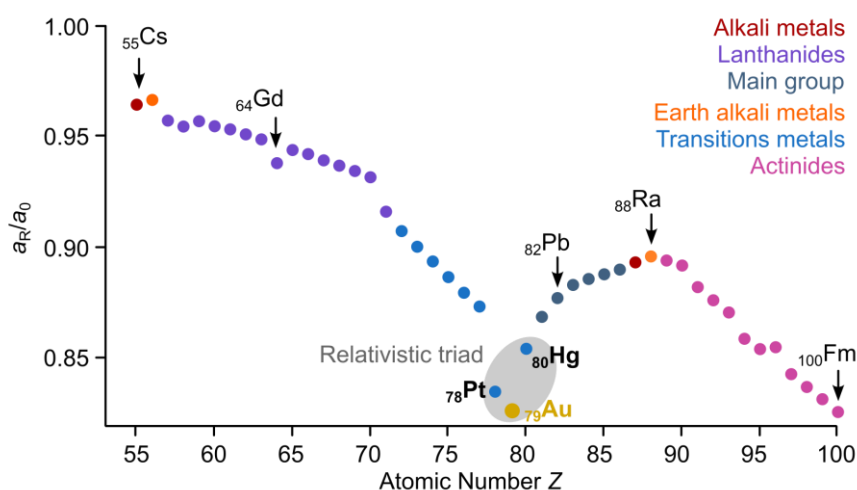


Figure 1.23 Ratio of the relativistic Bohr radius a_R and non-relativistic Bohr radius a_0 for the 6s shell of the elements from caesium (atomic number $Z = 55$) to francium ($Z = 100$).¹²⁷

The influence of the relativistic effects in gold are macroscopically evident in its yellow appearance, since the excitation energy from the valence band, formed by the 5d orbitals, to the Fermi level, formed by the 6s orbitals, is shifted from the ultraviolet to the visible region. In contrast, the 5s and 4d orbitals in silver

1.2 I An Incipient Success Story – Gold in its Oxidation State +II

undergo a much less pronounced alignment of their orbital energies, resulting in an excitation energy in the UV range. This was exemplarily calculated for the molecular hydrides of the nd^{10} coinage metals copper, silver and gold (Figure 1.24).¹²⁵

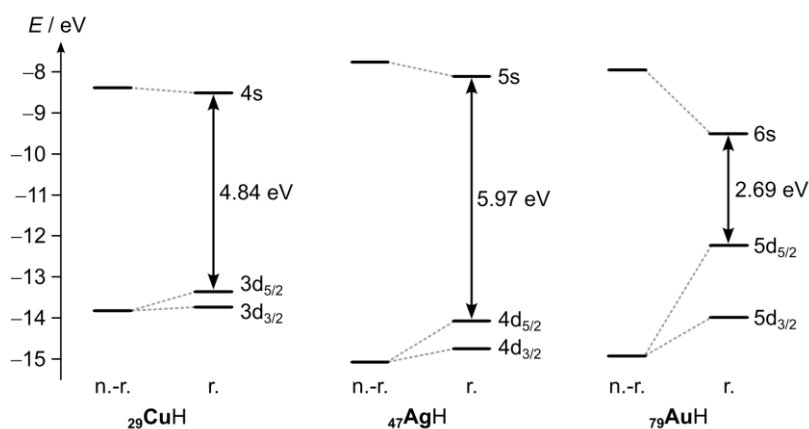


Figure 1.24 Calculated non-relativistic (n.-r.) and relativistic (r.) valence orbital energies for CuH, AgH and AuH.¹²⁸

Further consequences of the relativistic effects in gold include the stability of the oxidation state $-I$, as realized in caesium auride, is the formation of short gold(I)-gold(I) distances, called aurophilicity. Typical bond lengths range between 2.7 and 3.3 Å, falling below the twofold van der Waals radius of a single gold(I) ion. Typical Au-Au-bond energies range between 10 and 30 kJ mol⁻¹. This kind of interaction is not exclusively related to gold since it is also present in other metals underlying relativistic effects, however, much weaker.¹²⁹

The relativistically reduced energy gap between the $5d_{x^2-y^2}$ and 6s orbitals of gold allows a stronger mixing and results in the preference for the closed shell $5d^{10}$ oxidation state $+I$ in a linear coordination environment. Moreover, the comparatively high energy of the half-filled $5d_{x^2-y^2}$ orbital ($5d^9$ electron configuration) confers gold(II) the high tendency to undergo disproportionation into gold(I) and gold(III) (Figure 1.24). Another typical reaction pathway of gold(II) complexes is the dimerization under formation of a direct gold(II)-gold(II) σ bond repealing the energetically unfavoured situation of a singly occupied d orbital.^{129,130}

In summary, the intrinsically unfavourable-lying orbital energies of gold for the oxidation state $+II$ require a tailored ligand design with specific electronic and geometric properties.¹³⁰

1.2.2 Pseudo- and Binuclear Gold(II) Complexes

The propensity of gold(II) for the disproportionation into gold(I) and gold(III) is nicely reflected in the gold halide compound “AuCl₂”. The empirical sum formula suggests the oxidation state +II for gold. However, it is a mixed-valent species containing gold(I) and gold(III) in a linear and square planar coordination environment, respectively.¹³¹ The contraction of the Au^I-Cl bonds while simultaneously elongating the Au^{III}-Cl bonds under high pressure is an indication of the comproportionation into gold(II). A spectroscopic evidence had not been provided.¹³²⁻¹³⁴ The dimerization of gold(II) complexes under the formation of a direct gold(II)-gold(II) bond, incidentally thoroughly investigated for linear gold(I) complexes, was demonstrated by the groups of Wickleder and Marler. The formation of the gold-gold bond is advantaged by bridging ligands such as sulfate in [AuSO₄]₂ or the diethylmethylphosphonium methylid ligand in [AuCl(CH₂PEt₂CH₂)]₂ with gold-gold distances of 2.490 and 2.597 Å, respectively, in the solid state.^{135,136} The unbridged binuclear gold(II) complex [AuCl(dppn)]₂, whereas dppn = 1,8-bis(diphenylphosphano)naphthalene, exhibits in the solid state a slightly longer gold-gold distance of 2.6113 Å.¹³⁷ The bis(cyclometallated) binuclear pincer-type [Au^{II}(C[^]N[^]C)]₂ complex (C[^]N[^]C = 2,6-bis(4'-*tert*-butylphenyl)pyridine) was synthesized by the group of Bochmann via chemical reduction both of the corresponding mononuclear gold(III) complex or under reductive elimination of water from the hydrido or acetate gold(III) complexes. The luminescent, air-stable and moisture-resistant complex features an unsupported gold-gold bond (2.4941(4) Å) with high thermodynamic stability (198 ± 1 kJ mol⁻¹), but low photostability (Figure 1.25).^{138,139} The irradiation of a solution of [Au^{II}(C[^]N[^]C)]₂ in benzene with UV light yielded a mixed-valent aggregate containing of a macrocyclic core formed by gold(I) and surrounded by [Au^{III}(C[^]N[^]C)]⁺ fragments.^{138,140}

The obtained complexes thus provided additional experimental clarity regarding the aurophilic interactions between two gold(II) centers, as consistently evidenced by the comparatively short gold-gold distances. However, all these approaches have failed to provide spectroscopic evidence for a genuine mononuclear gold(II) species.

1.2 I An Incipient Success Story – Gold in its Oxidation State +II

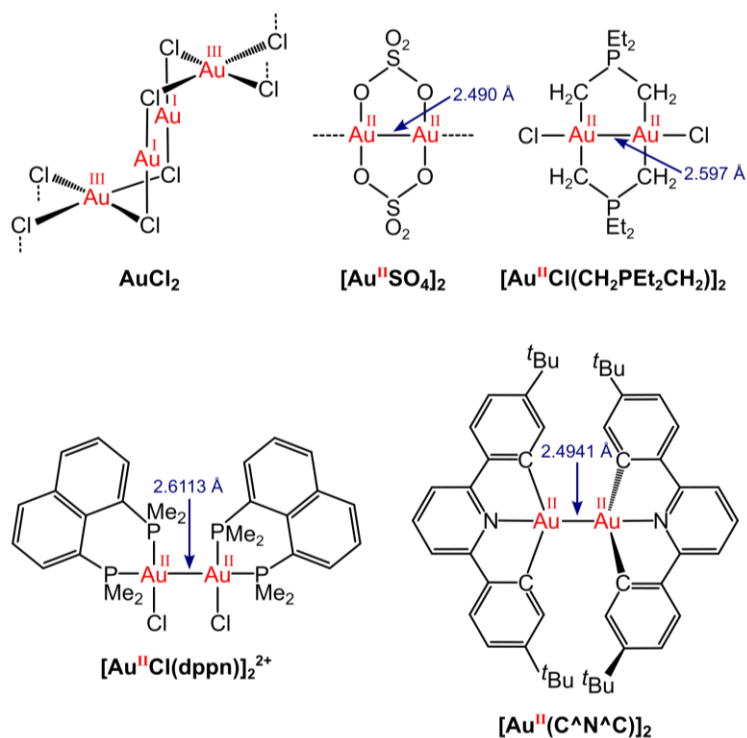


Figure 1.25 Structure of the mixed-valent gold halide salt “AuCl₂” and representative molecular structures of binuclear gold(II) complexes with supported and unsupported gold(II)-gold(II) and a cyclometalated pincer-type binuclear gold(II) complex.^{131,135–138}

1.2.3 Transient Gold(II) Complexes

Gold(III) porphyrins have been implemented as electron acceptor units in several mixed-metallic bis(porphyrin) dyads (Figure 1.26). The charge-shifted state [Zn(PQ⁺)-Au^{II}(PQ)]⁺ in the zinc(II) porphyrin/gold(III) porphyrin dyad, synthesized by the group of Fukuzumi, bears a distinct gold(II) signature based on EPR spectroscopy and a long lifetime of 9.1 μs according to transient absorption spectroscopy. The long lifetime has been attributed to a small outer-sphere reorganization energy in the non-polar solvent toluene implicating a high forward electron transfer rate and slow back-electron transfer (BET) rate lying in the Marcus inverted region.⁵⁶

Hammarström and co-workers realized for a zinc(II) phthaloyanine/gold(III) porphyrin dyad a ultrafast photoinduced electron transfer (PET) rate ($k_{\text{PET}} = 1 \cdot 10^{12} \text{ s}^{-1}$) over a distance of more than 3 nm resulting in a gold-centered reduced acceptor unit. The bridge-mediated strong electronic coupling between the donor and acceptor units facilitates a fast charge separation, initially leading to a ligand centered gold porphyrin reduction and subsequent relaxation to the gold(II) porphyrin. The weaker electronic interaction of the gold orbitals with the bridge compared to the porphyrin retards the charge recombination.⁵⁵

Heinze and co-workers have synthesized a series of amide-coupled zinc(II) porphyrin/gold(III) porphyrin dyads bearing different electron-donating or withdrawing aryl substituents (Figure 1.26). The

charge-shifted states $[\text{Zn}(\text{P}^{\bullet+})-\text{Au}^{\text{II}}(\text{P})]^+$ in each case featured a gold(II) center upon valence isomerization from the gold(III) porphyrin radical. The attachment of electron-withdrawing $-\text{C}_6\text{H}_4\text{CF}_3$ groups to the acceptor unit implicates a faster forward electron transfer compared with the $-\text{C}_6\text{H}_4\text{O}^t\text{Bu}$ substituent. The back electron transfer (BET) rate is significantly reduced for the dyad bearing the $-\text{C}_6\text{H}_4\text{CF}_3$ substituent at the donor moiety. This shifts the driving force of the BET to the Marcus inverted region, which is experimentally evident in lower BET rate and therefore a longer lifetime of the charge-shifted state.⁵⁴

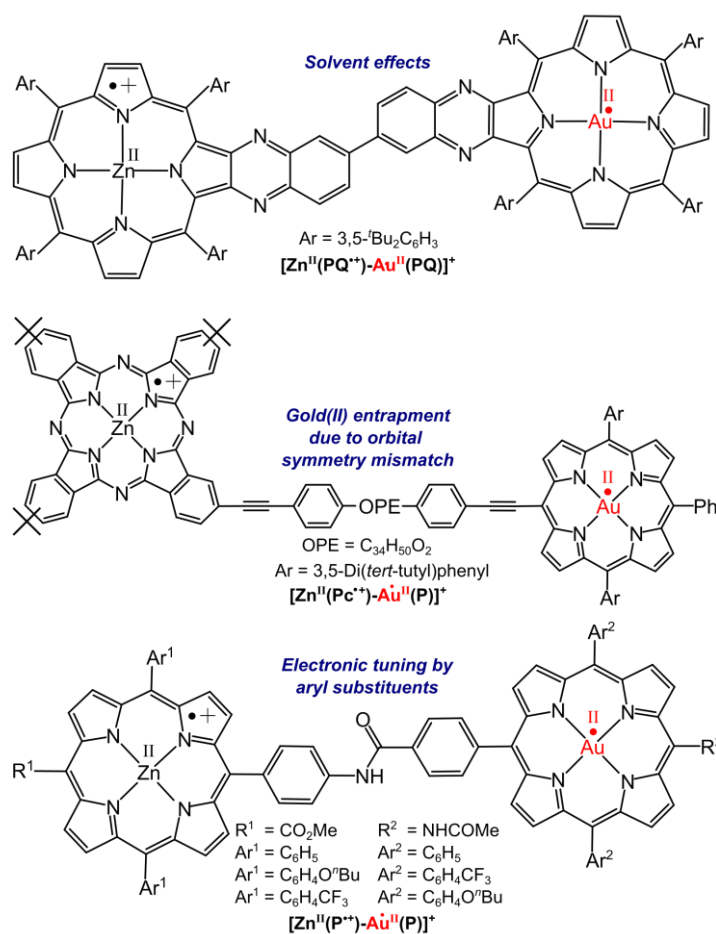


Figure 1.26 Molecular structures of zinc(II)porphyrin/phthalocyanine-gold(III)-porphyrin dyads in their charge-shifted states.⁵⁴⁻⁵⁶

In conclusion, the above findings demonstrate both the importance of nonpolar solvents and weak electronic interactions between the σ -type gold and π -type porphyrin orbitals for a long-lived charge-shifted state and, therefore, a long-lived gold(II) species. Intramolecular electronic fine tuning can further help to prolong the lifetime.⁵⁴⁻⁵⁶ Unfortunately, no further spectroscopic or structural properties have been elicited from the gold(II) containing charge-shifted states, beyond the capability of the reduced charge-shifted state $[\text{Zn}(\text{P})-\text{Au}^{\text{II}}(\text{P})]$, generated by the addition of diisopropylethylamine as sacrificial electron donor, to act as catalyst for the photoinduced reduction of an aromatic azide to aniline.¹⁴¹

1.2 I An Incipient Success Story – Gold in its Oxidation State +II

Mono- and binuclear gold(I) complexes featuring phosphane or (*N*-heterocyclic)carbene ligands have been deployed in the homogeneous catalysis of oxidative carbon-carbon couplings, cyclizations or 1,2-difunctionalization of alkynes.^{142–152}

In most catalytic cycles of these chemical transformations, a gold(II) species has been formulated as the truly catalytically active oxidation state, often without providing an unambiguous spectroscopic evidence. Exceptions to this are, for example, the cyclization of *N*(2-propyn-1-yl)benzamide to 2-phenyl-5-vinylidene-2-oxazoline (not shown) in presence of a mixed-valent Fischer-type carbene ferrocenyl gold(I)/iron(II) precatalyst $[\text{Au}^{\text{I}}/\text{Fe}^{\text{II}}]$ (Figure 1.27). The oxidation of the precatalyst to the mixed-valent $[\text{Au}^{\text{I}}/\text{Fe}^{\text{III}}]^+$ valence isomer implies a subsequent counterion- or sidechain mediated valence isomerization to the EPR and catalytically active $[\text{Au}^{\text{II}}/\text{Fe}^{\text{II}}]$ complex in its resting state. The detected broad EPR signal at room temperature at around $g = 2.014$ does not arise from ferrocenium, being EPR silent at under these conditions. While the EPR spectroscopic evidence for an intermediate gold(II) species was successful, further structural insights, however, could not be gained.^{143,153}

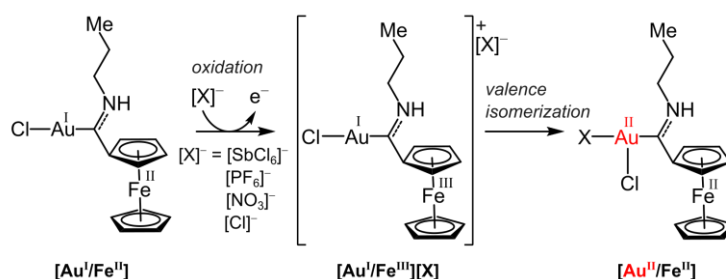


Figure 1.27 Chemical oxidation of the $[\text{Au}^{\text{I}}/\text{Fe}^{\text{II}}]$ precatalyst, exemplarily shown for the catalyst bearing a propyl sidechain and ferrocene moiety, to the mixed-valent $[\text{Au}^{\text{I}}/\text{Fe}^{\text{III}}][\text{X}]$ complex and subsequent valence isomerization to the EPR active catalyst in its resting state $[\text{Au}^{\text{II}}/\text{Fe}^{\text{II}}]$.

1.2.4 Suggested Gold(II) Complexes

Among the various experimental approaches for the synthesis of binuclear gold(II) complexes and transiently detected mononuclear gold(II) complexes, a series of putatively gold(II) complexes have been suggested.

The group of Roduner have pursued the strategy of compartmentation by introducing bis(ethylenediamine)gold(III) $[\text{Au}(\text{en})_2]^{3+}$ into the pores of zeolite Y (Figure 1.28). Subsequent treatment with oxygen yielded at high temperatures a highly anisotropic axial EPR spectrum ($g_z = 2.239$, $g_{x,y} = 2.051$) with considerable coupling constants to the ^{197}Au nucleus ($A_z = 188$ G, $A_{x,y} = 22$ G) and superhyperfine couplings to four ^{14}N nuclei proving the gold(II) center coordinated by four nitrogen atoms in a square-planar fashion. Both disproportionation or dimerization of the zeolite shielded $[\text{Au}(\text{en})_2]^{2+}$ complexes were inhibited, however, no further structural or spectroscopic properties have been provided.¹⁵⁴

Additional possible hint for a gold(II) species was provided by mass spectrometry. The evaporation of elemental gold, followed by the communitization with pyridine (py) and subsequent ionization of the neutral gold-pyridine adducts $[\text{Au}(\text{py})_n]^0$ yielded the dicationic $[\text{Au}(\text{py})_n]^{2+}$ complexes ($n = 1 - 4$) of different coordination numbers (Figure 1.28). The unequivocally non-innocent electronic nature of pyridines does not allow the assignment of the oxidation state of gold, not to mention any spectroscopic investigations.^{155,156}

The cyclic corrole ligand apparently differs structurally only from the porphyrin ligand by the absence of one methine bridge (see: section 1.1.1). The corresponding (triarylcorolato)gold(III) complexes $\text{Au}(\text{TPC}^{\text{Ar}})$ have been investigated regarding the site of the one-electron reduction (Figure 1.28). Spectroelectrochemical EPR studies at room temperature on the monoanionic (triarylcorolato)aurate complexes unveiled the formation of ligand-centered π radical anions ($g_{\text{iso}} = 1.995$ or 1.995) while the respective gold(III) centers remained unaffected. Based on DFT calculations, only one percent of the Löwdin spin population was located on the gold center in each case, whereas the remaining was distributed over the triarylcorolato ligand. The Soret band of the (triarylcorolato)gold(III) complexes almost vanished upon electroreduction in both cases, indicating ligand-centered reductions in agreement with the EPR results.³¹

However, the corresponding triarylcorolato complexes of the lighter homologous silver(III) and copper(III) are reduced metal-centered. This series of (triarylcorolato)complexes of the trivalent coinage metals Cu^{III} , Ag^{III} and Au^{III} concerning the site of the first reduction, metal- or ligand-centered, emphatically demonstrated the effect of the intrinsic ligand field strength. While in the case of copper(III) and silver(III) the $3d_{x^2-y^2}$ and $4d_{x^2-y^2}$ orbitals, respectively, remain susceptible for a reduction, the $5d_{x^2-y^2}$ orbital is – induced by the relativistic effects – at such a high energy, that it becomes inaccessible for the reduction. This trend is further enhanced by the smaller tetraaza cavity of corroles compared with porphyrins, implicating a larger destabilization of the $5d_{x^2-y^2}$ orbital compared to the $3d_{x^2-y^2}/4d_{x^2-y^2}$ orbitals of copper and silver due to better orbital overlap. Additionally, the trianionic nature of the trisarylcorolato ligand TPC^{3-} prefers the accomodation of high-valent metal ions or those with intrinsically lower ligand field splitting as demonstrated for $\text{Cr}^{\text{V/IV}}$, Fe^{IV} , Co^{V} , Ag^{III} , Cu^{III} or Cu^{IV} .^{26,31,157}

A gold-centered reduction of a (corolato)gold(III) complex $\text{Au}(\text{TPC}^{\text{F}})$, bearing four trifluormethyl groups at the β - and pentafluorophenyl substituents at the *meso* positions, have been reported by the group of Gross (Figure 1.28). Chemical reduction with decamethylcobaltocene or sodium borohydride gave an axial EPR spectrum ($g_{xy} = 2.004$, $g_z = 1.956$) in frozen solution at 150 K, allowing for the

1.2 I An Incipient Success Story – Gold in its Oxidation State +II

characterization as gold(II) complex. The absence of a hyperfine coupling to the gold nucleus, as well as spectroelectrochemical data suggested a description as ligand-reduced (corrolato)gold(III) complex.³⁹

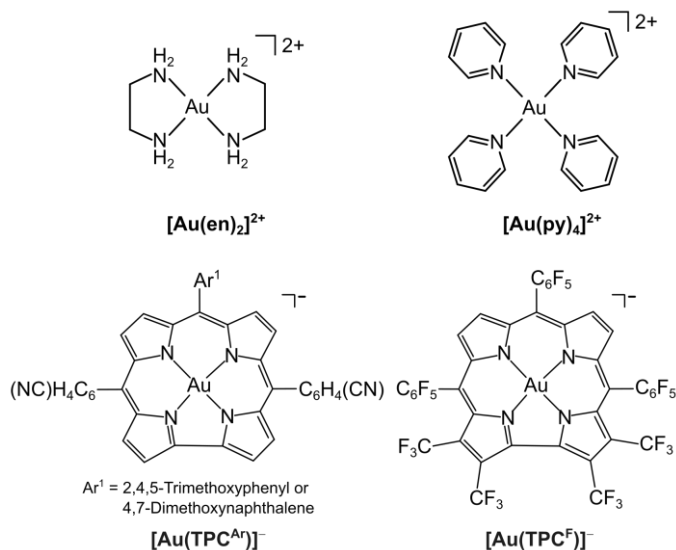


Figure 1.28 Molecular structures of suggested mononuclear gold(II) complexes.^{26,31,154-157}

The molecular stabilization of gold(II) has been, and continues to be, a challenging endeavour, leading to the limited spectroscopic and structural insights into the oxidation state +II. Most of them are based either on photoinduced short-lived species, speculations on mass spectra or on intermediates formulated as a part of a catalytic cycle. The next section is dedicated to the ligand design concepts that have enabled the trapping of gold(II) for spectroscopic and structural characterizations.

1.2.5 Affirmed Gold(II) Complexes

The inclusion of the gold(II) species into the rigid, three-dimensional enveloping structure of the thioether ligand 1,4,7-trithiacyclononane [9]aneS₃ for the purpose of a spectroscopic and structural characterization has been crowned with success. The strikingly simple synthesis involved the dissolving of the pro-ligand [9]aneS₃ in hydrogen tetrafluoroborate and subsequent addition of chloroauric acid H₂AuCl₄ to the solution, stirring for several minutes, some workup steps, followed by crystallisation (Figure 1.29). EPR spectroscopy of the air-stable, dicationic gold complex in frozen acetonitrile solution at 77 K manifested the mononuclear gold(II) character of $[\text{Au}^{\text{II}}([\text{9}]\text{aneS}_3)]^{2+}$. The relatively low anisotropy of the *g* tensor ($g_{1,2,3} = 2.032, 1.980, 1.999$) arises from a weak spin-orbit coupling, confirming the perpendicular orientation of the *z* axis to the *xy* plane. The lower coupling constant to the gold nucleus ($A(^{197}\text{Au}) = 57.3 \text{ G}$) compared with $[\text{Au}(\text{en})_2]^{2+}$ ($A(^{197}\text{Au}) = 188 \text{ G}$, see section 1.2.4 and Figure 1.28) could be due to the stronger nephelauxetic effect of the [9]aneS₃ ligand providing soft sulfur atoms and giving rise to a stronger delocalization of the spin density compared with ethylenediamine as pure σ

donor. Indeed, based on DFT calculations, the spin density mainly resides on the gold atom with $5d_{xy}$ character (27.7%) and on the surrounding sulfur atoms with 3p character (62.8%).^{158,159}

The $5d^9$ electron configuration of gold(II) induces a first-order Jahn-Teller complex distortion along the z axis with diverging gold-sulfur distances as extracted from X-ray diffraction analysis (2.839(5) Å and 2.452(5)/2.462(5) Å).¹⁶⁰

The $[\text{Au}^{\text{II}}([\text{9}]\text{aneS}_3)]^{2+}$ complex is oxidized reversibly to gold(III) at +0.46 V, and irreversibly reduced at +0.10 V to gold(I), referenced against the ferrocene/ferrocenium couple.¹⁶⁰

The group of Schröder extended the gold thioether complex family $[\text{Au}([\text{9}]\text{aneS}_3)]^{+2/+3+}$ by the coordination of gold to the 1-oxa-4,7-dithiacyclononane ligand $[\text{9}]\text{aneS}_2\text{O}$ – formally available by the replacement of one sulfur atom by oxygen in $[\text{9}]\text{aneS}_3$. The EPR spectrum of $[\text{Au}^{\text{II}}([\text{9}]\text{aneS}_2\text{O})]^{2+}$ at 125 K confirmed the paramagnetic character of the gold center ($A(^{197}\text{Au}) = 47.7$ G) and displays, again, a low anisotropy ($g_{1,2,3} = 2.037, 2.006, 2.010$). The small difference between the potentials for the $[\text{Au}^{\text{II}}([\text{9}]\text{aneS}_2\text{O})]^{3+/2+}$ and $[\text{Au}^{\text{II}}([\text{9}]\text{aneS}_2\text{O})]^{2+/+}$ redox events, respectively, awards the complex a relatively high thermodynamic instability towards disproportionation (see: section 1.3.2). However, this has not been an impediment for the isolation of single crystals of $[\text{Au}^{\text{II}}([\text{9}]\text{aneS}_2\text{O})]^{2+}$.¹⁶⁰

As confirmed by X-ray diffraction analysis, the gold(II) complex $[\text{Au}^{\text{II}}([\text{9}]\text{aneS}_2\text{O})]^{2+}$ adopts the same elongated octahedral coordination geometry as the parent $[\text{Au}^{\text{II}}([\text{9}]\text{aneS}_3)]^{2+}$ complex. The oxygen atoms are located on the axial positions and feature significantly shortened distances to the gold center compared with the gold-sulfur distances in the $[\text{Au}^{\text{II}}([\text{9}]\text{aneS}_2\text{O})]^{2+}$ complex (2.718(2) Å vs. 2.839(2) Å).¹⁶⁰

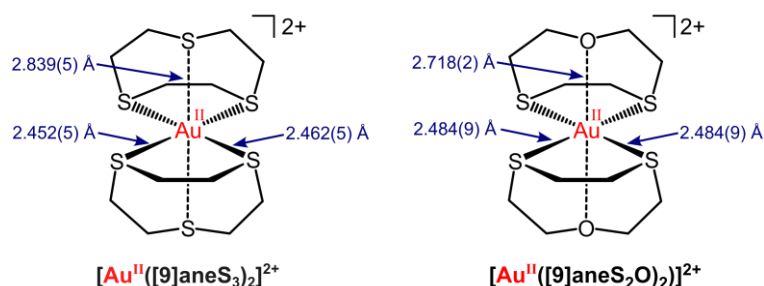


Figure 1.29 Molecular structures of isolated and structurally characterized $[\text{Au}^{\text{II}}([\text{9}]\text{aneS}_3)]^{2+}$ and $[\text{Au}^{\text{II}}([\text{9}]\text{aneS}_2\text{O})]^{2+}$ complexes with selected metrics.^{158,160}

The syntheses of the genuine gold(II) complexes $[\text{Au}^{\text{II}}([\text{9}]\text{aneS}_3)]^{2+}$ and $[\text{Au}^{\text{II}}([\text{9}]\text{aneS}_2\text{O})]^{2+}$ under non-inert gas conditions, in the presence of water and subsequent storage under ambient air, has been – in special regard to the aforementioned challenges – a simple, yet brilliant ligand design concept to hamper disproportionation or dimerization of the gold(II) complex.¹⁵⁸

1.2 I An Incipient Success Story – Gold in its Oxidation State +II

The group of Seppelt has synthesized a large number of gold-xenon complexes based on the prototype complex $[\text{Au}^{\text{II}}\text{Xe}_4][\text{Sb}_2\text{F}_{11}]_2$ obtained from a mixture of gold(III) fluoride and HF/SbF₅ in a reducing xenon permeated atmosphere at low temperatures (Figure 1.30). The exact coordination geometry of the gold-xenon complexes have been influenced by the xenon pressure or the acid strength of HF/SbF₅. The EPR spectra of the reaction solutions indicated the presence of a mixture of gold-xenon complex products. However, crystals could be obtained from the respective reactions solutions for X-ray diffraction analysis. The nature of the ligands required the storage of the complexes under xenon and at low temperatures. Interestingly, the oxidation state +II of gold has experienced a higher stability compared with the adjacent oxidation states +I and +III – an upside-down world for gold under these conditions.

Computational studies on $[\text{AuXe}_n]^{2+}$ ($n = 1 - 6$), applying natural bond orbital (NBO) and electron density properties analyses, suggest neither a pure covalent nor a pure ionic description of the gold-xenon bonds.^{161–163}

Prominent examples for ionic gold(II) complexes are the $\text{Au}^{\text{II}}(\text{SbF}_6)_2$ or $[\text{Au}(\text{HF})_2][\text{SbF}_6]_2$ complexes synthesized by the group of Bartlett and Seppelt, respectively (Figure 1.30). The $\text{Au}^{\text{II}}(\text{SbF}_6)_2$ complex is isostructural to the corresponding silver complex featuring a first-order Jahn-Teller distortion similar to the $[\text{Au}^{\text{II}}([\text{9}]\text{aneS}_3)]^{2+}$ and $[\text{Au}^{\text{II}}([\text{9}]\text{aneS}_2\text{O})]^{2+}$ complexes (Figure 1.29).^{164–166}

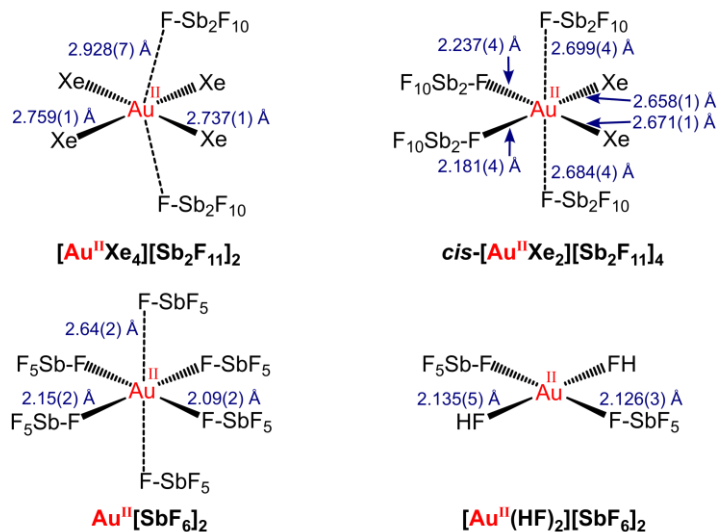


Figure 1.30 Molecular structures of representative gold-xenon complexes with selected metrics extracted from XRD analysis.^{165,166}

More recently, Karunadasa's group used the extended three-dimensional network of a perovskite for the stabilization of gold(II) in coexistence with gold(III) (Figure 1.31). The mixed-valent $\text{Au}^{\text{I}}\text{Au}^{\text{III}}_2\text{Cl}_{12}$ solid was obtained by the reduction of the appropriate gold(I)/gold(III) perovskite using ascorbic acid in aqueous hydrochloric acid. The axial Q-band EPR spectrum at 77 K ($g = 2.16, 2.01$), as well as ¹⁹⁷Au Mössbauer and X-ray absorption near-edge structure (XANES) spectra, confirmed the presence of

gold(II) in an axially elongated octahedral coordination.¹⁶⁷ The gold(III) and gold(II) ions are situated on distinct crystallographic sites featuring equidistant Au^{III}-Cl and Au^{II}-Cl distances of 2.290(6) Å and 2.417(7) Å, respectively.¹⁶⁷

The Au^{II}Au^{III}₂Cl₁₂ perovskite was found to be stable over months under ambient conditions as demonstrated by EPR analysis and thermally resistant in air at 150 °C. No significant changes in the powder XRD have been detected after heating the compound at 250 °C for 24 h.¹⁶⁷

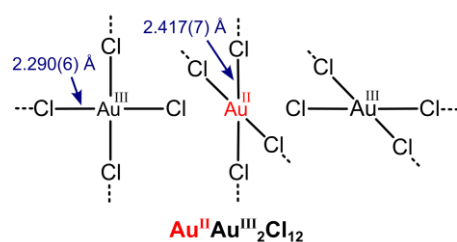


Figure 1.31 Extract of the solid state structure of the mixed-valent Au^{II}Au^{III}₂Cl₁₂ perovskite with relevant bond lengths determined from XRD analysis.¹⁶⁷

The incorporation of gold(II) into the tetraaza coordination environment provided by the tetraphenylporphyrinato ligand TPP²⁻ was a further breakthrough in the quest for stable mononuclear gold(II) complexes. For the first time, extensive spectroscopic and structural investigations of the gold(II) species itself and the associated overall complex properties were made possible. The most relevant ones with significance to this work will be briefly outlined below.

A The gold(III) precursor complex [Au(TPP)][PF₆] is easily accessible in a two-step synthesis. The subsequent chemical reduction with cobaltocene or potassium graphite yielded the neutral, paramagnetic gold(II) complex Au^{II}(TPP) – purification requires merely sublimation or crystallisation.^{46,141,168} The Au^{II}(TPP) complex is stable under inert gas, in solution and as solid at room temperature – decisive advantages over previously reported gold(II) complexes that required handling at low temperatures or the incorporation into the framework of zeolites.

B The EPR spectrum of Au^{II}(TPP) in frozen solution proves a clearly gold-centered localization of the spin density (44%, based on DFT calculations) and the distribution over the coordinating nitrogen atoms (56%). The unexpected rhombicity of the *g* tensor (*g*_{1,2,3} = 2.182, 2.056, 1.982) demonstrates an unsymmetric coordination of the gold(II) ion by the four nitrogen atoms. This constitutes an exception from the axial EPR spectra of the tetraphenylporphyrinato complexes of the lighter homologous Cu^{II} and Ag^{II}. The *g* tensor features a significantly higher rhombicity compared with the thioether gold(II) complexes [Au^{II}([9]aneS₃)]²⁺ and [Au^{II}([9]aneS₂O)]²⁺ (Figure 1.29).^{158,160} X-ray diffraction studies on single crystals of Au^{II}(TPP) revealed a 2+2 planar coordination of gold(II) with two shorter and two

1.2 I An Incipient Success Story – Gold in its Oxidation State +II

longer gold-nitrogen distances, mediated by the bending of two trans-located pyrrole subunits of the porphyrin ligand. The smallest gold-gold distance does not fall below 6 Å, confirming the mononuclear nature of Au^{II}(TPP).¹⁴¹

C The cyclic voltammogram shows a reversible reduction of [Au(TPP)]⁺ to Au^{II}(TPP) followed by a ligand-centered reduction yielding [Au(TPP)]⁻. This demonstrates the non-innocent character of porphyrin. The low equilibrium constant ($K_{\text{Dis}} = 3 \cdot 10^{-12}$) for the disproportionation of 2 Au^{II}(TPP) into [Au^{III}(TPP)]⁺ and [Au(TPP)]⁻ attests to its high thermodynamic stability and formed an essential prerequisite for its isolation. The dimerization of Au^{II}(TPP) under the formation of a direct gold-gold bond is sterically prevented due to the localization of the spin density in the xy plane and thus in the plane of the sterically demanding and rigid tetraphenylporphyrinato ligand.^{46,54}

D The 2+2 coordination of the gold(II) in the solid state due to a second-order Jahn-Teller effect and the associated distortion of the porphyrin macrocycle proved to be in solution as an equilibrium between two different conformational isomers with an energetically low-lying transition state (activation barrier $E_A = 15 \text{ kJ mol}^{-1}$) and a high interconversion rate at room temperature compared with the ¹H NMR timescale. The presence of the 2+2 coordination of gold(II) both in the solid state and in isolated complexes in frozen solution in EPR confirms an gold-induced intrinsic cause rather than packing effects in the crystal.¹⁴¹ This type of unsymmetric coordination of gold(II) by the chloride ligand was absent in [Au^{II}Au^{III}Cl₁₂]⁴⁺ indicating either a non-intrinsic reason or the suppression due to solid state effects.¹⁶⁷

E Earliest reactivity studies demonstrated the applicability of Au^{II}(TPP) to act as one-electron reductant. Oxygen is initially reduced to superoxide O₂⁻ and next to hydroxide, whereas Au^{II}(TPP) is oxidized to [Au^{III}(TPP)]⁺. The disappearance of the broad gold(II) resonance upon addition of nitrosobenzene PhNO as spin trapping agent and oxygen substitute confirmed the electron transfer from Au^{II}(TPP) to PhNO. The gold(II) complex exhibits stability in the presence of protons – the coordination of water, THF or pyridine to the gold(II) center does not occur.¹⁴¹

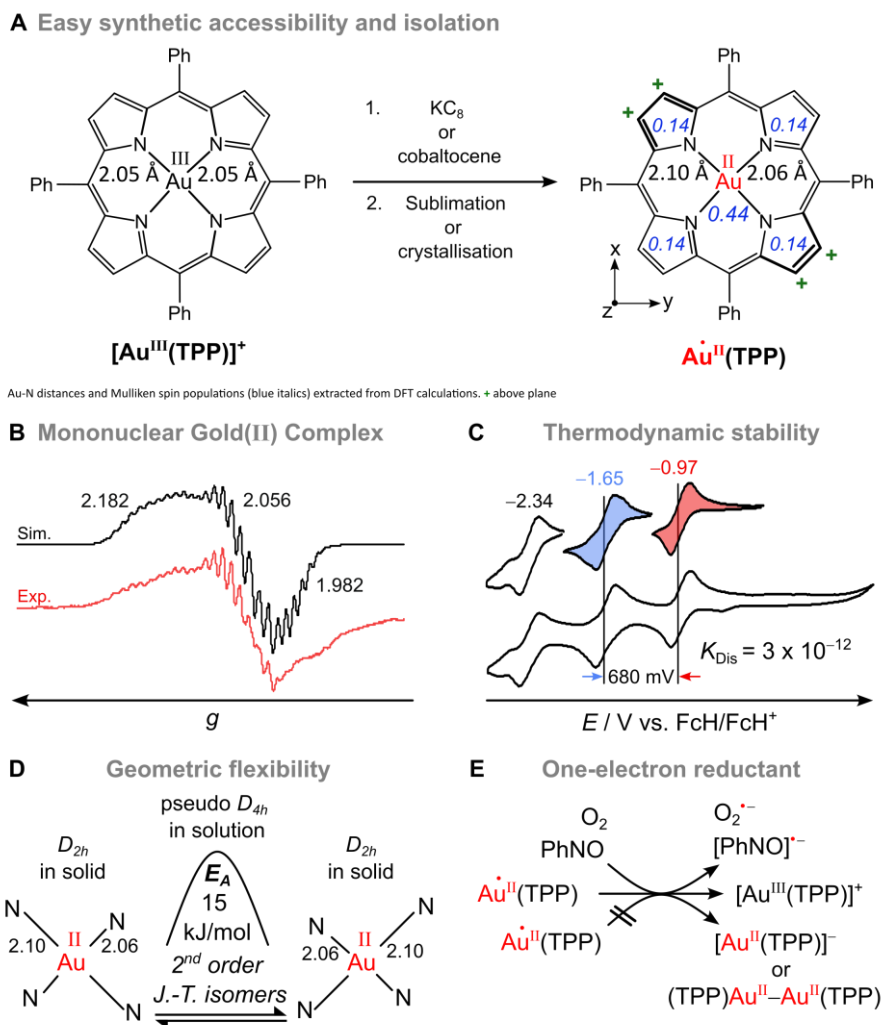


Figure 1.32 Synthesis (A) and selected properties of the mononuclear (tetraphenylporphyrinato)gold(II) complex $\text{Au}^{\text{II}}(\text{TPP})$ (B-E) discussed in this section.^{46,54}

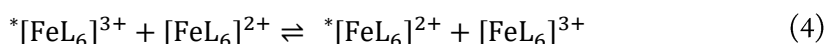
In conclusion, the limited number of publications is dedicated to binuclear gold(II) complexes or those in which the gold(II) species has been spectroscopically detected as photoinduced transient intermediate, albeit sometimes only postulated. Truly mononuclear gold(II) complexes suitable for spectroscopic and structural characterizations, aside from poorly accessible gold-xenon complexes requiring the storage under low temperature, were made possible by the use of encapsulating thioether ligands or the rigid tetraphenylporphyrinato macrocycle.^{130,141,158-160}

1.3 Fundamentals of Electron Transfer

The efficient electron transfer (ET) in the photosynthesis apparatus or metabolic processes are of fundamental importance for the preservation of life and a functioning ecosystem on earth. The successful oxidation of water to oxygen and several subsequent biochemical processes in the photosynthetic apparatus are closely linked to the rapid and efficient removal of four electrons from photosystem II. The fixation of nitrogen as ammonia is an overall eight electron process, whereas the reduction of oxygen by the cytochrome c oxidase requires four electrons. To meet this high demand, the catalytically active enzyme centers have available a sophisticated electron transport system. Unfortunately, this commonly elude a more detailed examination due to its high structural and functional complexity. At this point, Marcus theory of electron transfer comes into play, elucidating electron transfer through simplified systems. The theory of the *intermolecular* electron transfer is of secondary importance for this work. Therefore, the following section is intended to lay the foundations for a better understanding of the *intramolecular* electron transfer in section 1.3.2.

1.3.1 Marcus Theory of Electron Transfer

First attempts for the quantitative description of the electron transfer were made by Rudolph Marcus in the 1950s on the basis of the experimental results of the electron self-exchange between isotope-labeled iron(II) and iron(III) complexes (L = neutral ligand) (equation 4).^{169,170}



This simplified example combines several advantages: Firstly, the rate of the electron transfer is not influenced by the thermodynamic stability of the reactants or products, as they are identical. Secondly, the bonds remain intact while the electron transfer occurs, since no bonds are broken or formed.

The quantitative description of the electron transfer rate is based on two fundamental physical approximations: The nuclear coordinates do not change during the electron transfer (Franck-Condon principle) and energy conservation must be fulfilled. This requires an adjustment of the Fe^{II}-L and Fe^{III}-L bond lengths of the complexes. The potential of a complex of *n* atoms would have to be described through a $3n-6$ - and in case of two complexes through a $2(3n-6)$ dimensional potential hypersurface. Marcus theory, however, utilizes only one symmetric vibrational mode (“trapping mode”), allowing the quantitative description of electron transfer based on a one-dimensional electron transfer reaction coordinate *x* under the assumption of a harmonic potential (Figure 1.33, left). In case of $[\text{FeL}_6]^{2+/3+}$ it is the antisymmetric linear combination of the A_g modes. The individual symmetric vibrational modes of each complex are combined to an averaged potential of the reactants $G_R(x)$ and products $G_P(x)$. Thermal

electron transfer is allowed at the crossing point of both parabola, presuming the formation of an encounter complex, whereas photoinduced electron transfer can occur as vertical transition at any other point of the parabola. The activation barrier for the thermal electron transfer is given by ΔG^* . The geometric changes of both complexes and the surrounding solvent molecules accompanied by the electron transfer, are summarized in the reorganization energy λ , which is equal to the photon energy required for the optically induced electron transfer. In case of the electron transfer between two distinct centers A and B (“cross-reaction”), the driving force ΔG^0 of the electron transfer must be considered, since reactants and products feature a different thermodynamic stability. This is reflected in the vertical mutual shift of the parabola (Figure 1.33, right).¹⁷⁰

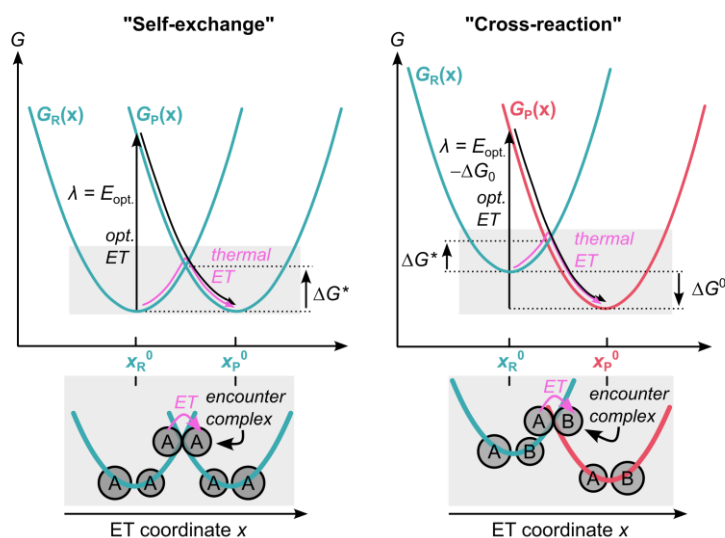


Figure 1.33 Isoenergetic “self-exchange” and non-degenerate “cross-reaction” free enthalpy profiles for a diabatic electron transfer reaction as a function of the reaction coordinate x . R = reactant, P = products, opt. ET = optical electron transfer.¹⁷⁰

The electron transfer rate k_{ET} for a “self-exchange” is given as follows (equation 5) whereas A can be interpreted as a temperature-dependent pre-exponential factor describing the probability of the formation of the encounter complex.¹⁷⁰

$$k_{ET} = A \cdot \exp\left(-\frac{\Delta G^*}{k_B T}\right) \quad (5)$$

In case of a “cross-reaction”, the driving force ΔG^0 and reorganization energy λ , consisting of the inner-sphere λ_i and outer-sphere reorganisation energy λ_o – mainly influenced by the surrounding solvent molecules – have to be considered (equation 6).¹⁷⁰

$$\Delta G^* = \frac{\lambda}{4} \left(1 + \frac{\Delta G^0}{\lambda} \right) \quad (6)$$

The calculated values for the electron transfer rate applying Marcus theory are predominantly in good agreement with the experimental data, despite many simplifying assumptions. Herein lies the strength of this model. However, Marcus theory is only valid for electronically weakly coupled electron transfer centers. The description of systems with strong electronic interactions, such as molecularly bridged electron transfer centers, is provided by Marcus-Hush theory.

1.3.2 Marcus-Hush Theory and Robin-Day Classification

If the extent of the electronic exchange between two redox sites approaches the thermal energy, given by $k_B T$, the motion of the electrons and nuclei can no longer be treated independently from each other. The wavefunctions of both redox centers start mixing with strong effects on the potential energy surface. This may happen, for instance, for bridged metal centers.^{171,172}

The extent of wave function mixing is given by the electronic coupling matrix element H_{RP} . The coupling of the two diabatic free enthalpy curves, representing the reactants R and products P (Figure 1.33), result in a diabatic free enthalpy surface (Figure 1.34).^{171,172}

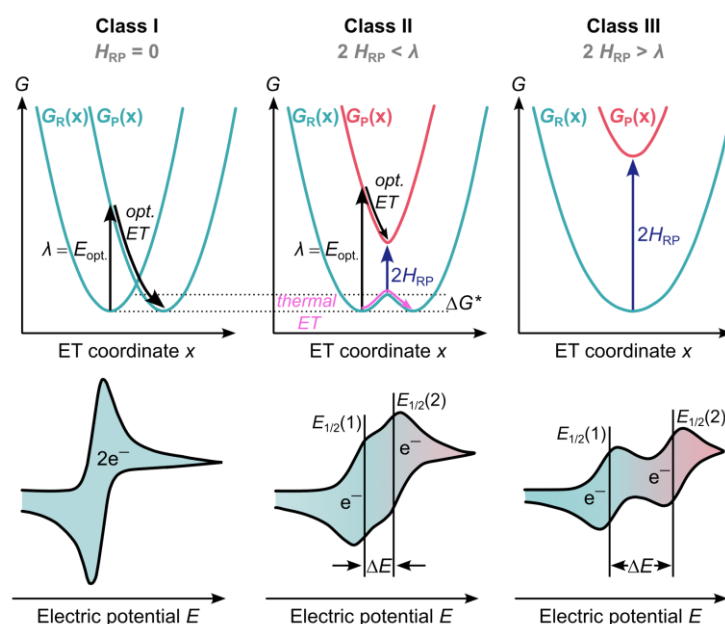


Figure 1.34 Effect of the electronic coupling on the potential energy surfaces as given in the Robin-Day classification and the corresponding cyclic voltammograms.¹⁷¹⁻¹⁷⁴

Depending on the extent of the electronic coupling, binuclear systems can be categorized, as suggested by Robin and Day. A valence-localized system with a high barrier for the electron transfer is denoted as class I system ($H_{RP} = 0$). The spectroscopic and electronic properties of the bimetallic system are

essentially identical to those of the individual components. This is typically detectable in the cyclic voltammogram by a single two-electron redox wave (Figure 1.34, left).¹⁷⁴

In a class II system, the electronic coupling matrix element is smaller than the reorganization energy ($2H_{\text{RP}} < \lambda$). Optical and thermal electron transfer is possible. The binuclear complex exhibits new spectroscopic features, such as an intervalence charge transfer band (IVCT) typically in the near infrared region. This allows for the calculation of H_{RP} based on the energy of the absorption band $\tilde{\nu}_{\text{max}}$, given in wavenumbers, the molar extinction coefficient ϵ_{max} and the full width at half maximum $\Delta\tilde{\nu}_{\text{max}}$ of the absorption band. The distance between both metal centers is given by R_{RP} (equation 7).^{172,174}

$$H_{\text{RP}} = 2.06 \cdot 10^{-2} \frac{\sqrt{\tilde{\nu}_{\text{max}} \cdot \epsilon_{\text{max}} \cdot \Delta\tilde{\nu}_{\text{max}}}}{R_{\text{RP}}} \quad (7)$$

Class II systems show two slightly separated redox waves (Figure 1.34 center). The energy barrier ΔG^* for the electron transfer can be calculated as given below.¹⁷²

$$\Delta G^* = \frac{(\lambda - 2H_{\text{RP}})^2}{4\lambda} \quad (8)$$

In case of a class III system, the electronic coupling is larger than the reorganization energy ($2H_{\text{RP}} > \lambda$) and the individual properties of both metal centers of the same element are averaged and the electron density is delocalized. Class III systems are identified in the cyclic voltammogram by two distinct one-electron redox waves (Figure 1.34).^{172,174}

The difference between both halfwave potentials $E_{1/2}(1)$ and $E_{1/2}(2)$, respectively, of each one-electron redox event can be used for the calculation of the equilibrium constant K_{Dis} for the disproportionation into the adjacent oxidation states, as given by equation 9. The number of transferred electrons is given by z , usually 1, F is the Faraday constant, R the ideal gas constant and T the temperature.¹⁷⁵

$$K_{\text{Dis}} = \exp\left(-\frac{z \cdot F \cdot \Delta E}{R \cdot T}\right) \quad (9)$$

Systems featuring a disproportionation constant $K_{\text{Dis}} > 10^{-2}$ are usually denoted as Class III, systems with $K_{\text{Dis}} < 10^{-6}$ are assigned to Class I. The disproportionation constant of systems with intermediate

electronic communication is typically in the range between $10^{-2} > K_{\text{Dis}} < 10^{-6}$. This assessment solely addresses the thermodynamic stability of an oxidation state.¹⁷⁴

The calculation of the equilibrium constant for the disproportionation of a mononuclear complex XL_6 into $[\text{XL}_6]^+$ and $[\text{XL}_6]^-$, as given in equation 10, can be calculated accordingly.



The difference ΔE between the redox potentials for the reduction $\text{X} \rightarrow \text{X}^-$ and oxidation $\text{X} \rightarrow \text{X}^+$ can be extracted from the cyclic voltammogram (Figure 1.35). The larger the difference, the lower the disproportionation constant K_{Dis} and the thermodynamic stability of XL_6 towards disproportionation.¹⁷⁵

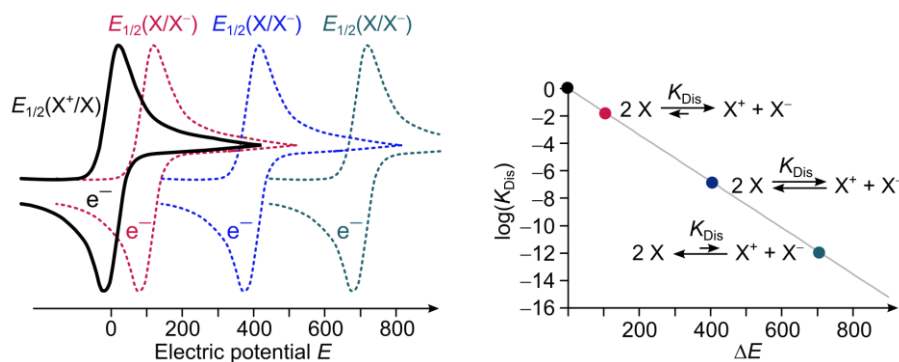
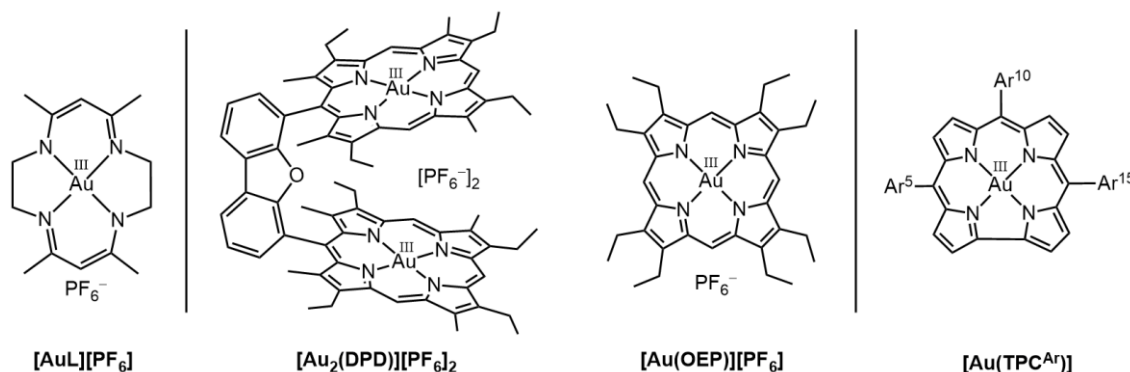


Figure 1.35 Cyclic voltammogram of a hypothetical compound XL_6 complex featuring a reversible redox-process X^+/X at 0.00 V and a second reversible redox-process X/X^- at 0.10, 0.40 and 0.70 V and logarithmic plot of the disproportionation constant K_{Dis} against the difference ΔE of two redox-processes.

2 Motivation and Aim of the Work

The privileged tetraphenylporphyrinato ligand TPP²⁻ combines geometric rigidity and energetically favourable-lying frontier molecular orbitals for the thermodynamic stabilization of gold in its oxidation state +II.

The overarching goal of this work is the development of a deeper understanding of the concept of the molecular stabilization of gold(II) by macrocyclic tetraaza ligands and the examination of the transferability both to β -alkyl-substituted mono(porphyrins) and cofacially engaged bis(porphyrins). Additionally, the possibility of a structurally simplified tetraaza ligand framework without compromising the thermodynamic stability of a potential mononuclear gold(II) complex will be investigated. A detailed description of these subprojects is provided below.



This subproject is, first, motivated by the search for novel mononuclear macrocyclic gold(II) complexes adopting the same local tetraaza coordination environment as porphyrins. Based on the gained insights from the detected equilibrium between the valence isomers of the gold(II) porphyrin and gold(III) porphyrin π radical anion due to solvents- and counterion effects, the bis(β -diiminato) ligand L²⁻ displays redox-innocent behaviour. Therefore, the initial reduction of the gold(III) precursor complex should be gold-centered and the ensuing equilibrium between two valence isomers of no significance. The gold(III) complex, synthetically accessible in a two-step synthesis, has been only described in the literature by a crystal structure, as well as absorption and NMR spectroscopy, electrochemical characterization has been lacking. The electrochemical analyses by cyclic- and square wave voltammetry, UV/Vis absorption and EPR spectroscopy, accompanied by DFT studies, will uncover the thermodynamic stability of the reduced gold(III) complex.

CHAPTER 2 | Motivation and Aim of the Work

The second goal of this work is, firstly, motivated by the extraordinary stability of Au^{II}(TPP) and, secondly, its applicability in electron transfer reactions. Capitalizing on this, a novel “Pacman”-like cofacial bis(porphyrinato)gold(III) complex [Au₂(DPD)][PF₆]₂ is intended to be synthesized, providing spectroscopic and structural insights into the unexplored complex family of binuclear cofacial bis(porphyrinato)gold complexes in different oxidation states gold(III)/gold(III), gold(II)/gold(III) and gold(II)/gold(II). A rigid dibenzofuran spacer ensures a well-defined lateral cofacial presentation of the (porphyrinato)gold subunits.

While the spin density, located in the 5d_{x₂-y₂} orbital of gold(II) and distributed on the coordinating nitrogen atoms, is shielded by the macrocyclic porphyrin ligand in the xy plane, the axial site is open for the coordination and subsequent redox ground state activation of a small molecule like oxygen. Furthermore, the spatially close positioning of two gold centers enables the investigation of any magnetic interactions. Inter-porphyrinoid electronic interactions should be extracted from the absorption spectra in comparison with the mono(porphyrinato)gold complex.

Electrochemical analyses should allow a Robin-Day classification of the mixed-valent species, as well as the evaluation of the thermodynamic stability of the twofold reduced gold(II) complex. Applying EPR spectroscopy, the site of the reduction – gold- or porphyrin-centered – or whether any electronic interactions between the paramagnetic subunits in the twofold reduced complex are present.

This work is concluded by a comprehensive computational study on the effect of electron-donating (aryl)-substituents on the location of the spin density in (corrolato)gold complexes in their doublet states. The energetically low-lying ligand-based LUMOs, concomitantly advantaged by intrinsically high-lying gold orbitals and additionally promoted by strong orbital overlap with the ligand molecular orbitals, prevent a gold-centered reduction of the (triarylcorrolato)gold(III) complexes as thoroughly described in the literature. The systematic introduction of π electron-donating substituents should give insights into the electronic impact of each substituent on the relative energy of the frontier molecular orbitals of the ligand and whether it is possible to determine the spin density distribution of the paramagnetic complex based on the DFT optimized geometry or energy of frontier molecular orbitals of the diamagnetic complex.

Moreover, the systematic screening should establish the basis for prospective experimental studies, including the synthesis of novel functionalized corrolato ligands for a molecular stabilization of gold(II).

3 Results and Discussion

Parts of the results of this dissertation have been submitted as scientific articles to peer-reviewed journals.

The article in **section 3.1** involves the synthesis of the bis(β -diiminato)gold(III) complex $[\text{AuL}][\text{PF}_6]$, which has only been described in the literature so far by a crystal structure, NMR and absorption spectroscopy. Electrochemical characterizations have not yet been reported. The chemical reduction of $[\text{AuL}]^+$ is monitored via NMR-, EPR- and UV/Vis absorption spectroscopy as well as (spectro)electrochemistry. Applying density functional theory methods, the fundamental electronic and geometric differences between the porphyrinato- and bis(β -diiminato)gold complexes in their different oxidation states +III and +II are pointed out.

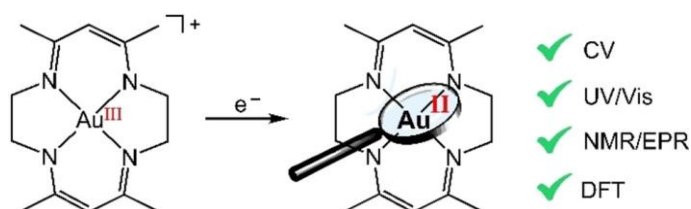
In **section 3.2**, the synthesis and spectroscopic characterization of the novel “Pacman”-like cofacial bis(porphyrinato)gold(III) complex $[\text{Au}_2(\text{DPD})][\text{PF}_6]_2$ is presented. The gold(III) complex is comprehensively characterized by multinuclear 1D- and 2D NMR spectroscopy, UV/Vis/NIR absorption- and IR spectroscopy as well as mass spectrometry. The electrochemical characteristics are examined by cyclic voltammetry and square wave voltammetry, electronic features of the one- and twofold reduced binuclear $[\text{Au}_2(\text{DPD})]^+$ and $\text{Au}_2(\text{DPD})$, respectively, via *in situ* X-band EPR spectroscopy and (low-temperature) absorption- and photoluminescence spectroscopy. Time-dependent density functional theory (TDDFT) methods are used to reveal the nature of intramolecular electronic transitions. The normal-coordinate structural decomposition (NSD) technique is used for a quantification of *out-of-plane* distortions of the porphyrine subunits.

The computational study presented in **section 3.3** concerns the DFT optimized geometries and electronic structures of substituted (corrolato)gold complexes in their singlet and doublet ground states. The dependency of the energy of the ligand-centered lowest unoccupied molecular orbitals upon systematic implementation of electron donating (aryl)substituents (4-methoxyphenyl, 4-(*N,N*-dimethyl)aminophenyl, 4-methoxy, *N,N*-dimethylamino) is analyzed. Furthermore, the localization of the Mulliken spin density is considered. The geometric distortions due to the introduction of bulky substituents are analyzed by the normal-coordinate structure decomposition (NSD) method.

3.1 14-Membered Macrocyclic beta-Diiminato Gold(II) – A New Member for the Gold(II) Complex Family?

Authors: Lukas Sorge, Julian Link, and Katja Heinze*. * = Corresponding author.

Chem. Eur. J. **2024**, e202400924.



Synthesis of a macrocyclic tetraaza gold(III) complex, subsequent chemical reduction and monitoring of the reaction products via UV/Vis absorption- and NMR-spectroscopy. The reduction products were identified as follow-up products of the irreversible disproportionation of gold(I) into gold(0) and gold(III).

Author contributions

Lukas Sorge performed the synthesis of the gold(III) complex, (spectro)electrochemical analyses, the reduction experiments as well as the characterization of the reaction products by absorption- and NMR spectroscopy, performed the DFT calculations and wrote the original manuscript. Julian Link synthesized the pro-ligand. Prof. Dr. Katja Heinze supervised the project and finalized the manuscript.

Supporting Information

for this article is found on page 107. Cartesian coordinates of DFT-optimized structures can be found online at: <https://chemistry-europe.onlinelibrary.wiley.com/doi/full/10.1002/chem.202400924>.



14-Membered Macrocyclic β -Diiminato Gold(II) – A New Member for the Gold(II) Complex Family?

Lukas Sorge,^[a] Julian Link,^[a] and Katja Heinze*^[a]

The chemistry of molecular gold compounds is dominated by the oxidation states +I and +III. For the intermediate oxidation state +II with 5d⁹ electron configuration, dimerization or disproportionation of the gold(II) radicals is favored, so that only a few mononuclear gold(II) complexes have been isolated to date. The present study addresses the one-electron reduction of the macrocyclic gold(III) complex [Au^{III}L]⁺ of the innocent β -diiminato ligand L²⁻ with a 14-membered macrocycle (L²⁻ = 5,7,12,14-tetramethyl-

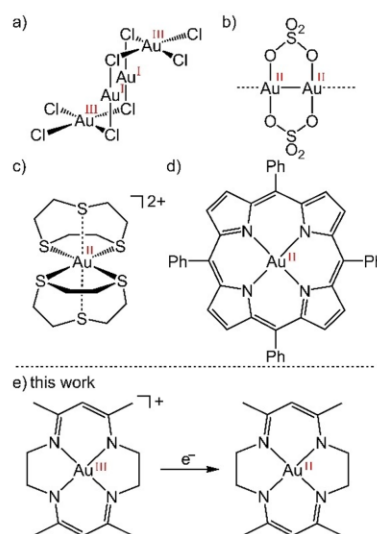
1,4,8,11-tetraazacyclotetradeca-5,7,12,14-tetraenoato). Electrochemistry, spectroelectrochemistry and chemical reduction of [Au^{III}L]⁺ monitored by UV/Vis, NMR and EPR spectroscopy together with density functional theory calculations reveal disproportionation of the initially generated but elusive gold(II) complex Au^{II}L and provide guidelines for prospective stable mononuclear tetraaza-macrocyclic gold(II) complexes.

Introduction

The gold(II) ion, especially in molecular environments, typically disproportionates into Au^I and Au^{III} or dimerizes to [Au^{II}-Au^{II}] with a gold(II)-gold(II) σ -bond, which can be bridged by a ligand or which can even be unsupported.^[1–3] The origin of these typical reaction pathways lies in the strong relativistic expansion and thus destabilization of the 5d orbitals.^[4–7] The half-filled 5d_{x²-y²} orbital is especially high in energy for the oxidation state +II in square-planar coordination geometry. Suitable environments to prevent disproportionation or dimerization are gas phase conditions in the mass spectrometer,^[8] noble gas matrices^[9–11] or zeolite encapsulation for a kinetic stabilization of mononuclear gold(II) species.^[12] Transient gold(II) species have also been proposed as intermediates in homogenous catalysis,^[2,13–19] artificial photosynthesis systems^[20–22] or radical^[23–26] and PCET^[27,28] chemistry. In solid state materials, such as in simple salts AuCl₂ or AuSO₄, either a mixed-valence situation Au^IAu^{III}Cl₄ or dimerization [Au^{II}(SO₄)₂]₂ occurs.^[1,29] A Au^{II}/Au^{III} mixed-valent perovskite Cs₂Au^IAu^{III}₂Cl₁₂ containing a square-planar coordinated gold(II) ion has been recently reported.^[30] Alternatively, tailored ligand environments are essential for the kinetic and/or thermodynamic stabilization of mononuclear gold(II). Schröder and co-workers exploited the rigid nature of chelating 1,4,7-trithiacyclononane ligands to stabilize the gold(II) ion in [Au^{II}([9]aneS₃)₂]²⁺ in a six-coordinate environment.^[31] A first-order Jahn-Teller effect arising from the

5d⁹ electron configuration leads to an elongated octahedral complex geometry.^[31] Even without the steric protection along the Jahn-Teller axis (z axis), mononuclear gold(II) can be stabilized as shown by the synthesis, isolation and full characterization of the tetraphenylporphyrinato gold(II) complex Au^{II}(tpp) as a truly mononuclear four-coordinate gold(II) complex (tpp²⁻ = 5,10,15,20-tetraphenylporphyrinato).^[32]

The gold(II) ion in Au^{II}(tpp) is located in a [2+2] slightly distorted square-planar [AuN₄] coordination environment with two shorter and two longer Au–N distances due to a second-order Jahn-Teller effect (Scheme 1).^[32] Dimerization of Au^{II}(tpp)



Scheme 1. Structural features of a) AuCl₂, b) AuSO₄, and molecular structures of c) [Au^{II}([9]aneS₃)₂]²⁺ and d) Au^{II}(tpp) as well as e) the reduction of [AuL]⁺ studied in this work.

[a] L. Sorge, J. Link, Prof. Dr. K. Heinze
Department of Chemistry,
Johannes Gutenberg University Mainz,
Duesbergweg 10–14, 55128 Mainz, Germany
E-mail: katja.heinze@uni-mainz.de

Supporting information for this article is available on the WWW under
<https://doi.org/10.1002/chem.202400924>

© 2024 The Authors. Chemistry - A European Journal published by Wiley-VCH GmbH. This is an open access article under the terms of the Creative Commons Attribution License, which permits use, distribution and reproduction in any medium, provided the original work is properly cited.

3.1 | 14-Membered Macrocyclic beta-Diiminato Gold(II) – A New Member for the Gold(II) Complex Family?

with formation of a $[\text{Au}^{\text{II}}-\text{Au}^{\text{II}}]$ σ bond from the half-filled $5d_{x^2-y^2}$ orbitals is inhibited by the rigid porphine macrocycle blocking the xy plane. The formation of gold(I) as a result of disproportionation is energetically unfavorable due to the rigid coordination environment preventing the formation of linearly coordinated gold(I). Instead, the porphyrin ligand is reversibly reduced forming $[\text{Au}^{\text{II}}(\text{tpp}^{\cdot-})]$. The latter radical anion is also thermodynamically comparably unfavorable so that the disproportionation constant of $\text{Au}(\text{tpp})$ amounts to merely $K_d = 3 \times 10^{-12}$ at room temperature.^[32,33] As gold(I) is avoided, further potentially irreversible reduction or disproportionation reactions to gold(0) species are prevented as well.^[32]

To question whether the porphine ligand is special in stabilizing gold(II) in a square-planar geometry by its rigid nature and its redox non-innocence prohibiting the formation of gold(I) and subsequent decomposition to gold(0), we investigated the redox chemistry of the known gold(III) complex $[\text{Au}^{\text{III}}\text{L}]^+$ with the redox-innocent dianionic macrocyclic 5,7,12,14-tetramethyl-1,4,8,11-tetraazacyclotetradeca-5,7,12,14-tetraenato ligand L^{2-} (Scheme 1). The parent gold(III) complexes $[\text{Au}^{\text{III}}(\text{tpp})]^{3+}$ ^[34] and $[\text{Au}^{\text{III}}\text{L}]^+$ ^[35,36] share a square-planar $[\text{AuN}_4]$ coordination geometry with similar Au–N distances. However, the one-electron reduction of $[\text{Au}^{\text{III}}\text{L}]^+$ to $\text{Au}^{\text{II}}\text{L}$ has not been reported yet. We describe the electrochemical, spectroelectrochemical and chemical reduction of $[\text{Au}^{\text{III}}\text{L}]^+$ and analyze the products by UV/Vis, EPR and NMR spectroscopy along with density functional theory (DFT) calculations to delineate ligand design strategies for four-coordinate molecular gold(II) complexes with respect to ring size, flexibility and redox activity of the macrocyclic ligand.

Results and Discussion

Synthesis and Spectroscopic Characterization. The gold(III) complex $[\text{AuL}][\text{PF}_6]$ with the 14-membered macrocyclic ligand L^{2-} is prepared according to literature procedures^[37,38] in a template reaction from $[\text{Au}(\text{en})_2]\text{Cl}_3$ (en = ethylenediamine)^[38] and acetylacetonate followed by counter ion exchange with $[\text{NH}_4][\text{PF}_6]$ in 60% overall yield. The air and moisture stable complex $[\text{AuL}][\text{PF}_6]$ is characterized by multinuclear NMR (Figures S1–S4), ESI⁺ mass spectrometry (Figure S7), IR spectroscopy (Figure S9) as well as UV/Vis absorption spectroscopy (Figures S20 and S21). The complex is sufficiently soluble in DMSO and DMF, but only poorly soluble in THF or 2-MeTHF. The ligand H_2L was prepared according to literature procedures^[39] and characterized by ESI⁺ mass spectrometry (Figure S8), ¹H and ¹³C{¹H} NMR (Figures S5 and S6) and UV/Vis absorption spectroscopy for comparative reasons (Figures S23 and S24). Coordination of the gold(III) ion to the ligand is clearly indicated by the ESI⁺ mass spectrometric data and the ¹H NMR coordination shift of the methylene and methine proton resonances from 3.31 and 4.44 ppm to 3.79 and 5.05 ppm, respectively. The PF_6^- counter ion is detected by its ¹⁹F and ³¹P NMR resonances as well as its characteristic IR frequencies (Figures S3, S4 and S9).

The UV/Vis absorption spectrum of $[\text{AuL}][\text{PF}_6]$ in DMSO is dominated by a band maximum at 286 nm ($\epsilon = 4245 \text{ M}^{-1} \text{ cm}^{-1}$), an intense transition at 372 nm ($\epsilon = 10730 \text{ M}^{-1} \text{ cm}^{-1}$) and a weaker shoulder located at ca. 450 nm ($\epsilon = 652 \text{ M}^{-1} \text{ cm}^{-1}$) (Figure S20). These band maxima are rather weakly sensitive to the solvents DMSO vs. DMSO:DMF:2-MeTHF 1:5:5 (v/v) mixture (Figure S21). This specific solvent mixture combines sufficient solubility, redox stability of the reduced species for electrochemical experiments and formation of glass at low temperatures for EPR spectroscopic experiments. According to time-dependent DFT (TDDFT) calculations on $[\text{AuL}]^+$ the intense band arises from a $\pi-\pi^*$ transition within the β -diiminato units of the macrocyclic ligand, while the low-energy shoulder arises from a ligand-to-metal (LMCT; π_{ligand} to $5d_{x^2-y^2}$) transition (Figure S20, Table S2). In agreement with this LMCT assignment, such a band is absent in the pro-ligand H_2L (Figures S23 and S24). The presence of an LMCT band suggests that gold(II) with $5d^9$ electron configuration might be accessible by one-electron reduction.

Cyclic and Square Wave Voltammetry. The gold(III) complex $[\text{AuL}][\text{PF}_6]$ shows a quasireversible reduction wave at -2.12 V and an irreversible wave at ca. -2.7 V vs. ferrocene/ferrocenium in DMSO:DMF:2-MeTHF 1:5:5 (v/v)/ $[\text{Bu}_4\text{N}][\text{PF}_6]$ (Figures 1 and 2). These values shift only slightly in DMSO/ $[\text{Bu}_4\text{N}][\text{PF}_6]$ (Figures S12 and S13).

The cathodic peak current $i_c(1)$ at -2.06 V exceeds that of its corresponding anodic counterpart $i_a(1)$ in the cyclic voltammogram (Figure 1b). The cathodic peak current $i_c(1)$ is also larger than the cathodic current at the second reduction wave $i_c(2)$ at -2.7 V (Figure 2). $i_c(1)$ is twice as large as that of the reductive FcH^+/FcH wave resulting from one equivalent of

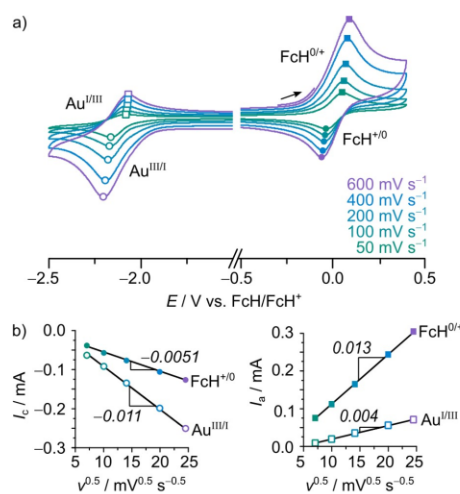


Figure 1. a) Cyclic voltammograms of $[\text{AuL}][\text{PF}_6]$ and 1 equivalent ferrocene as internal standard 10^{-3} M in $0.1 \text{ M } [\text{Bu}_4\text{N}][\text{PF}_6]/\text{DMSO}:\text{DMF}:\text{2-MeTHF } 1:5:5$ (v/v) at different scan rates. Scan direction indicated by a black arrow. b) Cathodic and anodic peak currents i_c and i_a plotted against the square root of the corresponding scan rates. Slope of the linear fits given in italics.

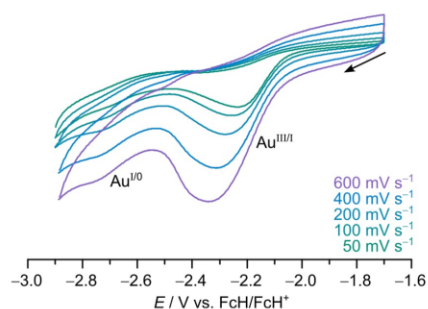


Figure 2. Cyclic voltammograms of $[\text{AuL}][\text{PF}_6] 10^{-3} \text{ M}$ in $0.1 \text{ M } [\text{tBu}_4\text{N}][\text{PF}_6]/\text{DMSO}:\text{DMF}:\text{2-MeTHF } 1:5:5 \text{ (v/v)}$ at different scan rates.

ferrocene as internal standard (Figure 1b). These data suggest, that $[\text{Au}^{\text{III}}\text{L}]^+$ is reduced in a quasi two-electron ($2e^-$) process to $[\text{Au}^{\text{I}}\text{L}]^+$ at around -2.06 V . The $[\text{Au}^{\text{I}}\text{L}]^+$ formed after the $2e^-$ reduction disproportionates into $\text{Au}^{\text{I}}\text{L}$ and $[\text{Au}^{\text{0}}\text{L}]^{2-}$. The latter species will irreversibly release the ligand with subsequent formation of gold(0). Hence, only one half of the current of the two-electron process is observed in the reverse anodic scan at -2.04 V (Figure 1). At higher potentials close to the FcH^+/FcH wave, the deposited gold(0) is re-oxidized, so that that the peak current of the FcH to FcH^+ oxidation increases correspondingly. At -2.7 V , residual, i.e. not yet disproportionated $[\text{Au}^{\text{I}}\text{L}]^+$ is reduced to gold(0).

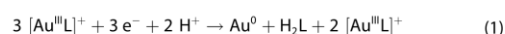
Assuming a maximum peak difference of 0.1 V for the $[\text{Au}^{\text{III}}\text{L}]^+/\text{Au}^{\text{I}}\text{L}$ and $\text{Au}^{\text{I}}\text{L}/[\text{Au}^{\text{I}}\text{L}]^+$ processes, a disproportionation constant of $\text{Au}^{\text{I}}\text{L}$ of $K_d(\text{Au}^{\text{I}}\text{L}) \approx 0.02$ can be estimated. These estimated values can be compared to the respective potentials -0.97 , -1.65 and -2.34 V of the reduction of $[\text{Au}^{\text{III}}(\text{tpp})]^+$ to $\text{Au}^{\text{I}}(\text{tpp})$ and to $[\text{Au}^{\text{II}}(\text{tpp}^+)]^-$.³¹ The disproportionation constant $K_d(\text{Au}^{\text{I}}(\text{tpp})) = 3 \times 10^{-12}$ is thus smaller by orders of magnitude. Similarly, the disproportionation constants for the anionic species $[\text{Au}^{\text{I}}\text{L}]^-$ and $[\text{Au}^{\text{I}}(\text{tpp}^+)]^-$ of $K_d([\text{Au}^{\text{I}}\text{L}]^-) \approx 5 \times 10^{-8}$ and $K_d([\text{Au}^{\text{I}}(\text{tpp}^+)]^-) = 2 \times 10^{-12}$ differ significantly. As the formal gold(0) complex $[\text{Au}^{\text{0}}\text{L}]^{2-}$ is unstable towards ligand loss, the quite large disproportionation constants of $\text{Au}^{\text{I}}\text{L}$ and $[\text{Au}^{\text{I}}\text{L}]^+$ provide an efficient and irreversible decay pathway towards gold(0).

A single $3e^-$ reduction of gold(III) to gold(0) has been observed for $[\text{Au}^{\text{III}}(\text{cyclam})]^{3+}$, while $[\text{Au}^{\text{III}}(\text{Me}_2\text{cyclam})]^{3+}$ shows three $1e^-$ reduction processes at 0.17 , -0.09 and -0.90 V vs. SCE (cyclam = 1,4,8,11-tetraazacyclotetradecane).⁴⁰ These data together with the present data and that of $[\text{Au}^{\text{III}}(\text{tpp})]^+$ demonstrate, that the macrocyclic ligand determines the susceptibility of gold(III) towards disproportionation.

Chemical Reduction. Potassium graphite KC_8 ,⁴¹ potassium⁴² or sodium anthracene (Figures S17 and S18) are sufficiently reducing to address the first $2e^-$ reduction wave of $[\text{Au}^{\text{III}}\text{L}][\text{PF}_6]$. A solution of $[\text{AuL}][\text{PF}_6]$ in $\text{DMSO}:\text{DMF}:\text{2-MeTHF } 1:5:5 \text{ (v/v)}$ was treated with one of these reductants and rapidly frozen by cooling with liquid nitrogen. Unfortunately, no EPR resonances (X-band) were observed, irrespective of the reductant employed. The EPR resonance of sodium anthracene

(Figure S18), however, is absent as well, suggesting a successful electron transfer. Obviously, disproportionation of the initially formed $\text{Au}^{\text{I}}\text{L}$ and $[\text{Au}^{\text{I}}\text{L}]^+$ is too fast for the duration of sample preparation and irreversible.

To detect the final products of the one-electron reduction, the gold(III) complex was reduced with one equivalent of KC_8 in $\text{DMSO}:\text{DMF}:\text{MeTHF } 1:5:5 \text{ (v/v)}$ over 2 h. After filtration, removal of the solvents and dissolution in CD_2Cl_2 a ^1H NMR spectrum was recorded (Figure 3). The ^1H NMR spectrum displays resonances, which can be assigned to $[\text{Au}^{\text{III}}\text{L}]^+$ ($\delta = 4.98, 3.82$ and 2.22 ppm) and the pro-ligand H_2L ($\delta = 4.50, 3.38$ and 1.87 ppm) in a 2:1 integral ratio. The NH proton resonance of H_2L is observed at $\delta = 11.60 \text{ ppm}$. The NH protons likely stem from the employed solvents. Consequently, one-electron reduction of $[\text{Au}^{\text{III}}\text{L}]^+$ is followed by several disproportionation reactions leading to gold(0), free ligand and back-formation of $[\text{Au}^{\text{III}}\text{L}]^+$ according to eq. 1.



Using one equivalent of sodium anthracene as reductant (Figure S18) similarly leads to the formation of H_2L (Figure S19).

The 2:1 ratio of $[\text{Au}^{\text{III}}\text{L}]^+$ and H_2L after one-electron reduction of $[\text{Au}^{\text{III}}\text{L}]^+$ with KC_8 is also observed in the UV/Vis absorption spectrum of the filtered reaction mixture as shown by the sum spectrum of $[\text{Au}^{\text{III}}\text{L}]^+$ and H_2L in a 2:1 ratio (Figure 4).

Clearly, the disproportionation of the gold(II) and gold(I) species is fast enough to prevent their spectroscopic characterization. This is also consistent with the observation of isosbestic points during the spectroelectrochemical reduction showing the decrease of the $[\text{Au}^{\text{III}}\text{L}]^+$ absorption band (Figure S22). For the gold(II) complex $\text{Au}^{\text{II}}\text{L}$, TDDFT calculations predict a low-energy absorption band at 933 nm , which possesses metal-to-ligand charge transfer (MLCT) character, namely from the half-filled $5d_{z^2-y^2}$ orbital of Au^{II} to one β -diimine unit of the ligand

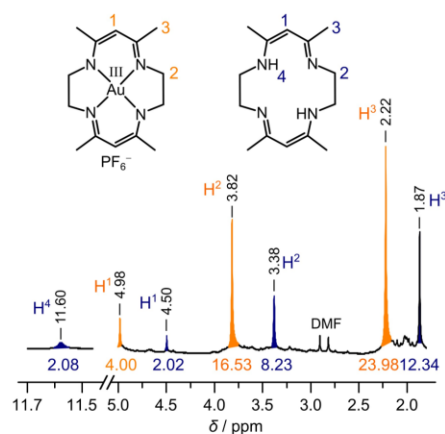


Figure 3. ^1H NMR spectrum of the reaction products of $[\text{AuL}][\text{PF}_6]$ with 1 equivalent KC_8 in $\text{DMSO}:\text{DMF}:\text{2-MeTHF } 1:5:5 \text{ (v/v)}$. Spectrum recorded in CD_2Cl_2 . Atom numbering given for proton assignments.

3.1 | 14-Membered Macrocyclic beta-Diiminato Gold(II) – A New Member for the Gold(II) Complex Family?

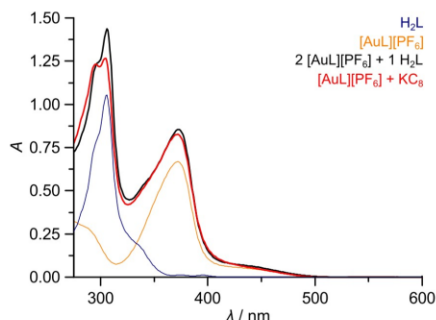


Figure 4. Absorption spectrum (red) of the reaction mixture after reduction of $[\text{AuL}][\text{PF}_6]$ with 1 equivalent KC_8 in DMSO:DMF:2-MeTHF 1:5:5 (v/v). Absorption spectra of $[\text{AuL}][\text{PF}_6]$ (orange), the pro-ligand H_2L (blue) and a sum spectrum of $[\text{AuL}][\text{PF}_6]$ and H_2L in a 2:1 ratio (black).

(Figure S25, Table S3). However, no such absorption band could be detected during the spectroelectrochemical reduction (Figure S22). The TDDFT calculated transitions of the aurate(I) $[\text{Au}^{\text{I}}\text{L}]^-$ are uncharacteristic according to TDDFT calculations (Figure S26, Table S4) and thus $[\text{Au}^{\text{I}}\text{L}]^-$ might not be detectable in the reaction mixture at low concentrations.

Quantum Chemical Calculations. In order to delineate the differences between the reversible $[\text{Au}(\text{tpp})]^{+/0/-}$ redox steps and the irreversible reductions of $[\text{Au}^{\text{III}}\text{L}]^+$ we optimized the geometries of $[\text{AuL}]^{+/0/-}$ as well as of $[\text{Au}(\text{tpp})]^{+/0/-}$ complexes for comparison on the same level of theory including relativistic and solvent effects.

The gold(III) complex $[\text{Au}^{\text{III}}\text{L}]^+$ had been crystallized with various counter ions.^[35,36,43,44] In all cases, a four-coordinate slightly twisted square-planar environment is found with essentially planar six-membered chelate rings and twisted five-membered chelate rings of the ethylene diamine parts of the macrocycle. The Au–N distances vary from 1.974 to 1.992 Å with Au–N = 1.974(2)–1.981(2) Å ($[\text{AuL}][\text{BPh}_4]$),^[36] 1.988(4)–1.992(4) Å ($[\text{AuL}][\text{ReO}_4]$),^[43] 1.981(3)–1.986(3) Å ($[\text{AuL}][\text{AuBr}_2]$)^[44] and Au–N 1.975(5)–1.9885(5) Å ($[\text{AuL}][\text{Br}]$).^[35] In the DFT optimized geometry of $[\text{AuL}]^+$, the Au–N distances were calculated as 1.995–1.996 Å in reasonable agreement with the solid state structural data (Figure 5). The DFT calculated distances of $[\text{Au}(\text{tpp})]^{+/}$ of 2.029 Å agree with those of $[\text{Au}(\text{tpp})][\text{ClO}_4]$ (2.032(5)–2.033(5) Å) as well.^[45] The shorter Au–N distances in $[\text{Au}^{\text{III}}\text{L}]^+$ as compared to $[\text{Au}^{\text{III}}(\text{tpp})]^{+/}$ likely arise from the smaller ring size of the macrocycle (14 vs. 16-membered rings) maintaining an essential square-planar $[\text{AuN}_4]$ coordination. The stronger Au–N interactions in $[\text{Au}^{\text{III}}\text{L}]^+$ substantially raise the energy of the $5d_{x^2-y^2}$ orbital as compared to the energy of the $5d_{x^2-y^2}$ orbital in $[\text{Au}^{\text{III}}(\text{tpp})]^{+/}$ (Figure 6). This rather high energy of the $5d_{x^2-y^2}$ orbital accounts for the more cathodic reduction potential of $[\text{Au}^{\text{III}}\text{L}]^+$ (see above).

Reduction of $[\text{Au}^{\text{III}}\text{L}]^+$ and $[\text{Au}^{\text{III}}(\text{tpp})]^{+/}$ leads to the gold(II) complexes $\text{Au}^{\text{II}}\text{L}$ and $\text{Au}^{\text{II}}(\text{tpp})$ with metal-centered spin densities of 0.374 and 0.328, respectively. In both cases, some spin density is delocalized onto the coordinating N atoms (0.116–

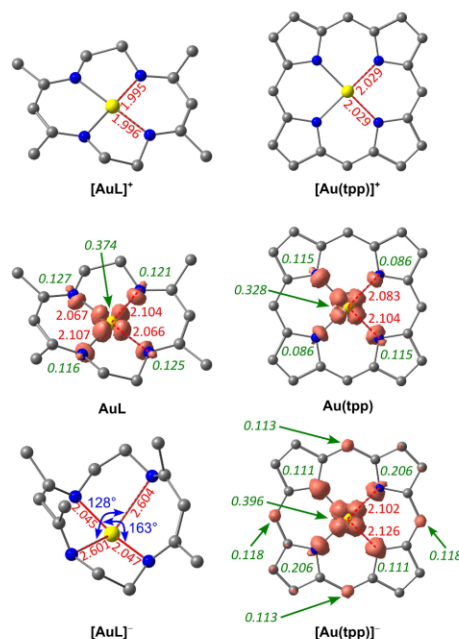


Figure 5. DFT optimized geometries of $[\text{AuL}]^+$, AuL , $[\text{AuL}]^-$ (left) and $[\text{Au}(\text{tpp})]^{+/}$, $\text{Au}(\text{tpp})$ and $[\text{Au}(\text{tpp})]^-$ (right) with Au–N distances given in Å (red), angles given in deg (blue), Mulliken spin populations given in green (italics). Spin density plots at an isosurface value of 0.015 a.u. (orange). Hydrogen atoms and phenyl substituents omitted for clarity.

0.127 and 0.086–0.115, respectively). The metal-centered reduction of $[\text{Au}^{\text{III}}\text{L}]^+$ to $\text{Au}^{\text{II}}\text{L}$ increases the calculated Au–N bond lengths to 2.066/2.067/2.104/2.107 Å. Similarly, the calculated Au–N distances of $[\text{Au}^{\text{III}}(\text{tpp})]^{+/}$ increased to 2.083/2.104 Å in $\text{Au}^{\text{II}}(\text{tpp})$ in agreement with the experimental data (2.0586(24)/2.0970(23) Å).^[30] The differences between the *trans* Au–N bond lengths are significant and reproduced by the calculations in both cases with the bond length difference in $\text{Au}^{\text{II}}\text{L}$ (0.038 Å) being larger than that calculated for $\text{Au}^{\text{II}}(\text{tpp})$ (0.021 Å). This symmetry-lowering had been suggested to arise from a second-order Jahn-Teller effect of the $(5d)^9$ electron configuration achieved by admixture of the $(5d)^9(6s)^1$ electron configuration.^[32] Obviously, the L^{2-} macrocycle with ethylene bridges can better accommodate Au–N bond length changes than the more rigid tpp^{2-} macrocycle lacking aliphatic bridges. This higher flexibility becomes even more obvious in the aurates $[\text{AuL}]^-$ and $[\text{Au}(\text{tpp})]^-$.

Due to the presence of a $\pi^*(\text{tpp})$ orbital of appropriate energy (Figure 6), the electronic structure of $[\text{Au}(\text{tpp})]^-$ is considered as a ligand centered radical anion coordinated to gold(II) $[\text{Au}^{\text{II}}(\text{tpp}^{\cdot-})]^-$ with balanced Au–N distances of 2.102/2.126 Å instead of a gold(I) complex with a twofold coordination. On the other hand, L^{2-} lacks suitable ligand-centered π^* orbitals (Figure 6). Consequently, $[\text{AuL}]^-$ is a genuine gold(I)

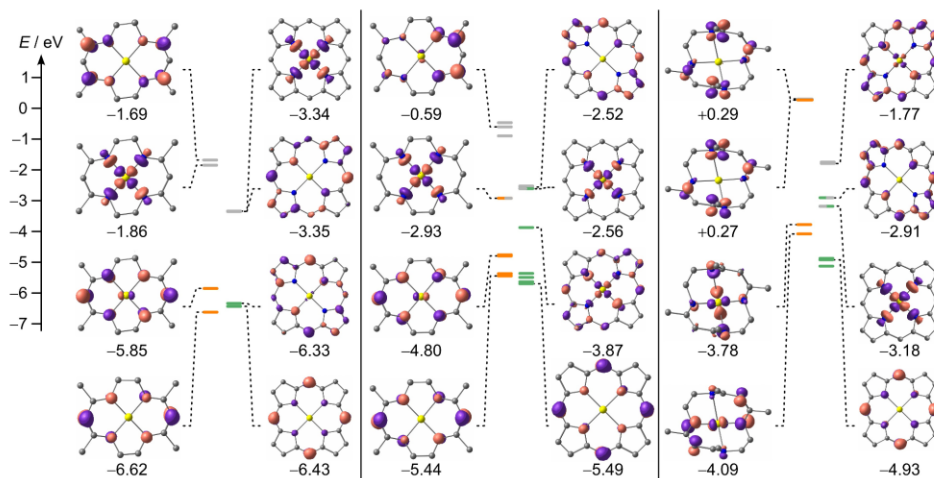


Figure 6. Molecular orbital diagrams for $[\text{AuL}]^+ / [\text{Au}(\text{tpp})]^+$ (left), $\text{AuL} / \text{Au}(\text{tpp})$ (center) and $[\text{AuL}]^- / [\text{Au}(\text{tpp})]^-$ (right) and frontier molecular orbitals derived from DFT geometry optimized structures. Occupied molecular orbitals are indicated by filled, singly occupied α molecular orbitals by half-filled and unoccupied molecular orbitals by grey bars. Hydrogen atoms and phenyl substituents omitted for clarity. Isosurface values at 0.018 a.u.

species. As gold(II) prefers a linear coordination mode, the macrocyclic ligand distorts to accommodate gold(II) in a twofold coordination with Au–N distances of 2.045/2.047 Å and an N–Au–N angle of 163°. With this small angle the coordination geometry significantly deviates from linear. The other two Au–N distances increased to 2.601/2.603 Å with an N–Au–N angle of 128°. This leads to a strained out-of-plane coordination of the gold(II) ion and hence instability with respect to disproportionation and ligand dissociation.

Consequently, it is the instability of the gold(II) species $[\text{AuL}]^+$ that prevents the observation of the gold(II) complex $\text{Au}^{\text{II}}\text{L}$. If the gold(II) complex would be stable towards disproportionation followed by ligand loss it should be possible to observe gold(III) in the presence of gold(III) and gold(I) at its equilibrium concentration, even if its concentration might be low. The energies obtained from DFT calculations of $[\text{AuL}]^+$, AuL and $[\text{AuL}]^-$ yield a small positive $\Delta G = 8 \text{ kJ mol}^{-1}$ for the disproportionation and $K_{\text{d}} = 0.04$ at 298 K. Hence, even though $\text{Au}^{\text{II}}\text{L}$ might be weakly stabilized, the adjacent labile gold(I) oxidation state prevents its observation. In contrast, $\text{Au}^{\text{II}}(\text{tpp})$ and $[\text{Au}^{\text{II}}(\text{tpp})]^+$ are stable towards disproportionation, which closes the decay path to gold(0) and allows the isolation of $\text{Au}^{\text{II}}(\text{tpp})$.^[32]

Conclusions

The gold(II) species $\text{Au}^{\text{II}}\text{L}$ with the flexible 14-membered macrocyclic ligand L^{2-} ($\text{L}^{2-} = 5,7,12,14$ -tetramethyl-1,4,8,11-tetraazacyclotetradeca-5,7,12,14-tetraenato) is slightly stabilized towards disproportionation. This thermodynamic stability should allow its *in situ* characterization at its equilibrium concentration with $[\text{AuL}]^+$ and $[\text{AuL}]^-$ being present as well. However, the aurate(II)

$[\text{AuL}]^-$ is susceptible towards irreversible disproportionation followed by ligand dissociation. This leads to an overall irreversible reduction to gold(0) so that the gold(II) and gold(I) complexes of L^{2-} are only transient species and remain elusive.

The moderate thermodynamic stability of $\text{Au}^{\text{II}}\text{L}$ as compared to $\text{Au}^{\text{II}}(\text{tpp})$ stems from its higher energy $5d_{x^2-y^2}$ orbital. The even more important insufficient kinetic inertness arises from the reactivity of the strongly distorted essentially two-coordinate aurate $[\text{AuL}]^-$ enabled by the flexible and redox-innocent L^{2-} macrocyclic ligand. The stability and hence the successful isolation of $\text{Au}(\text{tpp})$ ^[32] thus arises from the rigid and non-innocent 16-membered macrocycle that prevents the formation of distorted gold(II) species by formation of a ligand-centered radical with balanced Au–N distances instead.

Keys towards isolable mononuclear gold(II) complexes are thus employing i) rigid macrocyclic ligands that protect the gold(II) center from dimerization in the xy plane and ii) kinetically stable adjacent oxidation states. The present study shows that the macrocyclic ligand should stabilize the lower adjacent oxidation state, formally gold(I), for example by accommodating the additional electron in its π^* system to prevent a disproportionation cascade to gold(0).

Supporting Information

The Supporting Information contains the employed methods, the synthesis procedures, spectroscopic, analytical and computational data (pdf) and the Cartesian coordinates of DFT optimized geometries (xyz). The authors have cited additional references within the Supporting Information.^[46–61]

3.1 | 14-Membered Macrocyclic beta-Diiminato Gold(II) – A New Member for the Gold(II) Complex Family?

Acknowledgements

K. H. and L. S. thank the Deutsche Forschungsgemeinschaft DFG for funding via grant HE2778/16-1. Parts of this research were conducted using the supercomputer Elwetritsch and advisory services offered by the University of Kaiserslautern-Landau (<https://hpc.rz.rptu.de>). Open Access funding enabled and organized by Projekt DEAL.

Conflict of Interests

The authors declare no conflict of interest.

Data Availability Statement

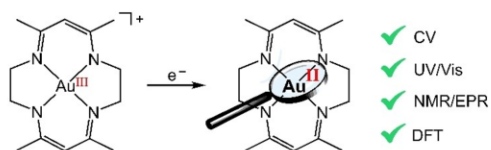
The data that support the findings of this study are available in the supplementary material of this article.

Keywords: disproportionation · gold · macrocycle · redox chemistry

- [1] D. B. Dell'Amico, F. Calderazzo, F. Marchetti, S. Merlino, *J. Chem. Soc. Dalton Trans.* **1982**, 2257–2260.
- [2] a) K. Heinze, *Angew. Chem. Int. Ed.* **2017**, *56*, 16126–16134; b) J. C. Pérez-Sánchez, R. P. Herrera, M. Concepción Gimeno, *Dalton Trans.* **2024**, *53*, 382–393.
- [3] a) H. Schmidbaur, *Acc. Chem. Res.* **1975**, *8*, 62–70; b) H. Schmidbaur, R. Franke, *Inorg. Chim. Acta* **1975**, *13*, 85–89; c) J. P. Fackler Jr., J. D. Basil, *Organometallics* **1982**, *1*, 871–873; d) V. W.-W. Yam, S. W.-K. Choi, K.-K. Cheung, *Chem. Commun.* **1996**, 1173–1174; e) S. K. Bhargava, F. Mohr, M. A. Bennett, L. L. Welling, A. C. Willis, *Organometallics* **2000**, *19*, 5628–5635; f) J. P. Fackler Jr., *Inorg. Chem.* **2002**, *41*, 6959–6972; g) K. Kitada, M. Takahashi, M. Takeda, S. K. Bhargava, S. H. Privér, M. A. Bennett, *Dalton Trans.* **2006**, 2560–2571; h) J. Coetzee, W. F. Gabrielli, K. Coetzee, O. Schuster, S. D. Nogai, S. Cronje, H. G. Raubenheimer, *Angew. Chem. Int. Ed.* **2007**, *46*, 2497–2500; i) A. A. Mohamed, H. E. Abdou, J. P. Fackler Jr., *Coord. Chem. Rev.* **2010**, *254*, 1253–1259.
- [4] L. F. Pašteka, E. Eliav, A. Borschevsky, U. Kaldor, P. Schwerdtfeger, *Phys. Rev. Lett.* **2017**, *118*, 023002.
- [5] V. W.-W. Yam, E. C.-C. Cheng, *Chem. Soc. Rev.* **2008**, *37*, 1806–1813.
- [6] H. Schmidbaur, *Gold Bull.* **2000**, *33*, 1–10.
- [7] P. Pyykkö, *Angew. Chem. Int. Ed.* **2004**, *43*, 4412–4456.
- [8] N. R. Walker, R. R. Wright, P. E. Barran, A. J. Stace, *Organometallics* **1999**, *18*, 3569–3571.
- [9] T. Drews, S. Seidel, K. Seppelt, *Angew. Chem. Int. Ed.* **2002**, *41*, 454–456.
- [10] S. Seidel, K. Seppelt, *Science* **2000**, *290*, 117–118.
- [11] K. Seppelt, *Z. Anorg. Allg. Chem.* **2003**, *629*, 2427–2430.
- [12] Z. Qu, L. Giurgiu, E. Roduner, *Chem. Commun.* **2006**, 2507–2509.
- [13] B. Sahoo, M. N. Hopkinson, F. Glorius, *J. Am. Chem. Soc.* **2013**, *135*, 5505–5508.
- [14] S. Kim, J. Rojas-Martin, F. D. Toste, *Chem. Sci.* **2016**, *7*, 85–88.
- [15] X. Shu, M. Zhang, Y. He, H. Frei, F. D. Toste, *J. Am. Chem. Soc.* **2014**, *136*, 5844–5847.
- [16] L. Huang, M. Rudolph, F. Rominger, A. S. K. Hashmi, *Angew. Chem. Int. Ed.* **2016**, *55*, 4808–4813.
- [17] a) P. Veit, C. Volkert, C. Förster, V. Ksenofontov, S. Schlicher, M. Bauer, K. Heinze, *Chem. Commun.* **2019**, *55*, 4615–4618; b) M. P. Schrick, G. K. Ramollo, C.-M. S. Hirschbiegel, M. Fernandes, A. Lemmerer, C. Förster, D. I. Bezuidenhout, K. Heinze, *Organometallics* **2024**, *43*, 69–84.
- [18] S. D. Waniek, C. Förster, K. Heinze, *Eur. J. Inorg. Chem.* **2022**, e202100905.
- [19] S. Xia, W. Li, H. Chen, C. Zhu, J. Han, J. Xie, *J. Am. Chem. Soc.* **2023**, *145*, 26756–26764.
- [20] S. Fukuzumi, K. Ohkubo, W. E. Z. Ou, J. Shao, K. M. Kadish, J. A. Hutchison, K. P. Ghiggino, J. J. Sentic, M. J. Crossley, *J. Am. Chem. Soc.* **2003**, *125*, 14984–14985.
- [21] A. M. Brun, A. Harriman, V. Heitz, J. P. Sauvage, *J. Am. Chem. Soc.* **1991**, *113*, 8657–8663.
- [22] E. Göransson, J. Boixel, J. Fortage, D. Jacquemin, H.-C. Becker, E. Blart, L. Hammarström, F. Odobel, *Inorg. Chem.* **2012**, *51*, 11500–11512.
- [23] A. Johnson, R. J. Puddephatt, *J. Chem. Soc. Dalton Trans.* **1975**, 115–120.
- [24] A. Johnson, R. J. Puddephatt, *J. Chem. Soc. Dalton Trans.* **1976**, 1360–1363.
- [25] M. N. Hopkinson, A. Tlahuext-Aca, F. Glorius, *Acc. Chem. Res.* **2016**, *49*, 2261–2272.
- [26] A. Tlahuext-Aca, M. N. Hopkinson, B. Sahoo, F. Glorius, *Chem. Sci.* **2016**, *7*, 89–93.
- [27] S. Engbers, I. F. Leach, R. W. A. Havenith, J. E. M. N. Klein, *Chem. Eur. J.* **2022**, *28*, e202200599.
- [28] K. M. Hess, I. F. Leach, L. Wijtenhorst, H. Lee, J. E. M. N. Klein, *Angew. Chem. Int. Ed.* **2024**, *63*, e202318916.
- [29] M. S. Wickleder, *Z. Anorg. Allg. Chem.* **2001**, *627*, 2112–2114.
- [30] K. P. Lindquist, A. Eghdami, C. R. Deschene, A. J. Heyer, J. Wen, A. G. Smith, E. I. Solomon, Y. S. Lee, J. B. Neaton, D. H. Ryan, H. I. Karunadasa, *Nat. Chem.* **2023**, *15*, 1780–1786.
- [31] A. J. Blake, J. A. Greig, A. J. Holder, T. I. Hyde, A. Taylor, M. Schröder, *Angew. Chem. Int. Ed.* **1990**, *29*, 197–198.
- [32] S. Preiß, C. Förster, S. Otto, M. Bauer, P. Müller, D. Hinderberger, H. Hashemi Haeri, L. Carella, K. Heinze, *Nat. Chem.* **2017**, *9*, 1249–1255.
- [33] S. Preiß, J. Melomedov, A. Wünsche von Leupoldt, K. Heinze, *Chem. Sci.* **2016**, *7*, 596–610.
- [34] E. B. Fleischer, A. Laszlo, *Inorg. Nucl. Chem. Lett.* **1969**, *5*, 373–376.
- [35] V. A. Afanas'eva, I. V. Mironov, L. A. Glinskaya, R. F. Klevtsova, *Russ. J. Coord. Chem.* **2010**, *36*, 9–21.
- [36] V. A. Afanas'eva, L. A. Glinskaya, D. A. Piryazev, S. A. Gromilov, P. E. Plyusnin, L. A. Sheludyakova, *Inorg. Chem. Commun.* **2017**, *83*, 70–75.
- [37] B. P. Block, J. C. Bailar, *J. Am. Chem. Soc.* **1951**, *73*, 4722–4725.
- [38] J.-H. Kim, G. W. Everett Jr., *Inorg. Chem.* **1979**, *18*, 3145–3149.
- [39] T. Tokumitsu, T. Hayashi, *Bull. Chem. Soc. Jpn.* **1981**, *54*, 2348–2351.
- [40] E. Kimura, Y. Kurogi, T. Koike, M. Shionoya, Y. Itaka, *J. Coord. Chem.* **1993**, *28*, 33–49.
- [41] S. A. Hodge, D. J. Buckley, H. C. Yau, N. T. Skipper, C. A. Howard, M. S. P. Shaffer, *Nanoscale* **2017**, *9*, 3150–3158.
- [42] N. G. Connelly, W. E. Geiger, *Chem. Rev.* **1996**, *96*, 877–910.
- [43] V. A. Afanas'eva, L. A. Glinskaya, D. A. Piryazev, S. A. Gromilov, *J. Struct. Chem.* **2015**, *56*, 787–791.
- [44] V. A. Afanas'eva, L. A. Glinskaya, R. F. Klevtsova, I. V. Mironov, *Russ. J. Coord. Chem.* **2011**, *37*, 325–332.
- [45] C.-M. Che, R. W.-Y. Sun, W.-Y. Yu, C.-B. Ko, N. Zhu, H. Sun, *Chem. Commun.* **2003**, 1718–1719.
- [46] F. Neese, *WIREs Comput. Mol. Sci.* **2022**, *12*, 12753.
- [47] A. D. Becke, *J. Chem. Phys.* **1993**, *98*, 5648–5652.
- [48] B. Miehlich, A. Savin, H. Stoll, H. Preuss, *Chem. Phys. Lett.* **1989**, *157*, 200–206.
- [49] F. Neese, F. Wennmohs, A. Hansen, U. Becker, *Chem. Phys.* **2009**, *356*, 98–109.
- [50] D. A. Pantazis, X.-Y. Chen, C. R. Landis, F. Neese, *J. Chem. Theory Comput.* **2008**, *4*, 908–919.
- [51] S. Miertuš, E. Scrocco, J. Tomasi, *Chem. Phys.* **1981**, *55*, 117–129.
- [52] A. Schäfer, H. Horn, R. Ahlrichs, *J. Chem. Phys.* **1992**, *97*, 2571–2577.
- [53] A. Schäfer, C. Huber, R. Ahlrichs, *J. Chem. Phys.* **1994**, *100*, 5829–5835.
- [54] S. Grimme, J. Antony, S. Ehrlich, H. Krieg, *J. Chem. Phys.* **2010**, *132*, 154104.
- [55] S. Grimme, S. Ehrlich, L. Goerigk, *J. Comput. Chem.* **2011**, *32*, 1456–1465.
- [56] F. Weigend, R. Ahlrichs, *Phys. Chem. Chem. Phys.* **2005**, *7*, 3297–3305.
- [57] D. A. Pantazis, X. Y. Chen, C. R. Landis, F. Neese, *J. Chem. Theory Comput.* **2008**, *4*, 908–919.
- [58] F. Weigend, *Phys. Chem. Chem. Phys.* **2006**, *8*, 1057–1065.
- [59] B. P. Block, J. C. Bailar, *J. Am. Chem. Soc.* **1951**, *73*, 4722–4725.
- [60] J.-H. Kim, G. W. Everett Jr., *Inorg. Chem.* **1979**, *18*, 3145–3149.
- [61] T. Tokumitsu, T. Hayashi, *Bull. Chem. Soc. Jpn.* **1981**, *54*, 2348–2351.

Manuscript received: March 5, 2024
Accepted manuscript online: April 16, 2024
Version of record online: ■■■

RESEARCH ARTICLE



One-electron reduction of the macrocyclic gold(III) complex yields an elusive transient gold(II) species as shown by experimental (cyclic voltam-

metry, UV/Vis, NMR, EPR spectroscopy) and quantum chemical methods (density functional theory).

*L. Sorge, J. Link, Prof. Dr. K. Heinze**

1 – 7

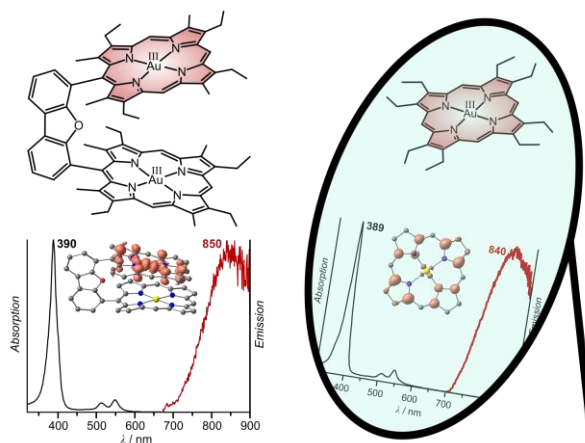
14-Membered Macrocyclic β -Diiminato Gold(II) – A New Member for the Gold(II) Complex Family?



3.2 Face-to-Face Gold Porphyrins

Authors: Lukas Sorge, Philipp Sikora, and Katja Heinze*. * = Corresponding author.

Inorg. Chem. **2024**, under revision.



Synthesis of a cofacial bis(porphyrinato)gold(III) complex and full characterization by multinuclear NMR spectroscopy, absorption spectroscopy and electrochemical investigations. EPR spectroscopy on the *in situ* reduced gold(III) complex unveiled a gold-centered reduction and a description of the mixed-valent gold(II)/gold(III) complex as Robin-Day Class I. Absorption spectra of the gold(II)/gold(II) complex, supported by time-dependent DFT calculations, indicate the involvement of the dibenzoburan bridge into the electron transfer between the two gold centers instead of a direct transfer. The binuclear and the parent mononuclear gold(III) complex exhibit weak short lived phosphorescence at room temperature in the nanosecond and in frozen solution at 77 K in the microsecond regime. Low-temperature absorption spectroscopy suggest excitonic interactions between both porphyrin subunits.

Author contributions

Lukas Sorge synthesized the bis(porphyrinato) and mono(porphyrinato)gold(III) complexes, performed the spectroscopic and electrochemical investigations, the reduction and EPR experiments, as well as the DFT calculations and wrote the first draft of the manuscript. Philipp Sikora and Lukas Sorge measured and interpreted the photoluminescence spectra. Prof. Dr. Katja Heinze supervised the project and finalized the manuscript.

Supporting Information

for this article is found on page 147.

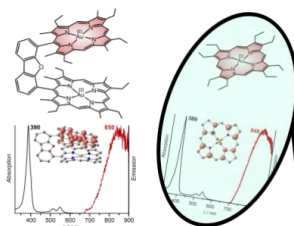
Face-to-Face Gold Porphyrins

Lukas Sorge, Philipp Sikora, and Katja Heinze*

Department of Chemistry, Johannes Gutenberg University Mainz, Duesbergweg 10-14, 55128 Mainz (Germany)

Keywords: gold, Pacman, photophysics, porphyrins, redox chemistry

ABSTRACT: The interaction of square-planar metal complexes through space is of fundamental interest and relevant for potential cooperative catalysis of two metal complex sites. In order elucidate gold-gold, gold/porphyrin and porphyrin/porphyrin interactions in the formal oxidation states +III and +II (after reduction) and in the excited triplet state after light excitation, a Pacman bis(gold(III)) complex $[\text{Au}_2(\text{DPD})][\text{PF}_6]_2$ with square-planar face-to-face gold(porphyrin) moieties has been prepared and characterized. Absorption and luminescence spectroscopy, cyclic voltammetry and EPR spectroscopy on $[\text{Au}_2(\text{DPD})]^{n+}$ and a mononuclear reference are complemented by DFT and TDDFT calculations.



INTRODUCTION

The spatial orientation of two redox-active metal centers for multielectron ground state activation of small molecules in a cooperative manner is a common structural motif in enzymes in nature such as heme containing cytochrome C oxidase or nitrogenase.^{1,2} The well-defined orientation and coordination environment provided by the enzyme scaffold promotes release of the preferred product while diminishing formation of undesired or even toxic side products.³

To gain mechanistic insights into biological mechanisms, biomimetic molecular Pacman-like cofacial bis(porphyrinato) complexes have been investigated structurally and spectroscopically over the past decades (Scheme 1a). Ligand design strategies involved different bridging units and porphyrin skeletons with various *β*- or *meso* substituents. Both variations influence the interplanar distance, geometric distortions of the porphyrinato subunit and the overall molecular geometry.^{4,5} Besides studies on free-base bis(porphyrins),^{5,7} corresponding Pacman complexes comprise mono-metallated,⁸ homobimetallic⁹⁻¹² or mixed-bimetallic¹³ with metal centers acting as redox active and/or as Lewis acidic sites.¹⁴⁻¹⁷

Nocera and co-workers demonstrated the effects of spacer and *meso* aryl substituents on the selectivity and the catalytic path of bis(porphyrinato)cobalt(III) Pacman complexes towards the proton-coupled four and two electron reduction of oxygen to water or peroxide, respectively. A dibenzofuran spacer imposes a larger interplanar and intermetallic distance compared with a xanthene space. The larger spacer diminishes electronic interaction between both porphyrin units and leads to a higher catalytic activity. Aryl substituents at the *meso* position opposite to the bridging unit hinder proton delivery resulting in increased peroxide formation instead of water irrespective of the spacers.^{8,9,16,18-20}

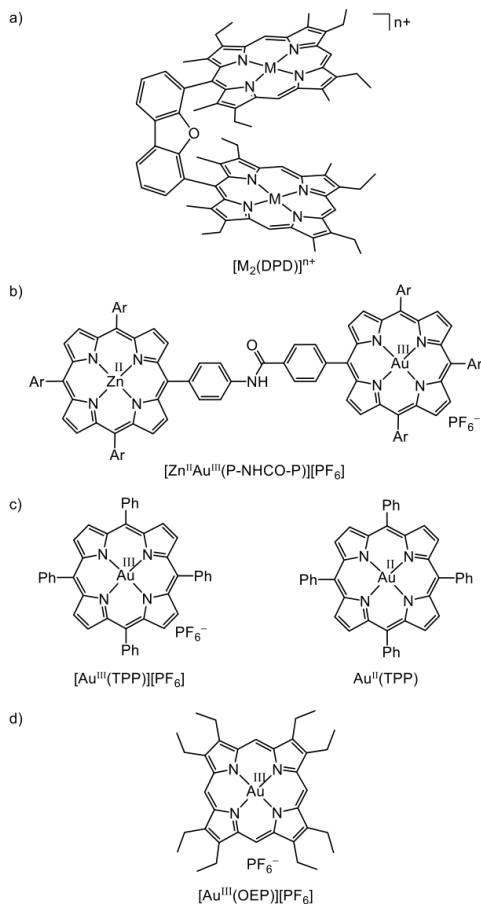
Besides cobalt based Pacman complexes, first row to third row transition metal ions such as copper,^{17,21,22} zinc,^{5,7,22-24} iron,^{8,24-28} manganese,^{11,24} nickel,^{22,24} ruthenium,¹⁴ osmium,¹⁴ rhodium,¹² palladium²⁹ and silver³⁰⁻³³ have found entrance in the field of cofacial bis(porphyrinato) complexes. Gold(III) or gold(II) Pacman complexes are unknown, although several applications of molecular gold(III) complexes have been reported, e.g. in medicinal chemistry,³⁴⁻³⁸ radical chemistry,³⁹⁻⁴¹ homogeneous catalysis,⁴²⁻⁴⁹ or sensing.⁵⁰

So far, the (porphyrinato)gold(III) moiety has been incorporated in linear mixed-metallic bis(porphyrinato) dyads by the groups of Fukuzumi, Hammarström and Heinze (see e.g. Scheme 1b).⁵¹⁻⁵³ In these linear arrangements, the gold(III) porphyrin acts as electron acceptor upon photoexcitation of the zinc(II) porphyrin. Ligand design enables control of the driving force for the (photoinduced) forward and backward electron transfer. In the final charge-shifted state, the spin density is largely localized on the gold center, i.e. in the Au–N σ orbitals. Porphyrin-mediated back-electron transfer is hindered due to the orthogonality of the σ orbitals of gold and the π -type porphyrin molecular orbitals. Hence, the charge-shifted state is relatively long-lived and available for reductive bimolecular excited state quenching, e.g. with amines which has been used in the photocatalytic reduction of aromatic azides to anilines (Scheme 1b).⁵¹

In these photocatalytic systems, mononuclear gold(II) species were detected indirectly by transient absorption spectroscopy or – after chemical reduction of the parent gold(III) complex – by electron paramagnetic resonance (EPR) spectroscopy.^{51,54,55} Molecular stabilization of the gold oxidation state +II is challenging and has been only rarely described in the literature.⁵⁶⁻⁶⁵ In fact, the oxidation state +II for gold with $(5d_{x^2-y^2})^1$ electron configuration is unfavorable due to strong relativistic effects. Dimerization to binuclear complexes

with a direct (supported or unsupported) gold(II)–gold(II) σ bond or disproportionation into gold(I) and gold(III) occurs with rearrangement of the coordination sphere.^{66–71}

Scheme 1 a) Face-to-face bis(porphyrins), b) gold(III) porphyrin as electron acceptor in a linear porphyrin dyad, c) monomeric *meso*-tetraphenylporphyrinato gold(III) and gold(II) complexes $[\text{Au}(\text{TPP})]^{+/-0}$ and d) 2,3,7,8,12,13,17,18-octaethylporphyrinato gold(III) complex $[\text{Au}(\text{OEP})]^+$.



The porphyrinato gold(III)/gold(II) redox couple represents an exception to this typical reactivity as exemplified by the mononuclear (tetraphenylporphyrinato)gold(II) complex $\text{Au}(\text{TPP})$ prepared by reduction of the parent gold(III) precursor (Scheme 1c).⁵⁴ The rigid porphyrinato ligand blocks dimerization with formation of an Au–Au σ bond via the singly occupied $5d_{x^2-y^2}$ in the xy plane and furthermore prevents the formation of labile gold(I) via disproportionation by acting as non-innocent ligand. $\text{Au}^{\text{II}}(\text{TPP})$ is thermodynamically very stable towards disproportionation into $[\text{Au}(\text{TPP})]^-$ and $[\text{Au}(\text{TPP})]^+$ with $K_d = 3 \times 10^{-12}$ at room temperature.^{54,55} On the other hand, self-exchange between $[\text{Au}(\text{TPP})]^+$ and $\text{Au}(\text{TPP})$ is fast on the ^1H NMR timescale at room temperature.⁵⁴ Oxidation of

$\text{Au}(\text{TPP})$ with oxygen initially yields superoxide and finally hydroxide suggesting facile electron transfer reactions. Coordination of ligands such as THF, water or pyridine at the axial positions of $\text{Au}(\text{TPP})$ is, however, not observed.⁵⁴

Excited states of gold porphyrins had been investigated by luminescence and transient absorption spectroscopy. Luminescence of $[\text{Au}(\text{OEP})][\text{BF}_4]$ and similar gold(III) porphyrins (Scheme 1d) had been reported in frozen matrices at 80 K peaking at ca. 690 nm with biexponential luminescence lifetimes around 10 and 100 μs . A dark triplet ligand-to-metal charge transfer ($^3\text{LMCT}$) state has been suggested to act as short-lived (50 ns) intermediate state between the initially excited singlet states and the two lowest degenerate porphyrin-centered triplet states T1(A)/T1(B), which decay in parallel. A triplet lifetime was determined by transient absorption spectroscopy as 1.5 ns at room temperature, but room temperature emission could not be observed.⁷²

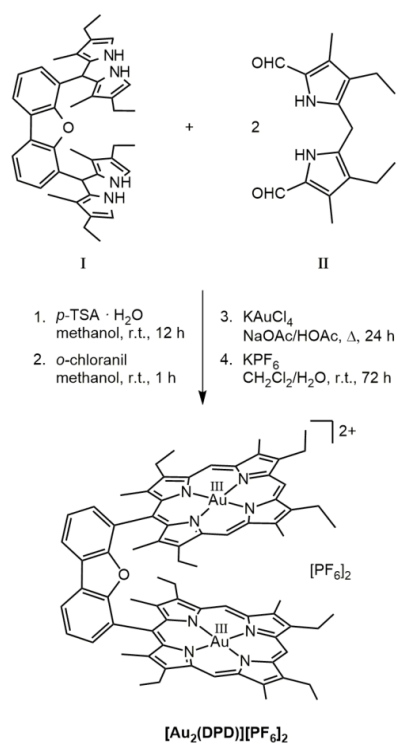
No gold face-to-face gold porphyrin dimers have been reported so far neither with gold(III) nor with gold(II) as central ions. In this study we probe potential cooperative effects in face-to-face gold dimers $[\text{Au}_2(\text{DPD})]^{n+}$ ($n = 2, 1, 0$) with Nocera's dibenzofuran spacer^{4,5,9,11,20,27} (Scheme 1a). We investigate interactions in the gold(III)-gold(III) complex ($n = 2$) in the ground and excited states as well as gold/gold, gold/porphyrin and porphyrin/porphyrin interactions with gold in the oxidation states +III and +II ($n = 1, 0$) in the face-to-face Pacman architecture to achieve deeper insight into metal-metal and metal-ligand cooperativity potentially relevant for future cooperative multi-electron (photo) catalysis with gold porphyrins by spectroscopy, electrochemistry and density functional theory (DFT) calculations (B3LYP functional, TZVPP basis set, SARC-ZORA-TZVPP(Au), dispersion and relativistic correction, continuum solvent).

RESULTS AND DISCUSSION

Synthesis and Characterization of the gold(III) complexes. The (monoporphyrinato)gold(III) complex $[\text{Au}(\text{OEP})][\text{PF}_6]$ – required for comparison with the Pacman system – was synthesized from H_2OEP (Figure S1), potassium tetrachloridoaurate(III) and sodium acetate analogous to literature procedures⁷³ and characterized by ^1H NMR spectroscopy (Figure S2), ESI⁺ mass spectrometry (Figure S3) and UV/Vis/NIR absorption (Figure S4) and IR spectroscopy (Figure S5).

The free-base cofacial bis(porphyrin) H_4DPD was prepared in nine steps according to slightly modified literature procedures (Scheme 2, for details see supporting information; Figures S6–S7)^{5,74–76} and characterized by ^1H NMR spectroscopy, ESI⁺ mass spectrometry and UV/Vis/NIR absorption (Figures S8–S10). ^1H NMR chemical shifts match literature values.⁵ H_4DPD displays in CH_2Cl_2 a single intense Soret band at 398 nm ($273000 \text{ M}^{-1} \text{ cm}^{-1}$) and four less intense Q bands at 501, 536, 571 and 624 nm with $\epsilon = 23000, 12000, 12000$ and $7000 \text{ M}^{-1} \text{ cm}^{-1}$, respectively, confirming the free-base porphyrin character (Figure S10).

Scheme 2. Synthesis of $[\text{Au}_2(\text{DPD})][\text{PF}_6]_2$ starting from 4,6-bis(4,4'-diethyl-3,3'-dimethyl-2,2'-dipyrrylmethyl)dibenzofuran I and 3,3'-diethyl-5,5'-diformyl-4,4'-dimethyl-2,2'-dipyrrylmethane II.



The novel cofacial bis(gold(III)) complex $[\text{Au}_2(\text{DPD})][\text{PF}_6]_2$ was obtained as bright red solid in 18 % yield by refluxing a suspension of H_4DPD with excess of potassium tetrachloroaurate(III) and sodium acetate in glacial acid,⁷³ followed by counterion exchange and purification by column chromatography (Scheme 2). The bimetallic complex was characterized by multinuclear 1D and 2D $^1\text{H}/^{13}\text{C}/^{31}\text{P}$ and ^{19}F NMR spectroscopy (Figures S11–S19), as well as ESI⁺ mass spectrometry (Figure S20), UV/Vis/NIR absorption (Figure S21) and IR spectroscopy (Figure S22). Due to the positive charge of the gold(III) ions, the proton resonances of the porphyrin moieties shift to lower field compared to the ^1H NMR resonances of H_4DPD . The methine proton resonances experience the largest coordination shift from 9.55 and 9.48 ppm to 10.30 and 10.22 ppm, respectively (Figures S8 and S11). The hexafluorophosphate counterions $[\text{PF}_6]^-$ display their characteristic septet and doublet resonances in the ^{31}P and ^{19}F NMR spectra at -144.7 and -74.7 ppm (Figures S18 and S19), respectively, and their intense IR absorption bands for deformation and stretching modes at 555 and 836 cm^{-1} , respectively (Figure S22).

Gold(III)-gold(III) interaction in the ground state – absorption spectroscopy. The Soret and Q bands of $[\text{Au}(\text{OEP})][\text{PF}_6]$ in CH_2Cl_2 at 293 K appear at 389, 511 and 546 nm with molar absorption coefficients of 98000, 5000 and $8400\text{ M}^{-1}\text{ cm}^{-1}$, respectively (Figure 1). The hypsochromic shifts as compared to H_2OEP absorption bands (Figure S1) are characteristic for hypso-porphyrins with occupied metal d orbitals of e_g symmetry (d_{xz} , d_{yz}) mixing with the porphyrin's $e_g(\pi^*)$ LUMO resulting in a larger $\pi-\pi^*$ energy gap.^{77,78} The full-width-at-half-maximum of the Soret band amounts to $\text{FWHM} = 1060\text{ cm}^{-1}$. In frozen EtOH:MeOH 3:2 (v/v) solution at

77 K, the Soret band shifts from 388 to 371 nm to higher energy by 1180 cm^{-1} (Figure 2a). The FWHM of the Soret band increases by 610 cm^{-1} from 1130 to 1740 cm^{-1} , which suggests some aggregation in frozen solution. Indeed, the hypsochromic shift and increased FWHM of the Soret band in frozen solution agrees with the TDDFT calculated transitions described by Gouterman's four orbital model of isolated $[\text{Au}(\text{OEP})]^+$ and a model dimer $\{[\text{Au}(\text{OEP})]_2\}^{2+}$ with an $\text{Au}\cdots\text{Au}$ distance of 3.70 \AA (Figures S23–S24).

The Pacman complex $[\text{Au}_2(\text{DPD})][\text{PF}_6]_2$ displays Soret and Q bands in CH_2Cl_2 at 293 K at 390, 514, 549 nm with roughly doubled molar absorption coefficients of 200000, 11000 and $15000\text{ M}^{-1}\text{ cm}^{-1}$, respectively, compared to $[\text{Au}(\text{OEP})][\text{PF}_6]$ (Figure 1). Typical for hypsochromic porphyrins, these bands are shifted to higher energy relative to the bands of the free-base porphyrin H_4DPD (Figure 1). The band width of the Soret band amounts to $\text{FWHM} = 1320\text{ cm}^{-1}$. The slight red-shift of the Soret and Q bands and the somewhat larger FWHM of the Soret band of the Pacman complex might be indicative of a very weak electronic ground state interaction between both porphyrin units at 293 K at best.^{10,21,79} Similarly, the isoelectronic palladium(II) Pacman complex $\text{Pd}_2(\text{DPD})$ shows essentially no excitonic coupling, when compared with a monomeric alkylated porphyrin palladium(II) complex at room temperature.¹⁰ In the solid state, two CH_2Cl_2 molecules are inserted between the porphyrin subunits in $\text{Pd}_2(\text{DPD})$ leading to a long Pd \cdots Pd distance of 6.81 \AA and preventing significant van der Waals overlap between two porphyrin planes and electronic coupling.¹⁰ In the absence of discrete solvent molecules, the $\text{Au}\cdots\text{Au}$ distance in $[\text{Au}_2(\text{DPD})]^{2+}$ has been calculated by DFT methods as 4.02 \AA . Yet solvent insertion cannot be excluded in the experimental scenario, which might explain the weak to negligible electronic coupling in $[\text{Au}_2(\text{DPD})]^{2+}$ at 293 K.

However, in frozen EtOH:MeOH 3:2 (v/v) solution at 77 K, the Soret band of $[\text{Au}_2(\text{DPD})][\text{PF}_6]_2$ splits into two bands peaking at $\lambda_{\text{max}} = 389$ and 375 nm with a significant splitting of 960 cm^{-1} (Figure 2b). The exchange splitting J , which is proportional to the magnitude of the $S_0 \rightarrow S_2$ transition dipole moments of each (porphyrinato)gold(III) moiety as well as their relative orientation, corresponds to half of the band splitting ($J = 480\text{ cm}^{-1}$).⁸⁰ The $[\text{M}_2(\text{DPD})]^{n+}$ architecture enables M \cdots M distances between 3.5 \AA ($\text{M} = \text{Fe}^{\text{III}}$) and 7.8 \AA ($\text{M} = \text{Zn}^{\text{II}}$).^{5,9} Significant excitonic coupling based on band broadening has been proposed for a Pd Pacman complex with a xanthene spacer and a Pd \cdots Pd distance of 3.97 \AA .¹⁰

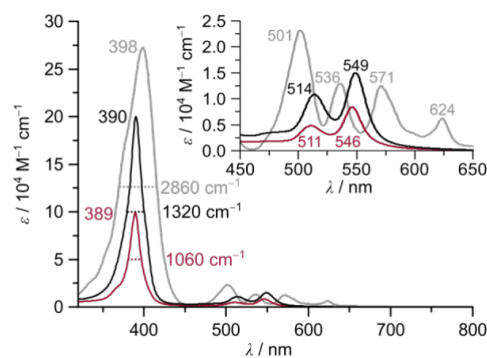


Figure 1. Absorption spectra of H₄DPD (grey), [Au₂(DPD)][PF₆]₂ (black) and [Au(OEP)][PF₆] (red) in CH₂Cl₂ at 293 K. FWHM given in cm⁻¹. Inset displays the Q band region.

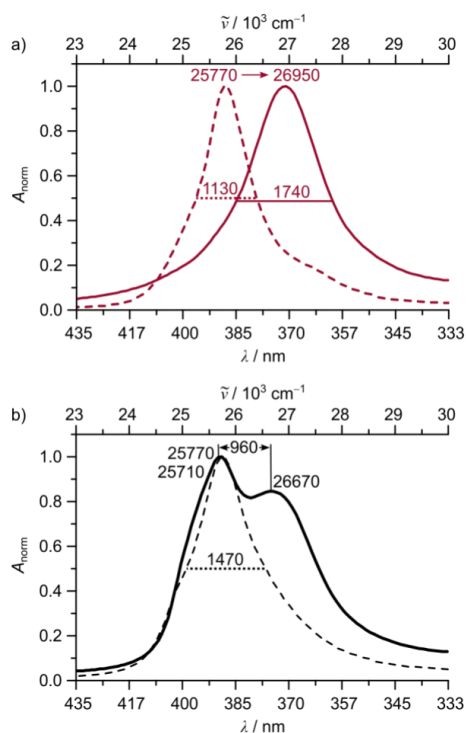


Figure 2. Absorption spectra of a) [Au(OEP)][PF₆] (red) and b) [Au₂(DPD)][PF₆]₂ (black) in EtOH:MeOH 3:2 (v/v) solution displayed in the Soret band region at 293 K (dashed traces) and at 77 K (bold traces). Band maxima, band shifts/splittings and FWHM are given in cm⁻¹.

Hence, we suggest that in frozen EtOH:MeOH solution, the Au^{III}-Au distance in [Au₂(DPD)]²⁺ must be within the van der Waals overlap of ca 4 Å as suggested by the DFT calculation without any inserted molecules. Consequently, the Pacman gold(III) complex [Au₂(DPD)]²⁺ seems to be able to accommodate small molecules such as CH₂Cl₂ – as found for Pd₂(DPD) – and to release these molecules under appropriate conditions.

Gold(III)-gold(III) interaction in the triplet state – photoluminescence spectroscopy. After excitation to the S₂ state (Soret band, 390 nm), [Au(OEP)][PF₆] shows an emission band peaking at λ_{em,77K} = 706 nm in frozen EtOH:MeOH 3:2 (v/v) solution at 77 K (Figure S25). The photoluminescence decay can be fitted biexponentially with τ_{1,77K} = 43 μs and τ_{2,77K} = 156 μs in a 50:50 ratio (Figure S26). Similarly, excitation to the S₁ state (Q band, 560 nm) yields an emission band with λ_{max} = 706 nm with τ_{1,77K} = 35 μs and τ_{2,77K} = 135 μs in a 44:56 ratio (Figures S25–S26). We were even able to detect weak phosphorescence from the T₁ state at 293 K after excitation to the S₂ state in fluid solution peaking at λ_{em,293K} = 840 nm with a τ_{293K} = 1.5 ns lifetime (Figure 3a; Figure S27). The excitation

spectrum (λ_{obs} = 840 nm) closely follows the absorption spectrum in the Q band region. The high sample concentration (A_{390nm} = 0.5) required for the weak phosphorescence signal causes some spectral distortion in the Soret band region of the excitation spectrum (Figure 3a). In spite of this minor (technical) discrepancy, the emission band observed at 293 K clearly arises from the gold(III) porphyrin. The luminescence lifetime data fully agrees with literature data obtained from transient absorption spectroscopy.⁷²

The respective photoluminescence data at 77 K for [Au₂(DPD)][PF₆]₂ are λ_{em,77K} = 713 nm, τ_{1,77K} = 29 μs and τ_{2,77K} = 120 μs in a 59:41 ratio (Soret band excitation), τ_{1,77K} = 28 μs and τ_{2,77K} = 121 μs in a 61:39 ratio (Q band excitation) (Figures S28–S29). Similar to [Au(OEP)][PF₆], we were able to detect the phosphorescence at 293 K peaking at λ_{em,293K} = 850 nm with a lifetime τ_{293K} = 1.0 ns (Figure 3b, Figure S30). The photoluminescence lifetimes of [Au₂(DPD)][PF₆]₂ are slightly shorter than those of [Au(OEP)][PF₆] both at 293 K and at 77 K. The faster decay of the Pacman complex could arise from the somewhat lower emission energy of [Au₂(DPD)][PF₆]₂ (energy gap law)⁸¹ or from the meso-dibenzofuranyl substituent, as aryl torsional motions can induce distorted non-planar conformations in the T₁ states enhancing non-radiative decay.^{10,82,83}

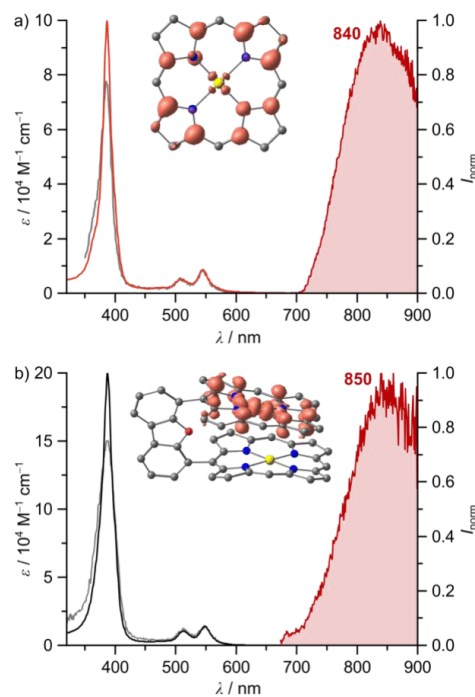


Figure 3. Absorption and excitation spectra (grey, λ_{obs} = 850 and 840 nm, respectively), and normalized photoluminescence (λ_{exc} = 390 nm) of a) [Au(OEP)][PF₆] (red; λ_{obs} = 840 nm) and b) [Au₂(DPD)][PF₆]₂ (black; λ_{obs} = 850 nm) in EtOH:MeOH 3:2 (v/v) at 293 K. Spin density plots of T₁ states are shown in the insets (isosurface value at 0.008 a.u.).

For a deeper understanding of the triplet photophysics, we optimized the geometry of the lowest energy triplet states T_1 of $[\text{Au}(\text{OEP})]^+$ and $[\text{Au}_2(\text{DPD})]^{2+}$ by DFT methods. The calculated energy differences between the singlet ground state S_0 and the lowest energy triplet state T_1 for $[\text{Au}(\text{OEP})]^+$ (1.82 eV) and $[\text{Au}_2(\text{DPD})]^{2+}$ (1.70 eV) qualitatively agrees with the slight bathochromic shift of the emission of $[\text{Au}_2(\text{DPD})]^{2+}$ compared to $[\text{Au}(\text{OEP})]^+$ (Figure 3, Figure S31). The Mulliken spin density of the optimized T_1 state of $[\text{Au}(\text{OEP})]^+$ is predominantly located in the porphyrin's π -system on the eight C_α carbon atoms (0.237/0.237/0.246/0.246 and 0.172/0.172/0.179/0.179) with a small contribution of the gold atom (0.048, $5d_{x^2-y^2}$) and two nitrogen atoms (0.057/0.057) (Figure 3a, Figure S31), suggesting a dominant ${}^3\pi\text{-}\pi^*$ character of the T_1 state with weak ${}^3\text{LMCT}$ admixture. The Au–N distances increased in the T_1 state with 2.041/2.041 Å and 2.037/2.037 Å compared to the S_0 state with 2.030 Å (4 \times) due to the partial population of the anti-bonding $5d_{x^2-y^2}$ orbital of gold (small LMCT character). Furthermore, the symmetry is slightly disturbed likely due to a second order Jahn-Teller effect in the excited state similar to $\text{Au}^{\text{II}}(\text{TPP})$ in its doublet ground state.⁵⁴

The Mulliken spin density of the DFT optimized T_1 state of $[\text{Au}_2(\text{DPD})]^{2+}$ (Au–Au 4.09 Å) is localized on a single porphyrin subunit (Figure 3b inset). Compared to the T_1 state of $[\text{Au}(\text{OEP})]^+$ (Figure 3a inset), the spin density is larger at the gold center (0.283) and the nitrogen atoms (0.083/0.022/0.068/0.027) and lower in the porphyrin's π -system (C_α : 0.123, 0.209, 0.172, 0.238, 0.123, 0.191, 0.155, 0.197) suggesting a larger ${}^3\text{LMCT}$ character (Figure 3, Figure S31). The gold center of the excited subunit adopts a 2+2 coordination mode with Au–N distances of 2.059/2.063 Å and 2.103/2.107 Å accompanied by bending of two *trans*-pyrrole subunits. This distortion, described by a saddling (B_{1u}) mode (0.621 Å) by normal-coordinate structure decomposition (NSD) analysis (Figure S32), is fully analogous to $\text{Au}^{\text{II}}(\text{TPP})$ in its electronic doublet ground state,⁵⁴ supporting the gold(II) character of $[\text{Au}_2(\text{DPD})]^{2+}$ in its T_1 state.

The DFT data suggest that the facilitated non-radiative decay of $[\text{Au}_2(\text{DPD})]^{2+}$ can be traced back to a larger ${}^3\text{LMCT}$ character, its resulting larger geometric distortion and lowered excited energy and the presence of a *meso*-aryl substituent. A specific effect of the presence of a face-to-face gold(III) porphyrin on the T_1 state is not apparent.

Gold(III)-gold(II) interaction in the mixed-valent state – electrochemistry, EPR and UV/Vis/NIR spectroscopy. Similar to $[\text{Au}(\text{TPP})]^+$ ($E_{1/2} = -0.97$ and -1.65 V vs. ferrocene),⁵⁴ $[\text{Au}(\text{OEP})]^+$ is reduced in two one-electron steps at $E_{1/2} = -1.20$ and -1.92 V in $[\text{tBu}_4\text{N}][\text{PF}_6]/\text{THF}$ solution (Figure 4a). The cathodic shift is likely due to the electron donating nature of alkyl substituents at the OEP²⁻. With a slightly larger potential difference of $\Delta E = 0.72$ V, the disproportionation constant $K_d = 7 \times 10^{-13}$ for the reaction of two $\text{Au}^{\text{II}}(\text{OEP})$ to $[\text{Au}(\text{OEP})]^+$ and $[\text{Au}(\text{OEP})]^-$ is even smaller than the corresponding value for $\text{Au}^{\text{II}}(\text{TPP})$ ($K_d = 3 \times 10^{-12}$).^{54,55}

Under the same conditions, the binuclear gold(III) complex $[\text{Au}_2(\text{DPD})]^{2+}$ shows two quasi-reversible two-electron reductions at $E_{1/2} = -1.13$ and -1.77 V (Figure 4b). The slight shift compared to $[\text{Au}(\text{OEP})]^+$ is likely due to the presence of the *meso*-aryl substituent in $[\text{Au}_2(\text{DPD})]^{2+}$. The observation, that both gold(III) centers are

reduced at virtually the same potential, suggests that the singly-reduced mixed-valent complex $[\text{Au}_2(\text{DPD})]^+$ belongs to the Robin-Day Class I with negligible metal-metal interaction and with a localized gold(II) ion. The same holds for the reduction of the porphyrins to $[\text{Au}_2(\text{DPD})]^-$ at lower potential as no significant splitting of the redox wave is observed as well. On the other hand, the neutral gold(II) dimer $\text{Au}_2(\text{DPD})$ is stabilized towards disproportionation into $[\text{Au}_2(\text{DPD})]^{2+}$ and $[\text{Au}_2(\text{DPD})]^{2-}$ with a small disproportionation constant $K_d = 1.5 \times 10^{-11}$.

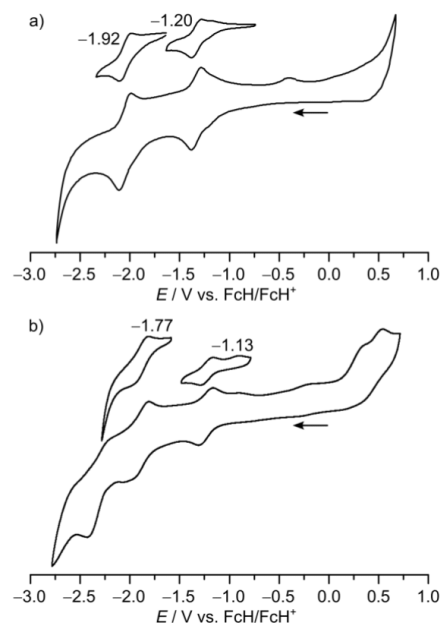


Figure 4. Cyclic voltammograms of a) $[\text{Au}(\text{OEP})][\text{PF}_6]$ (red) and b) $[\text{Au}_2(\text{DPD})][\text{PF}_6]_2$ (black) 10^{-3} M in 0.1 M $[\text{tBu}_4\text{N}][\text{PF}_6]/\text{THF}$ solution. Scan directions indicated by arrow. Numbers indicate $E_{1/2}$ values.

Chemical reduction of $[\text{Au}(\text{OEP})][\text{PF}_6]$ with one equivalent decamethylcobaltocene in THF and subsequent *in situ* X-band EPR spectroscopy of the frozen solution at 77 K yielded a characteristic EPR resonance pattern (Figure 5a) that could be simulated with $g_1 = 2.169$, $g_2 = 2.072$ and $g_3 = 1.984$ and $A_{1,2,3}(^{197}\text{Au}) = 42, 26, 27$ G (Table S1), similar to the EPR resonance of $\text{Au}^{\text{II}}(\text{TPP})$.^{54,55} The largely gold-centered radical is confirmed by DFT calculations on $\text{Au}(\text{OEP})$ with Mulliken spin densities at gold of 0.437 and at the nitrogen atoms of 0.133 each (Figure S33).

Analogously, the gold(III) Pacman complex $[\text{Au}_2(\text{DPD})]^{2+}$ was reduced with one or two equivalents of cobaltocene, respectively, and analyzed by EPR spectroscopy at 77 K (Figure 5b). Apart from the doubled EPR resonance intensity for the experiment with two equivalents cobaltocene (Table S2 and Figure S34), the EPR spectra are identical, confirming that the mixed-valent species $[\text{Au}_2(\text{DPD})]^+$ quantitatively disproportionates into EPR-silent $[\text{Au}_2(\text{DPD})]^{2+}$ and EPR-active $\text{Au}_2(\text{DPD})$.

3.2 | Face-to-Face Gold Porphyrins

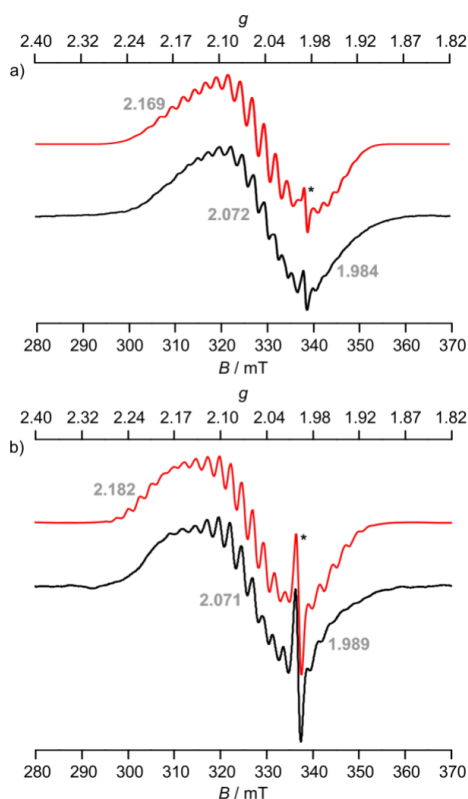


Figure 5. X-band EPR spectra of a) $[\text{Au}(\text{OEP})][\text{PF}_6]$ upon reduction with one equivalent decamethylcobaltocene in frozen THF solution at 77 K (black) and simulation (red) and b) $[\text{Au}_2(\text{DPD})][\text{PF}_6]_2$ upon reduction with two equivalents cobaltocene in frozen THF solution at 77 K. The asterisks denote the resonance of a minor species ($<0.1\%$ of the total intensity), likely gold(III) porphyrin π radical anion valence isomers.⁵⁵

UV/Vis/NIR spectroscopic monitoring of the single and double reduction of $[\text{Au}_2(\text{DPD})]^{2+}$ in THF further substantiates the absence of a mixed-valent species $[\text{Au}_2(\text{DPD})]^+$ as the intermediate spectra can be simulated satisfactorily by combining the spectra of $[\text{Au}_2(\text{DPD})]^{2+}$ and $\text{Au}_2(\text{DPD})$. Intervalence charge transfer bands could not be identified up to 1400 nm (Figure S35). Hence, UV/Vis/NIR and EPR spectroscopy suggest a non-stabilized and hence not observable mixed-valence species $[\text{Au}_2(\text{DPD})]^+$, as this species quantitatively disproportionates.

Gold(II)-gold(II) interaction – electrochemistry, EPR and UV/Vis/NIR spectroscopy. The bis(gold(II)) complex $\text{Au}_2(\text{DPD})$ was prepared by twofold reduction of $[\text{Au}_2(\text{DPD})]^{2+}$ in THF. An EPR spectrum was obtained at 77 K. A half-field resonance was not observed with our spectrometer. The largely gold-centered radicals in $\text{Au}_2(\text{DPD})$ are confirmed by DFT calculations on $\text{Au}_2(\text{DPD})$ (triplet state) with Mulliken spin densities at the gold centers of 0.375 and 0.376. The EPR resonance pattern of $\text{Au}_2(\text{DPD})$ somewhat differs from the EPR resonance pattern of the mononuclear gold(II) complexes $\text{Au}(\text{TPP})$ ⁵⁵ and $\text{Au}(\text{OEP})$ (Figure

5a). The small differences might arise from the lowered symmetry or from dipolar splitting. EPR spectra of $\text{Cu}_2(\text{DPD})$ ²² and other dicopper(II) cofacial bisporphyrins,⁸⁴ could be simulated with dipolar splittings of $D = 400\text{--}445\text{ G}$ resulting in inter-spin distances of 4.1–5.5 Å according to $r^3 = 1.3 \times 10^4\text{ g}/D$.⁸⁵ For the bis(gold(II)) complex $\text{Au}_2(\text{DPD})$, the number of required parameters (minimum number of parameters 16) precluded a meaningful simulation of the EPR spectrum. An approximation of the dipolar splitting $2D$ estimated from the high- and low-field parts of the EPR resonance pattern gives $D \approx 150\text{ G}$ and $g \approx 2.081$. With these values, the inter-spin distance would be estimated as $r \approx 5.65\text{ \AA}$. This value of r is larger than the $\text{Au}\cdots\text{Au}$ distance obtained from DFT calculations on $\text{Au}_2(\text{DPD})$ (4.2 Å) but smaller than the value obtained for $\text{Cu}_2(\text{DPD})$ by the same dipolar splitting method (8.0 Å).²² Hence, $\text{Au}_2(\text{DPD})$ seems to possess either non-interacting spins at the gold(II) centers or only weakly interacting centers at ca. 5.65 Å distance.

Reduction of $[\text{Au}_2(\text{DPD})]^{2+}$ to $\text{Au}_2(\text{DPD})$ shifts the Soret and Q bands in THF from 390 to 394 nm and from 514/549 to 521/555 nm, respectively, and decreases their intensity. Additionally, bands at 645 and 743 nm appear which are assigned to transitions from the gold(II) ion (d_{z^2})⁺ to a π^* orbital of the face-to-face porphyrin according to TDDFT calculations on $\text{Au}_2(\text{DPD})$ (interporphyrin transitions, Figure 6, Table S5).

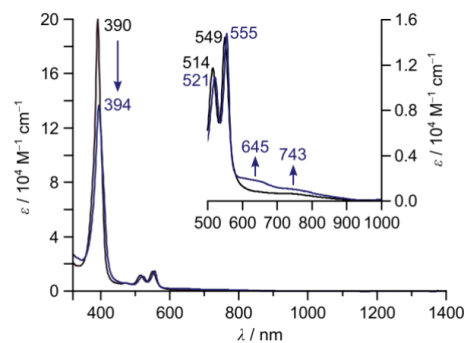


Figure 6. UV/Vis/NIR absorption spectra of $[\text{Au}_2(\text{DPD})][\text{PF}_6]_2$ before (black) and after reduction (blue) with two equivalents of cobaltocene in THF. The inset shows the Q bands and bands of interporphyrin transitions.

In summary, UV/Vis/NIR absorption spectroscopy evidences interactions of gold(II) with the face-to-face porphyrin in $\text{Au}_2(\text{DPD})$, while EPR spectroscopy supports only weak if any dipolar interactions between the gold(II) centers in $\text{Au}_2(\text{DPD})$.

Comparative quantum chemical calculations. The geometries of $[\text{Au}_2(\text{DPD})]^{2+}$ in its lowest singlet and triplet states as well as the radicals $[\text{Au}_2(\text{DPD})]^+$ and $\text{Au}_2(\text{DPD})$ were optimized via DFT methods in the absence of explicit small molecules such as solvent molecules (Figure S36). Details of the calculated metrics, porphyrin distortions (by normal-coordinate structure decomposition (NSD) analysis, Figure S37), energies of the frontier molecular orbitals (Figures S38–S40) and results of TDDFT calculations (Figures S4–S45, Tables S3–S8) are collected in the Supporting Information. In all optimized structures, gold(III) sites are characterized by Au–N distances of 2.03–2.04 Å in full agreement with the symmetric $5d^8$ electron configuration, while the gold(II) sites display pairs of long

and short Au–N distances of 2.10–2.12 Å and 2.06–2.09 Å, similar to Au(TPP).⁵⁴

In all optimized structures, the Au^{III}–Au distances amount to 4.0–4.2 Å. In principle, such distances allow for interactions of the two porphyrin subunits, which has been experimentally suggested for [Au₂(DPD)]²⁺ at 77 K (exciton splitting) and for Au₂(DPD) (possible small dipolar coupling at 77 K, inter-porphyrin transitions at 293 K). M₂(DPD) Pacman complexes can accommodate small molecules such as CH₂Cl₂,⁵ CH₃OH,⁵ 2-aminopyrimidine⁸⁶ or (CH₃)₂CO²² increasing the M^{III}–M distance up to 7.8 Å,⁵ but can also achieve short Fe^{III}–Fe distances of ca. 3.5 Å.⁹

According to the calculations, the T₁ state of [Au₂(DPD)]²⁺ possesses significant LMCT character, yet no significant interactions between the two porphyrin subunits. Similarly, the mixed-valent complex [Au₂(DPD)]⁺, which is not stabilized according to electrochemistry, UV/Vis/NIR and EPR spectroscopy, displays localized gold(II) and gold(III) sites as shown by calculated metrics and spin densities (Robin-Day class I).

SUMMARY AND CONCLUSIONS

We have prepared and characterized a Pacman bis(gold(III)) complex [Au₂(DPD)][PF₆]₂ in its ground state and excited triplet state as well as its bis(gold(II)) counterpart Au₂(DPD) to delineate potential gold/gold, gold/porphyrin and porphyrin/porphyrin interactions within the Pacman architecture. [Au₂(DPD)]²⁺ shows negligible excitonic interaction at 293 K in CH₂Cl₂, likely due to the insertion of solvent molecules between the porphyrins. At 77 K, however, significant excitonic coupling is observed, possibly thanks the expulsion of the solvent molecules and a decreased Au^{III}–Au distance. NIR phosphorescence is observed both at 293 and 77 K with ns and μs lifetimes, respectively. The triplet lifetimes are slightly shorter than that of a mononuclear model complex, which is assigned to higher ³LMCT admixture, lower triplet energy and excited state distortion rather than to a specific interaction between the porphyrin subunits. The gold(II)/gold(III) mixed-valent system [Au₂(DPD)]⁺ is not stabilized and belongs to the Robin-Day class I without electron delocalization between the porphyrinato gold subunits. The gold(II)/gold(II) Pacman complex Au₂(DPD) possesses electron spins essentially localized on the gold centers. These either show no or merely a weak dipolar interaction. However, Au₂(DPD) displays inter-porphyrin transitions from gold(II) to the π* orbitals of the face-to-face porphyrin.

Consequently, interactions within the Pacman architecture are governed by the environment (temperature, solvent) and oxidation state/charge of the subunits. The flexibility of the Pacman ligand thus could allow substrate binding and product release for potential (photo)catalytic applications, in particular two-electron transformations from the gold(II)/gold(II) complex prepared by electrochemical or photochemical reduction from the parent gold(III)/gold(III) Pacman system.

ASSOCIATED CONTENT

Supporting Information

The Supporting Information is available free of charge at xx. General methods, synthetic procedures, mass, NMR, EPR, IR, UV/Vis/NIR absorption and emission spectra, and quantum chemical calculations (PDF).

Cartesian coordinates of optimized geometries from quantum-chemical calculations (XYZ).

AUTHOR INFORMATION

Corresponding Author

***Katja Heinze** – Department of Chemistry, Johannes Gutenberg University Mainz, Duesbergweg 10-14, 55128 Mainz (Germany); orcid.org/0000-0003-1483-4156; E-Mail: katja.heinze@uni-mainz.de

Authors

Lukas Sorge – Department of Chemistry, Johannes Gutenberg University Mainz, Duesbergweg 10-14, 55128 Mainz (Germany)
Philipp Sikora – Department of Chemistry, Johannes Gutenberg University Mainz, Duesbergweg 10-14, 55128 Mainz (Germany)
 Complete contact information is available at xx

Author Contributions

L. S. performed the syntheses, characterization, analytical measurements and computational studies and visualized the data and wrote the original draft. P. S. and L. S. measured and interpreted the emission data. K.H. designed and supervised the project and finalized the manuscript.

Notes

The authors declare no conflict of interest.

ACKNOWLEDGMENTS

K. H. and L. S. thank the Deutsche Forschungsgemeinschaft DFG for funding via grants HE2778/16-1 and INST 247/1018-1 FUGG. Parts of this research were conducted using the supercomputer Elwetritsch and advisory services offered by the University of Kaiserslautern-Landau (<https://hpc.rz.rptu.de>) which is a member of the AHRP.

REFERENCES

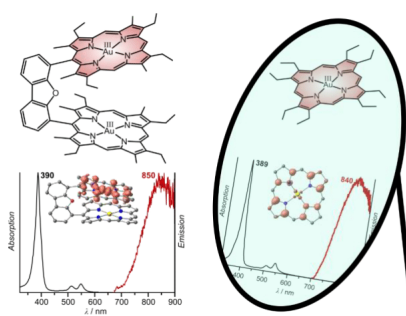
- (1) Tsukihara, T.; Aoyama, H.; Yamashita, E.; Tomizaki, T.; Yamaguchi, H.; Shinzawa-Itoh, K.; Nakashima, R.; Yaono, R.; Yoshikawa, S. The Whole Structure of the 13-subunit Oxidized Cytochrome c Oxidase at 2.8 Å. *Science* **1996**, *272*, 1136–1144. DOI: 10.1126/science.272.5265.1136.
- (2) Sippel, D.; Rohde, M.; Netzer, J.; Trncik, C.; Gies, J.; Grunau, K.; Djurdjevic, I.; Decamps, L.; Andrade, S. L. A.; Einsle, O. A bound reaction intermediate sheds light on the mechanism of nitrogenase. *Science* **2018**, *359*, 1484–1489. DOI: 10.1126/science.aar2765.
- (3) Ferguson-Miller, S.; Babcock, G. T. Heme/Copper Terminal Oxidases. *Chem. Rev.* **1996**, *96*, 2889–2908. DOI: 10.1021/cr950051s.
- (4) Chang, C. J.; Deng, Y.; Nocera, D. G.; Shi, C.; Anson, F. C.; Chang, C. K. Electrocatalytic four-electron reduction of oxygen to water by a highly flexible cofacial cobalt bisporphyrin. *Chem. Commun.* **2000**, 1355–1356. DOI: 10.1039/b001620i.
- (5) Deng, Y.; Chang, C. J.; Nocera, D. G. Direct Observation of the “Pacman” Effect from Dibenzofuran-Bridged Cofacial Bisporphyrins. *J. Am. Chem. Soc.* **2000**, *122*, 410–411. DOI: 10.1021/ja992955r.
- (6) Bolze, F.; Gros, C. P.; Drouin, M.; Espinosa, E.; Harvey, P. D.; Guillard, R. Fine tuning of the photophysical properties of cofacial diporphyrins via the use of different spacers. *J. Organomet. Chem.* **2002**, *643–644*, 89–97. DOI: 10.1016/S0022-328X(01)01346-8.
- (7) Chardon-Noblat, S.; Sauvage, J.-P.; Mathis, P. Efficient Photoinduced Intramolecular Energy Transfer in an Oblique Bis-Porphyrin System. *Angew. Chem. Int. Ed.* **1989**, *28*, 593–595. DOI: 10.1002/anie.198905931.
- (8) Ni, C. L.; Abdalmuhdi, I.; Chang, C. K.; Anson, F. C. Behavior of Four Anthracene-Linked Dimeric Metalloporphyrins as Electrocatalysts for the Reduction of Dioxygen. *J. Phys. Chem.* **1987**, *91*, 1158–1166. DOI: 10.1021/j100289a028.
- (9) Chang, C. J.; Loh, Z.-H.; Shi, C.; Anson, F. C.; Nocera, D. G. Targeted Proton Delivery in the Catalyzed Reduction of Oxygen to Water by Bimetallic Pacman Porphyrins. *J. Am. Chem. Soc.* **2004**, *126*, 10013–10020. DOI: 10.1021/ja049115j.

- (10) Loh, Z.-H.; Miller, S. E.; Chang, C. J.; Carpenter, S. D.; Nocera, D. G. Excited-State Dynamics of Cofacial Pacman Porphyrins. *J. Phys. Chem. A* **2002**, *106*, 11700–11708. DOI: 10.1021/jp026440p.
- (11) Chng, L. L.; Chang, C. J.; Nocera, D. G. Meso-Tetraaryl Cofacial Bisporphyrins Delivered by Suzuki Cross-Coupling. *J. Org. Chem.* **2003**, *68*, 4075–4078. DOI: 10.1021/jo026610u.
- (12) Collman, J. P.; Ha, Y.; Guillard, R.; Lopez, M. A. Chemistry of a Cofacial Dirhodium Diporphyrin: Synthesis and Reactivity of Rh2DPB. *Inorg. Chem.* **1993**, *32*, 1788–1794. DOI: 10.1021/ic00061a040.
- (13) Clement, T. E.; Nurco, D. J.; Smith, K. M. Synthesis and Characterization of a Series of Monometallo-, Bimetallo-, and Heterobimetallo-1,2-Ethene-Linked Cofacial Bisporphyrins. *Inorg. Chem.* **1998**, *37*, 1150–1160. DOI: 10.1021/ic970774p.
- (14) Collman, J. P.; Garner, J. M. Synthesis and Characterization of a Paramagnetic Osmium-Ruthenium Double Bond. *J. Am. Chem. Soc.* **1990**, *112*, 166–173. DOI: 10.1021/ja00157a027.
- (15) Guillard, R.; Lopez, M. A.; Tabard, A.; Richard, P.; Lecomte, C.; Brandes, S.; Hutchison, J. E.; Collman, J. P. Synthesis and Characterization of Novel Cobalt Aluminum Cofacial Porphyrins. First Crystal and Molecular Structure of a Heterobimetallic Biphenylene Pillared Cofacial Diporphyrin. *J. Am. Chem. Soc.* **1992**, *114*, 9877–9889. DOI: 10.1021/ja00051a021.
- (16) Guillard, R.; Brandes, S.; Tardieux, C.; Tabard, A.; L'Her, M.; Miry, C.; Gouerec, P.; Knop, Y.; Collman, J. P. Synthesis and Characterization of Cofacial Metallodiporphyrins Involving Cobalt and Lewis Acid Metals: New Dinuclear Multielectron Redox Catalysts of Dioxxygen Reduction. *J. Am. Chem. Soc.* **1995**, *117*, 11721–11729. DOI: 10.1021/ja00152a013.
- (17) Guillard, R.; Brandes, S.; Tabard, A.; Bouhmaid, N.; Lecomte, C.; Richard, P.; Latour, J.-M. Synthesis, Characterization, and Reactivity toward Dioxxygen of Copper Manganese Cofacial Porphyrins. Crystal and Molecular Structures of a Heterobimetallic Biphenylene-Pillared Cofacial Diporphyrin. *J. Am. Chem. Soc.* **1994**, *116*, 10202–10211. DOI: 10.1021/ja00101a046.
- (18) Chang, C. K.; Abdalmuhdi, I. Anthracene Pillared Cofacial Diporphyrin. *J. Org. Chem.* **1983**, *48*, 5388–5390. DOI: 10.1021/jo00174a056.
- (19) Liu, H. Y.; Abdalmuhdi, I.; Chang, C. K.; Anson, F. C. Catalysis of the Electroreduction of Dioxxygen and Hydrogen Peroxide by an Anthracene-Linked Dimeric Cobalt Porphyrin. *J. Phys. Chem.* **1985**, *89*, 665–670. DOI: 10.1021/j100250a021.
- (20) Rosenthal, J.; Nocera, D. G. Role of Proton-Coupled Electron Transfer in O-O Bond Activation. *Acc. Chem. Res.* **2007**, *40*, 543–553. DOI: 10.1021/ar7000638.
- (21) Kumar, A.; Sanfui, S.; Sciortino, G.; Maréchal, J.-D.; Garribba, E.; Rath, S. P. Stepwise Oxidations in a Cofacial Copper(II) Porphyrin Dimer: Through-Space Spin-Coupling and Interplay between Metal and Radical Spins. *Chem. Eur. J.* **2020**, *26*, 7869–7880. DOI: 10.1002/chem.202000348.
- (22) Chang, C. J.; Baker, E. A.; Pistorio, B. J.; Deng, Y.; Loh, Z.-H.; Miller, S. E.; Carpenter, S. D.; Nocera, D. G. Structural, Spectroscopic, and Reactivity Comparison of Xanthene- and Dibenzofuran-Bridged Cofacial Bisporphyrins. *Inorg. Chem.* **2002**, *41*, 3102–3109. DOI: 10.1021/ic0111029.
- (23) Faure, S.; Stern, C.; Guillard, R.; Harvey, P. D. Role of the Spacer in the Singlet-Singlet Energy Transfer Mechanism (Förster vs Dexter) in Cofacial Bisporphyrins. *J. Am. Chem. Soc.* **2004**, *126*, 1253–1261. DOI: 10.1021/ja0379823.
- (24) Chang, C. J.; Deng, Y.; Peng, S.-M.; Lee, G.-H.; Yeh, C.-Y.; Nocera, D. G. A Convergent Synthetic Approach Using Sterically Demanding Aryldipyrrylmethanes for Tuning the Pocket Sizes of Cofacial Bisporphyrins. *Inorg. Chem.* **2002**, *41*, 3008–3016. DOI: 10.1021/ic025507k.
- (25) Hodgkiss, J. M.; Chang, C. J.; Pistorio, B. J.; Nocera, D. G. Transient Absorption Studies of the Pacman Effect in Spring-Loaded Diiron(III) mu-Oxo Bisporphyrins. *Inorg. Chem.* **2003**, *42*, 8270–8277. DOI: 10.1021/ic034751o.
- (26) Rosenthal, J.; Luckett, T. D.; Hodgkiss, J. M.; Nocera, D. G. Photocatalytic Oxidation of Hydrocarbons by a Bis-Iron(III)-mu-oxo Pacman Porphyrin Using O₂ and Visible Light. *J. Am. Chem. Soc.* **2006**, *128*, 6546–6547. DOI: 10.1021/ja058731s.
- (27) Rosenthal, J.; Pistorio, B. J.; Chng, L. L.; Nocera, D. G. Aerobic Catalytic Photooxidation of Olefins by an Electron-Deficient Pacman Bisiron(III) mu-Oxo Porphyrin. *J. Org. Chem.* **2005**, *70*, 1885–1888. DOI: 10.1021/jo048570v.
- (28) Pistorio, B. J.; Chang, C. J.; Nocera, D. G. A Phototriggered Molecular Spring for Aerobic Catalytic Oxidation Reactions. *J. Am. Chem. Soc.* **2002**, *124*, 7884–7885. DOI: 10.1021/ja026017u.
- (29) Bolze, F.; Gros, C. P.; Harvey, P. D.; Guillard, R. Luminescence properties of a cofacial dipalladium porphyrin dimer under argon and in the presence of dioxxygen. *J. Porphy. Phthalocya.* **2001**, *5*, 569–574. DOI: 10.1002/jpp.362.
- (30) Lemon, C. M.; Powers, D. C.; Huynh, M.; Maher, A. G.; Phillips, A. A.; Triplet, B. P.; Nocera, D. G. Ag(III)–Ag(III) Argentophilic Interaction in a Cofacial Corrole Dyad. *Inorg. Chem.* **2023**, *62*, 3–17. DOI: 10.1021/acs.inorgchem.2c02285.
- (31) Singh, A. K.; Rath, S. P. Intermacrocyclic Interactions upon Stepwise Oxidations in a Monometallic Porphyrin Dimer: Ring versus Metal-Center Oxidations and Effect of Counter Anions. *Chem. Eur. J.* **2020**, *26*, 14405–14418. DOI: 10.1002/chem.202002188.
- (32) Singh, A. K.; Usman, M.; Sciortino, G.; Garribba, E.; Rath, S. P. Through-Space Spin Coupling in a Silver(II) Porphyrin Dimer upon Stepwise Oxidations: AgII–AgII, AgII–AgIII, and AgIII–AgIII Metallophilic Interactions. *Chem. Eur. J.* **2019**, *25*, 10098–10110. DOI: 10.1002/chem.201901731.
- (33) Singh, A. K.; Khan, F. S. T.; Rath, S. P. Silver(III)–Silver(III) Interactions that Stabilize the syn Form in a Porphyrin Dimer Upon Oxidation. *Angew. Chem. Int. Ed.* **2017**, *56*, 8849–8854. DOI: 10.1002/anie.201705108.
- (34) Lemon, C. M.; Brothers, P. J.; Boitrel, B. Porphyrin complexes of the period 6 main group and late transition metals. *Dalton Trans.* **2011**, *40*, 6591–6609. DOI: 10.1039/c0dt01711f.
- (35) Zou, T.; Lum, C. T.; Lok, C.-N.; Zhang, J.-J.; Che, C.-M. Chemical biology of anticancer gold(III) and gold(I) complexes. *Chem. Soc. Rev.* **2015**, *44*, 8786–8801. DOI: 10.1039/C5CS00132C.
- (36) Sun, R. W.-Y.; Che, C.-M. The anti-cancer properties of gold(III) compounds with dianionic porphyrin and tetradentate ligands. *Coord. Chem. Rev.* **2009**, *253*, 1682–1691. DOI: 10.1016/j.ccr.2009.02.017.
- (37) Sun, R. W.-Y.; Li, C. K.-L.; Ma, D.-L.; Yan, J. J.; Lok, C.-N.; Leung, C.-H.; Zhu, N.; Che, C.-M. Stable Anticancer Gold(III)-Porphyrin Complexes: Effects of Porphyrin Structure. *Chem. Eur. J.* **2010**, *16*, 3097–3113. DOI: 10.1002/chem.200902741.
- (38) Che, C.-M.; Sun, R. W.-Y. Therapeutic applications of gold complexes: lipophilic gold(III) cations and gold(I) complexes for anti-cancer treatment. *Chem. Commun.* **2011**, *47*, 9554–9560. DOI: 10.1039/C1CC10860C.
- (39) Johnson, A.; Puddephatt, R. J. Mechanistic Studies of Reactions of Benzenethiol with Methyl Derivatives of Platinum(II) and Gold(I) and - (III). *J. Chem. Soc., Dalton Trans.* **1975**, 115–120. DOI: 10.1039/DT9750000115.
- (40) Johnson, A.; Puddephatt, R. J. Reactions of Trifluoromethyl Iodide with Methylgold(I) Complexes. Preparation of Trifluoromethyl-gold(I) and -gold(III) Complexes. *J. Chem. Soc., Dalton Trans.* **1976**, 1360–1363. DOI: 10.1039/DT9760001360.
- (41) Hopkinson, M. N.; Tlahuext-Aca, A.; Glorius, F. Merging Visible Light Photoredox and Gold Catalysis. *Acc. Chem. Res.* **2016**, *49*, 2261–2272. DOI: 10.1021/acs.accounts.6b00351.
- (42) Pérez-Sánchez, J. C.; Herrera, R. P.; Concepción Gimeno, M. Unlocking the catalytic potential of gold(II) complexes: a comprehensive re-assessment. *Dalton Trans.* **2024**, *53*, 382–393. DOI: 10.1039/D3DT03687A.
- (43) Schrick, M. P.; Ramollo, G. K.; Hirschiel, C.-M. S.; Fernandes, M.; Lemmerer, A.; Förster, C.; Bezuidenhout, D. I.; Heinze, K. Redox Activation of Acyclic (Aryl)(amino)carbene Gold(I) Complexes. *Organometallics* **2024**, *43*, 69–84. DOI: 10.1021/acs.organomet.3c00395.
- (44) Sahoo, B.; Hopkinson, M. N.; Glorius, F. Combining Gold and Photoredox Catalysis: Visible Light-Mediated Oxy- and Aminoarylation of Alkenes. *J. Am. Chem. Soc.* **2013**, *135*, 5505–5508. DOI: 10.1021/ja400311h.
- (45) Huang, L.; Rudolph, M.; Rominger, F.; Hashmi, A. S. K. Photosensitizer-Free Visible-Light-Mediated Gold-Catalyzed 1,2-Difunctionalization of Alkynes. *Angew. Chem. Int. Ed.* **2016**, *55*, 4808–4813. DOI: 10.1002/anie.201511487.
- (46) Kim, S.; Rojas-Martin, J.; Toste, F. D. Visible light-mediated gold-catalyzed carbon(sp²)-carbon(sp) cross-coupling. *Chem. Sci.* **2016**, *7*, 85–88. DOI: 10.1039/C5SC03025K.
- (47) Shu, X.; Zhang, M.; He, Y.; Frei, H.; Toste, F. D. Dual Visible Light Photoredox and Gold-Catalyzed Arylative Ring Expansion. *J. Am. Chem. Soc.* **2014**, *136*, 5844–5847. DOI: 10.1021/ja500716j.

- (48) Tlahuext-Aca, A.; Hopkinson, M. N.; Sahoo, B.; Glorius, F. Dual gold/photoredox-catalyzed C(sp)-H arylation of terminal alkynes with diazonium salts. *Chem. Sci.* **2016**, *7*, 89–93. DOI: 10.1039/C5SC02583D.
- (49) Winston, M. S.; Wolf, W. J.; Toste, F. D. Photoinitiated Oxidative Addition of CF₃I to Gold(I) and Facile Aryl-CF₃ Reductive Elimination. *J. Am. Chem. Soc.* **2014**, *136*, 7777–7782. DOI: 10.1021/ja503974x.
- (50) Lemon, C. M.; Powers, D. C.; Brothers, P. J.; Nocera, D. G. Gold Corroles as Near-IR Phosphors for Oxygen Sensing. *Inorg. Chem.* **2017**, *56*, 10991–10997. DOI: 10.1021/acs.inorgchem.7b01302.
- (51) Prei, S.; Ppcke, A.; Burkhardt, L.; Gromann, L.; Lochbrunner, S.; Bauer, M.; Opatz, T.; Heinze, K. Gold(II) Porphyrins in Photoinduced Electron Transfer Reactions. *Chem. Eur. J.* **2019**, *25*, 5940–5949. DOI: 10.1002/chem.201900050.
- (52) Fukuzumi, S.; Ohkubo, K.; E, W.; Ou, Z.; Shao, J.; Kadish, K. M.; Hutchison, J. A.; Ghiggino, K. P.; Sinti, P. J.; Crossley, M. J. Metal-centered Photoinduced Electron Transfer Reduction of a Gold(III) Porphyrin Cation Linked with a Zinc Porphyrin to Produce a Long-Lived Charge-Separated State in Nonpolar Solvents. *J. Am. Chem. Soc.* **2003**, *125*, 14984–14985. DOI: 10.1021/ja037214b.
- (53) Gransson, E.; Boixel, J.; Fortage, J.; Jacquemin, D.; Becker, H.-C.; Blart, E.; Hammarstrm, L.; Odobel, F. Long-Range Electron Transfer in Zinc-Pthalocyanine-Oligo(Phenylene-ethylene)-Based Donor-Bridge-Acceptor Dyads. *Inorg. Chem.* **2012**, *51*, 11500–11512. DOI: 10.1021/ic3013552.
- (54) Prei, S.; Frster, C.; Otto, S.; Bauer, M.; Mller, P.; Hinderberger, D.; Hashemi Haeri, H.; Carella, L.; Heinze, K. Structure and reactivity of a mononuclear gold(II) complex. *Nat. Chem.* **2017**, *9*, 1249–1255. DOI: 10.1038/nchem.2836.
- (55) Prei, S.; Melomedov, J.; Wnsche von Leupoldt, A.; Heinze, K. Gold(III) tetraarylporphyrin amino acid derivatives: ligand or metal centred redox chemistry? *Chem. Sci.* **2016**, *7*, 596–610. DOI: 10.1039/c5sc03429a.
- (56) Blake, A. J.; Greig, J. A.; Holder, A. J.; Hyde, T. I.; Taylor, A.; Schrder, M. Bis(1,4,7-trithiacyclononane)gold Dication: A Paramagnetic, Mononuclear Au II Complex. *Angew. Chem. Int. Ed.* **1990**, *29*, 197–198. DOI: 10.1002/anie.199001971.
- (57) Drews, T.; Seidel, S.; Seppelt, K. Gold-Xenon Complexes. *Angew. Chem. Int. Ed.* **2002**, *41*, 454–456. DOI: 10.1002/1521-3773(20020201)41:3<454:AID-ANIE454>3.0.CO;2-7.
- (58) Elder, S. H.; Lucier, G. M.; Hollander, F. J.; Bartlett, N. Synthesis of Au(II) Fluoro Complexes and Their Structural and Magnetic Properties. *J. Am. Chem. Soc.* **1997**, *119*, 1020–1026. DOI: 10.1021/ja9630654.
- (59) Hwang, I.-C.; Seppelt, K. The Reduction of AuF₃ in Super Acidic Solution. *Z. Anorg. Allg. Chem.* **2002**, *628*, 765–769. DOI: 10.1002/1521-3749(200205)628:4<765:AID-ZAAC765>3.0.CO;2-E.
- (60) Lindquist, K. P.; Eghdami, A.; Deschene, C. R.; Heyer, A. J.; Wen, J.; Smith, A. G.; Solomon, E. I.; Lee, Y. S.; Neaton, J. B.; Ryan, D. H.; Karunadasa, H. I. Stabilizing Au₂⁺ in a mixed-valence 3D halide perovskite. *Nat. Chem.* **2023**, *15*, 1780–1786. DOI: 10.1038/s41557-023-01305-y.
- (61) Qu, Z.; Giurgiu, L.; Roduner, E. ESR observation of the formation of an Au(II) complex in zeolite Y. *Chem. Commun.* **2006**, 2507–2509. DOI: 10.1039/b601900e.
- (62) Seidel, S.; Seppelt, K. Xenon as a Complex Ligand: The Tetra Xenono Gold(II) Cation in AuXe(4)₂(Sb(2)F(11))₂. *Science* **2000**, *290*, 117–118. DOI: 10.1126/science.290.5489.117.
- (63) Seppelt, K. Metal-Xenon Complexes. *Z. Anorg. Allg. Chem.* **2003**, *629*, 2427–2430. DOI: 10.1002/zaac.200300226.
- (64) Walker, N. R.; Wright, R. R.; Barran, P. E.; Stace, A. J. Stable Gold(II) Complexes in the Gas Phase. *Organometallics* **1999**, *18*, 3569–3571. DOI: 10.1021/om990260t.
- (65) Heinze, K. The Quest for Mononuclear Gold(II) and Its Potential Role in Photocatalysis and Drug Action. *Angew. Chem. Int. Ed.* **2017**, *56*, 16126–16134. DOI: 10.1002/anie.201708349.
- (66) Dann, T.; Roca, D.-A.; Wright, J. A.; Wildgoose, G. G.; Bochmann, M. Electrochemistry of Au(II) and Au(III) pincer complexes: determination of the Au(II)-Au(II) bond energy. *Chem. Commun.* **2013**, *49*, 10169–10171. DOI: 10.1039/c3cc45984e.
- (67) Yam, V. W.-W.; Choi, S. W.-K.; Cheung, K.-K. Synthesis, photophysics and thermal redox reactions of a [Au(dppn)Cl]₂²⁺ dimer with an unsupported Au II – Au II bond. *Chem. Commun.* **1996**, 1173–1174. DOI: 10.1039/CC960001173.
- (68) Basil, J. D.; Murray, H. H.; Fackler, J. P.; Tocher, J.; Mazany, A. M.; Trzcinska-Bancroft, B.; Knachel, H.; Dudis, D.; Delord, T. J.; Marler, D. Experimental and Theoretical Studies of Dinuclear Gold(I) and Gold(II) Phosphorus Ylide Complexes. Oxidative addition, halide exchange, and structural properties including the crystal and molecular structures of [Au(CH₂)₂PPh₂]₂ and [Au(CH₂)₂PPh₂](CH₃)Br. *J. Am. Chem. Soc.* **1985**, *107*, 6908–6915. DOI: 10.1021/ja00310a028.
- (69) Dell'Amico, D. B.; Calderazzo, F.; Marchetti, F.; Merlino, S. Synthesis and Molecular Structure of [Au₄Cl₈], and the Isolation of [Pt(CO)Cl₅]- in Thionyl Chloride. *J. Chem. Soc., Dalton Trans.* **1982**, 2257–2260. DOI: 10.1039/dt9820002257.
- (70) Wickleder, M. S. AuSO₄: A True Gold(II) Sulfate with an Au₂⁺ Ion. *Z. Anorg. Allg. Chem.* **2001**, *627*, 2112–2114. DOI: 10.1002/1521-3749.
- (71) Sorge, L.; Link, J.; Heinze, K. 14-Membered Macrocyclic β -Diiminato Gold(II) - A New Member for the Gold(II) Complex Family? *Chem. Eur. J.* **2024**, e202400924. DOI: 10.1002/chem.202400924.
- (72) Eng, M. P.; Ljungdahl, T.; Andreasson, J.; Martensson, Jerker, Albinsson, Bo. Triplet Photophysics of Gold(III) Porphyrins. *J. Phys. Chem. A* **2005**, 1776–1784. DOI: 10.1021/jp0449399.
- (73) Fleischer, E. B.; Laszlo, A. Synthesis of a Gold Porphyrin. *Inorg. Nucl. Chem. Lett.* **1969**, *5*, 373–376. DOI: 10.1016/0020-1650(69)80083-8.
- (74) Lash, T. D. Porphyrins with Exocyclic rings. Part 10. Synthesis of meso, β -Propanoporphyrins from 4,5,6,7-Tetrahydro-1H-Indoles. *Tetrahedron* **1998**, *54*, 359–374. DOI: 10.1016/S0040-4020(97)10288-5.
- (75) Bobl, P.; Lightner, D. A. An Improved Coupling Procedure for the Barton-Zard Pyrrole Synthesis. *J. Heterocyclic Chem.* **2001**, *38*, 527–530. DOI: 10.1002/jhet.5570380239.
- (76) Chen, Q.; Huggins, M. T.; Lightner, D. A.; Norona, W.; McDonagh, A. F. Synthesis of a 10-Oxo-Bilirubin: Effects of the Oxo Group on Conformation, Transhepatic Transport, and Glucuronidation. *J. Am. Chem. Soc.* **1999**, *121*, 9253–9264. DOI: 10.1021/ja991814m.
- (77) Antipas, A.; Dolphin, D.; Gouterman, M.; Johnson, E. C. Porphyrins. 38. Redox potentials, charge transfer transitions, and emission of copper, silver, and gold complexes. *J. Am. Chem. Soc.* **1978**, *100*, 7705–7709. DOI: 10.1021/ja00492a044.
- (78) Antipas, A.; Buchler, J. W. Gouterman, M.; Smith, P. D. Porphyrins. 36. Synthesis and optical and electronic properties of some ruthenium and osmium octaethylporphyrins. *J. Am. Chem. Soc.* **1978**, *100*, 3015–3024. DOI: 10.1021/ja00478a013.
- (79) Dharmija, A.; Mondal, P.; Saha, B.; Rath, S. P. Induction, control, and rationalization of supramolecular chirogenesis using metalloporphyrin tweezers: a structure-function correlation. *Dalton Trans.* **2020**, *49*, 10679–10700. DOI: 10.1039/d0dt01874k.
- (80) Telfer, S. G.; McLean, T. M.; Waterland, M. R. Exciton coupling in coordination compounds. *Dalton Trans.* **2011**, *40*, 3097–3108. DOI: 10.1039/C0DT01226B.
- (81) Balzani, V.; Ceroni, P.; Juris, A. Photochemistry and Photophysics: Concepts, Research, Applications, 1st edition; Wiley-VCH, 2014.
- (82) Knyukshto, V.; Zenkevich, E.; Sagun, E.; Shulga, A.; Bachilo, S. Unusual dynamic relaxation of triplet-excited meso-phenyl-substituted porphyrins and their chemical dimers at room temperatures. *Chem. Phys. Lett.* **1998**, *297*, 97–108. DOI: 10.1016/S0009-2614(98)01096-3.
- (83) Avilov, I. V.; Zenkevich, E. I.; Sagun, E. I.; Filatov, I. V. Quantum-Chemical Investigation of the Conformational Dynamics of Mono- meso-phenyl-Substituted Octaalkylporphyrins in the Triplet Excited State. *J. Phys. Chem. A* **2004**, *108*, 5684–5691. DOI: 10.1021/jp048930i.
- (84) Eaton, S. S.; Eaton, G. R.; Chang, C. K. Synthesis and geometry determination of cofacial diporphyrins. EPR spectroscopy of dicopper diporphyrins in frozen solution. *J. Am. Chem. Soc.* **1985**, *107*, 3177–3184. DOI: 10.1021/ja00297a024.
- (85) Eaton, S. S.; More, K. M.; Sawant, B. M.; Eaton, G. R. Use of the ESR half-field transition to determine the interspin distance and the orientation of the interspin vector in systems with two unpaired electrons. *J. Am. Chem. Soc.* **1983**, *105*, 6560–6567. DOI: 10.1021/ja00360a005.
- (86) Chang, C. J.; Loh, Z.-H.; Deng, Y.; Nocera, D. G. The Pacman Effect: A Supramolecular Strategy for Controlling the Excited-State Dynamics of Pillared Cofacial Bisporphyrins. *Inorg. Chem.* **2003**, *42*, 8262–8269. DOI: 10.1021/ic034750w.

Insert Table of Contents artwork here

3.2 | Face-to-Face Gold Porphyrins



3.3 Pushing Molecular Orbitals to Higher Energy – A DFT Study on the Spin Distribution in Gold Corrole Complexes

3.3.1 Introduction

The formal coordination of gold in the oxidation state +II ($5d^9$ electron configuration) to the dianionic tetraphenylporphyrinato ligand TPP^{2-} (doublet ground state) results in a gold-centered Mulliken spin density of the DFT geometry-optimized structures, whereas the coordination to the trianionic triphenylcorrolato ligand TPC^{3-} results in a ligand-centered Mulliken spin density distribution – in agreement with the experimental data.³¹ The intrinsically high ligand field splitting of gold and the better overlap between the gold atomic orbitals and the corrolato molecular orbitals result in the energetically favourable spin redistribution from gold over the corrolato compared with the porphyrinato ligand.^{31,46,130,141}

The square-planar tetraaza coordination environment, as provided by the geometrically rigid TPP^{2-} ligand, was found to be the ideal location for the molecular stabilization of gold(II). The drive of the open-shell gold(II) for the energetic stabilization of the singly-occupied $5d_{x^2-y^2}$ orbital via dimerization is suppressed by the TPP^{2-} ligand in the xy plane. The disproportionation into gold(I) and gold(III), favoured due to the strong mixing of the $6s$ and $5d$ orbitals, arising from the relativistically lowered energy gap between these orbitals, is hindered due to the energetic destabilization of gold(I) in a square-planar coordination environment.¹⁴¹

It is conducted a comprehensive quantum chemical study, applying density functional theory (DFT) methods, on the effect of electron donating substituents, attached to the corrolato scaffold, on the energy of the ligand-centered lowest unoccupied molecular orbitals (LUMO). The energetic approximation to the gold-centered $5d_{x^2-y^2}$ orbitals (b_1) could facilitate a Mulliken spin population redistribution under involvement of the gold center. The geometric distortions of the corrolato macrocycle are analyzed via the normal-coordinate structural decomposition (NSD) method.⁶²

The electronic absorption spectra of corroles are similar to those of porphyrins and can be mostly explained by Gouterman's four orbital model.^{43,44} The loss of one methine bridge of the porphine macrocycle entails the lowering of the local symmetry from D_{4h} or D_{2h} respectively, to C_{2v} . The corrole-centered frontier molecular orbitals are described by a_2/b_2 (HOMO-1 and HOMO) and a_2/b_2 (LUMO and LUMO+1) symmetry.

The geometries of the (triphenylcorrolato) complexes of the coinage metals copper, silver and gold in their singlet ($^1[Cu(TPC)]$, $^1[Ag(TPC)]$, $^1[Au(TPC)]$) as well as doublet ground states ($^2[Cu(TPC)]^-$, $^2[Ag(TPC)]^-$, $^2[Au(TPC)]^-$) were also optimized via density functional theory methods for comparison reasons.

CHAPTER 3 | Results and Discussion

The highest occupied molecular orbitals of $^1[\text{Cu}(\text{TPC})]$ and $^1[\text{Ag}(\text{TPC})]$ are corrole-centered. The energy gap between the b_2 orbital and the b_1 orbital, which correspond to the $3d_{x^2-y^2}$ and $4d_{x^2-y^2}$, respectively, are 1.87 eV for $^1[\text{Cu}(\text{TPC})]$ and 2.39 eV for $^1[\text{Ag}(\text{TPC})]$. The increased energy gap between the ligand- and metal-centered molecular orbital is mainly attributed to the higher energy of the antibonding b_1 orbital rather than the energetic stabilization of the LUMO-1 (a_2) and LUMO (b_2). The coordination of gold(III) to triphenylcorrolato invokes a strong destabilization of the gold-centered b_1 orbital (-1.13 eV) as well as the inversion of the energy of the ligand-centered molecular orbitals (a_2 : -2.40 eV, b_2 : -1.93 eV, b_1 : -1.13 eV).

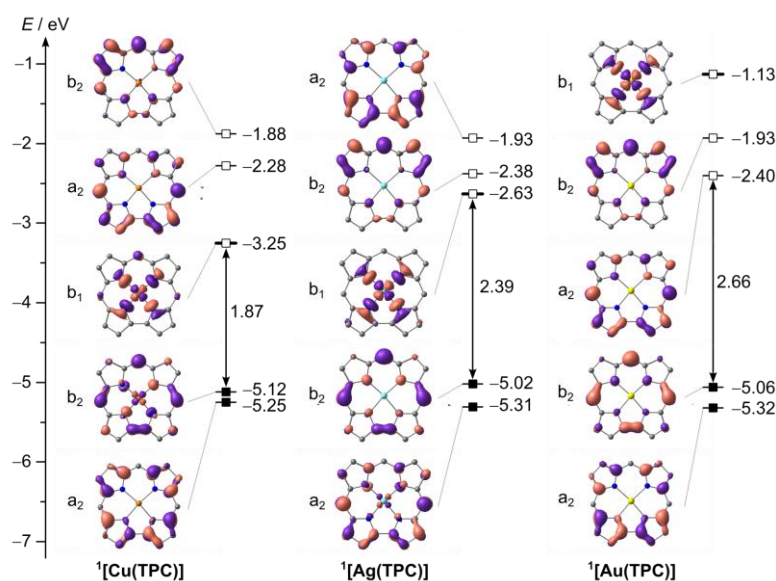


Figure 3.1 Energy diagram of the DFT geometry-optimized structures of $^1[\text{Cu}(\text{TPC})]$, $^1[\text{Ag}(\text{TPC})]$ and $^1[\text{Au}(\text{TPC})]$ in their singlet ground state. Isosurface value at 0.05 a.u. Phenyl groups and hydrogen atoms omitted for better visualisation. Filled square: occupied molecular orbital, empty square: unoccupied molecular orbital. Molecular orbital notation according to Gouterman's four orbital model.

Upon formal reduction of the diamagnetic complexes, the α - b_1 molecular orbitals, which correspond to the $3d_{x^2-y^2}$ orbital of copper and the $4d_{x^2-y^2}$ orbital of silver, are stabilized by 1.31 eV and 1.02 eV, respectively, whereas the gold- $5d_{x^2-y^2}$ is destabilized by 0.66 eV (Figure 3.2).

3.3 | Pushing Molecular Orbitals to Higher Energy – A DFT Study on the Spin Distribution in Gold Corrole Complexes

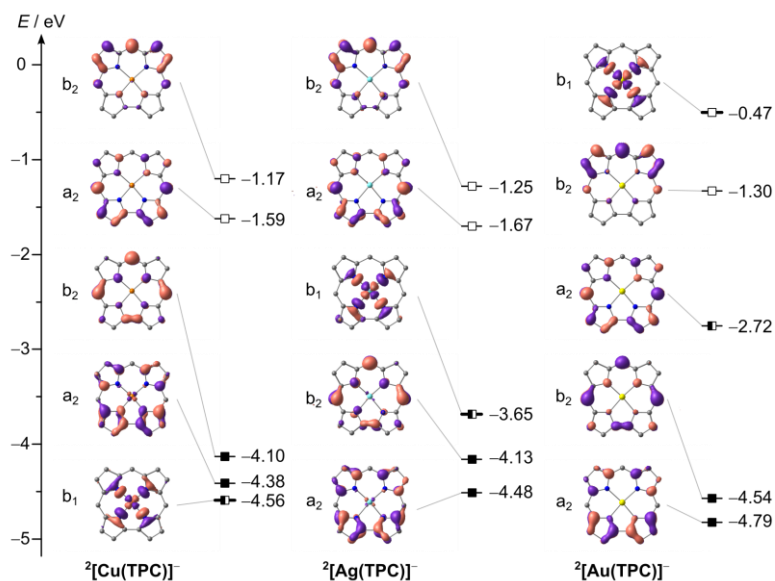


Figure 3.2 Energy diagram of the DFT geometry-optimized structures of $^2[\text{Cu}(\text{TPC})]^-$, $^2[\text{Ag}(\text{TPC})]^-$ and $^2[\text{Au}(\text{TPC})]^-$ in their doublet ground state. Isosurface value at 0.05 a.u. Phenyl groups and hydrogen atoms omitted for better visualisation. Filled square: occupied α molecular orbital, half-filled square: singly-occupied α molecular orbital, empty square: unoccupied α molecular orbital. Molecular orbital notation according to Gouterman's four orbital model.

The Cu/Ag/Au-N1/N2 distances in the diamagnetic complexes $^1[\text{Cu}(\text{TPC})]$, $^1[\text{Ag}(\text{TPC})]$ and $^1[\text{Au}(\text{TPC})]$ are in all cases slightly longer than the opposite Cu/Ag/Au-N3/N4 distances.

The Cu-N1/N2 distances are increased from 1.888/1.890 Å to 1.913/1.914 Å and the Cu-N3/N4 distances from 1.878/1.872 Å to 1.916/1.918 Å due to the population of the antibonding $3d_{x^2-y^2}$ orbital.

The Mulliken spin density is mainly localized on the copper atom (0.545) and the coordinating nitrogen atoms (0.100/0.100/0.114/0.115). The same accounts for the corresponding $^1[\text{Ag}(\text{TPC})]$ and $^2[\text{Ag}(\text{TPC})]^-$ complexes, respectively. The Ag-N1/N2 and Cu-N3/N4 distances are increased from 1.961/1.961 Å and 1.944/1.944 Å to 2.033/2.041 Å and 2.058/ 2.052 Å. The Mulliken spin density is located onto the silver atom (0.389) and the coordinating nitrogen atoms (0.129/0.124/0.134/0.139).

The $^1[\text{Au}(\text{TPC})]$ essentially features identical Au-N1/N2 and Au-N3/N4 distances (1.963/1.964 Å and 1.946/1.945 Å). In contrast to the copper- and silver corrolato complexes, the Mulliken spin density is distributed over the corrolato ligand, mainly onto the C^5/C^{15} atoms (0.271/0.265), α - (0.124/0.122) and β -atoms (0.118/0.115/0.109/0.106). The gold center is not involved. This is reflected in the Au-N1/N2 and Au-N3/N4, which are only slightly increased compared with the diamagnetic complex $^1[\text{Au}(\text{TPC})]$. The strong destabilization of the b_1 molecular orbital, which predominantly correspond to the metal-centered $5d_{x^2-y^2}$ orbital is not a consequence of the small corrole cavity, rather than a consequence of the intrinsically high ligand field splitting of gold compared with copper and silver.

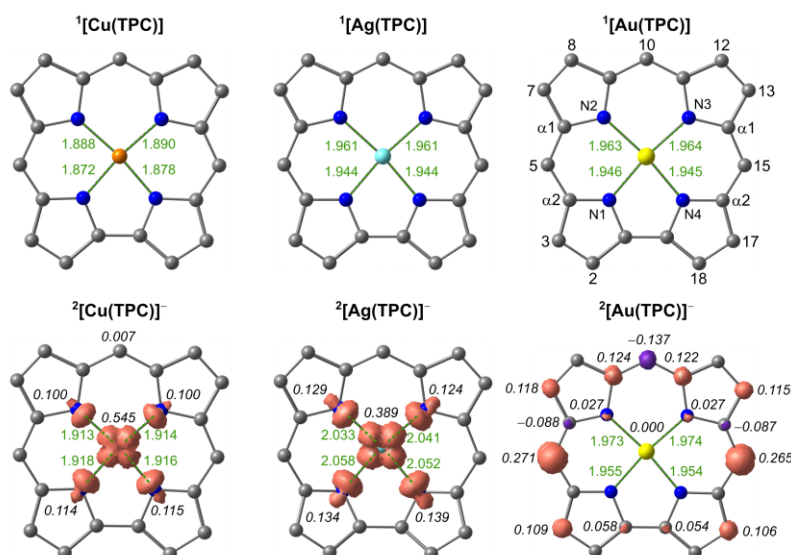


Figure 3.3 DFT geometry-optimized structures of $^{1/2}[\text{Cu}(\text{TPC})]^{0/-}$, $^{1/2}[\text{Ag}(\text{TPC})]^{0/-}$ and $^{1/2}[\text{Au}(\text{TPC})]^{0/-}$ in their singlet and doublet ground state, respectively. Mulliken spin density in italics, selected metrics given in Å. Iso-surface value at 0.008 a.u. Phenylgroups and hydrogen atoms omitted for better visualisation. Red: α Mulliken spin density, purple: β Mulliken density.

Based on the atomic orbital coefficients, the major impact on the energy of the corrole-centered LUMOs is given by the attachment of +M substituents at the C5/C15 and C10 atoms as well as the β -positions C7/C13 and C3/C17.

The aryl substituents 4-Methoxyphenyl, 2,4,6-Trimethoxyphenyl, 4-(Dimethylamino)phenyl- and 2,4,6-Tris(dimethylamino)phenyl as well as methoxy- and dimethylamino directly attached to the (corrolato)gold scaffold (Figure 3.4) were chosen. The geometries of the (corrolato)gold complexes were optimized in their electronic singlet and doublet ground states and analyzed regarding the energy of their frontier molecular orbitals, Mulliken spin distribution in the doublet ground state and geometric *out-of-plane* distortions both in the singlet and doublet ground state. It is distinguished between the C5/C15- and C10- as well as the C7/C13- and C3/C17-positions (structures 1 - 18). The effect of the exchange of the methine carbon atoms for the heteroatoms oxygen (oxa) and sulfur (thia) (19 - 24) is also investigated as well as the effect of methyl substituents at the *beta*-positions (structures 25 - 27) (Figure 3.4).

3.3 | Pushing Molecular Orbitals to Higher Energy – A DFT Study on the Spin Distribution in Gold Corrole Complexes

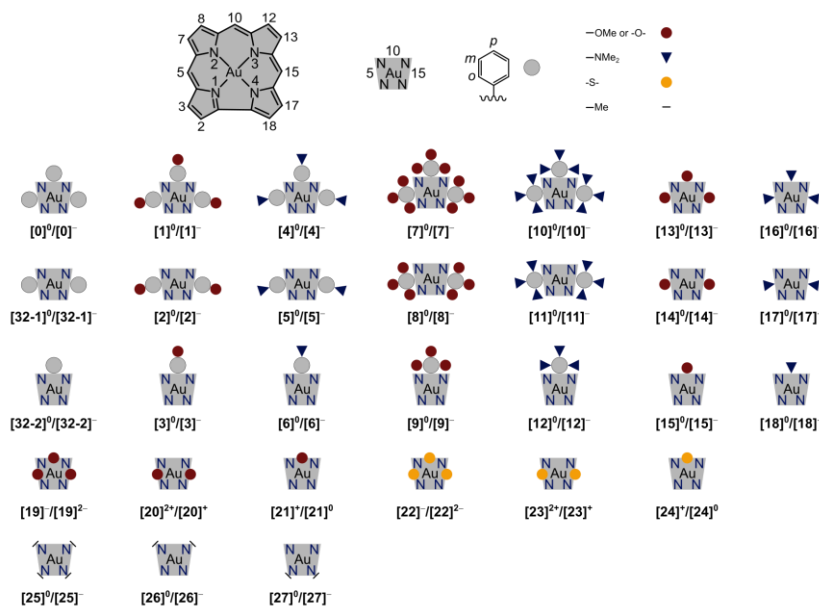


Figure 3.4 Pictograms of the structures of DFT geometry-optimized (corrolato)gold complexes in their singlet and doublet ground states.

3.3.2 Results and Discussion

The energies of the frontier molecular orbitals are raised upon introduction of identical electron donating (aryl)-substituents to all *meso*-positions. In general, the impact of 4-(Dimethylamino)phenyl (b_2 : +0.39 eV, a_2 : +0.16 eV, a_2 : 0.16 eV) is larger than for the 4-Methoxyphenyl-substituents (b_2 : +0.12 eV, a_2 : +0.06 eV, a_2 : +0.06 eV). Interestingly, the impact of 2,4,6-Trimethoxyphenyl on the corrole-centered frontier molecular orbitals is less pronounced (b_2 : +0.05 eV, a_2 : +0.12 eV, a_2 : +0.11 eV) than for 4-Methoxyphenyl, whereas the impact of 2,4,6-Tris(dimethylamino)phenyl (b_2 : +0.44 eV, a_2 : +0.26 eV, a_2 : +0.28 eV) is larger. This can be explained by the larger dihedral angle between the corrole and aryl-planes ($71.6^\circ/75.7^\circ/83.6^\circ$) of $[7]^-$ compared with $[1]^-$ ($57.5^\circ/65.8^\circ/57.5^\circ$) resulting in a smaller electronic contribution of the aryl molecular orbitals to the corrole-centered frontier molecular orbitals. The dihedral angle of $[10]^-$ ($67.9^\circ/69.1^\circ/69.1^\circ$) are slightly increased compared to $[4]^-$ ($53.6^\circ/63.1^\circ/57.4^\circ$) leading to a smaller electronic contribution of the aryl-substituents to the corrole-centered frontier molecular orbitals. This effect is probably compensated by the stronger electron donating nature of the dimethylamino substituents compared with methoxy substituents. The influence of methoxy- (b_2 : +0.07 eV, a_2 : +0.05 eV, a_2 : +0.06 eV) or dimethylamino-substituents (b_2 : + 0.44 eV, a_2 : + 0.22 eV, a_2 : + 0.14 eV) directly attached to the *meso*-positions to the corrole-centered frontier molecular orbitals is comparable to the corresponding aryl-substituted structures $[1]^0$, $[4]^0$, $[7]^0$ and $[10]^0$. The energies of the b_1 molecular orbital, which correspond to the gold-centered $5d_{x^2-y^2}$ orbital, are marginally raised in energy with a stronger influence of the dimethylamino-substituted corroles compared with the methoxy substituents ($[1]^0$: +0.04 eV, $[7]^0$: +0.12 eV and $[4]^0$: +0.11 eV, $[10]^0$: +0.27 eV).

CHAPTER 3 | Results and Discussion

Upon formal reduction of the diamagnetic compounds, the Mulliken spin density is mainly dislocated over the C5/C15, C10, C7/C13- and C3/C17-atoms similar to the $[\text{Au}(\text{TPC})]^-$ prototype, whereas the Mulliken spin density onto the gold atom amounts to 0.000 in all cases. The spin density is located in the a_2 molecular orbital whereas the unoccupied b_2 and b_1 molecular orbitals are energetically destabilized with respect to the diamagnetic structures.

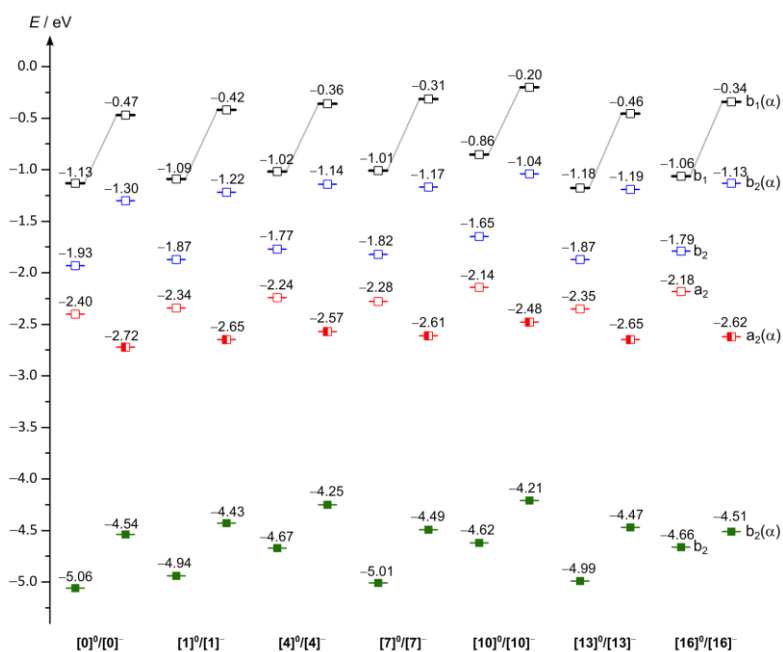


Figure 3.5 Energies of frontier molecular orbitals of the DFT geometry-optimized of 5,10,15-trisaryl-substituted (corrolato)gold complexes in their singlet and doublet (only α energies given) ground states.

The *out-of-plane* distortions of 5,10,15-trisaryl-substituted (corrolato)gold complexes are dominated by doming (B_1) and waving x (B_1) and do not significantly differ from each other for $^{1/2}[0]^{0/-}$, $^{1/2}[1]^{0/-}$, $^{1/2}[4]^{0/-}$ and $^{1/2}[7]^{0/-}$ (0.415/0.429 Å, 0.544/0.497 Å, 0.511/0.445 Å and 0.462/0.371 Å). The overall *out-of-plane* geometric distortion is significantly smaller for 0.173/0.153 Å for $^{1/2}[10]^{0/-}$ probably due to the larger dihedral angle between the aryl-substituents and macrocyclic corrole plane resulting in smaller steric hindrance and less geometric distortions. However, the attachment of dimethylamino substituents to C5 and C15 is accompanied by stronger overall *out-of-plane* distortions (+0.700 Å), which is dominated by doming (B_1) and waving x (B_1) (Figure 3.6).

3.3 | Pushing Molecular Orbitals to Higher Energy – A DFT Study on the Spin Distribution in Gold Corrole Complexes

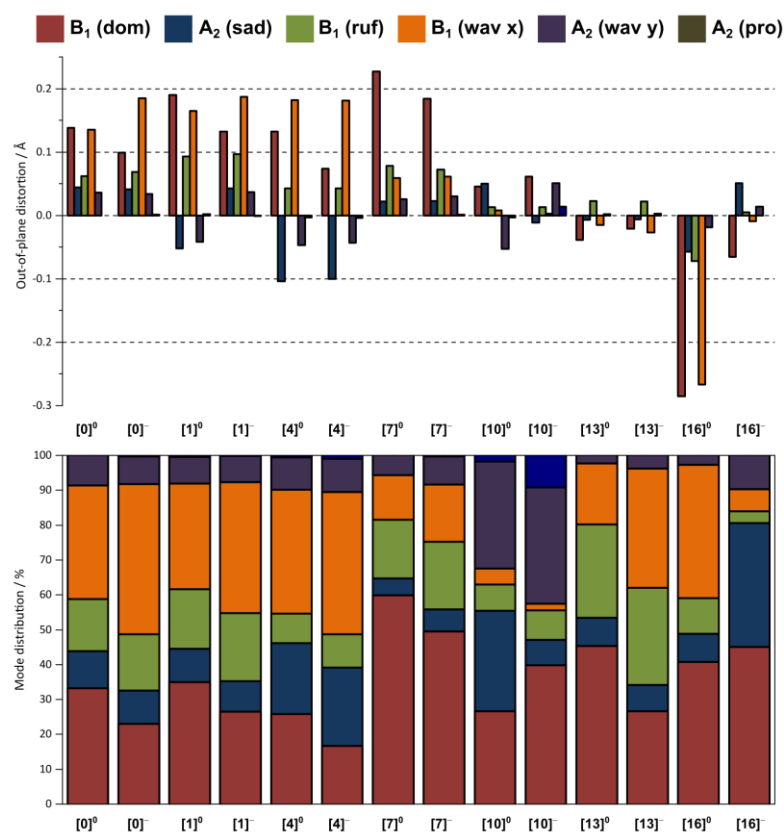


Figure 3.6 Normal-coordinate structural decomposition (NSD) analysis of the DFT geometry-optimized structures of 5,10,15-trisaryl-substituted (corrolato)gold complexes in their singlet and doublet ground states.

The attachment of electron-donating aryl-substituents to the C5/C15- (Figure 3.7) or C10-positions (Figure 3.8) is accompanied with an energetic destabilization of the corrole-centered frontier molecular orbitals, however less pronounced as for the 5,10,15-tris(aryl)-substituted complexes. The Mulliken spin density is distributed over the corrole ligand, predominantly under involvement of the C5/C10, C15, C7/C13 and C3/C17 atoms as already described for the 5,10,15-tris(aryl)-substituted complexes.

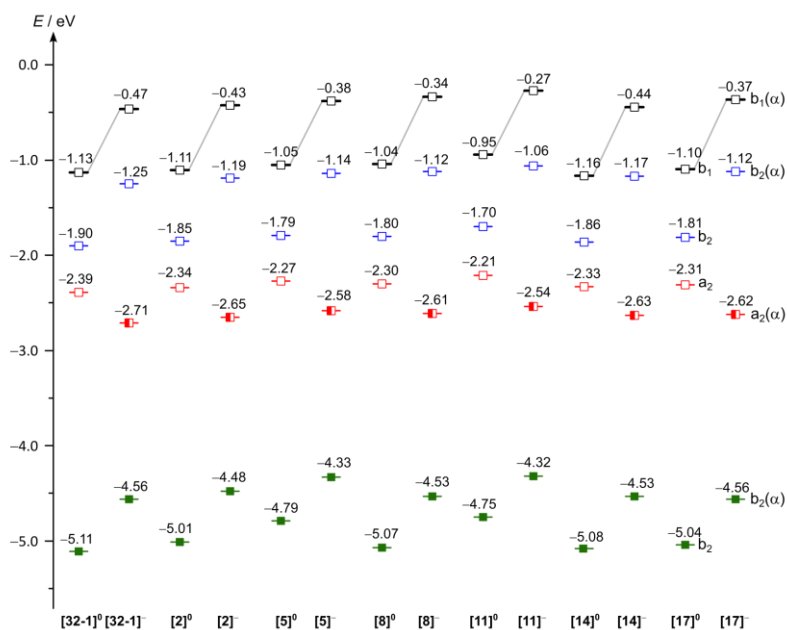


Figure 3.7 Energies of frontier molecular orbitals of the DFT geometry-optimized of 5,15-bisaryl-substituted (corrolato)gold complexes in their singlet and doublet (only α -energies given) ground states.

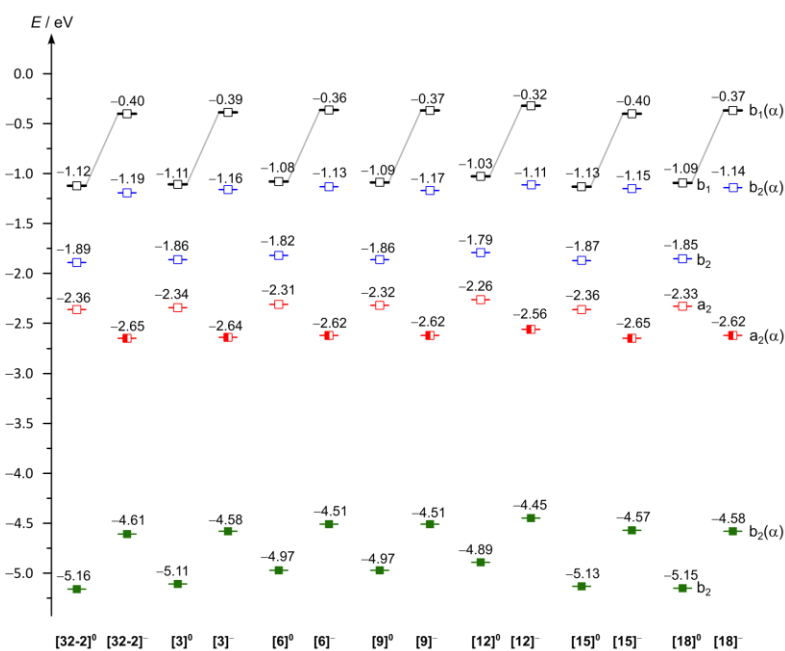


Figure 3.8 Energies of frontier molecular orbitals of the DFT geometry-optimized of 10-monoaryl-substituted (corrolato)gold complexes in their singlet and doublet (only α -energies given) ground states.

The C5/C15 aryl-substituted 4-methoxyphenyl and 4-(Dimethylamino)phenyl-substituted complexes $^{1/2}[2]^{0/-}$ and $^{1/2}[5]^{0/-}$ are dominated by doming (B_1) and waving x (B_1) *out-of-plane* distortions, whereas the 2,4,6-Trimethoxyphenyl and 2,4,6-Tris(dimethylamino)phenyl substituted complexes $^{1,2}[8]^{0/-}$ and $^{1/2}[11]^{0/-}$ are less affected by the waving x (B_1) mode and doming (B_1) is prevalent similar. The 5,15-dimethoxy-substituted (corrolato)gold complexes $^{1,2}[14]^{0/-}$ are much less distorted than the 5,15-dimethylamino-substituted (corrolato)gold complexes $^{1,2}[17]^{0/-}$. This is probably due to the larger dihedral angle between the corrole plane and oxygen-methyl bond (86°) compared with the dihedral angle between the corrole plane and nitrogen-methyl-bond (65°), which induces much weaker steric hindrance.

The energies of the corrole-centered frontier molecular orbitals of the C10 aryl-substituted structures are displayed in Figure 3.8. The general weak impact of the electron-donating substituents on HOMO/LUMO energy is confirmed and – as expected – less pronounced than for the C5/C10/C15 and C5/C15-substituted complexes. The Mulliken spin density remains ligand centered whereas the gold atom is not involved. The overall *out-of-plane* geometric distortions are much weaker compared with the C5/C10/C15- and C5/C15-substituted complexes (Figure 3.10). Interestingly, the distortions are dominated by the saddling (A_2) and waving y (B_2) mode, which have been of minor relevance for the C5/C10/C15 and C5/C15-substituted complexes.

3.3 | Pushing Molecular Orbitals to Higher Energy – A DFT Study on the Spin Distribution in Gold Corrole Complexes

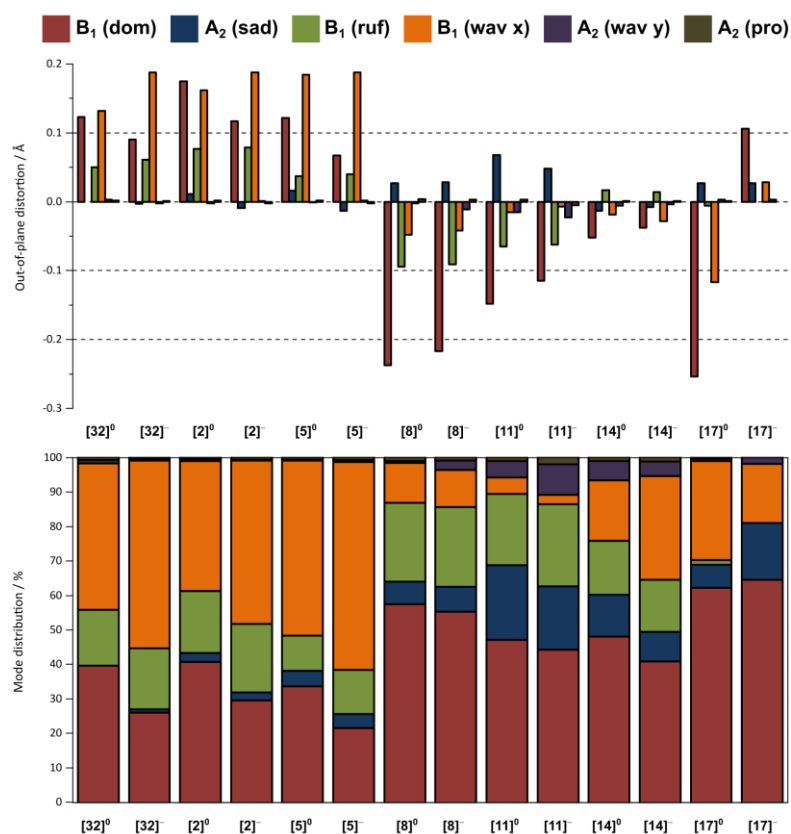


Figure 3.9 Normal-coordinate structural decomposition (NSD) analysis of the DFT geometry-optimized structures of 5,15-bisaryl-substituted (corrolato)gold complexes in their singlet and doublet ground states.

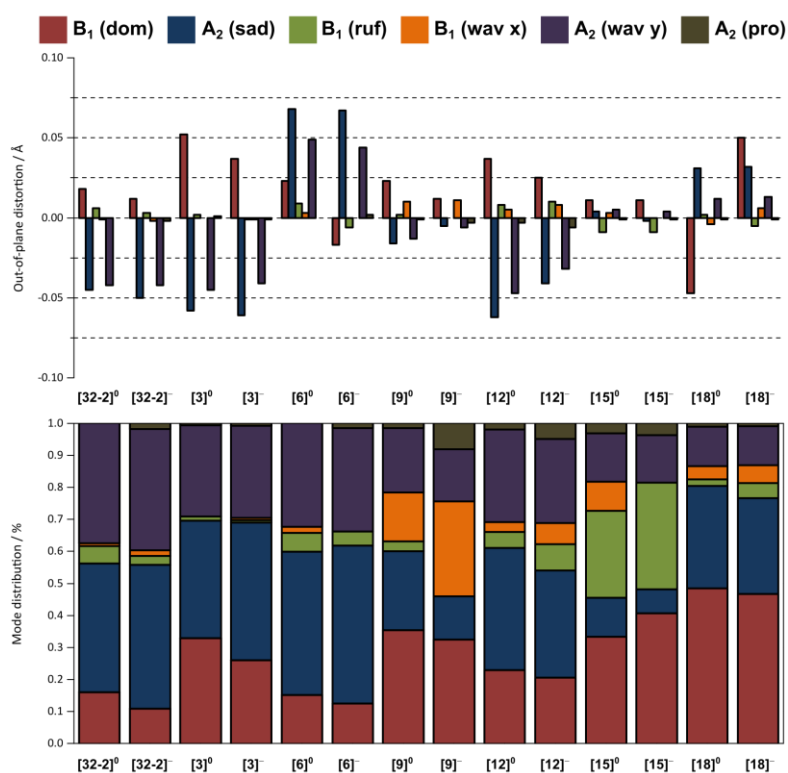


Figure 3.10 Normal-coordinate structural decomposition (NSD) analysis of the DFT geometry-optimized structures of 5-monoaryl-substituted (corrolato)gold complexes in their singlet and doublet ground states.

CHAPTER 3 | Results and Discussion

The formal substitution of the C5/C10/C15 carbon atoms positions with oxygen (oxa) or sulfur (thia) leads to an energetic destabilization of the a_2 corrole-centered HOMO by 0.96 eV or 0.91 eV, respectively. The LUMO and LUMO+1 are destabilized by 3.45 eV (a_2) and 2.08 eV (b_2) in case of $[19]^-$ and 2.78 eV (a_2) and 2.03 eV (b_2) in case of $[19]^-$ in comparison to $[32]^0$.

The substitution of the C5/C15- or C10-positions by oxygen or sulfur are accompanied by the stabilization of the HOMO (a_2) by 2.28/1.15 eV ($[20]^{2+}$, $[21]^+$) or 2.20/1.12 eV ($[23]^{2+}$, $[24]^+$). In contrast to $[19]^-$ and $[22]^-$ the energetic stabilization of b_2 involves a stabilization of a_2/b_2 (LUMO and LUMO+1) (Figure 3.11).

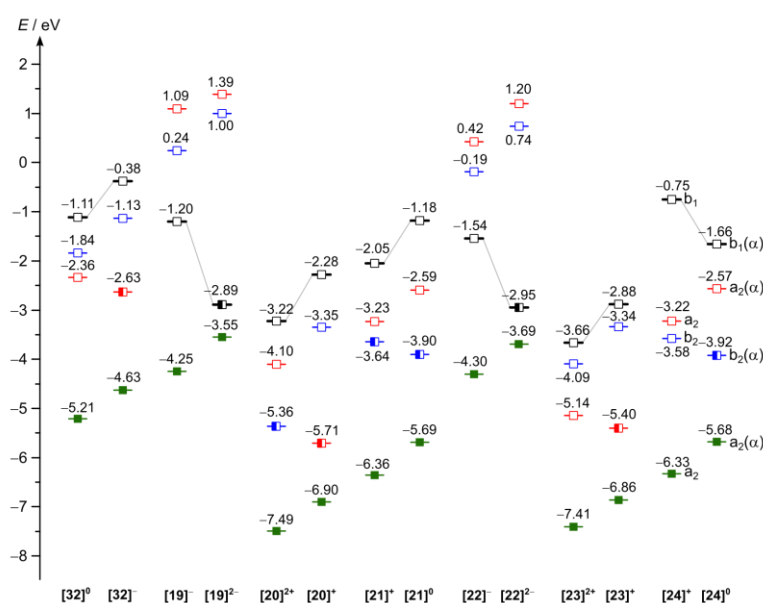


Figure 3.11 Energies of frontier molecular orbitals of the DFT geometry-optimized structures of C5,C10,C15-oxa- and thia-substituted (corrolato)gold complexes in their singlet and doublet (only α -energies given) ground states.

The *out-of-plane* distortions of $[19]^-$ and $[19]^{2-}$ are dominated by doming (B_1), and ruffling (B_1) and waving x (B_1), whereas the overall of of plane distortion of $[19]^-$ (2.402 Å) is smaller than for $[19]^{2-}$ (3.981 Å). The oxa-substituted complexes $[22]^-$ and $[22]^{2-}$ are dominated by ruffling, whereas doming (B_1) and waving x (B_1) are less pronounced (Figure 3.12).

3.3 | Pushing Molecular Orbitals to Higher Energy – A DFT Study on the Spin Distribution in Gold Corrole Complexes

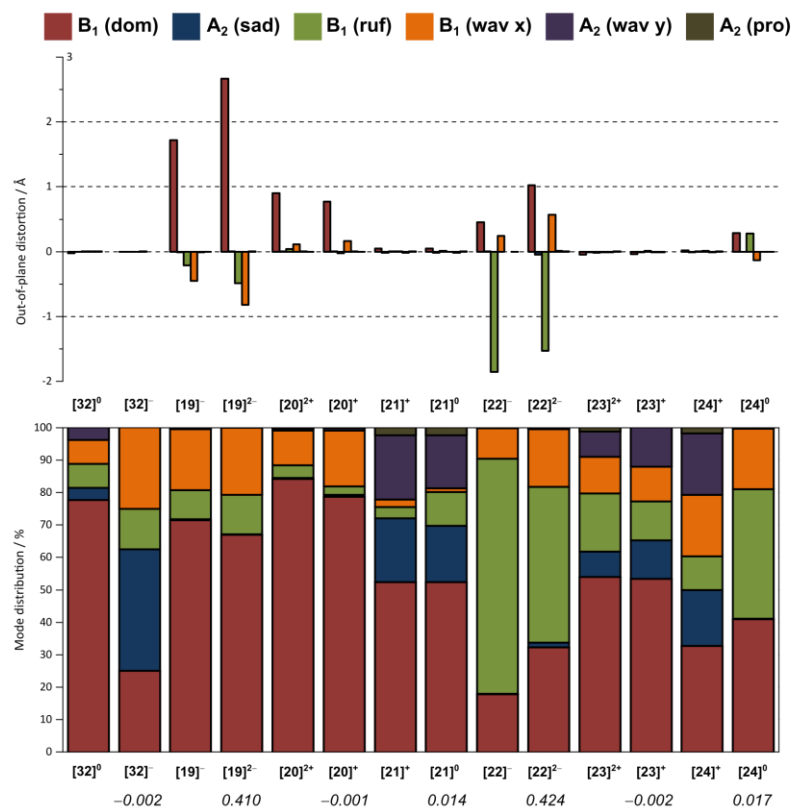


Figure 3.12 Normal-coordinate structural decomposition (NSD) analysis of the DFT geometry-optimized structures of C5,C10,C15-oxa- and thia-substituted (corrolato)gold complexes in their singlet and doublet ground states. Gold-Mulliken spin density given in italics.

The attachment of methyl groups to the β -positions leads to the destabilization of the HOMO (b_1) by 0.32 eV ($[25]^0$), 0.11 eV ($[26]^0$) and 0.17 eV ($[27]^0$). The LUMO (b_2) and LUMO+1 (a_2) are raised in energy as well by 0.33 eV ($[25]^0$), 0.09 eV ($[26]^0$) and 0.24 eV ($[27]^0$) (Figure 3.13). The inductive effect of methyl groups attached to the β -positions is weak – in accordance with the lower atomic orbital coefficients.

The overall geometric distortions of the corrole scaffold are much weaker than for the aryl-substituted (corrolato)gold complexes. The attachment of methyl groups to the positions 2,3,17 and 18 is accompanied with a slight saddling (A_2) and waving y (A_2). These *out-of-plane* distortions are not present for $^{1/2}[26]^{0/-}$. This is probably due to the greater spatial proximity of the methyl groups at the 8 and 12 ($C^{\text{methyl}}-C^{\text{methyl}}$ distance 3.605 Å) compared with positions 2 and 18 ($C^{\text{methyl}}-C^{\text{methyl}}$ distance 5.598 Å)

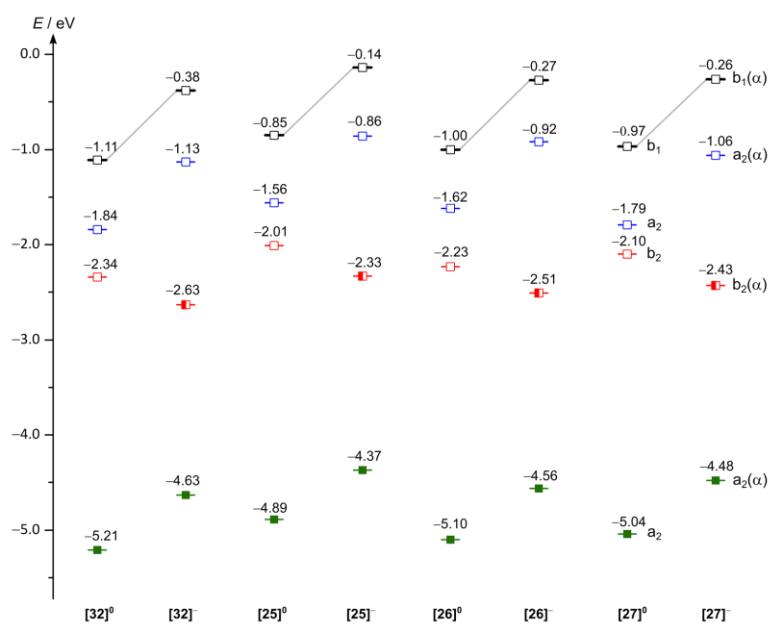


Figure 3.13 Energies of frontier molecular orbitals of the DFT geometry-optimized structures of β -methyl-substituted (corrolato)gold complexes in their singlet and doublet (only α -energies given) ground states.

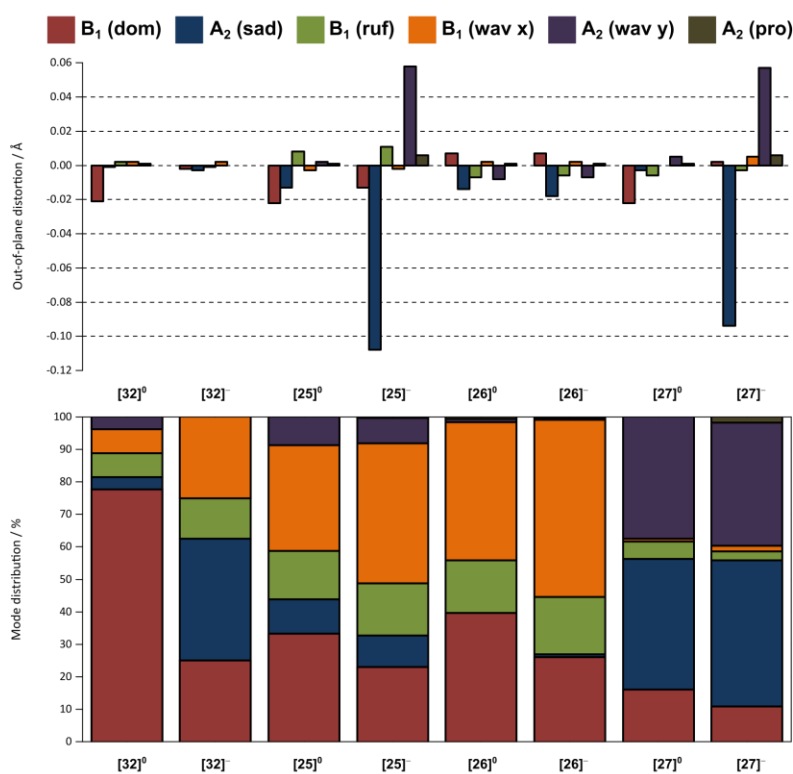


Figure 3.14 Normal-coordinate structural decomposition (NSD) analysis of the DFT geometry-optimized structures of β -methyl-substituted (corrolato)gold complexes in their singlet and doublet ground states.

3.3 | Pushing Molecular Orbitals to Higher Energy – A DFT Study on the Spin Distribution in Gold Corrole Complexes

In summary, the influence of +M *meso*-aryl-substituents on the energy of the ligand-centered frontier molecular orbitals and the location of the Mulliken spin density is rather low. The replacement of the methine positions by the heteroatoms oxygen (oxa) or sulfur (thia) is accompanied with a spin density redistribution from the ligand under involvement of the gold center. However, whether this is an effect of altered orbital energies or merely due to the enlargement of the [AuN₄] cavity and thus stabilization of the 5d_{x²-y²} orbital will be discussed next. To study the systematic effect of each substituent on the energy of the frontier molecular orbitals, a set of substituted (corrolato)gold complexes was chosen. [21]⁰ and [24]⁰ were chosen because the Mulliken spin density is already partly localized onto the gold atom (0.014 and 0.017, respectively). [32]⁰ was chosen as the starting point for the following comparative study and [17]⁰ bearing the strongly electron-donating and bulky dimethylamino group (Figure 3.15).

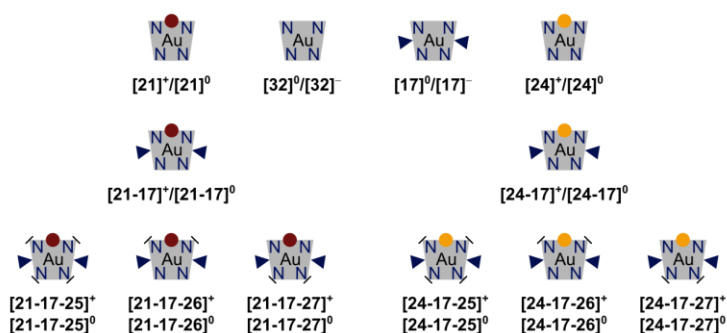


Figure 3.15 Pictograms of the structures of DFT geometry-optimized (corrolato)gold complexes in their singlet and doublet ground states.

The replacement of the C10 methine carbon atom by oxygen (¹[21]⁺) is accompanied with a contraction of the [AuN₄] cavity (7.499 Å²) and shorter gold-nitrogen distances compared with ¹[32]⁰ (7.599 Å²). This could be explained by the smaller covalent radius of oxygen (66(2) pm) compared to the sp² methine carbon atom (73(2) pm). However, the introduction of sulfur leads to an increase of the [AuN₄] cavity (7.740 Å²), probably due to the larger covalent radius of the third-row element sulfur (105(3) pm). This is also reflected in the destabilization of the b₁ molecular orbital for ^{1/2}[21]^{+ / 0} compared with ^{1/2}[21]^{+ / 0}. The formal reduction of the diamagnetic complexes is accompanied by a slight increase of the gold-nitrogen distances due to the partial localization of the spin density of the antibonding σ-type bond between gold and the coordinating nitrogen atoms.

The attachment of dimethylamino groups to the C5 and C15 positions to ²[32]⁻ does not lead to any significant changes in the Mulliken spin density distribution over the corrolato ligand or gold-nitrogen distances. This is also reflected in the α-energies of the frontier molecular orbitals, which are only slightly raised in energy compared with ²[32]⁻ (a₂: +0.07 eV, b₂: +0.01 eV, a₂: +0.01 eV, b₁: +0.01) (Figure S4).

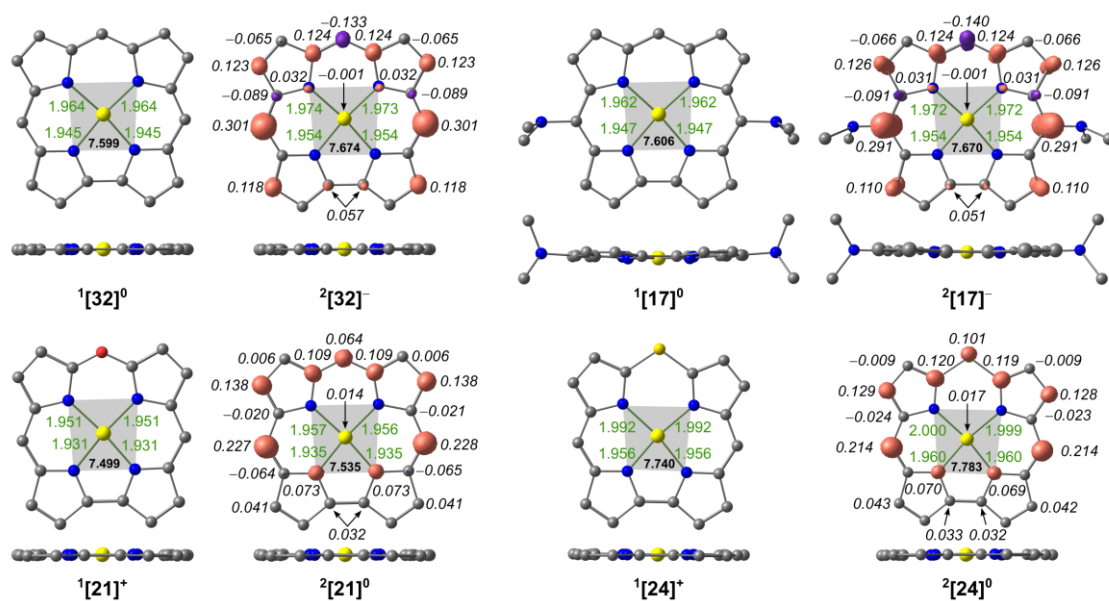


Figure 3.16 DFT geometry optimized structures of selected (corrolato)gold complexes in their singlet- and doublet ground states. Mulliken spin density given in italics. Gold-nitrogen distances given in \AA . $[\text{AuN}_4]$ cavity size given in \AA^2 (bold). Isosurface value at 0.008 a.u. Hydrogen atoms omitted for better visualizations.

Upon the attachment of dimethylamino substituents to the C5 and C15 positions to $^1[21-17]^+$ and $^1[24-17]^+$ the $[\text{AuN}_4]$ is increased by 0.101 and 0.112 \AA^2 , respectively (Figure 3.17). The overall *out-of-plane* distortion of $^1[21-17]^+$ and $^1[24-17]^+$ is increased to 0.668 \AA and 0.662 \AA , respectively, and dominated by saddling (A_2) in case of $^1[21-17]^+$ and waving x (B_1) and ruffling (B_1) in case of $^1[24-17]^+$. Upon formal reduction the α frontier molecular orbitals are energetically stabilized by 0.14 eV (a_2), 1.15 eV (b_2), 0.36 eV (a_2) and 0.12 (b_1) for $^2[21-17]^0$ and 0.19 eV (a_2), 1.30 eV (b_2), 0.35 eV (a_2) and 0.46 (b_1) for $^2[21-17]^0$ (Figure S4).

A minor part of the Mulliken spin density resides on the nitrogen atom of the dimethylamino substituents (0.054/0.055 and 0.049/0.049). The calculated spin density of the coordinating nitrogen atoms is located in π -type molecular orbitals. This could explain the decrease of the gold-nitrogen atoms instead of an increase upon reduction from 2.000/2.000/1.973/1.973 \AA to 1.997/1.997/1.969/1.969 \AA .

The geometries of the diamagnetic and paramagnetic complexes $^1[21-17]^+$ and $^2[21-17]^0$ are dominated by saddling (A_2), whereas the thia-substituted complexes $^1[24-17]^+$ and $^2[24-17]^0$ are dominated by waving x (B_1) and ruffling (B_1). The relatively small dihedral angle between the (corrolato)gold plane and the nitrogen- C^{methyl} bond of 33.4° allows for a mixing of the π -type corrolato-centered and the lone pair of the dimethylamino group (Figure 3.16).

3.3 | Pushing Molecular Orbitals to Higher Energy – A DFT Study on the Spin Distribution in Gold Corrole Complexes

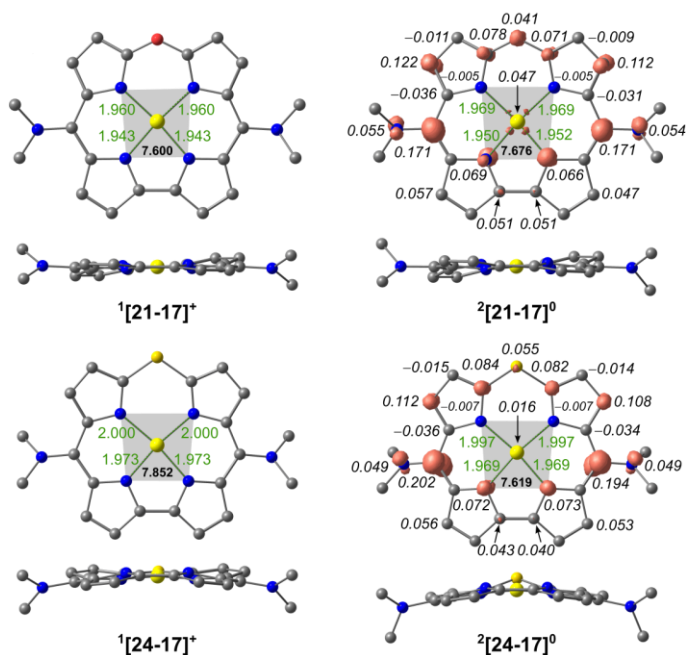


Figure 3.17 DFT geometry optimized structures of selected (corrolato)gold complexes in their singlet- and doublet ground states. Mulliken spin density given in italics. Gold-nitrogen distances given in Å. [AuN₄] cavity size given in Å² (bold). Isosurface value at 0.008 a.u. Hydrogen atoms omitted for better visualizations.

The attachment of methyl substituents of the β -positions of the (corrolato)gold complexes leads to strong geometric distortions of the corrolato scaffold, which are dominated by saddling (A_2) in the order $^{1/2}[21-17-27]^{+/0} < ^{1/2}[21-17-26]^{+/0} < ^{1/2}[21-17-25]^{+/0}$. This is probably due to the steric hindrance of the methyl groups at the positions 2/18 and 8/12, respectively (Figure 3.16).

The α HOMOs are raised in energy compared with $^2[21-17]^0$ in the order $< ^2[21-17-26]^0 < ^2[21-17-27]^0 < ^2[21-17-25]^0$ (a_2 : +0.11 eV, +0.15 eV, + 0.26 eV) whereas the corrolato-centered LUMO and LUMO+1, as well the b_1 energies are only marginally shifted in their energy (Figure S4).

Interestingly, the Mulliken spin density onto the gold atom is increased in the order $^2[21-17-27]^0 < ^2[21-17-26]^0 < ^2[21-17-25]^0$ upon stronger *out-of-plane* geometric distortions, although the energies of the corrole-centered frontier molecular orbitals are not significantly changed.

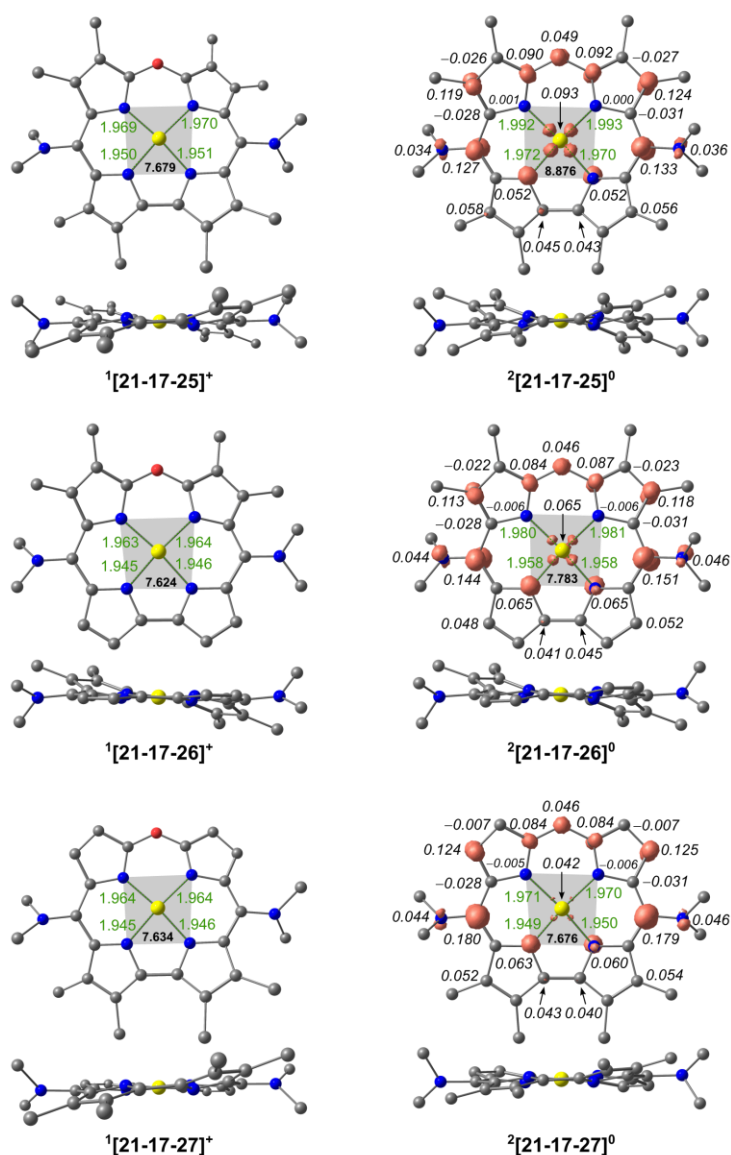


Figure 3.18 DFT geometry optimized structures of selected C10-oxa-substituted (corrolato)gold complexes in their singlet- and doublet ground states. Mulliken spin density given in italics. Gold-nitrogen distances given in Å. [AuN₄] cavity size given in Å² (bold). Isosurface value at 0.008 a.u. Hydrogen atoms omitted for better visualization

In case of the thia-substituted (corrolato)gold complexes the attachment of methyl substituents to the β -positions leads to a strong stabilization of the b_1 , which correspond to the $5d_{x^2-y^2}$ orbital, by 0.06 eV for ²[24-17-27]⁰, 2.08 eV for ²[21-17-26]⁰ and 2.13 eV for ²[21-17-25]⁰. This is accompanied by a strong destabilization of the corrole-centered molecular orbitals b_2 (−0.04 eV, +1.95 eV, +2.03 eV) (Figure S5). This results results in the metal-centered b_1 molecular orbitals being energetically located below the ligand-centered molecular orbitals and a significant localization of the Mulliken spin density onto the gold atom (0.121 for ²[24-17-27]⁰, 0.205 ²[24-17-26]⁰, 0.215 ²[24-17-25]⁰). The gold-nitrogen distances are successively increased from 2.028/2.027/2.001/1.991 Å, 2.054/2.046/2.026/2.016 Å to 2.065/2.054/2.037/2.024 Å. The significant localization of the Mulliken spin density onto the gold

3.3 | Pushing Molecular Orbitals to Higher Energy – A DFT Study on the Spin Distribution in Gold Corrole Complexes

atom leads to stronger *out-of-plane* distortions compared with those (corrolato)gold complexes having the Mulliken spin density delocalized over the corrolato ligand (Figure 3.19)

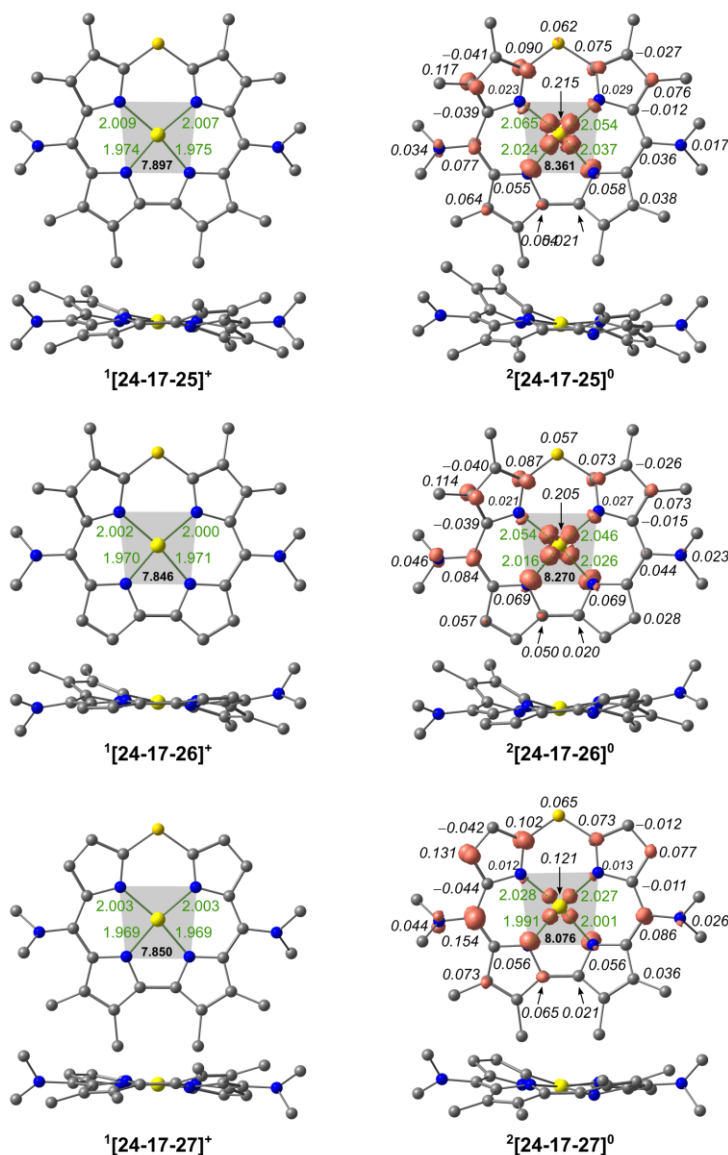


Figure 3.19 DFT geometry optimized structures of selected C10-thia-substituted (corrolato)gold complexes in their singlet- and doublet ground states. Mulliken spin density given in italics. Gold-nitrogen distances given in Å. $[AuN_4]$ cavity size given in Å² (bold). Isosurface value at 0.008 a.u. Hydrogen atoms omitted for better visualization

3.3.3 Conclusion

This comprehensive quantum chemical study investigated the influence of electron-donating *meso*-(aryl) substituents on the energy of the ligand-centered frontier molecular orbitals of (corrolato)gold complexes in their singlet and doublet ground states, the localization of the Mulliken spin density and the accompanied macrocyclic *out-of-plane* distortions. The HOMO/LUMO energies are only marginally changed in energy upon attachment of electron donating *meso*-aryl substituents. The Mulliken spin density remains on the ligand to the exclusion of the gold center. The redistribution of the Mulliken spin density upon substitution of the methine carbene atoms with oxygen or sulfur from the ligand to the gold

CHAPTER 3 | Results and Discussion

center is based on the larger $[\text{AuN}_4]$ cavity due to geometric distortions of the corrolato ligand and additional implementation of bulky substituents causing steric hindrance and strong *out-of-plane* distortions, rather than the result of the inductive energetic destabilization of the ligand-centered LUMOs.

This study further underlined the privileged electronic and geometric features of *meso*-tetraphenylporphyrin for a molecular stabilization of mononuclear gold(II). However, the corrolato ligand is – as frequently described in the literature – a competent ligand for the stabilization of the high-valent metal ions due to its trianionic nature and low-lying frontier molecular orbitals.

4 Summary and Outlook

This work accepted various challenges regarding the synthesis, spectroscopic and theoretical investigation of mono- and binuclear tetraaza gold complexes in their oxidation states +III and +II. Particularly, the research in the area of tetraaza gold(II) complexes is still in its early stages. Therefore, various experimental and theoretical approaches, both for the generalization and the transferability of this concept, have been scrutinized.

The first project addressed the synthesis and (spectro)electrochemical characterization of the tetraaza β (diiminato)gold(III) complex and its evaluation as potential precursor for a mononuclear gold(II) complex. The β (diiminato) ligand bears the same local square-planar tetraaza coordination environment as its big sibling porphine, which had already been proved in the stabilization of mononuclear gold(II). The β (diiminato)gold(III) complex exhibited a quasi-reversible two-electron reduction at -2.06 V vs. FcH/FcH⁺ and a decreasing ratio of the anodic and cathodic peak currents with decreasing scan rate implicating the kinetic lability of the gold(III) complex upon first electroreductions. This reduction became irreversible when the third reduction at -2.68 V was addressed, demonstrating the entire decomposition of the gold(III) complex upon twofold reduction under these conditions. The *in situ* chemical reduction of the gold(III) complex with potassium graphite or sodium anthracenide did not yield an EPR active species as it would be expected for a paramagnetic d⁹ gold(II) complex. The ¹H NMR spectrum of the final products of the chemical reduction of the gold(III) complex with one equivalent potassium graphite exhibited resonances, which could be assigned to the gold(III) complex and the pro-ligand in a ratio of 2:1. The absorption spectrum of the same reaction solution was consistent with the sum absorption spectrum assuming a 2:1 ratio of the gold(III) complex and pro-ligand. The DFT geometry-optimized structure of the gold(II) complex exhibited a slight distortion and spin densities located onto the gold center and equally distributed over the coordinating nitrogen atoms. However, the monoanionic complex showed a high distortion with genuine gold(I) in an almost linear coordination environment provided by two nitrogen atoms from the ligand and susceptible for disproportionation into gold(0) and gold(III).

The aforementioned experimental and theoretical findings necessitate further modifications of the β (diiminato) backbone with respect to the redox-innocence and geometric rigidity.

CHAPTER 4 | Summary and Outlook

A The first strategy involves the implementation of polycyclic aromatic hydrocarbons, such as benzyl or naphthyl, to the macrocyclic tetraaza prototype between the positions 2 and 3 (Figure 4.1). The resulting bis(benzo) or bis(naphthalene) ligands could possibly participate in redox-processes and accommodate an electron in the context of the equilibrium between the two valence isomers of the gold(II) bis(naphthalene) and gold(III) bis(naphthalene) π radical anion.

The ligand syntheses of the bis(benzo) and bis(naphthalene) ligands have been described in the literature according to the synthesis of their prototype $[\text{Au}^{\text{III}}\text{L}]^+$. The synthesis of the bis(anthracene) ligand could be performed accordingly (Figure 1.22).^{98,111,176} The electronic finetuning of the ligand-based frontier orbitals could be achieved by the attachment of electron-withdrawing substituents such as $-\text{NO}_2$, $-\text{Cl}$ or $-\text{Br}$.

This approach would presumptively effect the electrochemical properties of the complex. The high geometric flexibility would be preserved, however, it could prevent the formation of a gold(I) species due to a ligand-centered second reduction and the associated irreversible follow-up reactions. The reduction potentials of the free-ligands $\text{H}_2\text{L}^{\text{B}}$ and $\text{H}_2\text{L}^{\text{N}}$ were reported as -2.00 V and -1.52 V, respectively (acetonitrile, vs. FcH/FcH^+). The reduction potentials for the copper(II) complex CuL^{N} are -1.30 V ($\text{Cu}^{\text{II/I}}$), -1.65 V (ligand-centered) and -1.8 V ($\text{Cu}^{\text{I/0}}$).^{177,178}

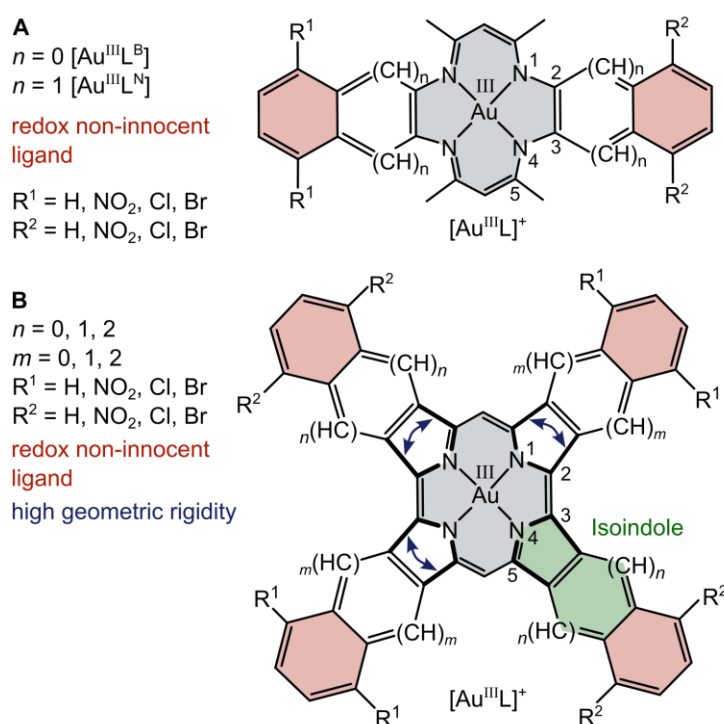


Figure 4.1 Prospective conceptual ligand design strategies for the β (diiminato)gold(III) complex.

The geometries of the benzo- and naphtho condensated β (diiminato)gold complexes were optimized by DFT methods (Figure 4.2, B3LYP functional, TZVPP basis set, SARC-ZORA-TZVPP(Au), dispersion and relativistic correction, continuum solvent). In both cases, the spin density is located onto the gold

atoms (0.211 and 0.229, respectively) under involvement of the coordinating nitrogen atoms (0.048/0.047/0.047/0.048 and 0.062/0.062/0.062/0.063) and the carbon atoms of the acetylacetonato fragment (0.121/0.120/0.119/0.120 and 0.108/0.108/0.107/0.106). The gold-nitrogen distances are slightly shorter compared with Au^{III}L (2.104 Å), probably due to the lower spin density and therefore less anti-bonding character of the gold-nitrogen bond.

Based on DFT calculations, the second reduction to the monoanionic complexes [AuL^B]⁻ and [AuL^B]⁻ under formation of a formal gold(I) species is favoured over a second ligand-centered reduction by 0.76 eV and 0.40 eV, respectively. The gold-nitrogen distances are enlarged (2.073/2.073/2.072/2.074 and 2.077/2.076/2.077/2.077 Å), the strong deformation of the ligand, as calculated for [AuL]⁻, is not present – probably due to the overall ligand rigidity conferred by the benzo- and naphthyl cycles. This more rigid complex geometry could suppress the formation of gold(I), subsequent irreversible follow-up reactions and allow for a spectroscopic detection of a gold(II) signature.

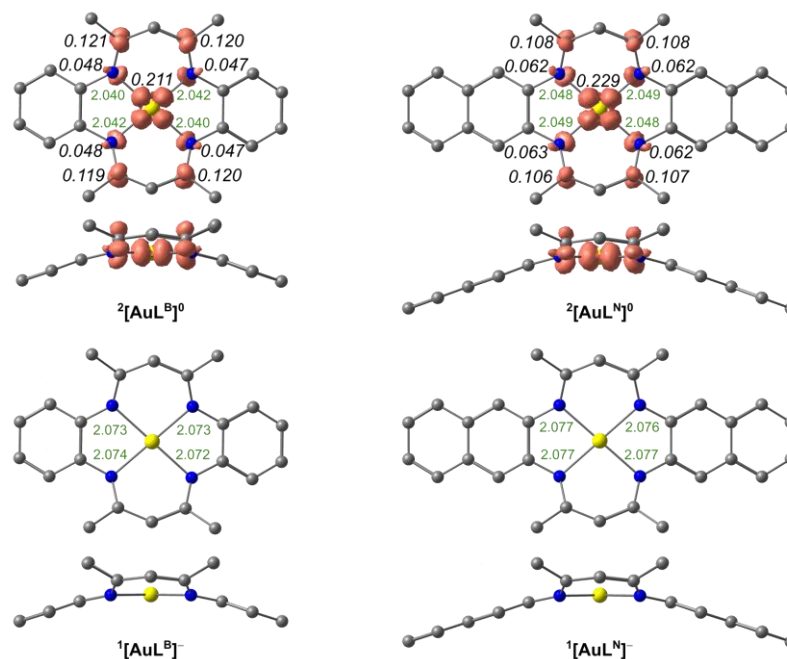


Figure 4.2 DFT geometry-optimized structures (including spin density plots) of derivatives of the β (diiminato)gold complex $^{1/2}[\text{AuL}]^{+/-}$ in its doublet and singlet ground states. Hydrogen atoms omitted for better visualisation. Isosurface value at 0.008 a.u.

B The second concept concerns both the electrochemical and geometric properties of the [Au^{III}]⁺ prototype. The highly distorted geometry of the [Au^IL]⁻ complex has been primarily reflected, based on the DFT-optimized geometry, in the mutual twisting of the C⁴-C³ and C⁴-C⁵ bonds. The implementation of isoindole-type moieties between the positions 3 and 5 could confer the complex both a higher (axial) stability and electrochemical properties analogous to concept A. The synthesis could be performed starting from 2,2'-diyrrole,¹⁷⁹ subsequent one-pot reaction with an appropriate aldehyde^{180,181} followed by oxidation and subsequent metallation.¹⁶⁸

CHAPTER 4 | Summary and Outlook

In the second subproject, the synthesis of the novel “Pacman”-like bis(porphyrinato)gold(III) complex was realized. This type of porphyrin arrangement should allow first insights into the class of binuclear genuine gold complexes without direct gold-gold bond.

The free-base bis(porphyrin) ligand was obtained in a multistep synthesis, subsequent auration was accomplished according to Fleischer’s procedure using potassium tetrachlorido aurate as gold(III) precursor. The parent mononuclear (octaethylporphyrinato)gold(III) complex was synthesized for comparison reasons.

The bis(porphyrinato)gold(III) complex showed a single slightly bathochromically shifted Soret band, compared to the Soret band of the mononuclear (porphyrinato)gold(III) complex, indicating weak ground-state excitonic interactions between both porphyrin subunits at room temperature, whereas significant excitonic coupling is observed at 77 K in frozen solution. The cyclic voltammogram of the bis(porphyrinato)gold(III) complex showed a single two-electron reduction wave with no visible separation. This confirmed the absence of any ground state electronic communication between both gold centers and a description of the mixed-valent $\text{Au}^{\text{II}}/\text{Au}^{\text{III}}$ complex as Robin-Day class I system. However, the electrochemical data revealed a high thermodynamic stability of the mono-valent $\text{Au}^{\text{II}}/\text{Au}^{\text{II}}$ bis(porphyrin) complex, which is reflected in the low disproportionation constant of $K_{\text{Dis}} = 1.5 \cdot 10^{-11}$. The absorption spectrum of the two-fold reduced complex shows an intensity-reduced and bathochromically shifted Soret band confirming the gold-centered reductions. The additional very weak absorption bands between 600 and 800 nm suggest, based on TDDFT calculations, a bridge-mediated electron transfer rather than a direct gold-to-gold electron transfer. The X-band EPR spectra of the $\text{Au}^{\text{II}}/\text{Au}^{\text{III}}$ and $\text{Au}^{\text{II}}/\text{Au}^{\text{II}}$ brought the spectroscopic evidence for gold-centered reductions. The spectra were dominated by broad resonances due to the hyperfine coupling to a single ^{197}Au nucleus and superhyperfine couplings to the four ^{14}N nuclei of the coordinating nitrogen atoms. The presence of the equilibrium between the valence isomers of a gold(II) porphyrin and gold(III) porphyrin π radical anion was apparent in the sharp resonance at around $g=2$. Onefold chemical reduction with cobaltocene yielded the 1:1 mixture between the diamagnetic $[\text{Au}_2(\text{DPD})]^{2+}$ and paramagnetic $\text{Au}_2(\text{DPD})$ complexes, yielding the half intensity of the EPR signal compared with the reaction solution upon reduction with two equivalents cobaltocene. Both the binuclear and mononuclear gold(III) complex showed weak phosphorescence with lifetimes in the nanosecond range at room temperature and microsecond range in frozen solution at 77 K.

The promising results from the synthesis and spectroscopic characterization of the novel bis(porphyrinato)gold(III) complex should not remain at this stage and could serve as the starting point for a series of further investigations. These initially involve further spectroscopic and structural studies

on this complex, followed by potential applications, and in the long term, the synthesis of ligand-modified bis(porphyrinato)gold(III) complexes. These approaches are described below.

The neutral bis(porphyrinato)gold(II) $\text{Au}_2(\text{DPD})$ features, based on electrochemical analyses, a high thermodynamic stability and should be therefore synthetically accessible and isolable. This could be used for the study of the reactivity towards small molecules like oxygen. The ground electronic ground state with two independent paramagnetic gold-centers could facilitate a concerted ground-state activation of oxygen similar to Nocera's complex.⁸³

The high axial flexibility of the dibenzofuran spacer allows for further reactivity studies towards main group elements (sulfur, phosphorus, iodine) as well as Brønsted acids or bases. The coordination of a halide to one or two gold(II) atoms – either from inside the cavity or from outside – would be reflected in a different coupling pattern in the EPR spectra.

Temperature-dependent EPR- or NMR spectroscopy could give information about the inner-sphere electron transfer rate, concentration-dependent EPR- or NMR spectroscopy could give information about the outer-sphere electron transfer rate.

The use of a different rigid spacer such as xanthene or anthracene could facilitate a more closed form of the bis(porphyrin) complex and allow for comparative studies regarding the dibenzofuran anchored bis(porphyrinato)gold complexes.

Ethane- or ethene-bridged bis(porphyrinato)gold complexes in different oxidation states could be used for the study of possible metallophilic interactions analogous to the copper- and silver complexes synthesized by the groups of Rath and Nocera.^{28,91–93,95}

Gold(III) porphyrins have been implemented as electron acceptor upon photoinduced electron transfer in donor-acceptor dyads. The charge-shifted state was long enough to undergo a bimolecular reaction with a sacrificial electron donor yielding the zinc(II)-porphyrin-gold(II) porphyrin state, which has been used for the catalytic reduction of an aromatic azide to the aniline derivative. The cofacial “Pacman” and the linear “donor-acceptor” concept could be combined by the synthesis of a cofacial bis(porphyrinato)gold(III) complex bearing amide-linked (porphyrinato)zinc(II) moieties at each *meso*-position trans to the bridge (Figure 4.3). This could facilitate a concerted photoinduced electron transfer from both zinc(II) porphyrin subunits to both gold(III) porphyrin moieties resulting in a twofold charge-shifted state. This could be further used for a concerted activation of a small molecule such as oxygen. This purpose requires a rigid spacer with large bite angle between both bis[bis(porphyrin)] subunits to prevent energy transfer between both zinc(II) porphyrin chromophores. The rates of the forward- and back electron transfer and therefore lifetime of the charge-shifted state could be influenced by electron-withdrawing and -donating *meso*-arylsubstituents.⁵⁴

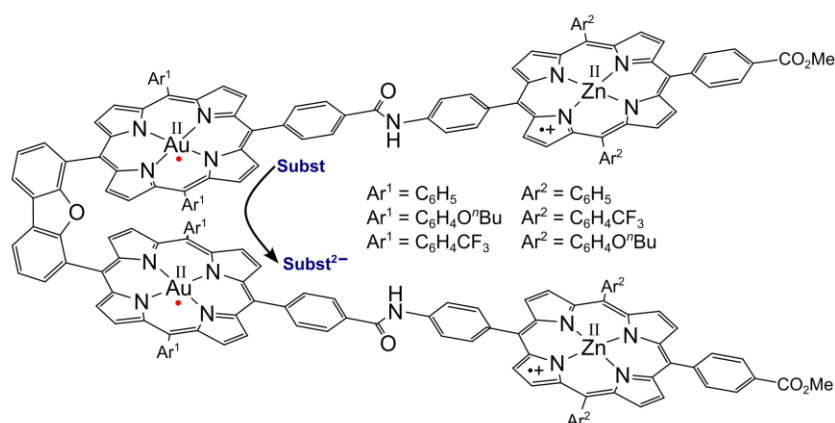


Figure 4.3 Molecular structure of the proposed dibenzofuran-bridged bis[bis(porphyrin)] complex in its charge-shifted state.

The third subproject – applying density function theory methods – addressed the question whether electron-donating *meso*-(aryl)substituents attached to the (corrolato)gold scaffold could induce an energetic destabilization of the ligand-centered lowest unoccupied molecular orbitals and energetic alignment to the gold-centered unoccupied atomic orbital to succeed in a redistribution of the Mulliken spin density from the ligand under involvement of the gold center. The corrolato-centered frontier molecular orbitals exhibited a high insensitivity towards the electron-donating since they were only marginally raised in energy. However, the implementation of bulky aryl-substituents led to strong *out-of-plane* distortions – dominated by waving x and doming – due to steric hindrance. The replacement of one methine-bridge with oxygen (oxa) or sulfur (thia) – inducing the expansion of the tetraaza cavity and the energetic stabilization of the $5d_{x^2-y^2}$ orbital – and the attachment of methyl groups to the β -positions entailed a gold-involved Mulliken spin density up to 22%. The geometries of these complexes were strongly distorted and dominated by saddling.

In summary, the outcome of this work underlined the extraordinary geometric and electronic properties of the porphyrinato ligand for the molecular stabilization of gold(II). The applicability of the porphyrin's scaffold for this purpose seems to be essentially unperturbed by the exact electronic nature of the substituents and even by the presence of a second covalently linked (porphyrinato)gold(II) moiety. The combination of rigidity and energetically favourable-lying molecular orbitals is the ideal periphery for mononuclear gold in the oxidation state +II. The β (diiminato) ligand does not meet these criteria due to its higher flexibility and inability to accommodate an electron as required for a reversible equilibrium between the valence isomers.

The strong destabilization of the gold's orbital, caused by the intrinsically high ligand field splitting, as well as the small corrolato tetraaza cavity, accompanied by a high insensitivity to the electronic influence of substituents, makes a gold-centered reduction unlikely.

However, the high stability of the porphyrin's liaison with gold(II) allows for a tailored conceptional ligand design with prospective applications in the field of (photoredox) catalysis in the short term or fundamental research – the means of curiosity and the foundation for applications in the long term.

5 References

- [1] W. Kaim, B. Schwederski, A. Klein, *Bioinorganic Chemistry: Inorganic Elements in the Chemistry of Life*, WILEY-VCH, Weinheim, **2013**.
- [2] J. C. Kendrew, G. Bodo, H. M. Dintzis, R. G. Parrish, H. Wyckoff, D. C. Phillips, *Nature* **1958**, *181*, 662–666.
- [3] M. F. Perutz, M. G. Rossmann, A. F. Cullis, H. Muirhead, G. Will, A. C. North, *Nature* **1960**, *185*, 416–422.
- [4] J.-H. Fuhrhop, *Angew. Chem. Int. Ed.* **1974**, *13*, 321–335.
- [5] J. Deisenhofer, O. Epp, K. Miki, R. Huber, H. Michel, *Nature* **1985**, *318*, 618–624.
- [6] P. G. Lenhert, D. C. Hodgkin, *Nature* **1961**, *192*, 937–938.
- [7] H. Fischer, W. Gleim, *Justus Liebigs Ann. Chem.* **1936**, *521*, 157–160.
- [8] S. Hiroto, Y. Miyake, H. Shinokubo, *Chem. Rev.* **2017**, *117*, 2910–3043.
- [9] J. F. B. Barata, M. G. P. M. S. Neves, M. A. F. Faustino, A. C. Tomé, J. A. S. Cavaleiro, *Chem. Rev.* **2017**, *117*, 3192–3253.
- [10] J. K. M. Sanders, N. Bampos, Z. Clyde-Watson, S. L. Darling, J. C. Hawley, Kim, H.-J., Mak, C. C., Webb, S. J., *The Porphyrin Handbook*, Academic Press, New York, **2000**.
- [11] G. P. Moss, *Pure Appl. Chem.* **1987**, *59*, 779–832.
- [12] E. Vogel, *Pure Appl. Chem.* **1993**, *65*, 143–152.
- [13] P. Schaeffer, R. Ocampo, H. J. Callot, P. Albrecht, *Nature* **1993**, *364*, 133–136.
- [14] A. Mahammed, J. J. Weaver, H. B. Gray, M. Abdelas, Z. Gross, *Tetrahedron Lett.* **2003**, *44*, 2077–2079.
- [15] S. Liu, K. Mase, C. Bougher, S. D. Hicks, M. M. Abu-Omar, S. Fukuzumi, *Inorg. Chem.* **2014**, *53*, 7780–7788.
- [16] T. Pain, S. Mondal, S. Jena, D. Dutta Gupta, H. S. Biswal, S. Kar, *ACS Omega* **2022**, *7*, 28138–28147.
- [17] H.-Y. Liu, F. Yam, Y.-T. Xie, X.-Y. Li, C. K. Chang, *J. Am. Chem. Soc.* **2009**, *131*, 12890–12891.

CHAPTER 5 | References

- [18] H. Shi, R. Liang, D. L. Phillips, H. K. Lee, W.-L. Man, K.-C. Lau, S.-M. Yiu, T.-C. Lau, *J. Am. Chem. Soc.* **2022**, *144*, 7588–7593.
- [19] P. Leeladee, G. N. L. Jameson, M. A. Siegler, D. Kumar, S. P. de Visser, D. P. Goldberg, *Inorg. Chem.* **2013**, *52*, 4668–4682.
- [20] W. Sinha, A. Mahammed, N. Fridman, Z. Gross, *ACS Catal.* **2020**, *10*, 3764–3772.
- [21] D. K. Dogutan, S. A. Stoian, R. McGuire, M. Schwalbe, T. S. Teets, D. G. Nocera, *J. Am. Chem. Soc.* **2011**, *133*, 131–140.
- [22] N. I. Neuman, U. Albold, E. Ferretti, S. Chandra, S. Steinhauer, P. Rößner, F. Meyer, F. Doctorovich, S. E. Vaillard, B. Sarkar, *Inorg. Chem.* **2020**, *59*, 16622–16634.
- [23] K. Sudhakar, A. Mahammed, Q.-C. Chen, N. Fridman, B. Tumanskii, Z. Gross, *ACS Appl. Energy Mater.* **2020**, *3*, 2828–2836.
- [24] Y. K. Maurya, K. Noda, K. Yamasumi, S. Mori, T. Uchiyama, K. Kamitani, T. Hirai, K. Ninomiya, M. Nishibori, Y. Hori, Y. Shiota, K. Yoshizawa, M. Ishida, H. Furuta, *J. Am. Chem. Soc.* **2018**, *140*, 6883–6892.
- [25] K. E. Thomas, H. Vazquez-Lima, Y. Fang, Y. Song, K. J. Gagnon, C. M. Beavers, K. M. Kadish, A. Ghosh, *Chem. Eur. J.* **2015**, *21*, 16839–16847.
- [26] W. Sinha, M. G. Sommer, N. Deibel, F. Ehret, M. Bauer, B. Sarkar, S. Kar, *Angew. Chem. Int. Ed.* **2015**, *54*, 13769–13774.
- [27] C. Brückner, C. A. Barta, R. P. Briñas, J. A. Krause Bauer, *Inorg. Chem.* **2003**, *42*, 1673–1680.
- [28] C. M. Lemon, D. C. Powers, M. Huynh, A. G. Maher, A. A. Phillips, B. P. Tripet, D. G. Nocera, *Inorg. Chem.* **2023**, *62*, 3–17.
- [29] B. Patra, S. Sobottka, W. Sinha, B. Sarkar, S. Kar, *Chem. Eur. J.* **2017**, *23*, 13858–13863.
- [30] A. B. Alemayehu, N. U. Day, T. Mani, A. B. Rudine, K. E. Thomas, O. A. Gederaas, S. A. Vinogradov, C. C. Wamser, A. Ghosh, *ACS Appl. Mater. Interfaces* **2016**, *8*, 18935–18942.
- [31] W. Sinha, M. G. Sommer, M. van der Meer, S. Plebst, B. Sarkar, S. Kar, *Dalton Trans.* **2016**, *45*, 2914–2923.
- [32] R. D. Teo, H. B. Gray, P. Lim, J. Termini, E. Domeshek, Z. Gross, *Chem. Commun.* **2014**, *50*, 13789–13792.
- [33] A. B. Alemayehu, A. Ghosh, *J. Porphyrins Phthalocyanines* **2011**, *15*, 106–110.

- [34] K. Sahu, S. Angeloni, J. Conradie, M. Villa, M. Nayak, A. Ghosh, P. Ceroni, S. Kar, *Dalton Trans.* **2022**.
- [35] K. E. Thomas, A. B. Alemayehu, J. Conradie, C. Beavers, A. Ghosh, *Inorg. Chem.* **2011**, *50*, 12844–12851.
- [36] K. E. Thomas, C. M. Beavers, A. Ghosh, *Mol. Phys.* **2012**, *110*, 2439–2444.
- [37] K. E. Thomas, K. J. Gagnon, L. J. McCormick, A. Ghosh, *J. Porphyrins Phthalocyanines* **2018**, *22*, 596–601.
- [38] C. M. Lemon, D. C. Powers, P. J. Brothers, D. G. Nocera, *Inorg. Chem.* **2017**, *56*, 10991–10997.
- [39] K. Sudhakar, A. Mizrahi, M. Kosa, N. Fridman, B. Tumanskii, M. Saphier, Z. Gross, *Angew. Chem. Int. Ed.* **2017**, *56*, 9837–9841.
- [40] S.-L. Lai, L. Wang, C. Yang, M.-Y. Chan, X. Guan, C.-C. Kwok, C.-M. Che, *Adv. Funct. Mater.* **2014**, *24*, 4655–4665.
- [41] Y. Deng, C. J. Chang, D. G. Nocera, *J. Am. Chem. Soc.* **2000**, *122*, 410–411.
- [42] H. Günther, *NMR Spectroscopy. Basic Principles, Concepts, and Applications in Chemistry*, WILEY-VCH, Weinheim, **2013**.
- [43] M. Gouterman, *J. Chem. Phys.* **1959**, *30*, 1139–1161.
- [44] M. Gouterman, *J. Mol. Spectrosc.* **1961**, 138–163.
- [45] M. Gouterman, G. H. Wagniere, *J. Mol. Spectrosc.* **1963**, 108–127.
- [46] S. Preiß, J. Melomedov, A. Wünsche von Leupoldt, K. Heinze, *Chem. Sci.* **2016**, *7*, 596–610.
- [47] P. J. Spellane, M. Gouterman, A. Antipas, S. Kim, Y. C. Liu, *Inorg. Chem.* **1980**, *19*, 386–391.
- [48] K. S. Suslick, R. A. Watson, *New. J. Chem.* **1992**, 633–642.
- [49] A. Antipas, D. Dolphin, M. Gouterman, E. C. Johnson, *J. Am. Chem. Soc.* **1978**, *100*, 7705–7709.
- [50] W. R. Osterloh, J. Conradie, A. B. Alemayehu, A. Ghosh, K. M. Kadish, *ACS Org. Inorg. Au* **2023**, *3*, 35–40.
- [51] A. Dhamija, P. Mondal, B. Saha, S. P. Rath, *Dalton Trans.* **2020**, *49*, 10679–10700.
- [52] F. Bolze, C. P. Gros, M. Drouin, E. Espinosa, P. D. Harvey, R. Guillard, *J. Organomet. Chem.* **2002**, *643-644*, 89–97.
- [53] V. Balzani, P. Ceroni, A. Juris, *Photochemistry and Photophysics. Concepts, Research, Applications*, 1. Aufl., WILEY-VCH, Weinheim, **2014**.

CHAPTER 5 | References

- [54] S. Preiß, A. Pöpcke, L. Burkhardt, L. Großmann, S. Lochbrunner, M. Bauer, T. Opatz, K. Heinze, *Chem. Eur. J.* **2019**, *25*, 5940–5949.
- [55] E. Göransson, J. Boixel, J. Fortage, D. Jacquemin, H.-C. Becker, E. Blart, L. Hammarström, F. Odobel, *Inorg. Chem.* **2012**, *51*, 11500–11512.
- [56] S. Fukuzumi, K. Ohkubo, W. E. Z. Ou, J. Shao, K. M. Kadish, J. A. Hutchison, K. P. Ghiggino, P. J. Sentic, M. J. Crossley, *J. Am. Chem. Soc.* **2003**, *125*, 14984–14985.
- [57] M. P. Eng, T. Ljungdahl, J. Andreasson, Martensson, Jerker, Albinsson, Bo, *J. Phys. Chem. A* **2005**, 1776–1784.
- [58] S. G. Telfer, T. M. McLean, M. R. Waterland, *Dalton Trans.* **2011**, *40*, 3097–3108.
- [59] E. E. Jelley, *Nature* **1936**, *138*, 1009–1010.
- [60] W. Jentzen, J. G. Ma, J. A. Shelnut, *Biophysical journal* **1998**, *74*, 753–763.
- [61] W. Jentzen, X.-Z. Song, J. A. Shelnut, *J. Phys. Chem.* **1997**, 1684–1699.
- [62] J. Krumsieck, M. Bröring, *Chem. Eur. J.* **2021**, 11580–11588.
- [63] Nobel Lectures, *Chemistry 1922-1941*, Elsevier Publishing Company, Amsterdam, **1966**.
- [64] Nobel Lectures, *Chemistry 1942-1962*, Elsevier Publishing Company, Amsterdam, **1964**.
- [65] F. P. Guengerich, *J. Biol. Chem.* **1991**, *266*, 10019–10022.
- [66] T. Förster, *Ann. Phys.* **1948**, *437*, 55–75.
- [67] D. Gerster, J. Reichert, H. Bi, J. V. Barth, S. M. Kaniber, A. W. Holleitner, I. Visoly-Fisher, S. Sergani, I. Carmeli, *Nat. Nanotechnol.* **2012**, *7*, 673–676.
- [68] I. Ishigami, R. G. Sierra, Z. Su, A. Peck, C. Wang, F. Poitevin, S. Lisova, B. Hayes, F. R. Moss, S. Boutet, R. E. Sublett, C. H. Yoon, S.-R. Yeh, D. L. Rousseau, *Nat. Commun.* **2023**, *14*, 5752.
- [69] J. Castresana, M. Lübber, M. Saraste, D. G. Higgins, *EMBO J.* **1994**, *13*, 2516–2525.
- [70] A. G. Khan, S. V. Eswaran, *Resonance* **2003**, *8*, 8–16.
- [71] J. S. Lindsey, *Acc. Chem. Res.* **2010**, *43*, 300–311.
- [72] G. P. Arsenault, E. Bullock, S. F. MacDonald, *J. Am. Chem. Soc.* **1960**, *82*, 4384–4389.
- [73] T. D. Lash, *J. Porphyrins Phthalocyanines* **2016**, *20*, 855–888.
- [74] M. O. Senge, N. N. Sergeeva, K. J. Hale, *Chem. Soc. Rev.* **2021**, *50*, 4730–4789.
- [75] S. Hiroto, Y. Miyake, H. Shinokubo, *Chem. Rev.* **2017**, *117*, 2910–3043.

- [76] D. H.R. Barton, J. Kervagoret, S. Z. Zard, *Tetrahedron* **1990**, *46*, 7587–7598.
- [77] J. L. Sessler, A. Mozaffari and M. R. Johnson, *Org. Synth.* **1992**, *70*, 68.
- [78] H. H. Inhoffen, J.-H. Fuhrhop, H. Voigt, H. Brockmann, *Justus Liebigs Ann. Chem.* **1966**, *695*, 133–143.
- [79] D. H. R. Barton, S. Z. Zard, *J. Chem. Soc., Chem. Commun.* **1985**, 1098.
- [80] M. G. H. Da Vicente, K. M. Smith, *Curr. Org. Synth.* **2014**, *11*, 3–28.
- [81] J. Rosenthal, D. G. Nocera, *Acc. Chem. Res.* **2007**, *40*, 543–553.
- [82] Z.-H. Loh, S. E. Miller, C. J. Chang, S. D. Carpenter, D. G. Nocera, *J. Phys. Chem.* **2002**, *106*, 11700–11708.
- [83] C. J. Chang, Z.-H. Loh, C. Shi, F. C. Anson, D. G. Nocera, *J. Am. Chem. Soc.* **2004**, *126*, 10013–10020.
- [84] I. V. Avilov, E. I. Zenkevich, E. I. Sagun, I. V. Filatov, *J. Phys. Chem. A* **2004**, *108*, 5684–5691.
- [85] V. Knyukshto, E. Zenkevich, E. Sagun, A. Shulga, S. Bachilo, *Chem. Phys. Lett.* **1998**, *297*, 97–108.
- [86] C. J. Chang, Y. Deng, D. G. Nocera, C. Shi, F. C. Anson, C. K. Chang, *Chem. Commun.* **2000**, 1355–1356.
- [87] T. E. Clement, D. J. Nurco, K. M. Smith, *Inorg. Chem.* **1998**, *37*, 1150–1160.
- [88] D. Arnold, A. W. Johnson, M. Winter, *J. Am. Chem. Soc., Perkin Trans. 1* **1977**, *14*, 1643–1647.
- [89] D. Sil, S. P. Rath, *Dalton Trans.* **2015**, *44*, 16195–16211.
- [90] A. K. Singh, F. S. T. Khan, S. P. Rath, *Angew. Chem.* **2017**, *129*, 8975–8980.
- [91] A. K. Singh, M. Usman, G. Sciortino, E. Garribba, S. P. Rath, *Chem. Eur. J.* **2019**, *25*, 10098–10110.
- [92] A. Kumar, S. Sanfui, G. Sciortino, J.-D. Maréchal, E. Garribba, S. P. Rath, *Chem. Eur. J.* **2020**, *26*, 7869–7880.
- [93] A. K. Singh, S. P. Rath, *Chem. Eur. J.* **2020**, *26*, 14405–14418.
- [94] S. Dey, D. Sil, S. P. Rath, *Angew. Chem. Int. Ed.* **2016**, *128*, 1008–1012.
- [95] S. Dey, S. P. Rath, *Dalton Trans.* **2014**, *43*, 2301–2314.
- [96] D. Sil, S. Dey, A. Kumar, S. Bhowmik, S. P. Rath, *Chem. Sci.* **2016**, *7*, 1212–1223.
- [97] S. Dey, D. Sil, Y. A. Pandit, S. P. Rath, *Inorg. Chem.* **2016**, *55*, 3229–3238.
- [98] R. H. Holm, T. J. Truex, *J. Am. Chem. Soc.* **1971**, *93*, 285–286.

CHAPTER 5 | References

- [99] M. Fujiwara, H. Wakita, I. Masuda, T. Matsushita, T. Shono, *Chem. Lett.* **1986**, *15*, 907–910.
- [100] M. J. S. Dewar, E. F. Healy, J. Ruiz, *Pure Appl. Chem.* **1986**, *58*, 67–74.
- [101] J. C. Medina, N. Gabriunas, E. Páez-Mozo, *J. Mol. Cat. A-Chem.* **1997**, *115*, 233–239.
- [102] Z. Li, S. Wu, Y. Ma, H. Liu, J. Hu, L. Liu, Q. Huo, J. Guan, Q. Kan, *Transition Met. Chem* **2013**, *38*, 243–251.
- [103] J.-P. Costes, *Polyhedron* **1987**, *6*, 2169–2175.
- [104] M. Fujiwara, Y. Nakajima, T. Matsushita, T. Shono, *Polyhedron* **1985**, *4*, 1589–1594.
- [105] K. Sakata, H. Taziri, F. Yamaura, M. Hashimoto, *Synth. React. Inorg. Met.-Org. Chem.* **1990**, *20*, 757–771.
- [106] K. Hussain Reddy, M. Radhakrishna Reddy, K. Mohana Raju, *Polyhedron* **1997**, *16*, 2673–2679.
- [107] M. Fujiwara, T. Matsushita, T. Shono, *Polyhedron* **1984**, *3*, 1357–1363.
- [108] M. Fujiwara, Y. Nakajima, T. Matsushita, T. Shono, *Polyhedron* **1985**, *4*, 1859–1863.
- [109] M. Fujiwara, H. Wakita, T. Matsushita, T. Shono, *Bull. Chem. Soc. Jpn.* **1990**, *63*, 3443–3449.
- [110] T. Tokumitsu, T. Hayashi, *Bull. Chem. Soc. Jpn.* **1981**, *54*, 2348–2351.
- [111] Jong-Ho Kim and Grover W. Everett, Jr., *Inorg. Chem.* **1979**, 3145–3149.
- [112] J.-H. Kim, G. W. Everett, *Inorg. Chem.* **1981**, *20*, 853–856.
- [113] V. A. Afanas'eva, I. V. Mironov, L. A. Glinskaya, R. F. Klevtsova, *Russ. J. Coord. Chem.* **2010**, *36*, 9–21.
- [114] V. A. Afanas'eva, L. A. Glinskaya, R. F. Klevtsova, I. V. Mironov, *Russ. J. Coord. Chem.* **2011**, *37*, 325–332.
- [115] V. A. Afanasieva, L. A. Glinskaya, D. A. Piryazev, S. A. Gromilov, *J. Struct. Chem.* **2015**, *56*, 787–791.
- [116] V. A. Afanas'eva, L. A. Glinskaya, D. A. Piryazev, S. A. Gromilov, P. E. Plyusnin, L. A. Sheludyakova, *Inorg. Chem. Commun.* **2017**, *83*, 70–75.
- [117] Sharon A. Brawner, Ivan J. B. Lin, Jong-Ho Kim, Grover W. Everett Jr., *Inorg. Chem.* **1978**, 1304–1308.
- [118] D. J. Olszanski, G. A. Melson, *Inorg. Chem. Acta* **1977**, *23*, L4-L6.
- [119] S. C. Tang, S. Koch, G. N. Weinstein, R. W. Lane, R. H. Holm, *Inorg. Chem.* **1973**, *12*, 2589–2595.

- [120] B. U. Nair, T. Ramasami, D. Ramaswamy, *Inorg. Chem.* **1986**, *25*, 51–55.
- [121] M. Fujiwara, T. Matsushita, R. Kiraly, E. Brucher, H. Wakita, *Thermochimica Acta* **1992**, *208*, 261–267.
- [122] D. G. Black, D. C. Swenson, R. F. Jordan, R. D. Rogers, *Organometallics* **1995**, *14*, 3539–3550.
- [123] D. G. Black, R. F. Jordan, R. D. Rogers, *Inorg. Chem.* **1997**, *36*, 103–108.
- [124] C.-M. Che, R. W.-Y. Sun, W.-Y. Yu, C.-B. Ko, N. Zhu, H. Sun, *Chem. Commun.* **2003**, 1718–1719.
- [125] P. Pyykko, J. P. Desclaux, *Acc. Chem. Res.* **1978**, 276–281.
- [126] P. Pyykkö, *Annu. Rev. Phys. Chem.* **2012**, *63*, 45–64.
- [127] P. Pyykko, *Chem. Rev.* **1988**, *88*, 563–594.
- [128] J. P. Desclaux, P. Pyykkö, *Chem. Phys. Lett.* **1976**, *39*, 300–303.
- [129] M. C. Gimeno, *The Chemistry of Gold*, WILEY-VCH, Weinheim, **2008**.
- [130] K. Heinze, *Angew. Chem. Int. Ed.* **2017**, *56*, 16126–16134.
- [131] D. B. Dell'Amico, F. Calderazzo, F. Marchetti, S. Merlino, *J. Chem. Soc., Dalton Trans.* **1982**, 2257–2260.
- [132] N. Kojima, M. Hasegawa, H. Kitagawa, T. Kikegawa, O. Shimomura, *J. Am. Chem. Soc.* **1994**, *116*, 11368–11374.
- [133] J. Strähle, J. Gelinek, M. Kölmel, *Z. anorg. allg. Chem.* **1979**, *456*, 241–260.
- [134] W. Denner, H. Schulz, H. d'Amour, *Acta Cryst.* **1979**, *35*, 360–365.
- [135] M. S. Wickleder, *Z. anorg. allg. Chem.* **2001**, *627*, 2112–2114.
- [136] H. Schmidbaur, J. R. Mandl, A. Frank, G. Huttner, *Chem. Ber.* **1976**, 466–472.
- [137] V. W.-W. Yam, S. W.-K. Choi, K.-K. Cheung, *Chem. Commun.* **1996**, 1173–1174.
- [138] D.-A. Roşca, D. A. Smith, D. L. Hughes, M. Bochmann, *Angew. Chem. Int. Ed.* **2012**, *51*, 10643–10646.
- [139] T. Dann, D.-A. Roşca, J. A. Wright, G. G. Wildgoose, M. Bochmann, *Chem. Commun.* **2013**, 49, 10169–10171.
- [140] D.-A. Roşca, M. Bochmann, *Organometallics* **2016**, *35*, 27–31.
- [141] S. Preiß, C. Förster, S. Otto, M. Bauer, P. Müller, D. Hinderberger, H. Hashemi Haeri, L. Carella, K. Heinze, *Nat. Chem.* **2017**, *9*, 1249–1255.

CHAPTER 5 | References

- [142] R. Casado, M. Contel, M. Laguna, P. Romero, S. Sanz, *J. Am. Chem. Soc.* **2003**, *125*, 11925–11935.
- [143] P. Veit, C. Volkert, C. Förster, V. Ksenofontov, S. Schlicher, M. Bauer, K. Heinze, *Chem. Commun.* **2019**, *55*, 4615–4618.
- [144] A. Fürstner, *Chem. Soc. Rev.* **2009**, *38*, 3208–3221.
- [145] A. S. K. Hashmi, *Angew. Chem. Int. Ed.* **2010**, *49*, 5232–5241.
- [146] L.-P. Liu, G. B. Hammond, *Chem. Soc. Rev.* **2012**, *41*, 3129–3139.
- [147] A. S. K. Hashmi, *Acc. Chem. Res.* **2014**, *47*, 864–876.
- [148] J. C. Pérez-Sánchez, R. P. Herrera, M. Concepción Gimeno, *Dalton Trans.* **2024**, *53*, 382–393.
- [149] R. P. Herrera, M. C. Gimeno, *Chem. Rev.* **2021**, *121*, 8311–8363.
- [150] R. Jazzar, M. Soleilhavoup, G. Bertrand, *Chem. Rev.* **2020**, *120*, 4141–4168.
- [151] L. Rocchigiani, M. Bochmann, *Chem. Rev.* **2021**, *121*, 8364–8451.
- [152] L. Huang, M. Rudolph, F. Rominger, A. S. K. Hashmi, *Angew. Chem. Int. Ed.* **2016**, *55*, 4808–4813.
- [153] M. P. Schrick, G. K. Ramollo, C.-M. S. Hirschbiegel, M. Fernandes, A. Lemmerer, C. Förster, D. I. Bezuidenhout, K. Heinze, *Organometallics* **2024**, *43*, 69–84.
- [154] Z. Qu, L. Giurgiu, E. Roduner, *Chem. Commun.* **2006**, 2507–2509.
- [155] N. R. Walker, R. R. Wright, P. E. Barran, A. J. Stace, *Organometallics* **1999**, *18*, 3569–3571.
- [156] N. R. Walker, R. R. Wright, P. E. Barran, J. N. Murrell, A. J. Stace, *J. Am. Chem. Soc.* **2001**, *123*, 4223–4227.
- [157] W. Sinha, M. G. Sommer, N. Deibel, F. Ehret, B. Sarkar, S. Kar, *Chem. Eur. J.* **2014**, *20*, 15920–15932.
- [158] A. J. Blake, J. A. Greig, A. J. Holder, T. I. Hyde, A. Taylor, M. Schröder, *Angew. Chem. Int. Ed.* **1990**, *29*, 197–198.
- [159] J. L. Shaw, J. Wolowska, D. Collison, J. A. K. Howard, E. J. L. McInnes, J. McMaster, A. J. Blake, C. Wilson, M. Schröder, *J. Am. Chem. Soc.* **2006**, *128*, 13827–13839.
- [160] D. Huang, X. Zhang, E. J. L. McInnes, J. McMaster, A. J. Blake, E. S. Davies, J. Wolowska, C. Wilson, M. Schröder, *Inorg. Chem.* **2008**, *47*, 9919–9929.
- [161] L. Xinying, *J. Chem. Phys.* **2012**, *137*, 124301.
- [162] W. P. Hu, C. H. Huang, *J. Am. Chem. Soc.* **2001**, *123*, 2340–2343.

- [163] S. Berski, Z. Latajka, J. Andrés, *Chem. Phys. Lett.* **2002**, 356, 483–489.
- [164] I.-C. Hwang, K. Seppelt, *Z. anorg. allg. Chem.* **2002**, 628, 765.
- [165] S. Seidel, K. Seppelt, *Science* **2000**, 290, 117–118.
- [166] T. Drews, S. Seidel, K. Seppelt, *Angew. Chem. Int. Ed.* **2002**, 41, 454–456.
- [167] K. P. Lindquist, A. Eghdami, C. R. Deschene, A. J. Heyer, J. Wen, A. G. Smith, E. I. Solomon, Y. S. Lee, J. B. Neaton, D. H. Ryan, H. I. Karunadasa, *Nat. Chem.* **2023**, 1–7.
- [168] E. B. Fleischer, A. Laszlo, *Inorg. Nucl. Chem. Lett.* **1969**, 373–376.
- [169] R. A. Marcus, *J. Chem. Phys.* **1956**, 24, 966–978.
- [170] R. A. Marcus, *Angew. Chem. Int. Ed.* **1993**, 1111–1121.
- [171] N. S. Hush, *Coord. Chem. Rev.* **1985**, 64, 135–157.
- [172] B. S. Brunshwig, N. Sutin, *Coord. Chem. Rev.* **1999**, 187, 233–254.
- [173] M. Parthey, M. Kaupp, *Chem. Soc. Rev.* **2014**, 43, 5067–5088.
- [174] M. B. Robin, N. U. Day, *Adv. Inorg. Chem. Radiochem.* **1967**, 10, 247–422.
- [175] D. E. Richardson, H. Taube, *Inorg. Chem.* **1981**, 20, 1278–1285.
- [176] B. P. Block, J. C. Bailar, *J. Am. Chem. Soc.* **1951**, 73, 4722–4725.
- [177] J. Costamagna, G. Ferraudi, M. Villagran, E. Wolcan, *J. Chem. Soc., Dalton Trans.* **2000**, 2631–2637.
- [178] R. Mondal, G. Chakraborty, K. M. van Vliet, N. P. van Leest, B. de Bruin, N. D. Paul, *Inorg. Chem. Acta* **2020**, 500, 119190.
- [179] T. Dohi, K. Morimoto, A. Maruyama, Y. Kita, *Org. Lett.* **2006**, 8, 2007–2010.
- [180] X. Songlin, L. Xiaojuan, X. Bentian, D. Yuting, CN116375720A.
- [181] E. Kimura, Y. Kurogi, T. Koike, M. Shionoya, Y. Iitaka, *J. Coord. Chem.* **1993**, 28, 33–49.

6 Appendix

- 6.1 Supporting Information to 3.1: 14-Membered Macrocyclic beta-Diiminato Gold(II) – A New Member for the Gold(II) Complex Family?

Chemistry–A European Journal

Supporting Information

14-Membered Macrocyclic β -Diiminato Gold(II) – A New Member for the Gold(II) Complex Family?

Lukas Sorge, Julian Link, and Katja Heinze*

6.1 | Supporting Information to 3.1: 14-Membered Macrocyclic beta-Diiminato Gold(II) – A New Member for the Gold(II) Complex Family?

1. Methods

General procedures. All reagents were used as received from commercial suppliers (ABCR, AcrosOrganics, AlfaAesar, Fischer, Sigma-Aldrich and TCI). DMSO, DMF and 2-MeTHF were received dried, degassed with argon and stored over molecular sieves. All reactions and measurements were performed under an argon and water-free atmosphere unless otherwise noted. A glovebox (UniLab/MBraun–Ar 5.0, O₂ < 0.1 ppm, H₂O < 0.1 ppm) was used to store and weigh sensitive compounds for synthesis as well as to prepare samples that required the absence of oxygen and/or water.

NMR spectra were recorded on a Bruker AV2-400 spectrometer at 400 MHz for ¹H, 100.61 MHz for ¹³C, 56.76 MHz for ¹⁹F and 161.97 MHz for ³¹P NMR spectra. All signals are given in ppm and referenced against the solvent signal as internal standard (*d*₆-DMSO: 1H: δ = 2.50 ppm, ¹³C: δ = 39.52 ppm) or H₃PO₄ (85%) (δ = 0.00 ppm) or CFCl₃ (δ = 0.00 ppm) as external standard. (s) = singlet, (sept.) = septett.

ESI mass spectra were recorded on an Agilent 6545 QTOF MS mass spectrometer.

The **ATR IR spectrum** was recorded on an Agilent Cary 630 FTIR spectrometer with an ATR unit containing a diamond crystal. The intensities are qualitatively indicated with weak (w), medium (m) and strong (s).

Electrochemical experiments were carried out on a BioLogic SP-200 voltammetric analyzer using platinum wire as counter- and working electrodes and 0.01 M Ag/AgNO₃ as the reference electrode. The measurements were carried out at scan rates of 50, 100, 200, 400, 600 or 800 mV s⁻¹ for cyclic voltammetry experiments using 0.1 M [^tBu₄N][PF₆] as supporting electrolyte and 1 mM of the [AuL][PF₆] in DMSO or a mixture of DMSO:DMF:2-MeTHF 1:5:5 (v/v). Potentials are referenced to the ferrocene/ferrocenium couple.

Spectroelectrochemical experiments were carried out using a TSC 1600 closed measuring cell from RHD Instruments. Glassy carbon was used as counter electrode, a silver wire as pseudo reference electrode and a platinum mesh as working electrode. A J&M TIDAS S MMS was used as UV/Vis/NIR detector, a Hamamatsu L10290 as excitation source.

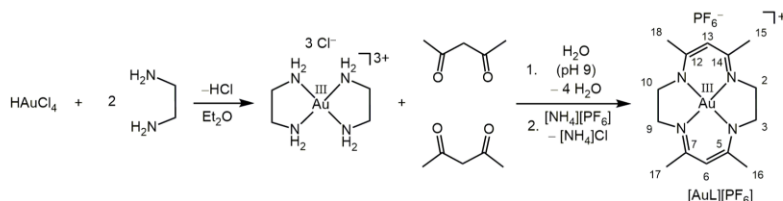
Absorption spectra were recorded on a Jasco V770 spectrometer using 1.0 cm quartz cells with a Schott valve to maintain an inert atmosphere.

X-band EPR spectra were recorded on a Magnetech MS 300 at 77 K or at room temperature. Samples were cooled with liquid nitrogen in a finger dewar (Magnetech).

Density functional theory calculations were carried out using the ORCA program package 5.0.3.^[1] The DFT calculations were performed using the B3LYP functional^[2,3] employing the *RIJCOSX* approximation.^[4] Tight convergence criteria were chosen for DFT-UKS calculations (keywords *tightscf* and *tightopt*). Relativistic effects were calculated at the zeroth order regular approximation (keyword *ZORA*) level.^[5] To account for solvent effects, a conductor-like screening model (keyword *CPCM*) modeling DMSO was used in all calculations.^[6] For a higher accuracy for the gold atom the keyword *SpecialGridIntAcc 7* for the gold atom was used.^[7,8] Atom pair-wise dispersion correction was performed with the Becke-Johnson damping scheme (keyword *D3BJ*).^[9,10] Geometry optimizations were performed using Ahlrichs' polarized valence triple- ζ basisset def2-TZVPP^[11] recontracted by Pantazis^[12] and the SARC/J auxiliary basis.^[13] The energy of the electronic states and the presence of energy minima were checked by numerical frequency calculations. Explicit counterions and/or solvent molecules were not taken into account. TDDFT calculations were performed at the same level of theory. Fifty vertical spin-allowed transitions were calculated.

2. Syntheses

[AuL][PF₆] was synthesized according to procedures described in the literature.^[14,15]



¹H NMR (400 MHz, *d*₆-DMSO): δ /ppm = 5.05 (s, 2H, H^{6,13}), 3.79 (s, 8H, H^{2,3,9,10}), 2.19 (s, 12H, H^{15,16,17,18}).

¹³C{¹H}NMR (101 MHz, *d*₆-DMSO): δ /ppm = 158.9 (C^{6,13}), 99.1 (C^{5,7,12,14}), 57.5 (C^{2,3,9,10}), 20.7 (C^{15,16,17,18}).

³¹P NMR (162 MHz, *d*₆-DMSO): δ /ppm = -144.1 (sept., ¹J_{PF} = 711 Hz).

¹⁹F NMR (57 MHz, *d*₆-DMSO): δ /ppm = 71.3 (d, ¹J_{FP} = 711 Hz).

MS (ESI⁺): Calculated for [C₁₄H₂₂AuN₄]⁺: *m/z* (%) = 443.1505, found: *m/z* = 443.150 (100).

IR (ATR): $\tilde{\nu}$ (cm⁻¹) = 3008 (w), 2979 (w), 2930 (w), 2874 (w), 1551 (m), 1527 (m), 1467(m), 1436 (m), 1414 (m), 1356 (m), 1283 (w), 1243 (w), 1226 (w), 1115 (w), 1047 (w), 1018 (w), 997 (w), 832 (s, PF), 638 (w), 556 (s, PF_{6,def}).

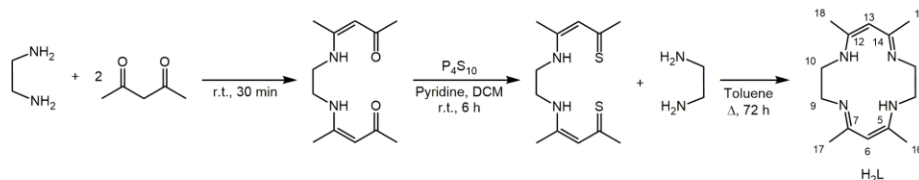
CV (0.1 M [ⁿBu₄N][PF₆]/DMSO, vs. FcH/FcH⁺): *E*_{1/2} / V = +0.67 (irrev), -2.14 (qrev), -2.68 (irrev).

CV (0.1 M [ⁿBu₄N][PF₆]/DMSO/DMF/2-MeTHF 1:5:5, vs. FcH/FcH⁺): *E*_{1/2} / V = +0.72 (irrev), -2.12 (qrev), -2.67 (irrev), -3.16 (irrev).

UV-Vis (DMSO): λ / nm (ϵ / M⁻¹ cm⁻¹) = 450 (650), 372 (10730), 286 (4245).

UV-Vis (DMSO:DMF:2-MeTHF 1:5:5 (v/v)): λ / nm (ϵ / M⁻¹ cm⁻¹) = 372 (13375), 286 (4125), 273 (4310).

H₂L was synthesized according to procedures described in the literature.^[16]



¹H NMR (400 MHz, *d*₆-DMSO): δ /ppm = 11.48 (s, 2H, NH), 4.44 (s, 2H, H^{6,13}), 3.31 (s, 8H, H^{2,3,9,10}), 1.81 (s, 12H, H^{15,16,17,18}).

¹³C{¹H}NMR (101 MHz, *d*₆-DMSO): δ /ppm = 159.7 (C^{6,13}), .94.2 (C^{5,7,12,14}), 46.4 (C^{2,3,9,10}), 19.3 (C^{15,16,17,18}).

MS (ESI⁺): Calculated for [C₁₄H₂₇N₄]⁺: *m/z* (%) = 249.2074, found: *m/z* = 249.207 (100).

CV (0.1 M [ⁿBu₄N][PF₆]/DMSO/DMF/2-MeTHF 1:5:5, vs. FcH/FcH⁺): *E*_{1/2} / V = +0.23 (irrev).

UV-Vis (DMSO:DMF:2-MeTHF 1:5:5 (v/v)): λ / nm (ϵ / M⁻¹ cm⁻¹) = 305 (32820), 375(380), 396 (340).

UV-Vis (DMSO): λ / nm (ϵ / M⁻¹ cm⁻¹) = 307 (31530).

6.1 | Supporting Information to 3.1: 14-Membered Macrocyclic beta-Diiminato Gold(II) – A New Member for the Gold(II) Complex Family?

3. NMR spectra

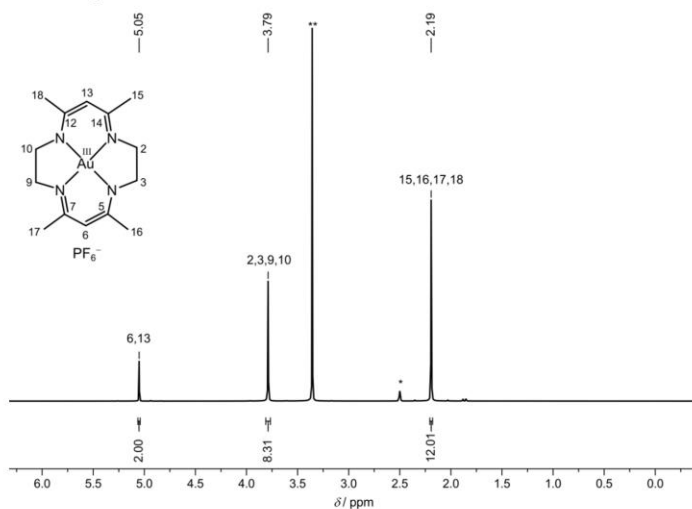


Figure S1 ^1H NMR spectrum of $[\text{AuL}][\text{PF}_6]$ in d_6 -DMSO. * residual partially deuterated DMSO, ** H_2O .

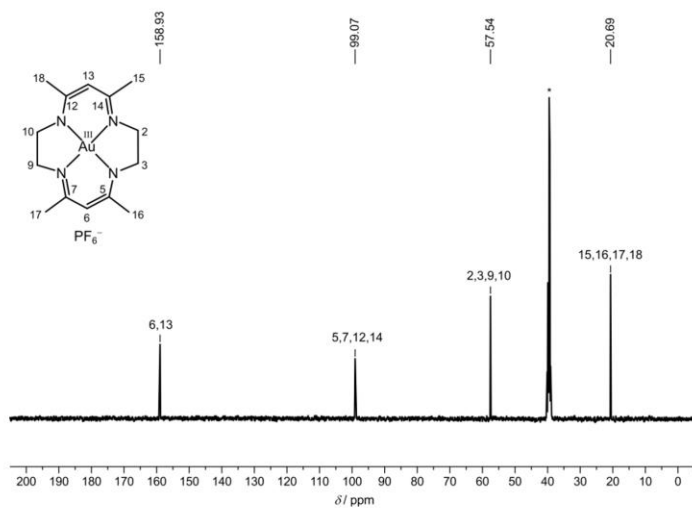


Figure S2 ^{13}C NMR spectrum of $[\text{AuL}][\text{PF}_6]$ in d_6 -DMSO. * d_6 -DMSO.

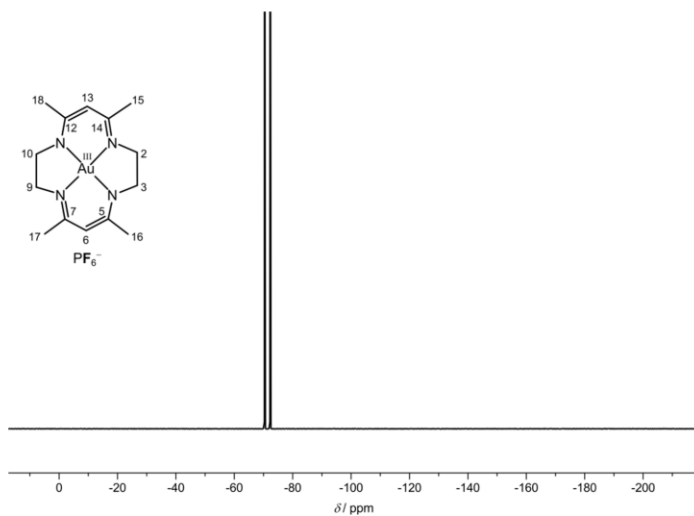


Figure S3 ¹⁹F NMR spectrum of [AuL][PF₆] in *d*₆-DMSO.

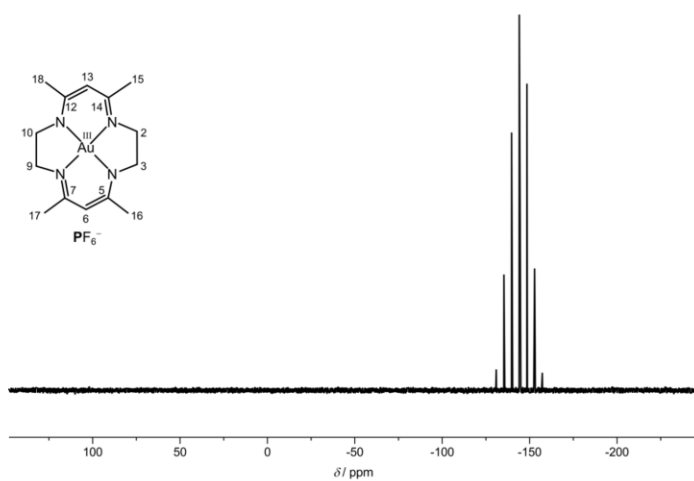


Figure S4 ³¹P NMR spectrum of [AuL][PF₆] in *d*₆-DMSO.

6.1 | Supporting Information to 3.1: 14-Membered Macrocyclic beta-Diiminato Gold(II) – A New Member for the Gold(II) Complex Family?

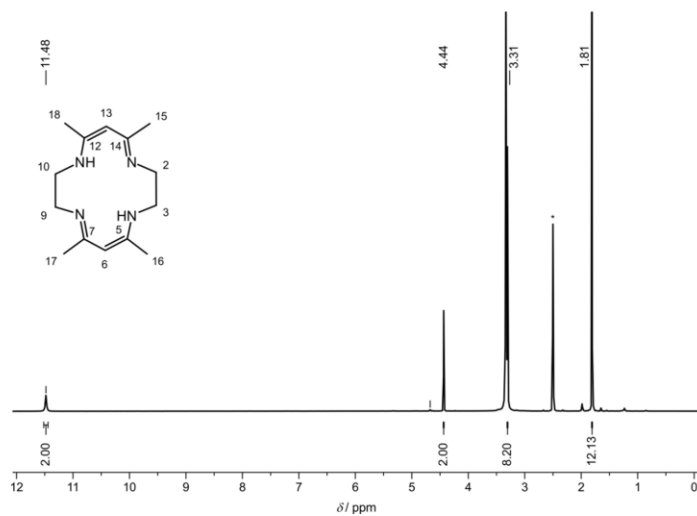


Figure S5 ^1H NMR spectrum of H_2L in d_6 -DMSO. * d_6 -DMSO.

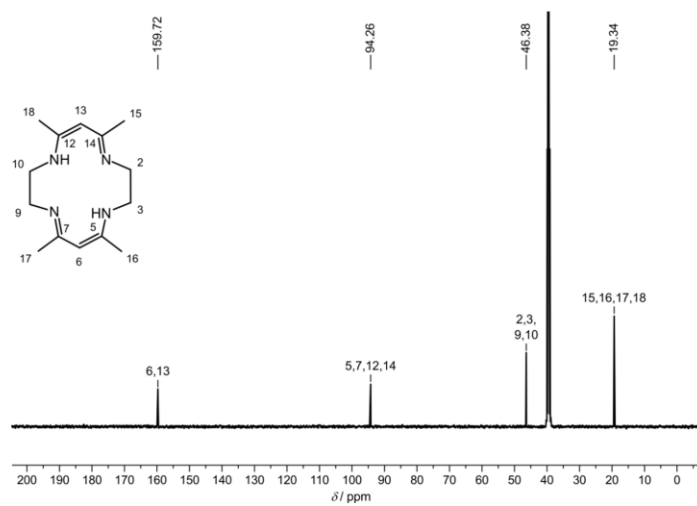


Figure S6 $^{13}\text{C}\{^1\text{H}\}$ NMR spectrum of H_2L in d_6 -DMSO.

4. ESI mass spectra

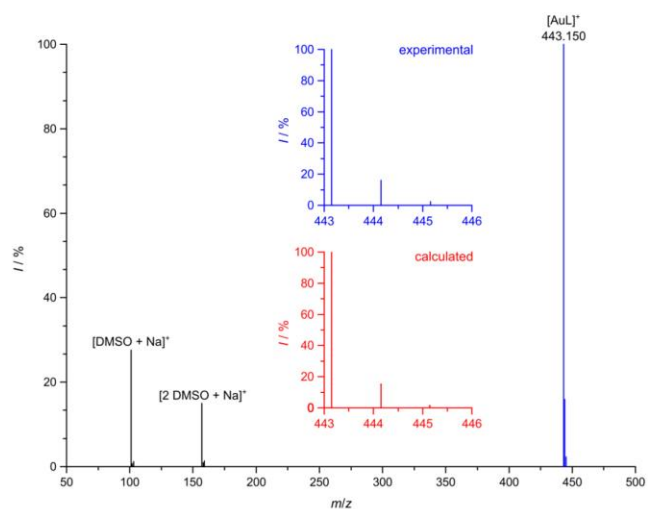


Figure S7 ESI⁺ mass spectrum of [AuL][PF₆] in MeOH + 1vol% DMSO. The insets display the experimental (blue) and calculated (red) isotopic pattern of the peak at $m/z = 443.150$.

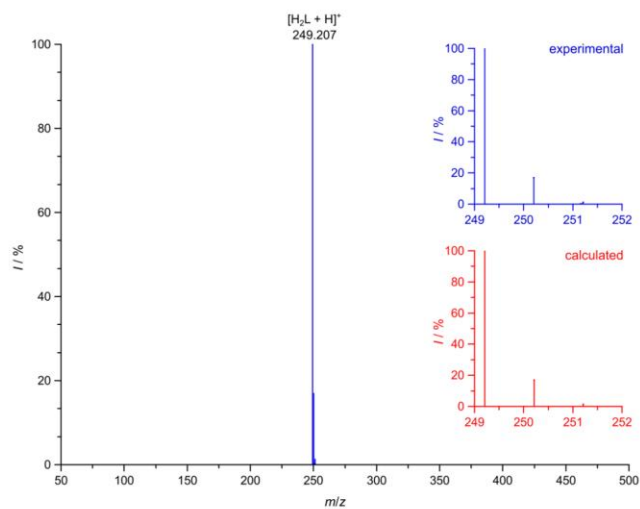


Figure S8 ESI⁺ mass spectrum of H₂L. The insets display the experimental (blue) and calculated (red) isotopic pattern of the peak at $m/z = 249.207$.

6.1 | Supporting Information to 3.1: 14-Membered Macrocyclic beta-Diiminato Gold(II)
– A New Member for the Gold(II) Complex Family?

5. IR spectrum

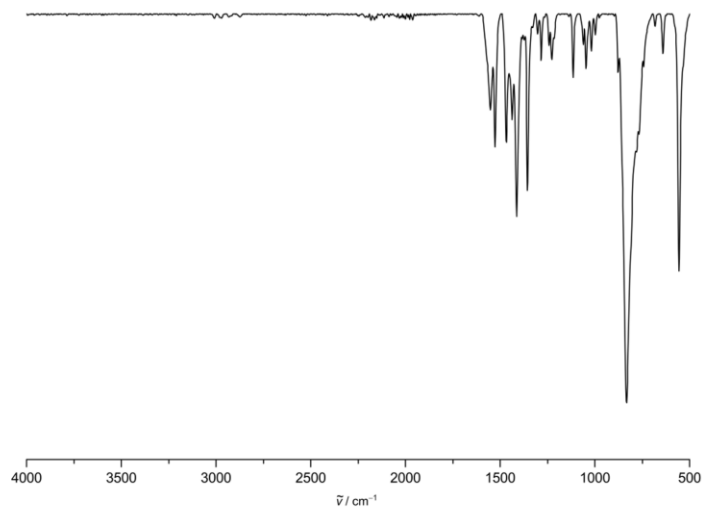


Figure S9 ATR IR spectrum of [AuL][PF₆].

6. Electrochemistry

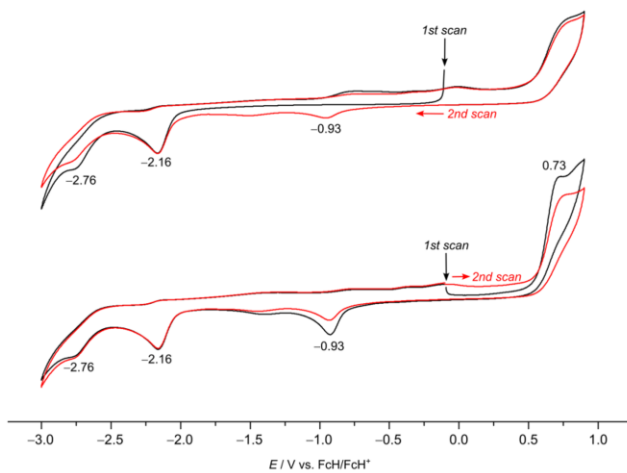


Figure S10 Cyclic voltammograms of $[\text{AuL}][\text{PF}_6]$ 10^{-3} M in 0.1 M $[\text{tBu}_4\text{N}][\text{PF}_6]$ /DMSO:DMF:2-MeTHF 1:5:5 (v/v). Scan directions indicated by arrows.

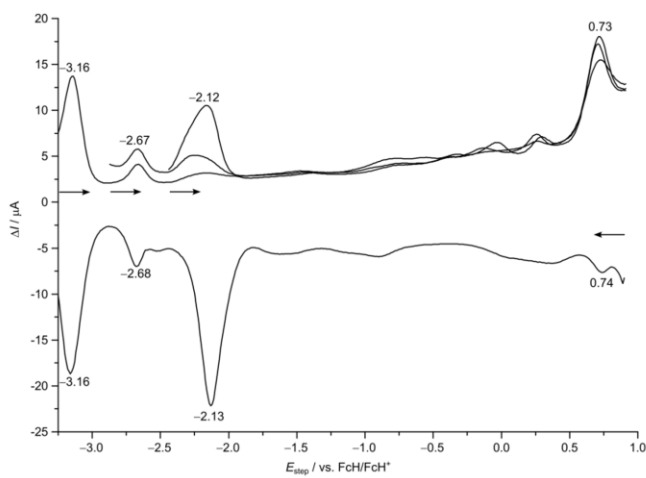


Figure S11 Square wave voltammograms of $[\text{AuL}][\text{PF}_6]$ 10^{-3} M in 0.1 M $[\text{tBu}_4\text{N}][\text{PF}_6]$ /DMSO:DMF:2-MeTHF 1:5:5 (v/v). Scan directions indicated by arrows.

6.1 | Supporting Information to 3.1: 14-Membered Macrocyclic beta-Diiminato Gold(II)
– A New Member for the Gold(II) Complex Family?

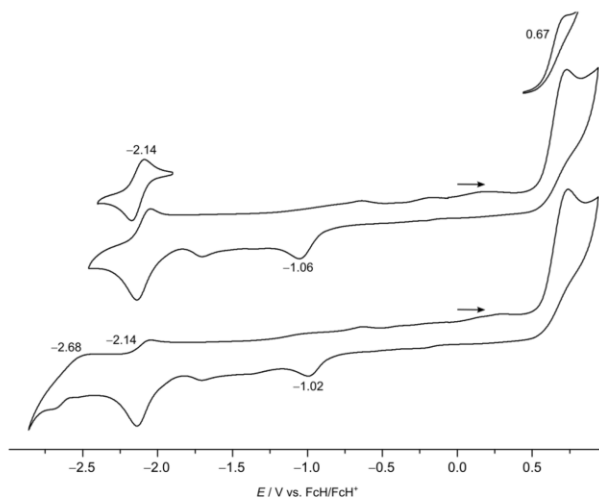


Figure S12 Cyclic voltammograms of $[\text{AuL}][\text{PF}_6]$ 10^{-3} M in 0.1 M $[\text{tBu}_4\text{N}][\text{PF}_6]/\text{DMSO}$. Scan directions indicated by arrows.

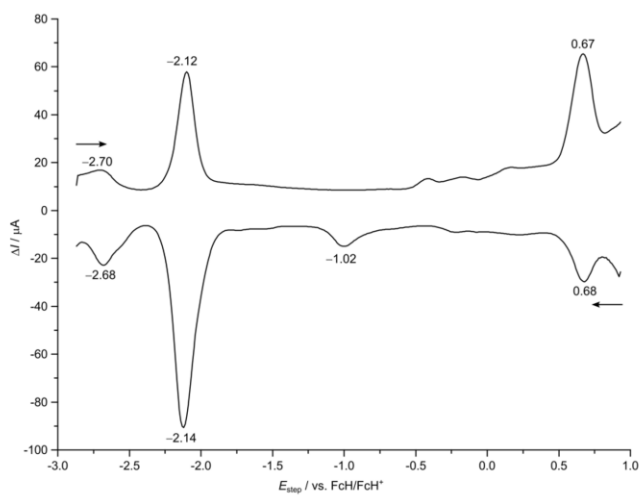


Figure S13 Square wave voltammograms of $[\text{AuL}][\text{PF}_6]$ 10^{-3} M in 0.1 M $[\text{tBu}_4\text{N}][\text{PF}_6]/\text{DMSO}$. Scan directions indicated by arrows.

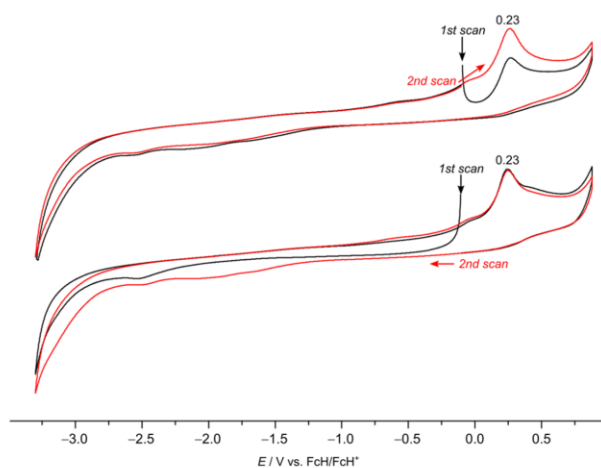


Figure S14 Cyclic voltammograms of H_2L 10^{-3} M in 0.1 M $[\text{nBu}_4\text{N}][\text{PF}_6]/\text{DMSO}:\text{DMF}:\text{2-MeTHF}$ 1:5:5 (v/v). Scan directions indicated by arrows.

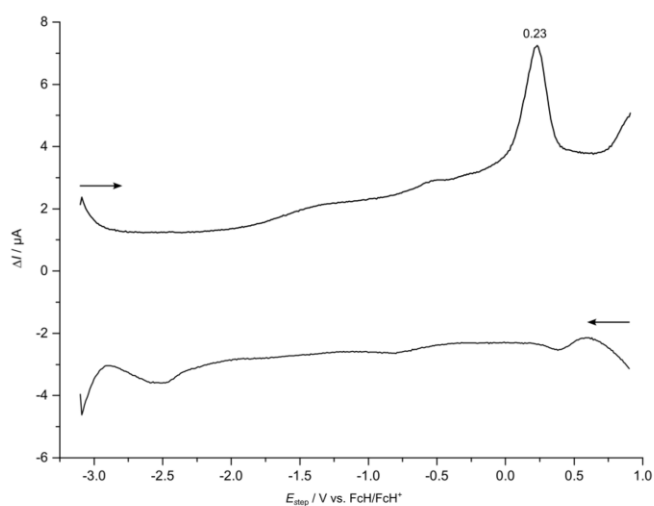


Figure S15 Square wave voltammograms of H_2L 10^{-3} M in 0.1 M $[\text{nBu}_4\text{N}][\text{PF}_6]/\text{DMSO}:\text{DMF}:\text{2-MeTHF}$ 1:5:5 (v/v). Scan directions indicated by arrows.

6.1 | Supporting Information to 3.1: 14-Membered Macrocyclic beta-Diiminato Gold(II) – A New Member for the Gold(II) Complex Family?

Table S1 Cathodic peak currents i_{cat} of the $\text{Au}^{\text{III/I}}$ and $\text{FcH}^{+/0}$ reductions and anodic peak currents i_{Anod} of the $\text{Au}^{\text{I/III}}$ and $\text{FcH}^{0/+}$ oxidations, respectively, at different scan rates.

Cathodic peak currents i_c				
Scan rate / mV s^{-1}	E / V	$i_c(\text{FcH}^{+/0}) / \text{mA}$	E / V	$i_c(\text{Au}^{\text{III/I}}) / \text{mA}$
50	0.062	-0.0373	-2.064	-0.0634
100	0.058	-0.0565	-2.069	-0.0918
200	0.053	-0.0769	-2.079	-0.134
400	0.047	-0.1058	-2.094	-0.1991
600	0.041	-0.1265	-2.103	-0.2508

Anodic peak currents i_a				
Scan rate / mV s^{-1}	E / V	$i_a(\text{Au}^{\text{I/III}}) / \text{mA}$	E / V	$i_a(\text{FcH}^{0/+}) / \text{mA}$
50	-1.980	0.007975	0.155	0.0754
100	-1.981	0.0196	0.158	0.1112
200	-1.975	0.03475	0.169	0.1642
400	-1.971	0.05542	0.181	0.2432
600	-1.969	0.06996	0.193	0.3041

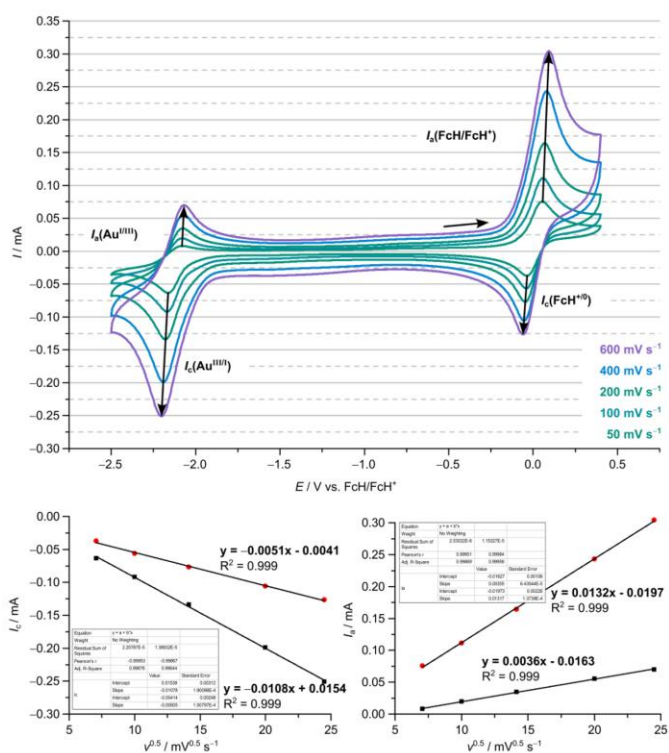


Figure S16 Top: Cyclic voltammograms of [AuI][PF₆] 10⁻³ M and 1 equivalent ferrocene in 0.1 M [tⁿBu₄N][PF₆]/DMSO:DMF:2-MeTHF 1:5:5 (v/v) at different scan rates. Bottom: Cathodic peak currents I_c and anodic peak currents I_a plotted against the square root of the scan rate and linear fit of the data points.

6.1 | Supporting Information to 3.1: 14-Membered Macrocyclic beta-Diiminato Gold(II)
– A New Member for the Gold(II) Complex Family?

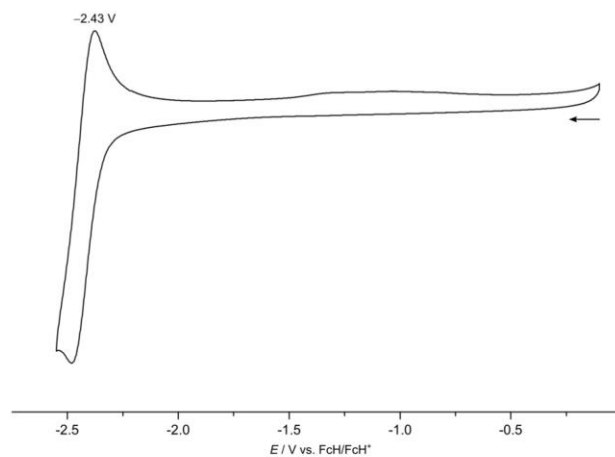


Figure S17 Cyclic voltammogram of anthracene 10^{-3} M in 0.1 M [ⁿBu₄N][PF₆]/DMSO:DMF:2-MeTHF 1:5:5 (v/v). Scan direction indicated by arrow.

7. EPR spectrum

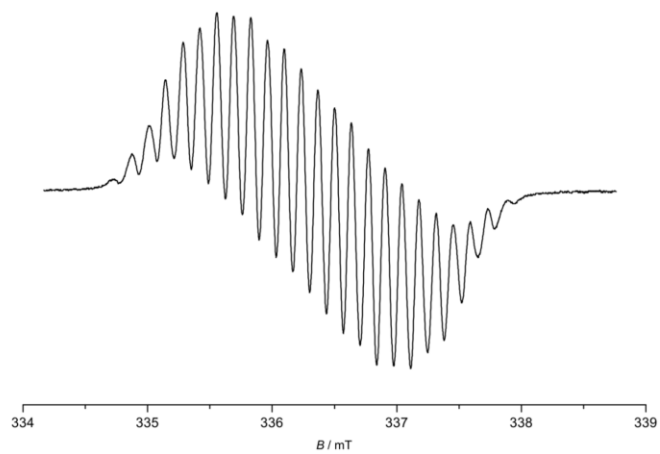


Figure S18 X-band EPR spectrum (9.416 GHz) of the anthracenide radical anion in 2-MeTHF at room temperature.

6.1 | Supporting Information to 3.1: 14-Membered Macrocyclic beta-Diiminato Gold(II) – A New Member for the Gold(II) Complex Family?

8. NMR monitoring of the reduction

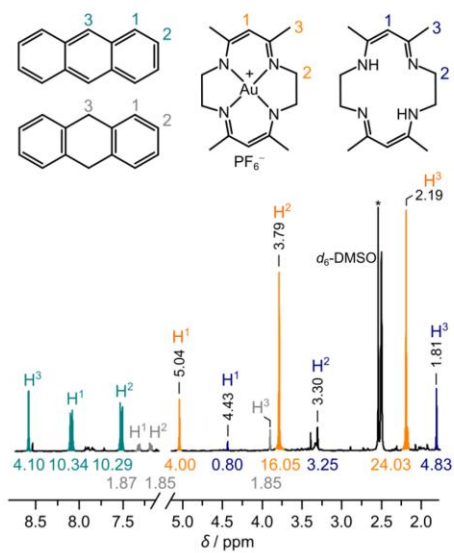


Figure S19 ¹H NMR spectrum of the reaction products of [AuL][PF₆] with 1 equivalent sodium anthracene radical anion in DMSO:DMF:2-MeTHF 1:5:5 (v/v). Spectrum recorded in d₆-DMSO. The asterisk marks non-deuterated residual DMSO from the reaction mixture. Hydrogenation of anthracene (light blue resonances) to 9,10-dihydroanthracene (DHA; grey resonances) occurs additionally.

9. UV/Vis Absorption spectra

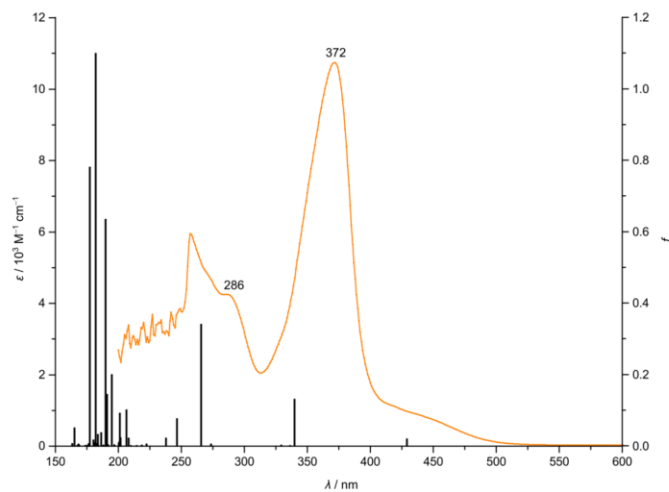


Figure S20 Absorption spectrum of $[\text{AuL}][\text{PF}_6]$ in DMSO at room temperature and TDDFT calculated transitions and oscillator strengths f .

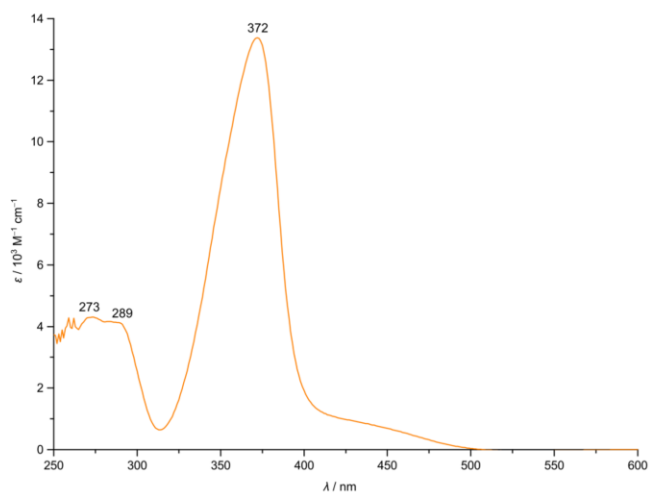


Figure S21 Absorption spectrum of $[\text{AuL}][\text{PF}_6]$ in DMSO:DMF:2-MeTHF 1:5:5 (v/v) at room temperature.

6.1 | Supporting Information to 3.1: 14-Membered Macrocyclic beta-Diiminato Gold(II) – A New Member for the Gold(II) Complex Family?

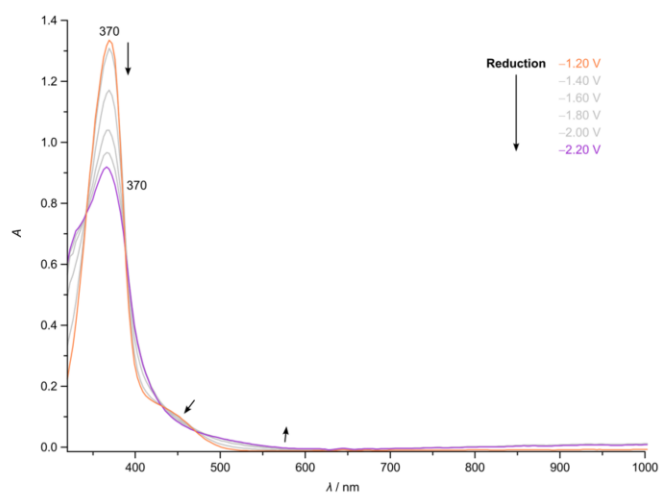


Figure S22 Absorption spectra during electroreduction of [AuL][PF₆] in 0.1 M [tⁿBu₄N][PF₆]/DMSO:DMF:2-MeTHF 1:5:5 (v/v).

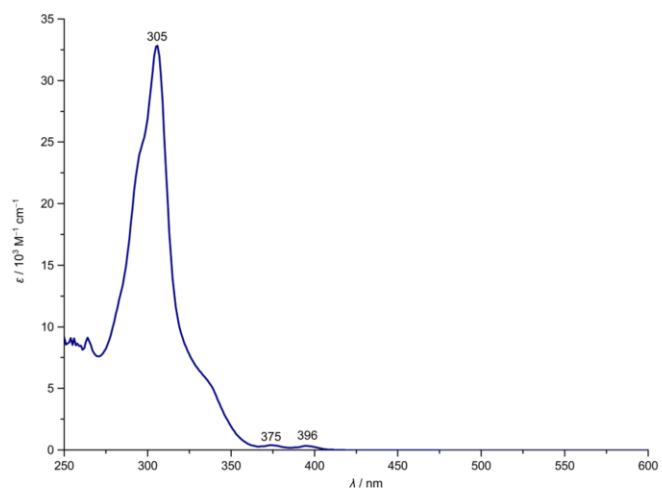


Figure S23 Absorption spectrum of H₂L in DMSO:DMF:2-MeTHF 1:5:5 (v/v) at room temperature.

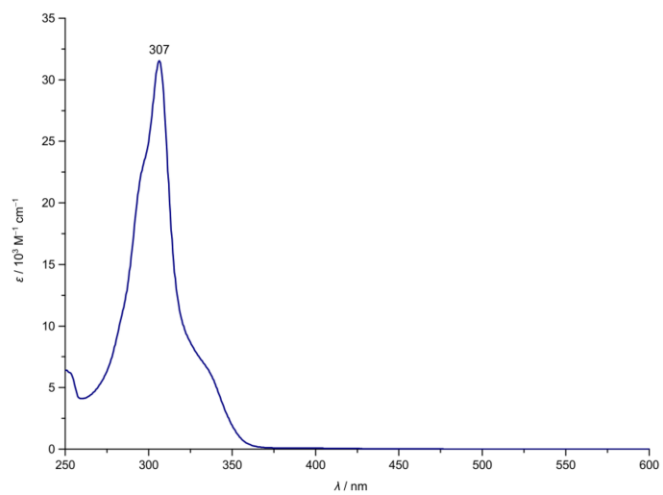
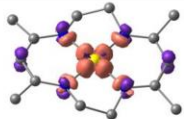
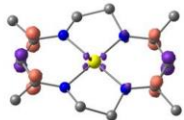
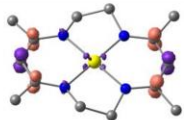
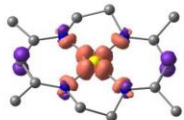
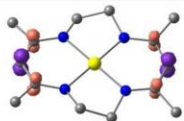
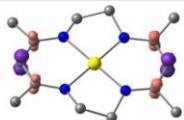
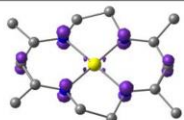
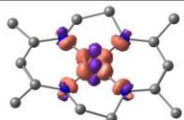


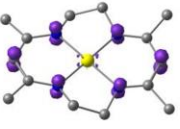
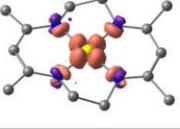
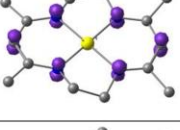
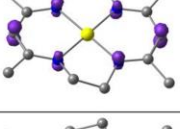
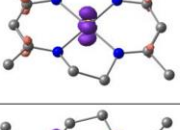
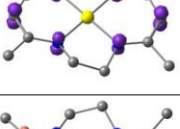
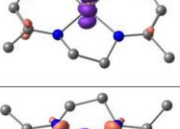
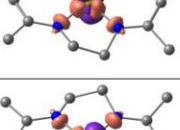
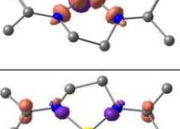
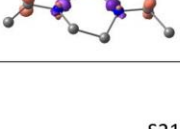
Figure S24 Absorption spectrum of H₂L in DMSO at room temperature.

6.1 | Supporting Information to 3.1: 14-Membered Macrocyclic beta-Diiminato Gold(II) – A New Member for the Gold(II) Complex Family?

10. Computational studies

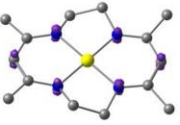
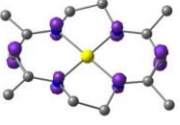
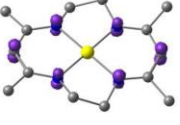
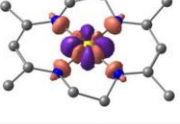
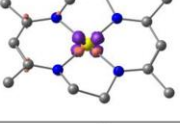
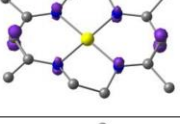
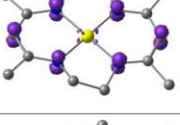
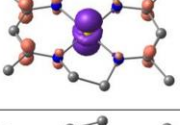
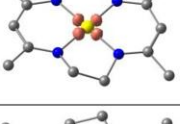
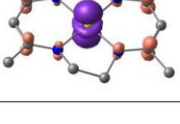
Table S2 TDDFT calculated transitions of [AuL]⁺.

#	λ / nm	f	Difference electron density (purple = electron loss; orange = electron gain). isosurface value at 0.012 a.u.)
1	422	0.01669692	
2	342.9	0.14576038	
3	330.6	0.00137242	
4	329.4	5.18E-01	
5	276.6	0.00286685	
6	269.7	0.32633420	
7	240.3	0.09586057	
8	237.7	0.01857798	

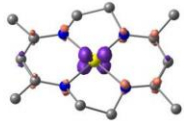
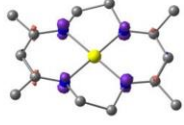
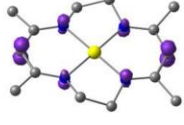
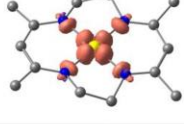
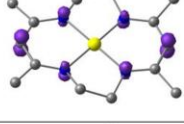
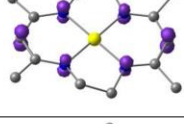
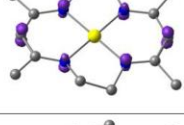
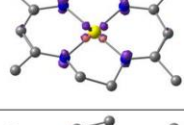
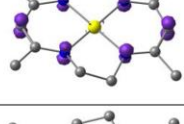
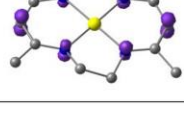
9	221.9	0.00367134	
10	216.5	0.00116708	
11	210.6	2.44E-03	
12	207.3	6.71E-01	
13	206.3	0.19182678	
14	205.9	0.01927591	
15	201.6	0.00090292	
16	201.2	0.06915075	
17	201.1	0.12107923	
18	200.5	0.00295071	

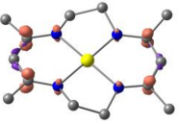
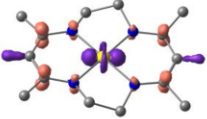
6.1 | Supporting Information to 3.1: 14-Membered Macrocyclic beta-Diiminato Gold(II)
– A New Member for the Gold(II) Complex Family?

19	196.9	0.00785355	
20	196.3	0.00131094	
21	194.4	0.56726659	
22	192.2	0.51402473	
23	191.1	0.00207640	
24	190.4	0.00026650	
25	190.3	0.02650456	
26	189.7	0.00100619	
27	187.6	0.00012723	
28	186.3	0.01103734	

29	184.8	0.05475805	
30	183.3	0.00071845	
31	182.6	0.53408661	
32	181.2	0.00013504	
33	180.6	0.06309280	
34	179.3	0.16607651	
35	179.2	0.03168510	
36	178.8	4.10E-02	
37	178.5	0.72920757	
38	177.1	0.00125714	

6.1 | Supporting Information to 3.1: 14-Membered Macrocyclic beta-Diiminato Gold(II)
– A New Member for the Gold(II) Complex Family?

39	176.7	0.00071673	
40	176.5	0.00013751	
41	173.4	0.00644829	
42	172.5	3.91E-03	
43	170.8	3.32E-03	
44	168.2	5.91E-01	
45	166.9	2.59E-02	
46	164.4	0.04307676	
47	164.3	3.34E-01	
48	164.2	0.01040116	

49	163.2	0.00580131	
50	163.1	5.24E-01	

6.1 | Supporting Information to 3.1: 14-Membered Macrocyclic beta-Diiminato Gold(II)
– A New Member for the Gold(II) Complex Family?

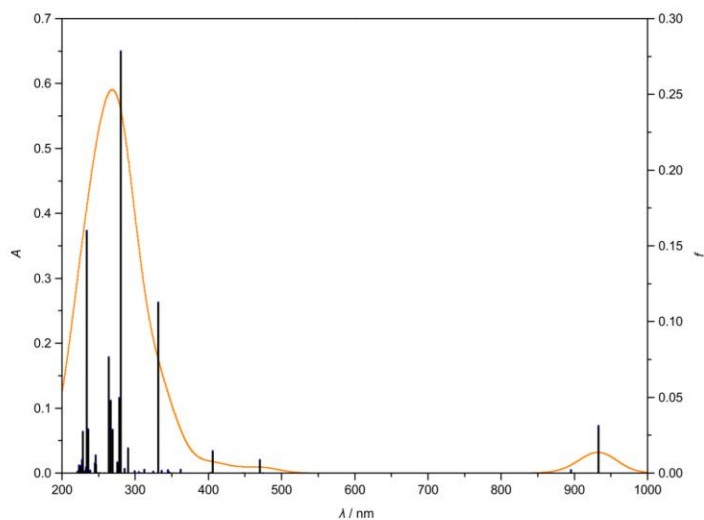
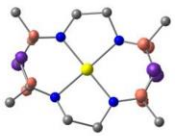
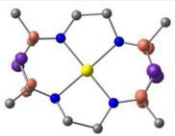
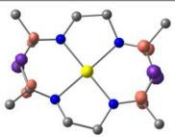
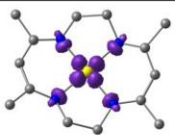
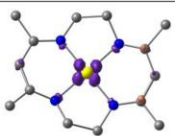
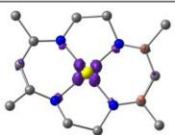
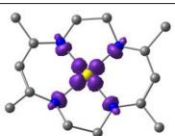
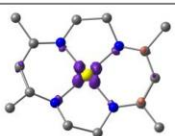
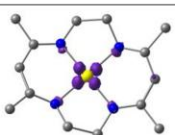


Figure S25 TDDFT calculated transitions and oscillator strengths f of AuL.

Table S3 TDDFT calculated transitions of AuL.

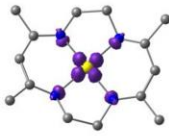
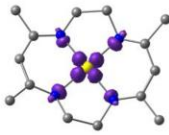
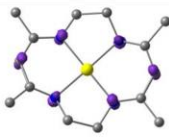
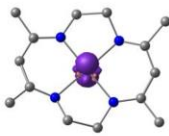
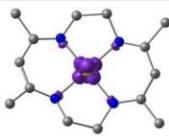
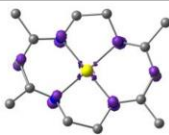
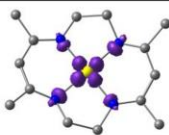
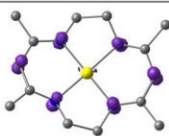
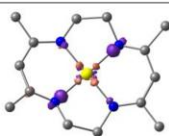
#	λ / nm	f	Difference electron density (purple = electron loss; orange = electron gain). isosurface value at 0.012 a.u.)
1	933.2	0.03131282	
2	895.5	0.00209481	
3	474.6	5.34E-01	
4	470.5	0.00876181	

5	446.9	2.37E-01	
6	405.7	0.01463287	
7	402.7	0.00032723	
8	362	0.00221295	
9	347	0.00054195	
10	344.9	0.00200795	
11	336.3	0.00160399	
12	331.7	0.11272684	
13	324.5	0.00100124	

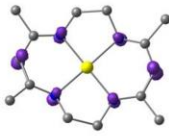
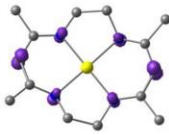
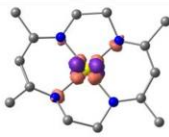
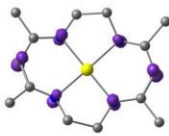
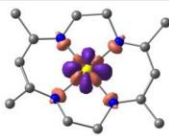
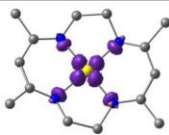
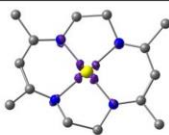
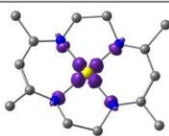
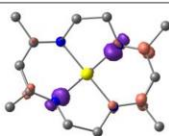
6.1 | Supporting Information to 3.1: 14-Membered Macrocyclic beta-Diiminato Gold(II)
– A New Member for the Gold(II) Complex Family?

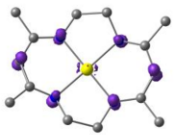
14	312.5	0.00231069	
15	309	1.92E-01	
16	305.1	0.00073247	
17	299.5	0.00122894	
18	290.5	0.01626044	
19	285.4	0.00286390	
20	280.1	0.27842518	
21	278.2	0.04966007	
22	276.2	0.00538723	

S28

32	245.9	0.01169446	
33	245	0.00661544	
34	244.3	0.688E-01	
35	238.3	0.00173457	
36	237.8	0.00030464	
37	237.5	1.78E-02	
38	236.1	0.02893623	
39	233.6	0.00176067	
40	233.6	0.15998418	

6.1 | Supporting Information to 3.1: 14-Membered Macrocyclic beta-Diiminato Gold(II)
– A New Member for the Gold(II) Complex Family?

41	233	0.00379222	
42	231.1	0.00127053	
43	228.3	0.02741181	
44	227.5	0.00907153	
45	226.3	0.00089219	
46	225.7	0.00486044	
47	223.3	0.00519814	
48	223.3	0.00424629	
49	221	0.00099828	

50	220.6	4.20E-01	
----	-------	----------	---

6.1 | Supporting Information to 3.1: 14-Membered Macrocyclic beta-Diiminato Gold(II)
– A New Member for the Gold(II) Complex Family?

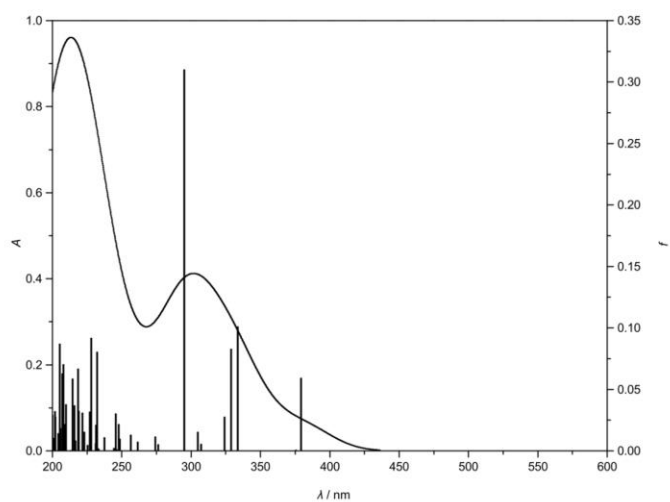
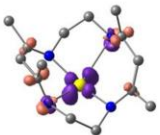
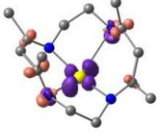
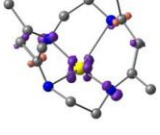
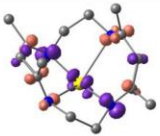
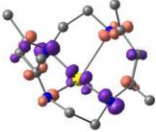
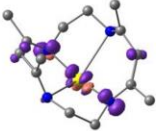
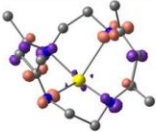
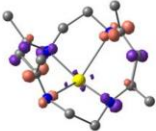
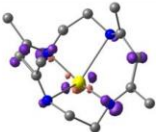
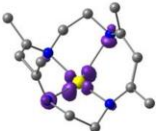
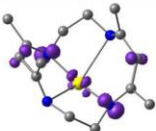
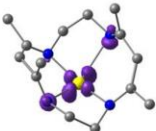
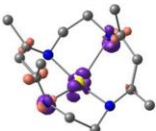


Figure S26 TDDFT calculated transitions and oscillator strengths f of $[\text{AuL}]^-$.

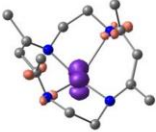
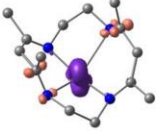
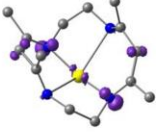
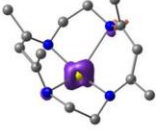
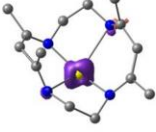
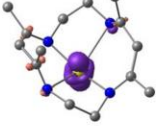
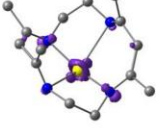
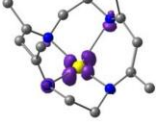
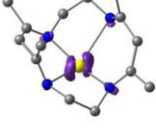
Table S4 TDDFT calculated transitions of $[\text{AuL}]^-$.

#	λ / nm	f	Difference electron density (purple = electron loss; orange = electron gain). Isosurface value at 0.012 a.u.)
1	379.30	0.058753669	
2	375.60	0.000285879	
3	333.50	0.100517394	
4	328.80	0.082551317	

5	324.20	0.027117350	
6	307.30	0.005009137	
7	304.90	0.014846035	
8	295.10	0.309662202	
9	276.20	0.004878375	
10	274.30	0.011168668	
11	261.40	0.006974925	
12	256.40	0.012624640	
13	248.60	0.009218507	

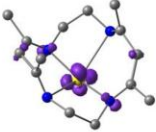
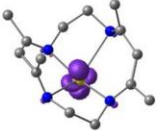
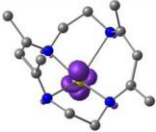
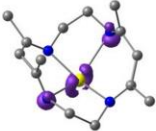
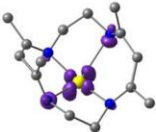
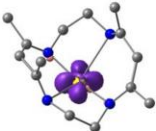
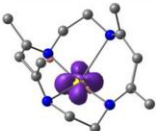
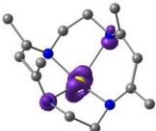
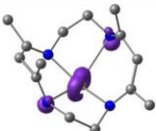
6.1 | Supporting Information to 3.1: 14-Membered Macrocyclic beta-Diiminato Gold(II)
– A New Member for the Gold(II) Complex Family?

14	247.80	0.021235521	
15	246.20	0.000871432	
16	245.80	0.029947732	
17	244.30	0.001643134	
18	237.40	0.010317490	
19	233.20	0.001216015	
20	232.30	0.080118467	
21	231.40	0.020672279	
22	231.20	0.005815269	

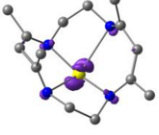
23	228.00	0.091294922	
24	226.80	0.031321744	
25	225.30	0.004192449	
26	222.90	0.014992864	
27	222.50	0.000534342	
28	221.60	0.030604910	
29	219.10	0.031910313	
30	218.40	0.066351151	
31	216.60	0.007733212	

6.1 | Supporting Information to 3.1: 14-Membered Macrocyclic beta-Diiminato Gold(II)
– A New Member for the Gold(II) Complex Family?

32	215.90	0.036508547	
33	215.90	0.008079442	
34	214.40	0.058246784	
35	213.20	4.41E-02	
36	209.70	0.037194169	
37	209.20	0.006970673	
38	208.80	0.021058666	
39	208.00	0.069853404	
40	207.10	0.062285618	

41	205.90	0.017953189	
42	205.20	0.086538437	
43	204.30	0.013837122	
44	202.20	0.027321696	
45	201.80	0.031704170	
46	201.10	0.010002201	
47	200.00	0.028572506	
48	199.60	0.124730614	
49	198.60	0.002278530	

6.1 | Supporting Information to 3.1: 14-Membered Macrocyclic beta-Diiminato Gold(II)
– A New Member for the Gold(II) Complex Family?

50	197.40	0.033775372	
----	--------	-------------	---

6.2 Supporting Information to 3.2: Face-to-Face Gold Porphyry

Face-to-Face Gold Porphyrins

Lukas Sorge, Philipp Sikora, and Katja Heinze*

Department of Chemistry, Johannes Gutenberg University Mainz,
Duesbergweg 10-14, 55128 Mainz, Germany

6.2 | Supporting Information to 3.2: Face-to-Face Gold Porphyrins

1 Procedures and Methods

General procedures. All reagents were used as received from commercial suppliers (ABCR, AcrosOrganics, AlfaAesar, Fischer, Sigma-Aldrich and TCI). THF and DCM for spectroscopic and electrochemical analyses were received dried, degassed with argon and stored over molecular sieves. All measurements were performed under an argon and water-free atmosphere unless otherwise noted. A glovebox (UniLab/MBraun–Ar 5.0, O₂ < 0.1 ppm, H₂O < 0.1 ppm) was used to store and weigh sensitive compounds for synthesis as well as to prepare samples that required the absence of oxygen and/or water.

NMR spectra were recorded on a Bruker AVII+400 NMR spectrometer at 400.31 MHz (¹H), 100.61 (¹³C), 376.50 MHz (¹⁹F) or ³¹P (161.98 MHz). All signals are given in ppm and referenced against the solvent signal as internal standard (CDCl₃: δ(¹H) = 7.26 ppm, CD₂Cl₂: δ(¹H) = 5.32 ppm, δ(¹³C) = 53.84 ppm) or H₃PO₄ (85 %) (δ(³¹P) = 0.00 ppm) or CFC₃ (δ(¹⁹F) = 0.00 ppm) as external standard. (s) = singlet, (d) = doublet, (t) = triplet, (q) = quartet, (m) = multiplet, (sept) = septet.

ESI⁺ mass spectra were recorded on a Micromass Q-TOF-Ultima spectrometer by the central analytical facility of the Department of Chemistry of the Johannes Gutenberg University Mainz, Germany.

ATR IR spectra were recorded on an Agilent Cary 630 FTIR spectrometer with an ATR unit containing a diamond crystal. The intensities are qualitatively indicated with weak (w), medium (m) and strong (s).

Electrochemical measurements were carried out on a BioLogic SP-200 voltammetric analyzer using platinum wires as counter and working electrodes and a 0.01 M Ag/AgNO₃ electrode as reference electrode. Cyclic voltammetry measurements were carried out at a scan rate of 50 or 100 mV s⁻¹ using 0.1 M [ⁿBu₄N][PF₆] in THF as supporting electrolyte. Potentials are referenced against the ferrocene/ferrocenium couple.

X-band cw EPR measurements were carried out using a Magnettech Miniscope MS 300 in THF with a concentration of 5 mM at 77 K cooled by liquid nitrogen in a finger dewar (Magnettech GmbH, Berlin, Germany). *g* factors are referenced to external Mn²⁺ in ZnS (*g* = 2.118, 2.066, 2.027, 1.986, 1.946, 1.906). *Microwave frequency*: 9.41 GHz, *center field*: 3350 G, *sweep*: 1200 G, *modulation amplitude* 5000 mG, *receiver gain* = 5, *microwave attenuation* 5 dB, *sweep time*: 120 s. Simulations of the experimental spectra were performed with *EasySpin* (5.2.35) for *Matlab* R2022a.¹

UV/Vis/NIR absorption spectra were recorded on a Jasco V770 spectrometer using 1.0 cm quartz cells and equipped with a Schott valve to maintain an inert atmosphere if necessary. Low-temperature measurements were carried out with a Cary 5000 UV-Vis-NIR spectrometer using a liquid cooled cryostat Optistat DN from Oxford Instruments.

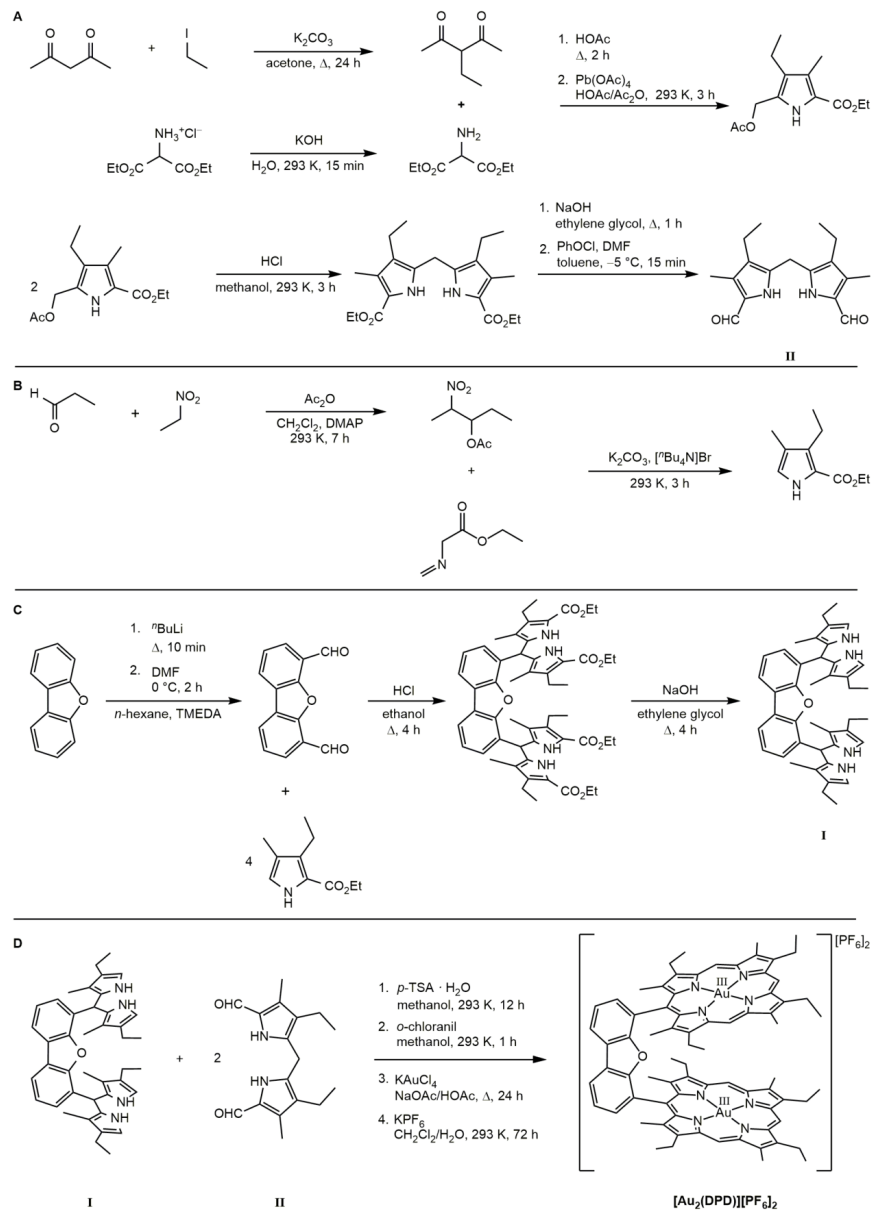
Steady-state emission spectra and photoluminescent decay curves in solution at 293 K and in frozen solution at 77 K were measured with a FLS1000 spectrometer from Edinburgh Instruments equipped with a cooled photomultiplier detector PMT-980 and a Lifetime HSPMT-920. A xenon arc lamp Xe2 (450 W) was used for excitation in steady-state measurements. Time-resolved luminescence experiments were conducted using the μs-xenon-flashlamp μF2 (pulse width ca. 2 μs) and a picosecond-pulsed laser (NKT-FIU-6 SuperK Fianium FIU-6) as excitation source. Luminescence decays were fitted using the software Fluoracle (Edinburgh Instruments). Measurements at low temperature were carried out using a liquid nitrogen cooled cryostat Optistat DN from Oxford Instruments.

DFT calculations were carried out using the *ORCA* 5.0.3 program package.² Tight convergence criteria were chosen for all calculations (keywords *tightscf* and *tightopt*). For geometry optimizations and energy calculations, the B3LYP^{3,4} formulation of density functional theory was used employing the ZORA-def2-TZVPP basis set for the porphyrin macrocycle and Au-SARC-ZORA-def2-TZVPP basis set for the gold center^{5,6} with the zeroth order regular approximation (keyword *ZORA*),⁷ and the *RIJCOSX* approximation.⁸ To account for solvent effects, a conductor-like polarizable continuum model (*CPCM*, CH₂Cl₂) modelling dichloromethane was used in all calculations.⁹ Grimme's empirical dispersion correction *D3BJ* was employed.^{10,11} No symmetry constraints were imposed on the molecules. The presence of energy minima of the ground states was checked by numerical frequency calculations on the same level of theory. Ethyl substituents were replaced by methyl substituents throughout to avoid the presence of conformers and to reduce computational costs. Explicit counterions and/or solvent molecules were not taken into account. TDDFT calculations were performed at the same level of theory. Fifty vertical spin-allowed transitions were calculated. The assignment of the character of transitions by charge transfer number analysis was done using the *TheoDORE* 2.4 software package.^{12,13} Analyses of non-planar distortions of the DFT optimized geometries of the porphin scaffolds were conducted using *PorphyStruct* applying the normal-coordinate structure decomposition (NSD) method.^{14,15}

6.2 | Supporting Information to 3.2: Face-to-Face Gold Porphyrins

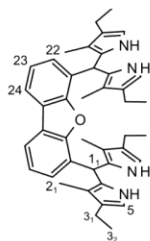
2 Syntheses and Spectra

Scheme S1 Synthesis of the bis(porphyrinato)gold(III) complex $[\text{Au}_2(\text{DPD})][\text{PF}_6]_2$.¹⁶⁻²³



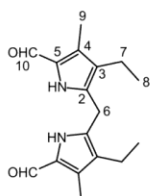
Intermediate **I** was synthesized according to procedures described in the literature.^{16,20,22}

¹H NMR (400 MHz, CD₂Cl₂): δ / ppm = 7.86 (d, 2H, H²⁴, ³J_{HH} = 8.8 Hz), 7.58 (s, 4H, NH), 7.30 (t, 2H, H²³, ³J_{HH} = 7.8 Hz), 7.22 (d, 2H, H²², ³J_{HH} = 6.8 Hz), 6.33 (d, 4H, H⁵), 5.76 (s, 2H, H¹₁), 2.40 (q, 8H, H³₁, ³J_{HH} = 7.3 Hz), 1.81 (s, 12H, H²₁), 1.14 (t, 12H, H³₂, ³J_{HH} = 7.3 Hz).



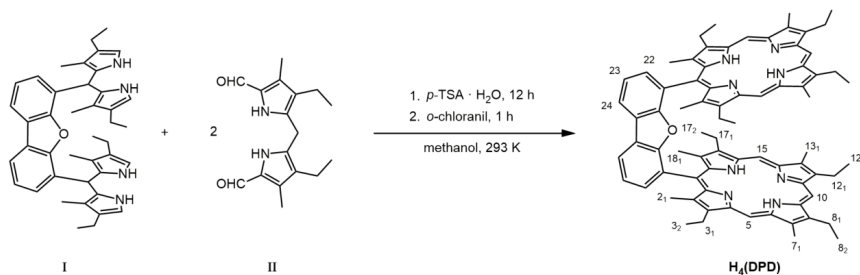
Intermediate **II** was synthesized according to procedures described in the literature.^{18,21}

¹H NMR (400 MHz, CDCl₃): δ / ppm = 10.90 (s, 2H, NH), 8.48 (s, 2H, H¹⁰), 3.95 (s, 2H, H⁶), 2.47 (q, 4H, H⁷, ³J_{HH} = 7.6 Hz), 2.28 (s, 6H, H⁹), 1.07 (t, 6H, H⁸, ³J_{HH} = 7.6 Hz).



6.2 I Supporting Information to 3.2: Face-to-Face Gold Porphyrins

Synthesis of H₄DPD (according to slightly modified procedures described in the literature²³): Under an argon atmosphere, **I** (1.036 g, 1.66 mmol) and **II** (0.975 g, 3.40 mmol) were dissolved in deaerated MeOH (300 mL) and stirred at 293 K for 30 min in the dark. A solution of *p*-TSA · H₂O (2.11 g, 11.07 mmol) in MeOH (120 mL) was added over a period of 12 h and the solution was stirred for 24 h at 293 K. *o*-Chloranil (852 mg, 3.75 mmol) was added as a solid and stirring was continued for 1 h. The solvent was removed under reduced pressure. The crude product was purified via column chromatography (silica, CH₂Cl₂/MeOH 30:1) to yield H₄DPD (209 mg, 0.18 mmol, 11 %) as purple powder.

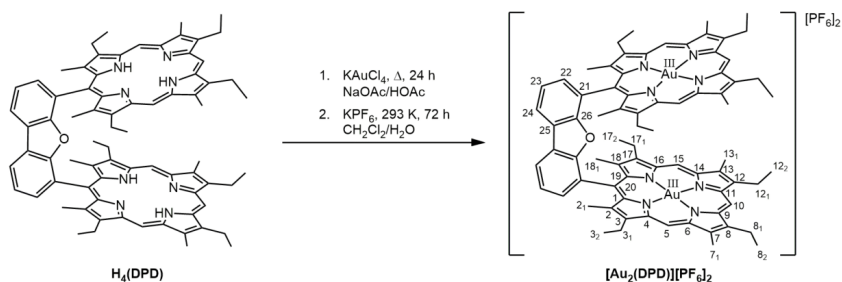


¹H NMR (400 MHz, CDCl₃): δ / ppm = 9.55 ppm (s, 4H, H^{5,15}), 9.48 ppm (s, 2H, H¹⁰), 8.69 (d, 2H, H²⁴, ³J_{HH} = 7.6 Hz), 8.69 (d, 2H, H²², ³J_{HH} = 7.4 Hz), 7.90 (t, 2H, H²³, ³J_{HH} = 7.6 Hz), 3.74 (q, 8H, H^{3,1,17,1}, ³J_{HH} = 7.7 Hz), 3.65 (q, 8H, H^{8,1,12,1}, ³J_{HH} = 7.8 Hz), 3.24 (s, 12H, H^{2,1,18,1}), 2.25 (s, 12H, H^{7,1,13,1}), 1.62 (t, 12H, H^{3,2,17,2}), 1.39 (t, 12H, H^{8,2,12,2}). NH proton resonances were not observed due to exchange by deuterium in the employed solvent.

UV/Vis (CH₂Cl₂): λ / nm (ϵ / 10⁴ M⁻¹ cm⁻¹) = 398 (27.3), 501 (2.3), 536 (1.2), 571 (1.2), 624 (0.7).

MS (ESI⁺, MeOH): Calculated for [C₇₆H₈₁N₈O]⁺: m/z (%) = 1121.653, found: m/z = 1121.651; calculated for [C₇₆H₈₁N₈O]²⁺: m/z (%) = 561.330, found: m/z = 561.330.

Synthesis of $[\text{Au}_2(\text{DPD})][\text{PF}_6]_2$ (analogous to slightly modified procedures for porphyrin auration described in the literature^{17,19}): H_4DPD (209 mg, 0.186 mmol), potassium tetrachloridoaurate(III) (563 mg, 1.49 mmol) and sodium acetate (1.31 g, 15.97 mmol) were suspended in glacial acetic acid (90 mL). The suspension was heated to reflux for 24 h, allowed to cool to 293 K and diluted with CH_2Cl_2 (250 mL). The organic phase was washed with water (100 mL), saturated sodium carbonate solution (50 mL) and dried over anhydrous magnesium sulfate and filtered. The solvent was removed under reduced pressure and the residue was redissolved in CH_2Cl_2 (80 mL). The solution was stirred with a saturated aqueous solution of potassium hexafluorophosphate (15 mL) for 72 h. The organic phase was separated, washed with water (10 mL), dried over magnesium sulfate and filtered. The residue was subjected to column chromatography (aluminum oxide, CH_2Cl_2 : MeOH 50:1) to yield $[\text{Au}_2(\text{DPD})][\text{PF}_6]_2$ (26 mg, 0.01 mmol, 18 %) as red powder.



^1H NMR (400 MHz, CD_2Cl_2): δ / ppm = 10.30 ppm (s, 4H, $\text{H}^{5,15}$), 10.22 (s, 2H, H^{10}), 8.89 (d, 2H, H^{24} , $^3J_{\text{HH}} = 7.0$ Hz, 1.0 Hz), 8.03 (t, 2H, H^{23} , $^3J_{\text{HH}} = 7.7$ Hz), 7.78 (dd, 2H, H^{22} , $^3J_{\text{HH}} = 7.7$ Hz, 1.2 Hz), 3.96 (dq, 16H, $\text{H}^{3, 8, 12, 17, 1}$, $^3J_{\text{HH}} = 12.8$ Hz, 8.0 Hz), 3.51 (s, 12H, $\text{H}^{2, 18, 1}$), 2.56 (s, 12H, $\text{H}^{7, 13, 1}$), 1.63 (m, 24H, $\text{H}^{3, 8, 2, 12, 2, 17, 2}$).

$^{13}\text{C}\{^1\text{H}\}$ NMR (101 MHz, CD_2Cl_2): δ / ppm = 156.9 (C^{26}), 146.3 ($\text{C}^{6,14}$), 144.7 ($\text{C}^{1,19}$), 138.8 ($\text{C}^{8,12}$), 138.2 ($\text{C}^{2,18}$), 135.1 ($\text{C}^{9,11}$), 135.0 ($\text{C}^{3,17}$), 133.9 (C^{25}), 133.7 ($\text{C}^{7,13}$), 133.5 ($\text{C}^{4,16}$), 125.5 (C^{23}), 124.6 (C^{24}), 124.5 (C^{22}), 115.4 (C^{21}), 100.3 ($\text{C}^{5,15}$), 99.6 (C^{10}), 20.4 ($\text{C}^{3, 8, 12, 17, 1}$), 17.4 ($\text{C}^{3, 8, 2, 12, 2, 17, 2}$), 15.3 ($\text{C}^{7, 13, 2}$), 12.0 ($\text{C}^{7, 13, 1}$).

^{31}P NMR (162 MHz, CD_2Cl_2): δ / ppm = -144.7 (sept, $^1J_{\text{PF}} = 711$ Hz).

^{19}F NMR (57 MHz, CD_2Cl_2): δ / ppm = -74.7 (d, $^1J_{\text{PF}} = 711$ Hz).

MS (ESI⁺, MeCN): Calculated for $[\text{C}_{76}\text{H}_{76}\text{Au}_2\text{N}_8\text{O}]^{2+}$: m/z (%) = 755.273, found: $m/z = 755.273$; calculated for $\{[\text{C}_{76}\text{H}_{76}\text{Au}_2\text{N}_8\text{O}][\text{PF}_6]\}^+$: m/z (%) = 1655.511, found: $m/z = 1655.512$.

IR (ATR): $\tilde{\nu}$ / cm^{-1} = 2951 (m), 2912 (m), 2844 (w), 1716 (w), 1662 (w), 1597 (w), 1451 (w), 1373 (w), 1256 (vs), 1091 (m), 1011 (s), 836 (m), 791 (vs), 725 (m), 555 (m).

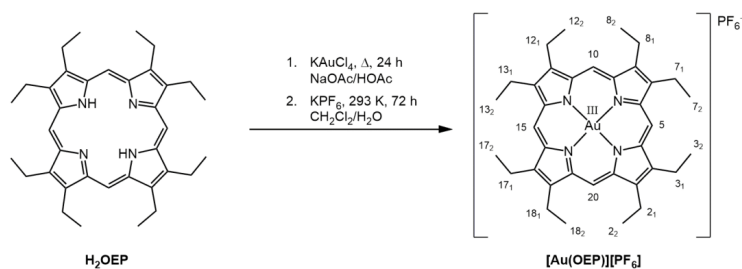
CV (0.1 M [$^n\text{Bu}_4\text{N}$][PF_6]/THF, FcH/FcH⁺): $E_{1/2} / \text{V} = -1.13$ (qrev), -1.77 (qrev), -2.22 (qrev).

UV/Vis (CH_2Cl_2): λ / nm ($\epsilon / 10^4 \text{ M}^{-1} \text{ cm}^{-1}$) = 390 (20), 514 (1.1), 549 (1.5).

6.2 | Supporting Information to 3.2: Face-to-Face Gold Porphyrins

[Au(OEP)][PF₆] was synthesized adapted from methods described in the literature.^{17,19} H₂OEP was kindly donated by Prof. Matthias O. Senge (Trinity College Dublin, Ireland).

H₂OEP (51 mg, 0.095 mmol), potassium tetrachloroaurate(III) (563 mg, 1.49 mmol, 0.38 mmol) and sodium acetate (348 mg, 4.36 mmol) were suspended in glacial acetic acid (10 mL). The suspension was heated to reflux for 24 h, allowed to cool to 293 K and diluted with CH₂Cl₂ (20 mL). The organic phase was washed with water (2 x 50 mL), saturated sodium carbonate solution (2 x 50 mL) and dried over anhydrous magnesium sulfate and filtered. The solvent was removed under reduced pressure and the residue was redissolved in CH₂Cl₂ (150 mL). The solution was stirred with a saturated aqueous solution of potassium hexafluorophosphate (30 mL) for 72 h. The organic phase was separated, washed with water (10 mL), dried over magnesium sulfate and filtered. The residue was subjected to column chromatography (silica, CH₂Cl₂ : MeOH 10:1) to yield [Au(OEP)][PF₆] (55 mg, 0.06 mmol, 66 %) as purple powder.



¹H NMR (400 MHz, CD₂Cl₂): δ / ppm = 10.74 ppm (s, 4H, H^{5,10,15,20}), 4.31 (q, 16H, H^{2,3,7,8,12,13,17,18,1}, ³J_{HH} = 7.8 Hz), 2.02 (t, 24H, H^{2,3,7,8,12,13,17,18,2}, ³J_{HH} = 7.5 Hz).

MS (ESI⁺, MeOH): Calculated for [C₃₆H₄₄AuN₄]⁺: m/z (%) = 729.232, found: m/z = 729.232.

IR (ATR): $\tilde{\nu}$ / cm⁻¹ = 2963 (w), 2926 (m), 2855 (w), 1714 (w), 1663 (w), 1604 (w), 1516 (w), 1455 (w), 1375 (w), 1365 (w), 1263 (m), 1095 (w), 1055 (m), 1025 (m), 965 (w), 838 (s), 733 (m), 700 (w), 558 (m).

CV (0.1 M [ⁿBu₄N][PF₆]/THF, FcH/FcH⁺): $E_{1/2}$ / V = -1.20 (rev), -1.92 (rev).

UV/Vis (CH₂Cl₂): λ / nm (ϵ / 10⁴ M⁻¹ cm⁻¹) = 389 (9.8), 511 (0.5), 546 (0.8).

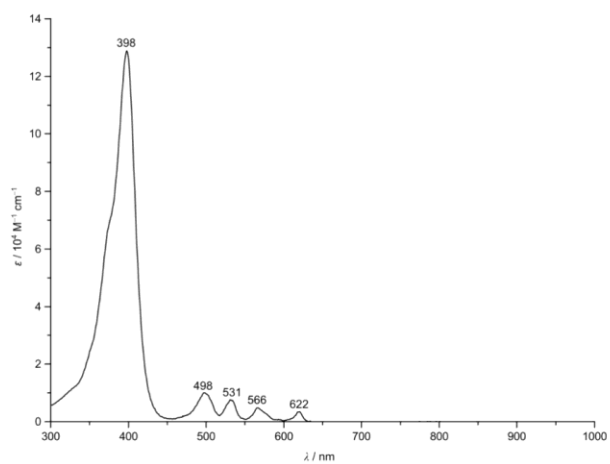


Figure S1 UV/Vis/NIR absorption spectrum of H₂OEP in CH₂Cl₂.

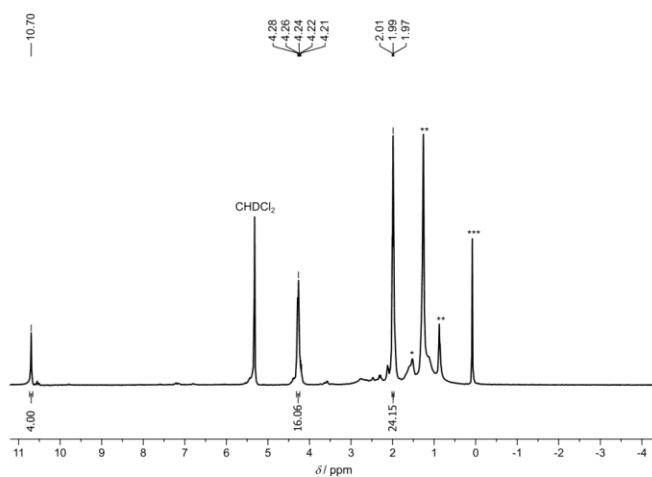


Figure S2 ¹H NMR spectrum of [Au(OEP)][PF₆] in CD₂Cl₂. * H₂O, ** H grease, *** silicon grease.

6.2 | Supporting Information to 3.2: Face-to-Face Gold Porphyrins

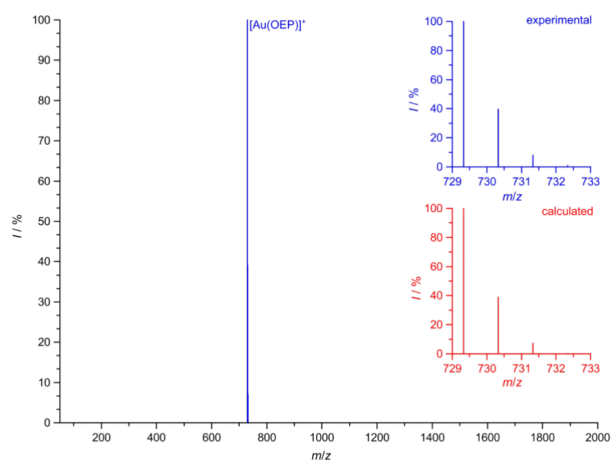


Figure S3 ESI⁺ mass spectrum of [Au(OEP)][PF₆] in MeOH. The insets display the experimental (blue) and calculated (red) isotopic pattern of the peak at $m/z = 729.323$ (C₃₆H₄₄AuN₄).

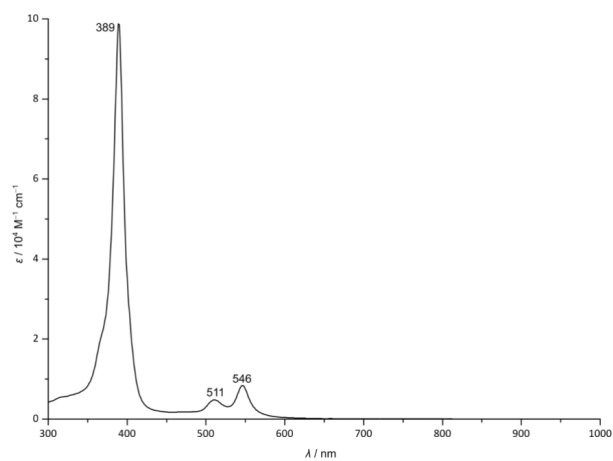


Figure S4 UV/Vis/NIR absorption spectrum of [Au(OEP)][PF₆] in CH₂Cl₂.

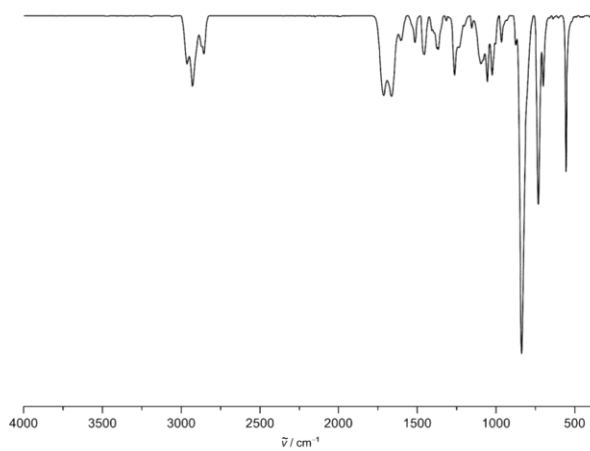
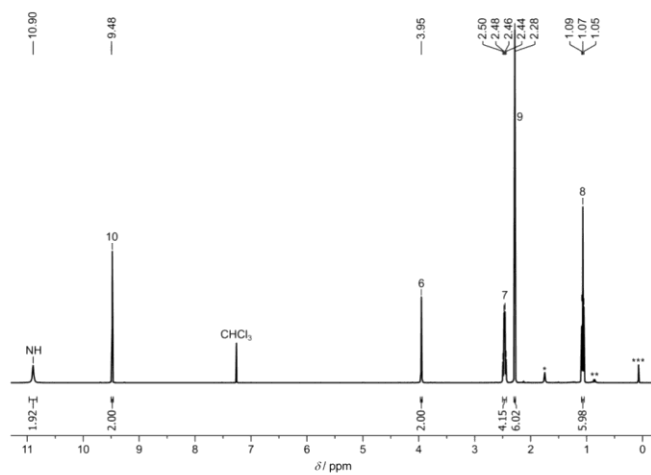
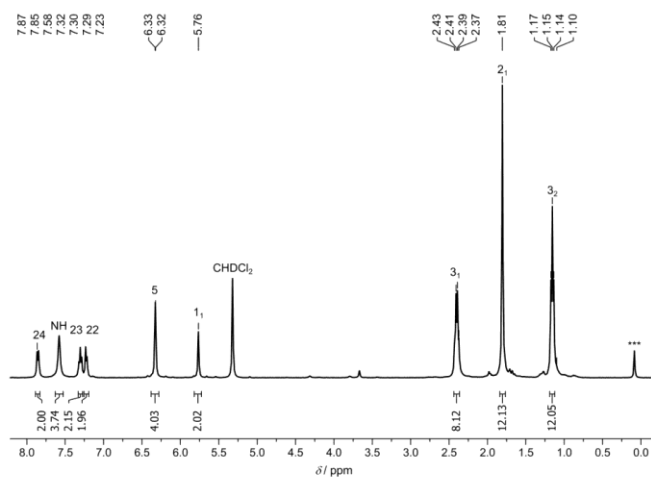


Figure S5 ATR IR spectrum of [Au(OEP)](PF₆).

6.2 | Supporting Information to 3.2: Face-to-Face Gold Porphyrins



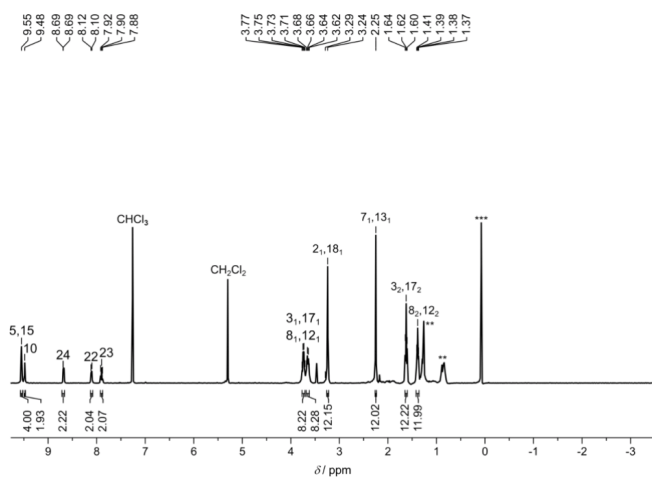


Figure S8 ^1H NMR spectrum of H_4DPD in CDCl_3 . ** H grease, *** silicon grease.

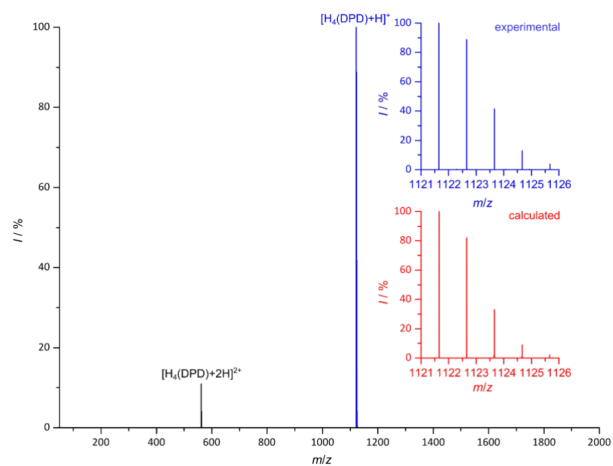


Figure S9 ESI $^+$ mass spectrum of H_4DPD in MeOH. The insets display the experimental (blue) and calculated (red) isotopic pattern of the peak at $m/z = 1121.653$ ($\text{C}_{76}\text{H}_{81}\text{N}_8\text{O}$).

6.2 | Supporting Information to 3.2: Face-to-Face Gold Porphyrins

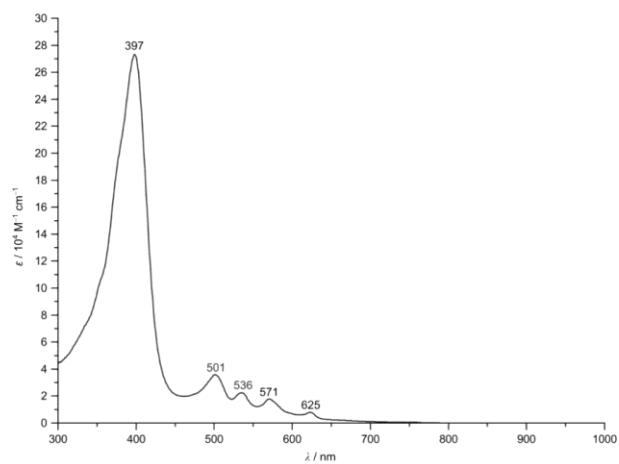


Figure S10 UV/Vis/NIR absorption spectrum of H₄DPD in CH₂Cl₂.

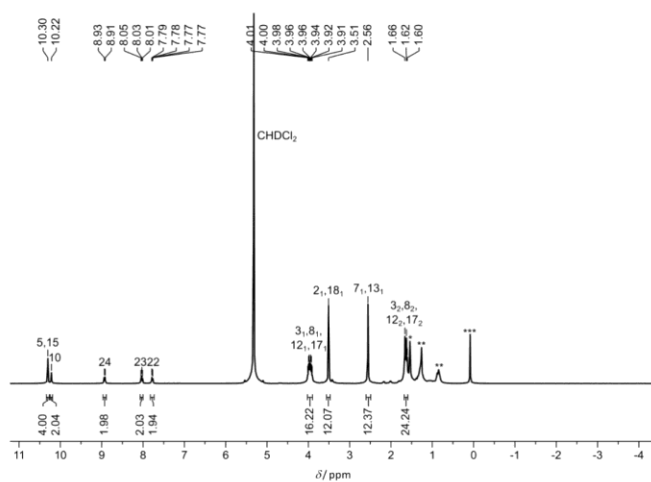


Figure S11 ^1H NMR spectrum of $[\text{Au}_2(\text{DPD})][\text{PF}_6]_2$ in CD_2Cl_2 . * H_2O , ** H grease, *** silicon grease.

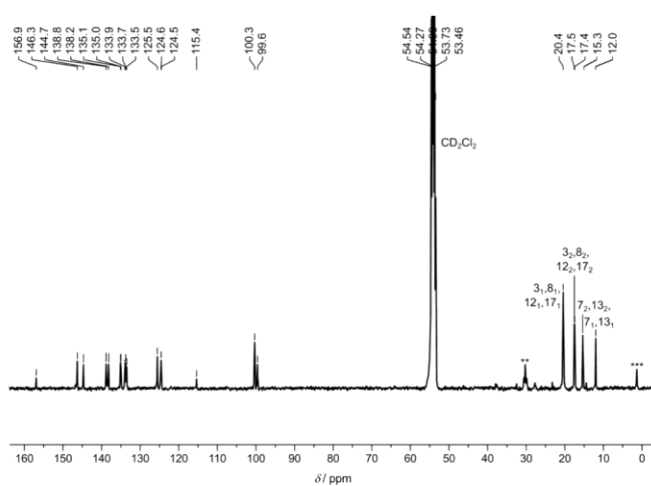


Figure S12 ^{13}C NMR spectrum of $[\text{Au}_2(\text{DPD})][\text{PF}_6]_2$ in CD_2Cl_2 . ** H grease, *** silicon grease.

6.2 | Supporting Information to 3.2: Face-to-Face Gold Porphyrins

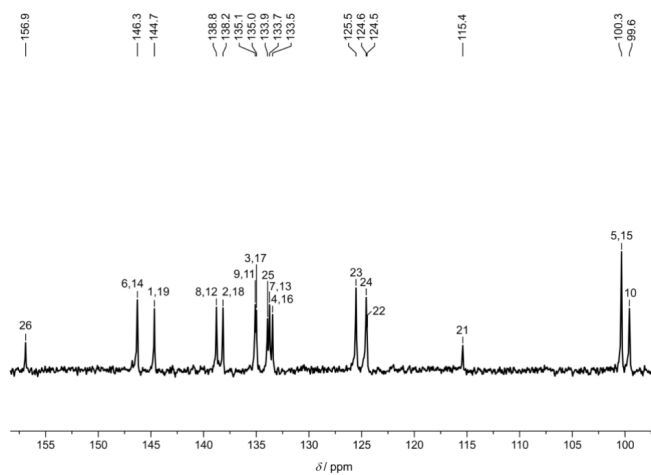


Figure S13 Part of the $^{13}\text{C}\{^1\text{H}\}$ NMR spectrum of $[\text{Au}_2(\text{DPD})][\text{PF}_6]_2$ in CD_2Cl_2 .

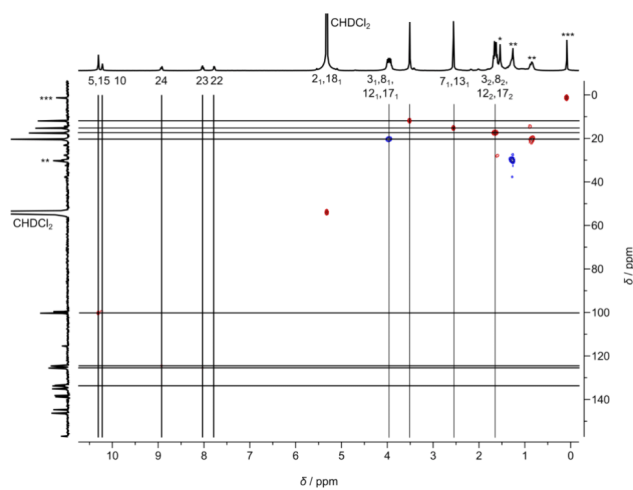


Figure S14 ^1H - ^{13}C HSQC NMR spectrum of $[\text{Au}_2(\text{DPD})][\text{PF}_6]_2$ in CD_2Cl_2 . * H_2O , * H grease, *** silicon grease.

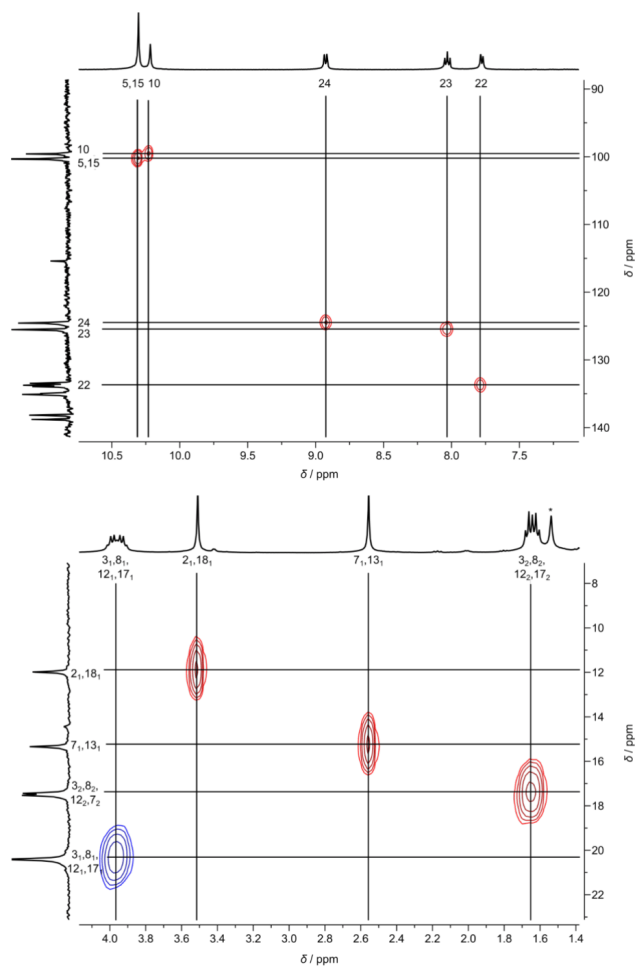


Figure S15 Parts of the ^1H - ^{13}C HSQC NMR spectrum of $[\text{Au}_2(\text{DPD})][\text{PF}_6]_2$ in CD_2Cl_2 . * H_2O .

6.2 | Supporting Information to 3.2: Face-to-Face Gold Porphyrins

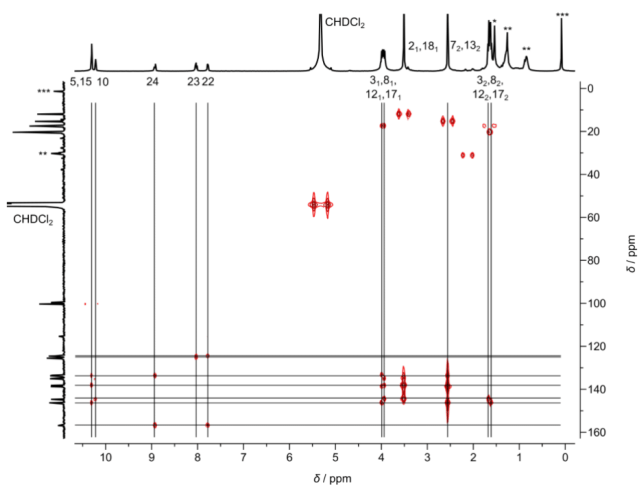


Figure S16 ^1H - ^{13}C HMBC NMR spectrum of $[\text{Au}_2(\text{DPD})][\text{PF}_6]_2$ in CD_2Cl_2 . * H_2O , ** H grease, *** silicon grease.

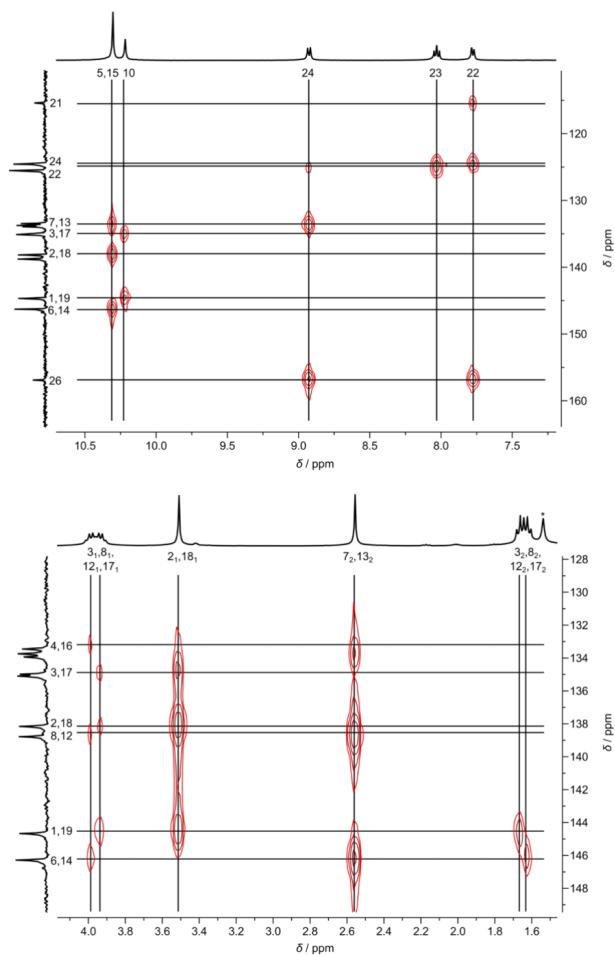


Figure S17 Parts of the ^1H - ^{13}C HMBC NMR spectrum of $[\text{Au}_2(\text{DPD})][\text{PF}_6]_2$ in CD_2Cl_2 . * H_2O .

6.2 | Supporting Information to 3.2: Face-to-Face Gold Porphyrins

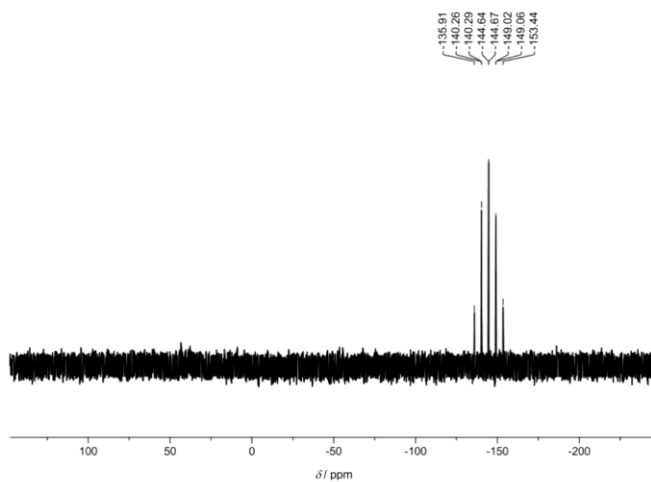


Figure S18 ^{31}P NMR spectrum of $[\text{Au}_2(\text{DPD})][\text{PF}_6]_2$ in CD_2Cl_2 .

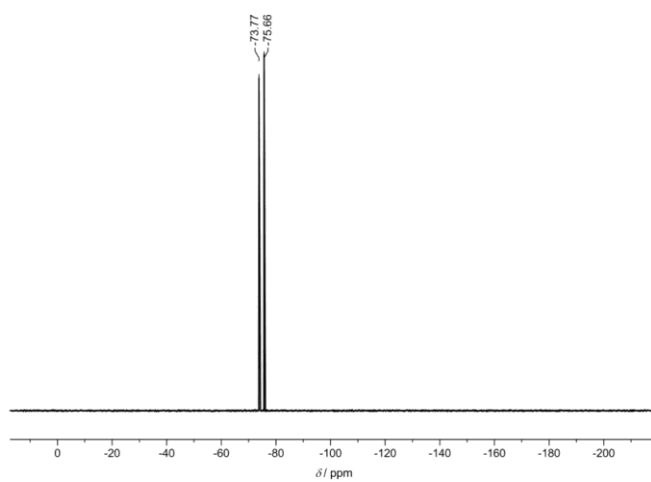


Figure S19 ^{19}F NMR spectrum of $[\text{Au}_2(\text{DPD})][\text{PF}_6]_2$ in CD_2Cl_2 .

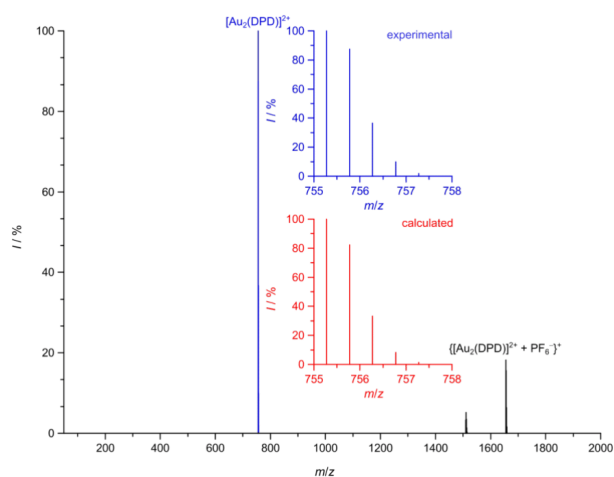


Figure S20 ESI⁺ mass spectrum of [Au₂(DPD)][PF₆]₂ in MeCN. The insets display the experimental (blue) and calculated (red) isotopic pattern of the peak at $m/z = 755.273$ (C₇₆H₇₆Au₂N₆O).

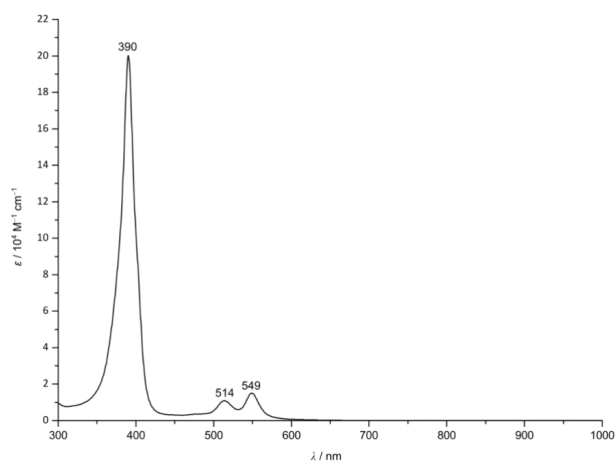


Figure S21 UV/Vis/NIR absorption spectrum of [Au₂(DPD)][PF₆]₂ in CH₂Cl₂.

6.2 | Supporting Information to 3.2: Face-to-Face Gold Porphyrins

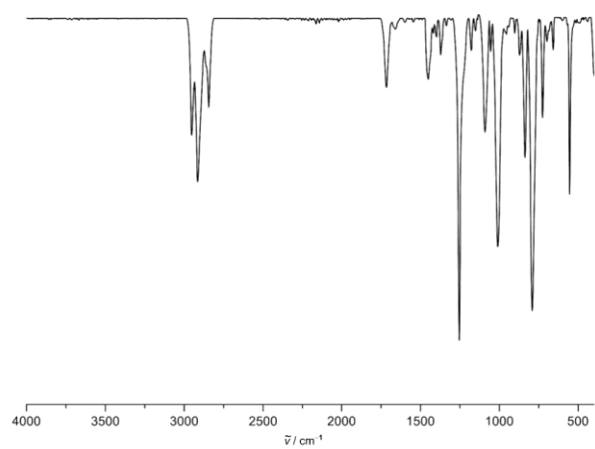


Figure S22 ATR IR spectrum of $[\text{Au}_2(\text{DPD})][\text{PF}_6]_2$.

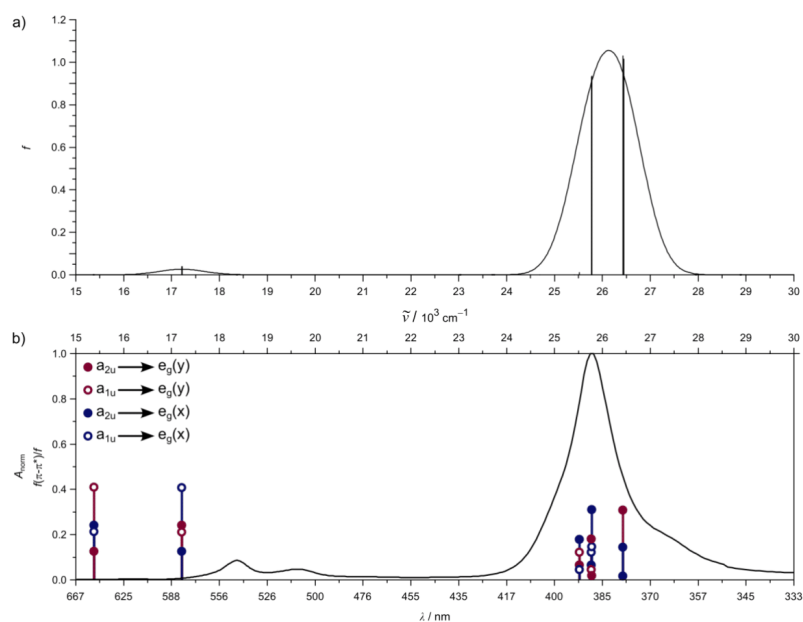


Figure S23 a) TDDFT calculated oscillator strengths of $^1[\text{Au}(\text{OEP})]^+$ including Gaussian broadening (FWHM = 1100 cm^{-1}). b) Normalized experimental UV/Vis absorption spectrum of $[\text{Au}(\text{OEP})][\text{PF}_6]$ in EtOH:MeOH 3:2 (v/v) at 77 K and TDDFT-calculated transitions with relevance to Gouterman's four orbital model ($f(\pi-\pi^*)$) relative to the Soret band. Calculated transitions hypsochromically shifted by 3000 cm^{-1} .²⁴⁻²⁶

6.2 | Supporting Information to 3.2: Face-to-Face Gold Porphyrins

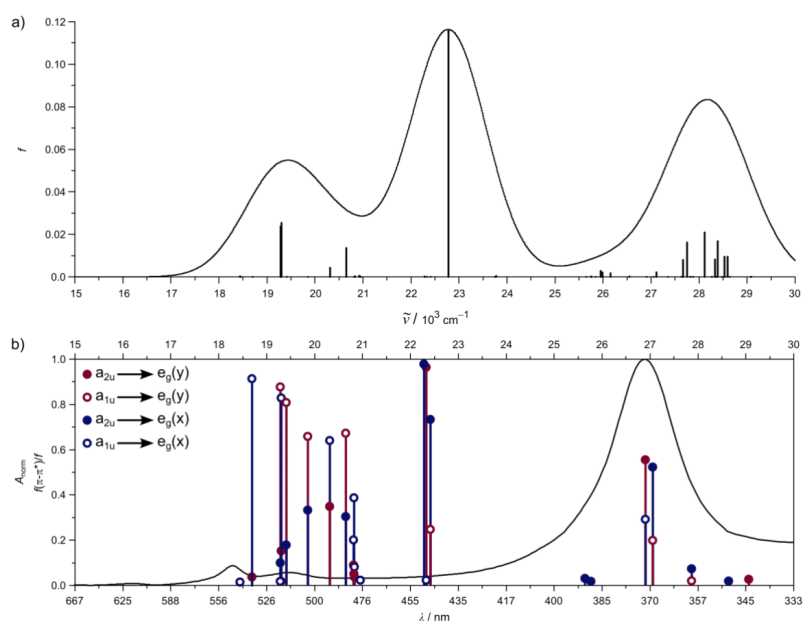


Figure S24 a) TDDFT calculated oscillator strengths of $^{1}[\text{Au}(\text{OEP})]_2^{2+}$ including Gaussian broadening (FWHM = 1800 cm^{-1}). b) Normalized experimental UV/Vis absorption spectrum of $[\text{Au}(\text{OEP})][\text{PF}_6]$ in frozen EtOH:MeOH 3:2 (v/v) solution at 77 K and TDDFT-calculated transitions with relevance to Gouterman's four orbital model ($f(\pi-\pi^*)$) relative to the magnitude of the Soret band.²⁴⁻²⁶

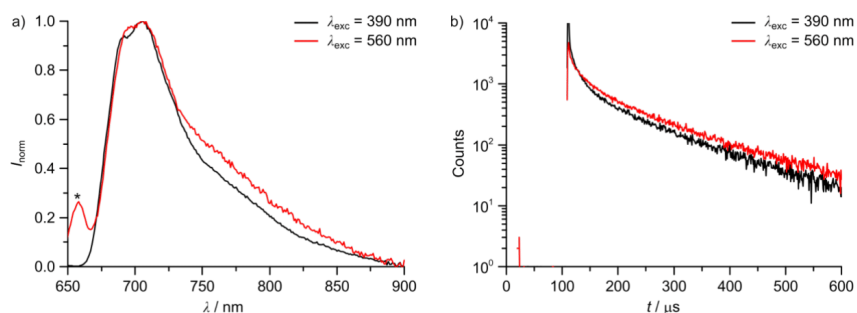


Figure S25 a) Emission spectra of $[\text{Au}(\text{OEP})][\text{PF}_6]$ ($\lambda_{\text{exc}} = 390 \text{ nm}$ and $\lambda_{\text{exc}} = 560 \text{ nm}$, respectively) in frozen EtOH:MeOH 3:2 (v/v) solution at 77 K. Asterisk denotes scattering band. b) Emission decay curves of $[\text{Au}(\text{OEP})][\text{PF}_6]$ ($\lambda_{\text{exc}} = 390 \text{ nm}$ and $\lambda_{\text{exc}} = 560 \text{ nm}$, respectively, $\lambda_{\text{em}} = 706 \text{ nm}$).

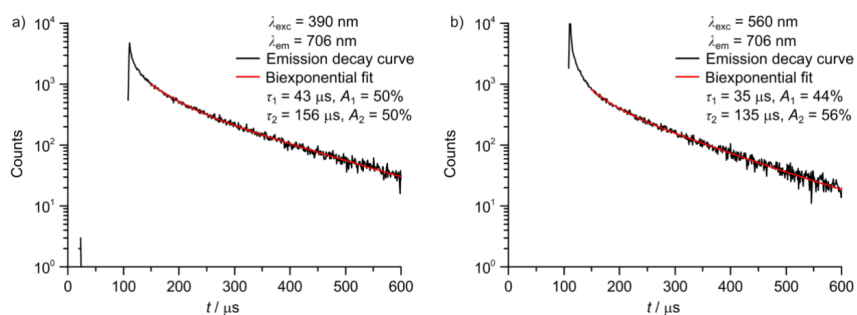


Figure S26 Emission decay curves, biexponential fits and emission lifetimes of $[\text{Au}(\text{OEP})][\text{PF}_6]$ at a) $\lambda_{\text{exc}} = 390 \text{ nm}$ and $\lambda_{\text{em}} = 706 \text{ nm}$ and b) at $\lambda_{\text{exc}} = 560 \text{ nm}$ and $\lambda_{\text{em}} = 706 \text{ nm}$ in frozen EtOH:MeOH 3:2 (v/v) solution at 77 K.

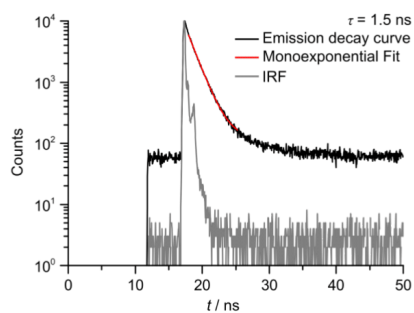


Figure S27 Emission decay curve, monoexponential fit, instrument response function (IRF) and emission lifetimes of $[\text{Au}(\text{OEP})][\text{PF}_6]$ ($\lambda_{\text{exc}} = 390 \text{ nm}$, $\lambda_{\text{em}} = 840 \text{ nm}$) in EtOH:MeOH 3:2 (v/v) at 293 K.

6.2 | Supporting Information to 3.2: Face-to-Face Gold Porphyrins

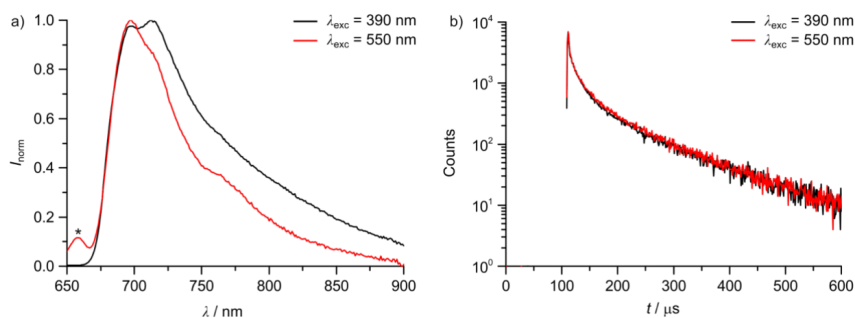


Figure S28 a) Emission spectra of $[\text{Au}_2(\text{DPD})][\text{PF}_6]_2$ ($\lambda_{\text{exc}} = 390$ nm and $\lambda_{\text{exc}} = 550$ nm, respectively) in frozen EtOH:MeOH 3:2 (v/v) solution at 77 K. Asterisk denotes scattering band. b) Emission decay curves of $[\text{Au}_2(\text{DPD})][\text{PF}_6]_2$ ($\lambda_{\text{exc}} = 390$ nm and $\lambda_{\text{exc}} = 550$ nm, respectively, $\lambda_{\text{em}} = 712$ nm and $\lambda_{\text{em}} = 698$ nm).

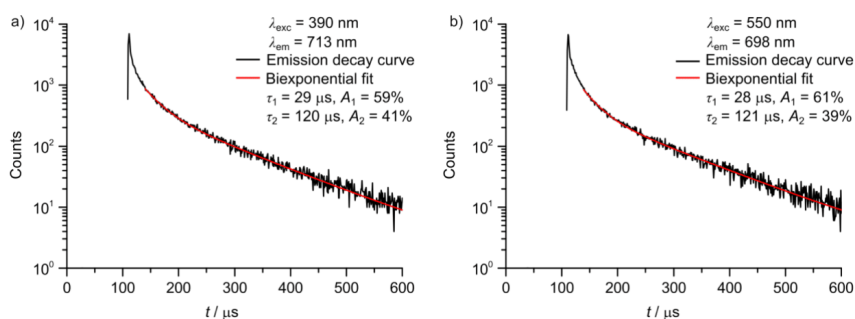


Figure S29 Emission decay curves, biexponential fits and emission lifetimes of $[\text{Au}_2(\text{DPD})][\text{PF}_6]_2$ at a) $\lambda_{\text{exc}} = 390$ nm and $\lambda_{\text{em}} = 713$ nm and b) at $\lambda_{\text{exc}} = 550$ nm and $\lambda_{\text{em}} = 698$ nm in frozen EtOH:MeOH 3:2 (v/v) solution at 77 K.

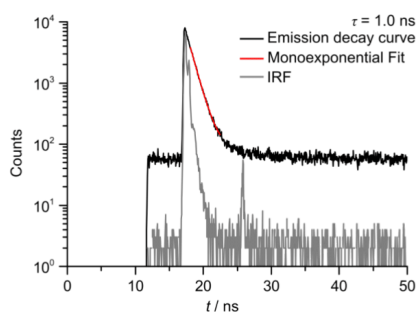


Figure S30 Emission decay curves, monoexponential fit, instrument response function (IRF) and emission lifetimes of $[\text{Au}_2(\text{DPD})][\text{PF}_6]_2$ ($\lambda_{\text{exc}} = 390$ nm, $\lambda_{\text{em}} = 850$ nm) in EtOH:MeOH 3:2 (v/v) at 293 K.

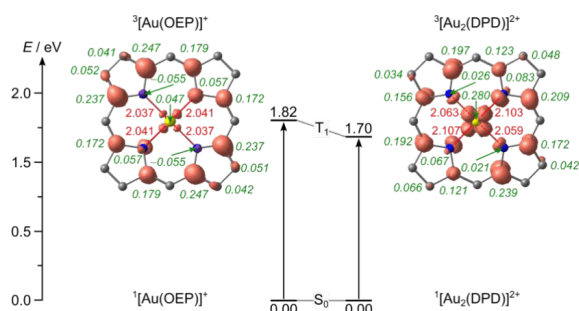


Figure S31 Relative energies of the DFT geometry optimized structures in their singlet ground states and lowest excited triplet states of $^1/{}^3[\text{Au}(\text{OEP})]^+$ and $^1/{}^3[\text{Au}_2(\text{DPD})]^{2+}$ and spin density plots. α spin density red, β spin density purple, isosurface value at 0.008 a.u., Mulliken spin densities given in green (italics) and selected distances in red in Å. Hydrogen atoms and methyl groups omitted for clarity.

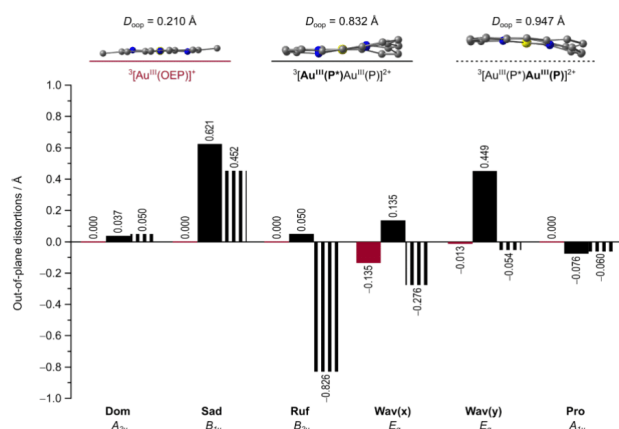


Figure S32 Normal-coordinate structure decomposition (NSD) analysis of mononuclear ${}^3[\text{Au}^{\text{III}}(\text{OEP})]^+$ complexes and separate $[\text{Au}^{\text{III}}(\text{P})]^+$ and $\text{Au}^{\text{II}}(\text{P})$ subunits of the bis(porphyrinato)gold complex ${}^3[\text{Au}_2(\text{DPD})]^{2+}$ in their lowest excited triplet states.

6.2 | Supporting Information to 3.2: Face-to-Face Gold Porphyrins

Table S1 X-band EPR data of Au(OEP) obtained from reduction of [Au(OEP)][PF₆] with one equivalent decamethylcobaltocene in frozen THF solution (77 K).

Major species					
$g_{1,2,3}$	$A_{1,2,3} (^{197}\text{Au}) / \text{G}$	$4 A_{1,2,3} (^{14}\text{N}) / \text{G}$	$H_{\text{strain}}(1,2,3) / \text{G}$	$A_{\text{strain}}(1,2,3) / \text{G}$	Fraction
2.169	42	28	20	2	0.999
2.072	26	25	18	1	
1.984	27	23	19	2	
Minor species					
$g_{1,2,3}$	$4 A_{1,2,3} (^{14}\text{N}) / \text{G}$		Line width (Gaussian) / Gauss	Line width (Lorentzian) / Gauss	Fraction
2.008	2		0.4	0.35	0.001
2.008	2				
2.008	2				

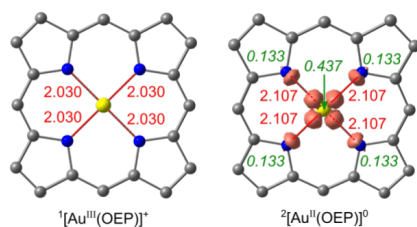


Figure S33 Selected distances in Å (red) of the DFT geometry optimized structures of $^1[\text{Au}^{\text{III}}(\text{OEP})]^+$ and $^2[\text{Au}^{\text{II}}(\text{OEP})]^0$. Mulliken spin densities are given in green (italics). Spin density is shown in orange (isosurface 0.02 a.u.). Hydrogen atoms and methyl groups omitted for clarity.

Table S2 X-band EPR data obtained from reduction of $[\text{Au}_2(\text{DPD})][\text{PF}_6]_2$ with one and two equivalents of cobaltocene in frozen THF solution at 77 K.

Major species					
$g_{1,2,3}$	$A_{1,2,3}(^{197}\text{Au}) / \text{G}$	$4 A_{1,2,3}(^{14}\text{N}) / \text{G}$	$H_{\text{strain}}(1,2,3) / \text{G}$	$A_{\text{strain}}(1,2,3) / \text{G}$	Fraction
2.182	33	24	19	2	0.994
2.071	22	23	18	1	
1.989	16	24	19	2	
Minor species					
$g_{1,2,3}$	$4 A_{1,2,3}(^{14}\text{N}) / \text{G}$		Line width (Gaussian) / Gauss	Line width (Lorentzian) / Gauss	Fraction
2.004	2		0.57	0.44	0.006
2.007	1				
2.007	2				

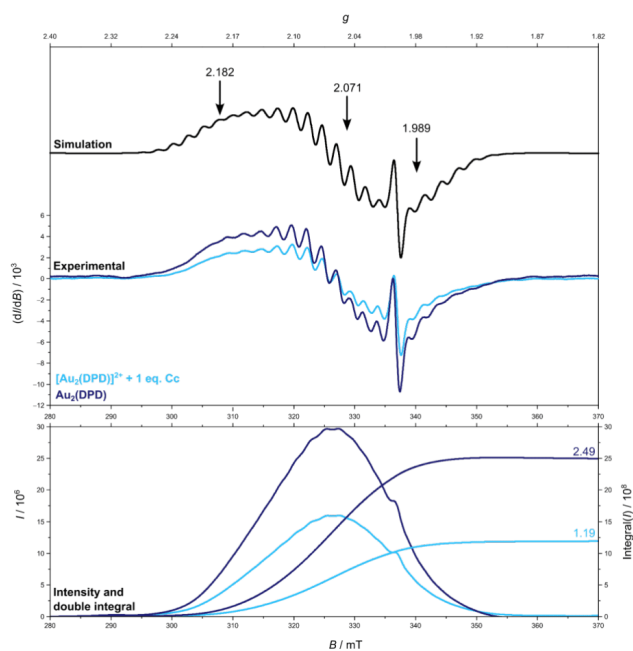


Figure S34 Top: Simulated EPR spectrum of the experimental X-band EPR spectra of $[\text{Au}_2(\text{DPD})]^+$ and $\text{Au}_2(\text{DPD})$ at 77 K in frozen THF solution. Bottom: Integral and double integral of the corresponding X-band EPR spectra.

6.2 | Supporting Information to 3.2: Face-to-Face Gold Porphyrins

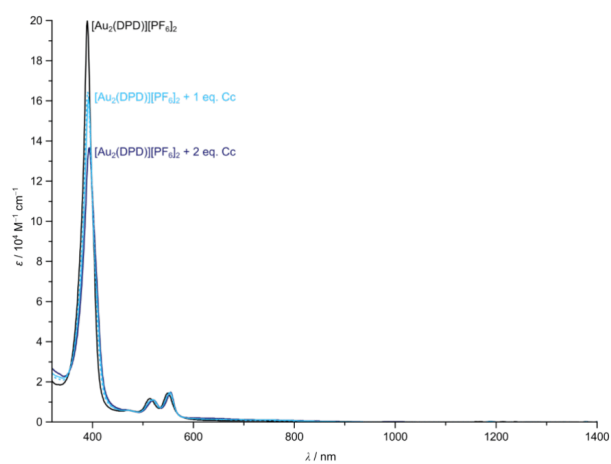


Figure S35 UV/Vis/NIR absorption spectra of $[\text{Au}_2(\text{DPD})][\text{PF}_6]_2$ (solid black) in THF upon addition of one (solid light blue) and two (solid blue) equivalents of cobaltocene and sum spectrum of $0.5 [\text{Au}_2(\text{DPD})][\text{PF}_6]_2 + 0.5 \text{ Au}_2(\text{DPD})$ (dashed light blue).

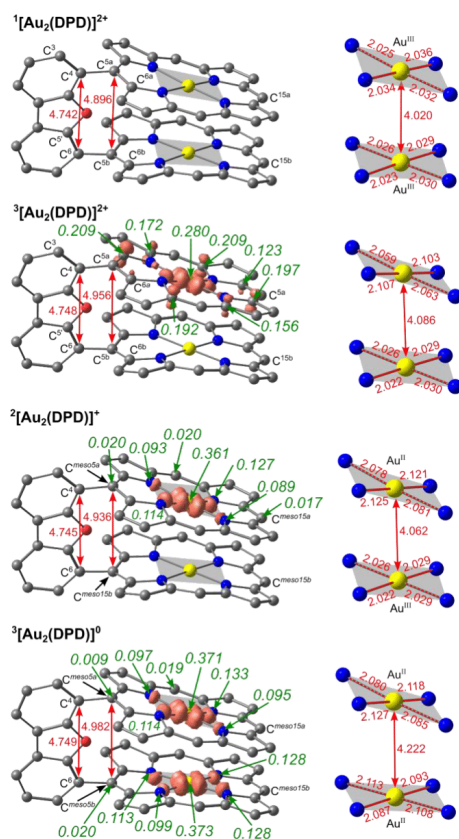


Figure S36 Left: DFT geometry optimized structures of $^1[\text{Au}_2(\text{DPD})]^{2+}$, $^3[\text{Au}_2(\text{DPD})]^{2+}$, $^2[\text{Au}_2(\text{DPD})]^+$ and $^3[\text{Au}_2(\text{DPD})]^0$ with Mulliken spin densities (italics, green) and C⁴/C⁵ and C^{meso}/C^{meso} distances given in Å (red). Spin density plots are shown at an isosurface value of 0.02 a.u. Right: Corresponding [AuN₄] coordination with Au-Au and Au-N distances given in Å (red). Hydrogen atoms and methyl groups omitted for clarity.

6.2 | Supporting Information to 3.2: Face-to-Face Gold Porphyrins

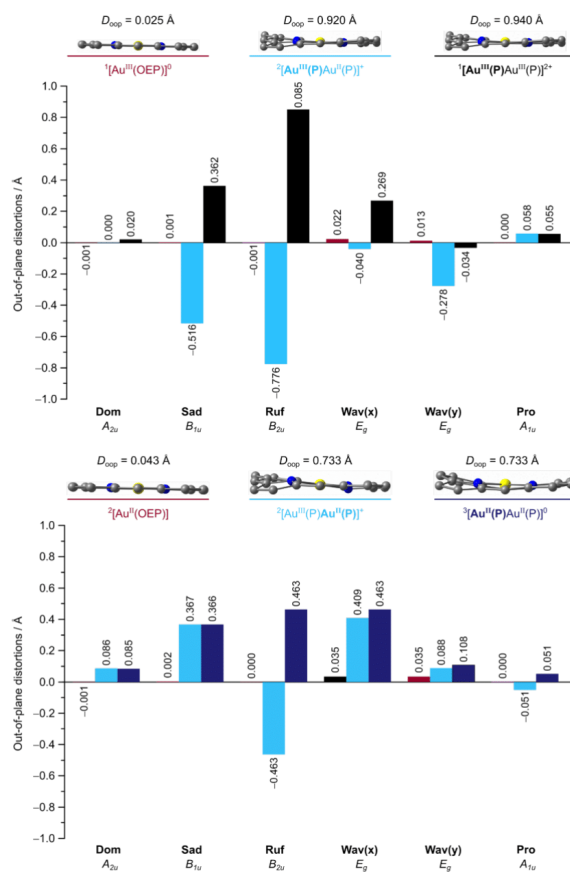


Figure S37 Normal-coordinate structure decomposition (NSD) analysis of mononuclear $^1[\text{Au}^{\text{III}}(\text{OEP})]^{2+}/^2[\text{Au}^{\text{II}}(\text{OEP})]^0$ complexes and separate $[\text{Au}^{\text{III}}(\text{P})]^+$ and $\text{Au}^{\text{II}}(\text{P})$ subunits of the bis(porphyrinato)gold complexes $^1[\text{Au}_2(\text{DPD})]^{2+}/^2[\text{Au}_2(\text{DPD})]^+/^3[\text{Au}_2(\text{DPD})]^0$.

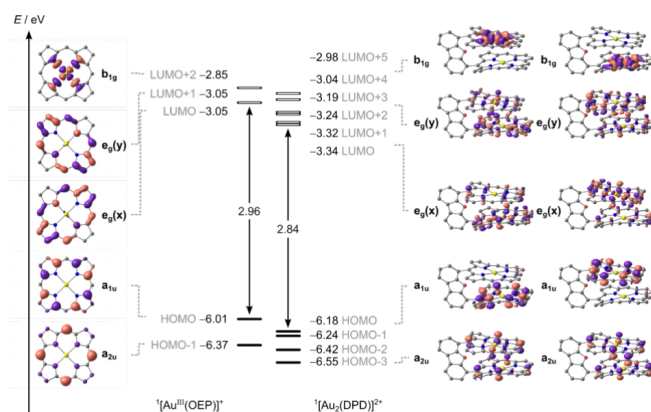


Figure S38 Molecular orbital diagrams of $^1[\text{Au}^{\text{III}}(\text{OEP})]^+$ and $^1[\text{Au}_2(\text{DPD})]^{2+}$ and frontier molecular orbitals and symmetry description according to Gouterman's four orbital model²⁴⁻²⁶ obtained from DFT geometry optimized structures. Occupied molecular orbitals are indicated by filled and unoccupied molecular orbitals by empty bars. Hydrogen atoms and methyl substituents omitted for clarity. Isosurface value at 0.05 a.u.

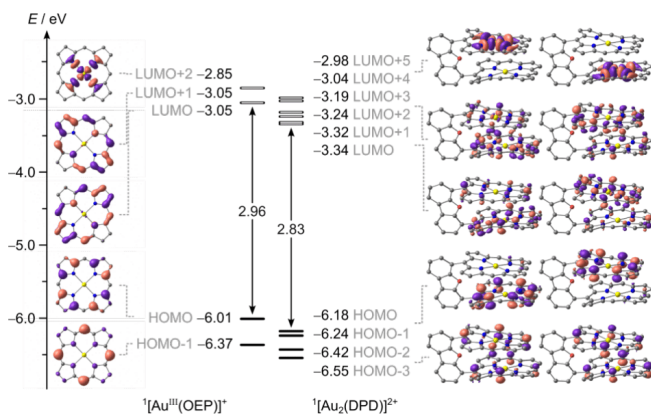


Figure S39 Molecular orbital diagrams of $^1[\text{Au}^{\text{III}}(\text{OEP})]^+$ and $^1[\text{Au}(\text{OEP})_2]^{2+}$, frontier molecular orbitals and symmetry description according to Gouterman's four orbital model obtained from DFT geometry optimized structures.²⁴⁻²⁶ Occupied molecular orbitals are indicated by filled and unoccupied molecular orbitals by empty bars. Hydrogen atoms and methyl substituents omitted for clarity. Isosurface value at 0.05 a.u.

6.2 | Supporting Information to 3.2: Face-to-Face Gold Porphyrins

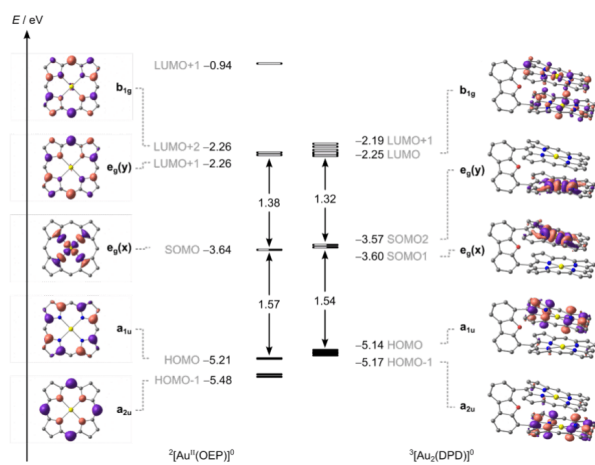


Figure S40 Molecular orbital diagrams of $^2[\text{Au}(\text{OEP})]_0$ and $^3[\text{Au}_2(\text{DPD})]_0$ and frontier molecular orbitals description according to Gouterman's four orbital model²⁴⁻²⁶ obtained from DFT geometry optimized structures. Occupied molecular orbitals are indicated by filled, singly occupied α molecular orbitals by half-filled and unoccupied molecular orbitals by empty bars. Hydrogen atoms and methyl substituents omitted for clarity. Isosurface value at 0.05 a.u.

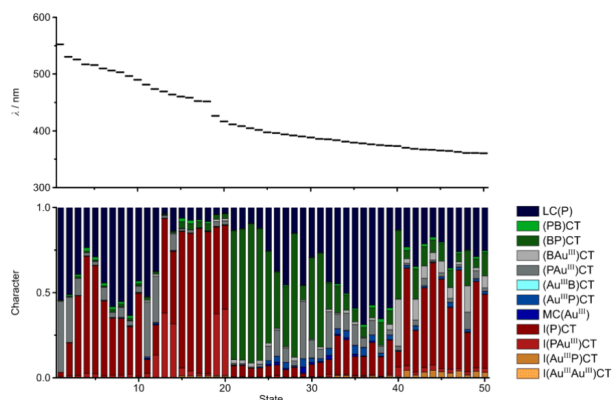


Figure S41 TDDFT-RKS charge transfer numbers of $^1[\text{Au}_2(\text{DPD})]^{2+}$ defined from 0 to 1 of the energetically lowest-lying 50 singlet states applying the TheoDORE software package.¹² LC: Ligand-centered, MC = metal centered, P = porphyrin, B = bridge, ICT = interplanar(porphyrin-to-porphyrin, porphyrin-to-gold, gold-to-porphyrin, inter-gold-to-gold)charge transfer.

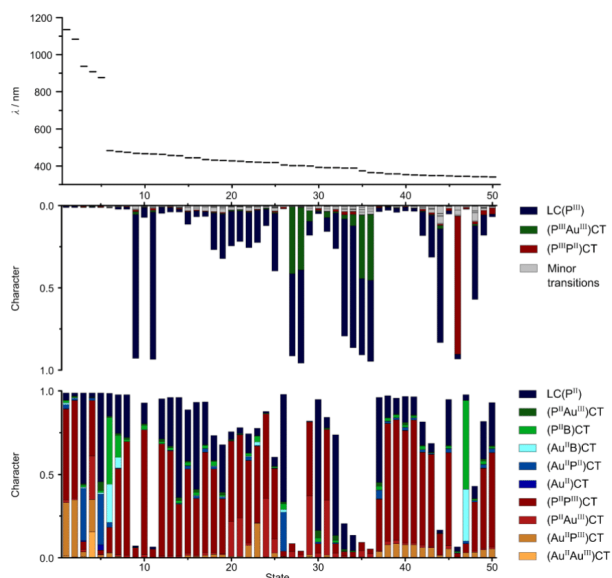


Figure S42 TDDFT-UKS calculated charge transfer numbers of $^2[\text{Au}_2(\text{DPD})]^+$ defined from 0 to 1 of the energetically lowest-lying 50 doublet states applying the TheoDORE software package.¹² LC: Ligand-centered, MC = metal centered, P = porphyrin, B = bridge, ICT = interplanar(porphyrin-to-porphyrin, porphyrin-to-gold, gold-to-porphyrin, inter-gold-to-gold)charge transfer.

6.2 | Supporting Information to 3.2: Face-to-Face Gold Porphyrins

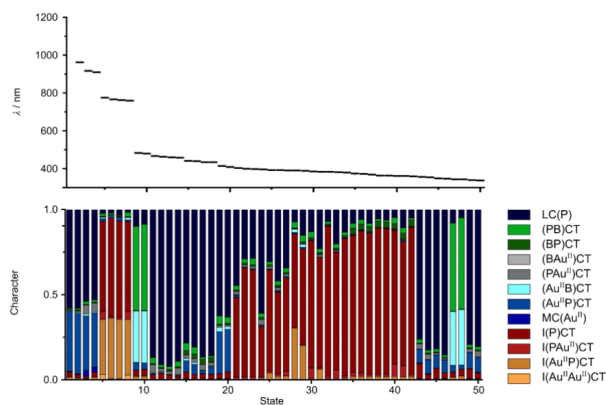


Figure S43 TDDFT-UKS calculated charge transfer numbers of $^3[\text{Au}_2(\text{DPD})]_0$ defined from 0 to 1 of the energetically lowest-lying 50 triplet states applying the TheoDORÉ software package.¹² LC: Ligand-centered, MC = metal centered, P = porphyrin, B = bridge, ICT = interplanar(porphyrin-to-porphyrin, porphyrin-to-gold, gold-to-porphyrin, inter-gold-to-gold)charge transfer.

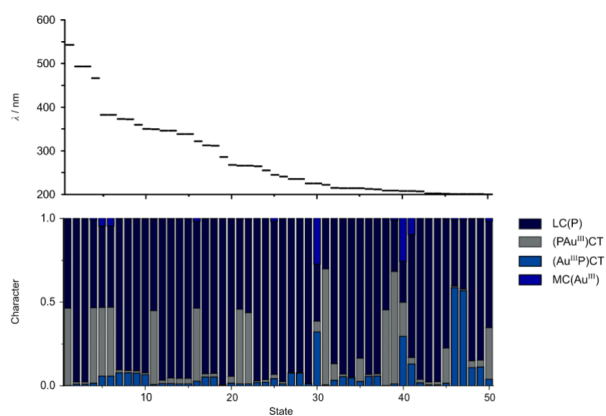


Figure S44 TDDFT-RKS calculated charge transfer numbers of $^1[\text{Au}^{\text{III}}(\text{OEP})]^-$ defined from 0 to 1 of the energetically lowest-lying 50 singlet states applying the TheoDORÉ software package.¹² LC: Ligand-centered, MC = metal centered, P = porphyrin, CT = charge transfer.

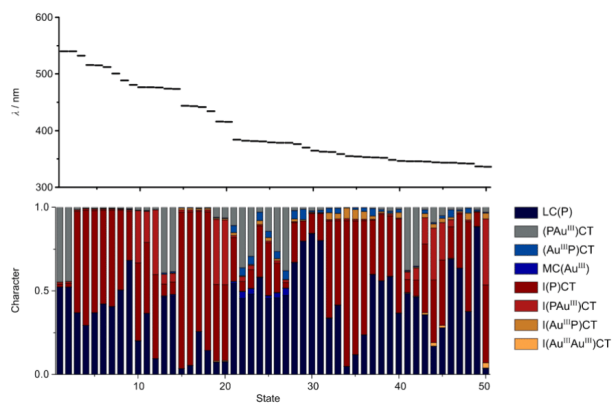
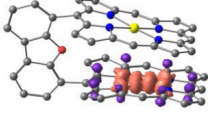
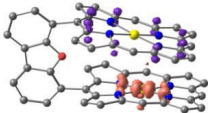
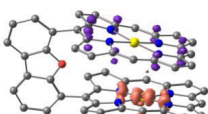
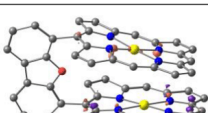
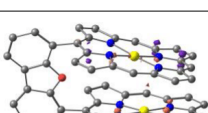
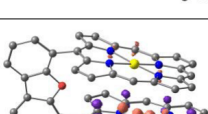
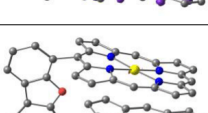
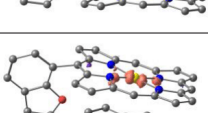
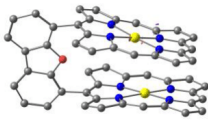
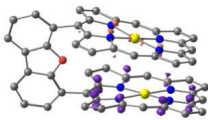
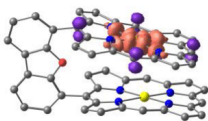
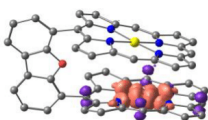
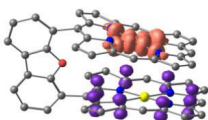
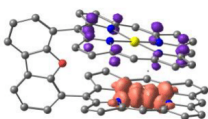
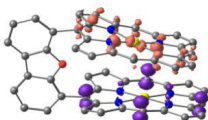
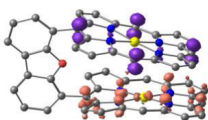
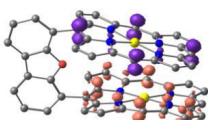


Figure S45 TDDFT-RKS calculated charge transfer numbers of $^1\{[\text{Au}^{\text{III}}(\text{OEP})]_2\}^{2+}$ defined from 0 to 1 of the energetically lowest-lying 50 singlet states applying the TheoDORÉ software package. LC: Ligand-centered, MC = metal centered, P = porphyrin, ICT = interplanar(porphyrin-to-porphyrin, porphyrin-to-gold, gold-to-porphyrin, inter-gold-to-gold)charge transfer.

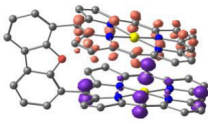
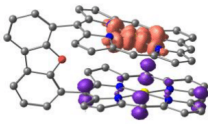
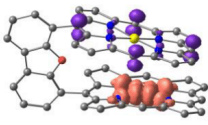
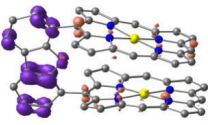
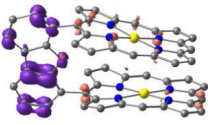
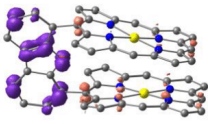
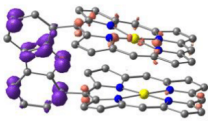
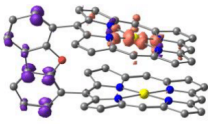
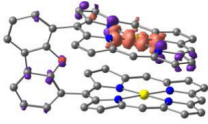
6.2 | Supporting Information to 3.2: Face-to-Face Gold Porphyrins

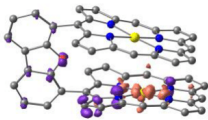
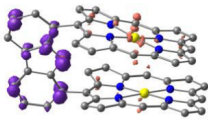
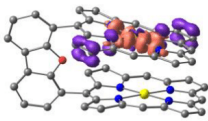
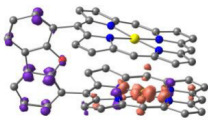
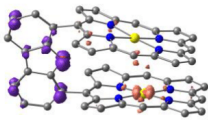
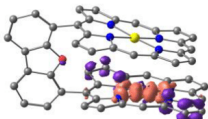
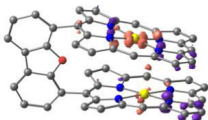
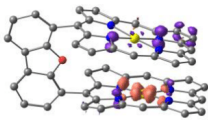
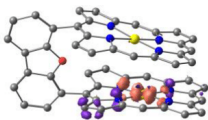
Table S3 TDDFT calculated transitions of $^1[\text{Au}_2(\text{DPD})]^{2+}$.

#	λ / nm (Hypsochromically shifted by 5000 cm^{-1})	f	Difference electron density (purple = electron loss; orange = electron gain). Isosurface value at 0.008 a.u.
1	432.8	0.003770983	
2	419.3	0.002193893	
3	416.3	0.006264071	
4	410.9	0.012938221	
5	410.0	0.001944983	
6	406.1	0.008007671	
7	403.8	0.001693523	
8	401.9	0.00184558	

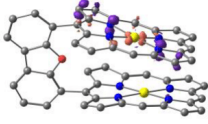
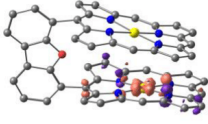
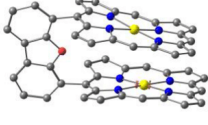
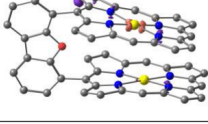
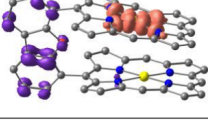
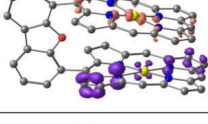
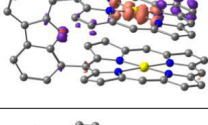
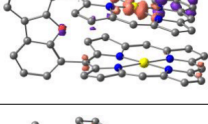
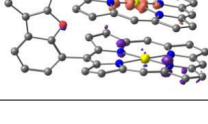
9	397.6	0.013162902	
10	393.7	0.003769657	
11	387.9	0.0062474	
12	383.1	0.002967485	
13	380.0	0.000883919	
14	376.4	0.001612568	
15	374.3	0.012161372	
16	373.1	0.00204654	
17	369.1	0.030038843	

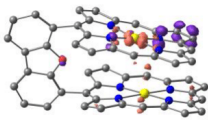
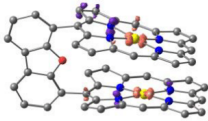
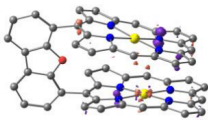
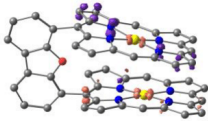
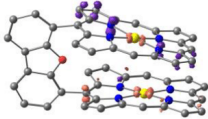
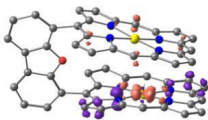
6.2 | Supporting Information to 3.2: Face-to-Face Gold Porphyrins

18	368.5	0.000299785	
19	351.6	0.005709986	
20	345.0	0.001702765	
21	341.1	0.00188138	
22	339.1	0.008406662	
23	336.4	0.004565721	
24	334.7	0.038799327	
25	331.4	0.005483376	
26	330.5	0.002512495	

27	328.9	0.00060966	
28	327.7	0.007775241	
29	326.6	0.000267583	
30	325.1	0.014730331	
31	323.3	0.008160128	
32	322.9	0.002456899	
33	321.8	0.002539461	
34	320.0	0.000904634	
35	318.6	0.000795518	

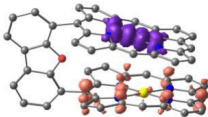
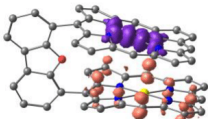
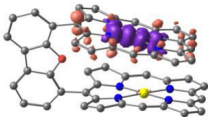
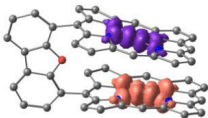
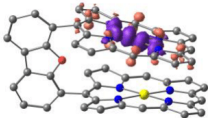
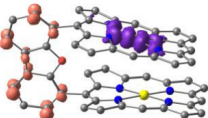
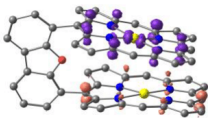
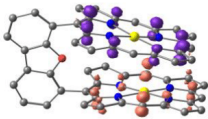
6.2 | Supporting Information to 3.2: Face-to-Face Gold Porphyrins

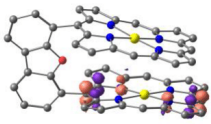
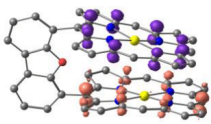
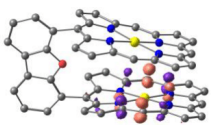
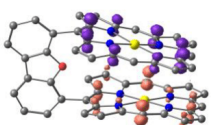
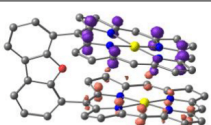
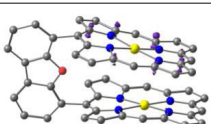
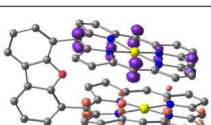
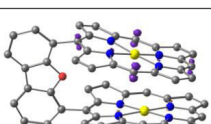
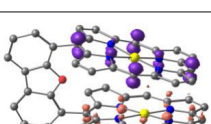
36	318.0	0.00151417	
37	316.8	0.001592524	
38	316.0	0.006287548	
39	315.1	0.011779292	
40	314.4	0.00230408	
41	312.2	0.010628748	
42	311.0	0.00326052	
43	310.3	0.014254915	
44	309.6	0.001131485	

45	308.8	0.022807708	
46	308.5	0.00367731	
47	307.2	0.002649792	
48	306.0	0.010454088	
49	305.9	0.018431816	
50	305.2	0.009096259	

6.2 | Supporting Information to 3.2: Face-to-Face Gold Porphyrins

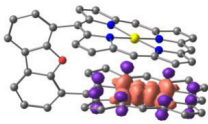
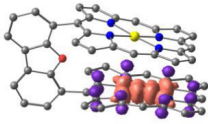
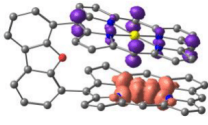
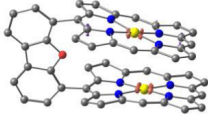
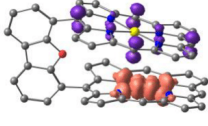
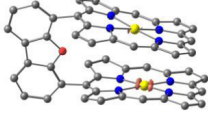
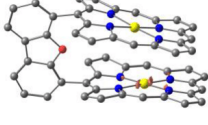
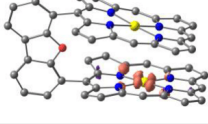
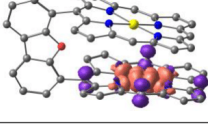
Table S4 TDDFT calculated transitions of $^2[\text{Au}_2(\text{DPD})]^+$.

#	λ / nm (Hypsochromically shifted by 5000 cm^{-1})	f	Difference electron density (purple = electron loss; orange = electron gain). Isosurface value at 0.008 a.u.
1	1250.8	4.6663E-5	
2	1188.0	0.00214355	
3	1014.6	4.1271E-5	
4	980.5	1.69E-6	
5	944.4	0.000135284	
6	501.6	0.003050478	
7	497.5	0.003494762	
8	493.2	0.000764185	

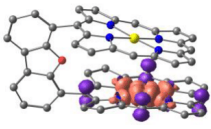
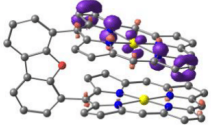
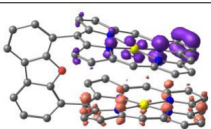
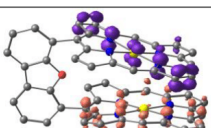
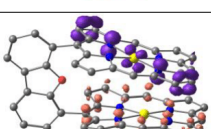
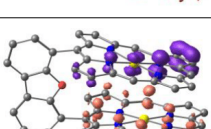
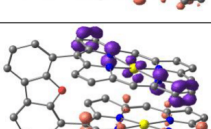
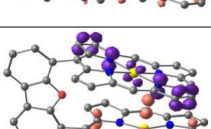
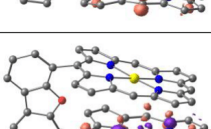
9	486.5	0.000104284	
10	484.3	0.000918011	
11	481.9	9.5799E-5	
12	479.8	0.00158499	
13	473.6	0.000705818	
14	472.3	0.000364105	
15	461.6	0.000302889	
16	459.8	0.0016135	
17	449.9	0.000584096	

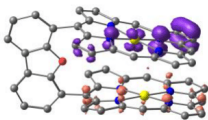
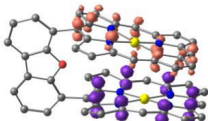
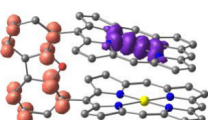
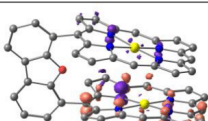
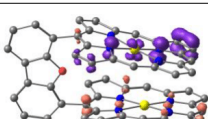
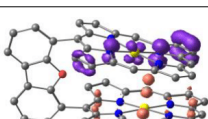
6.2 | Supporting Information to 3.2: Face-to-Face Gold Porphyrins

18	447.1	0.002588961	
19	444.4	0.001033616	
20	441.9	0.000910697	
21	441.8	0.001075202	
22	436.3	0.00069091	
23	435.0	0.000558215	
24	432.7	5.6091E-5	
25	432.3	0.000419559	
26	419.5	0.003350995	

27	414.6	0.000436457	
28	414.2	0.003846801	
29	412.8	0.000605576	
30	405.9	0.026434696	
31	403.7	0.00078379	
32	402.9	0.001921293	
33	402.0	0.012797276	
34	400.6	0.018694565	
35	386.3	1.0659E-5	

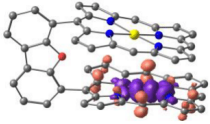
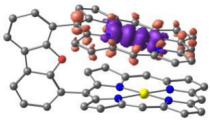
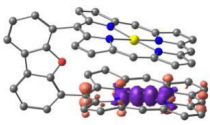
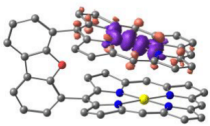
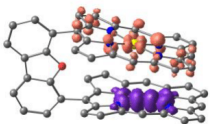
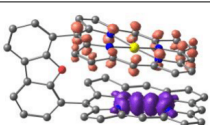
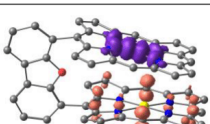
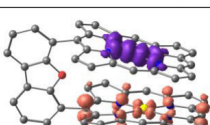
6.2 | Supporting Information to 3.2: Face-to-Face Gold Porphyrins

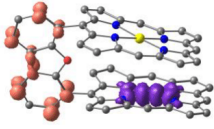
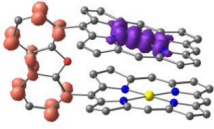
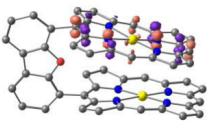
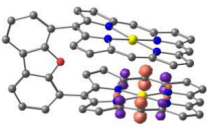
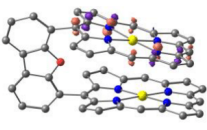
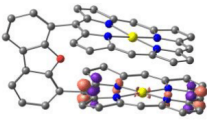
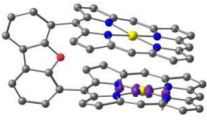
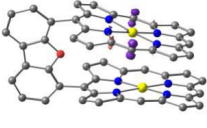
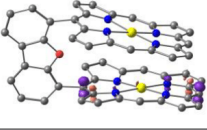
36	376.5	0.00430797	
37	374.0	0.000264029	
38	368.2	0.000572557	
39	367.1	0.000653469	
40	363.3	0.002112165	
41	362.6	0.00024669	
42	360.8	0.001053312	
43	359.0	0.00148685	
44	358.7	0.000229656	

45	357.1	0.000461325	
46	354.9	0.00110569	
47	354.3	8.2781E-5	
48	352.3	0.000204041	
49	352.1	0.000264253	
50	349.9	5.5691E-5	

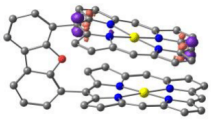
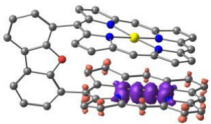
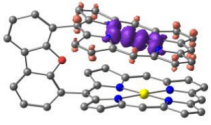
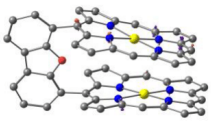
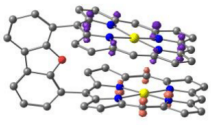
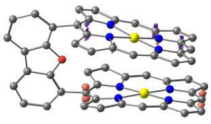
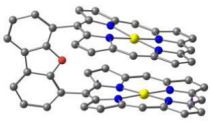
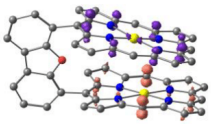
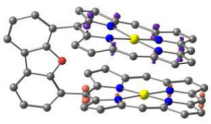
6.2 | Supporting Information to 3.2: Face-to-Face Gold Porphyrins

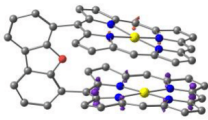
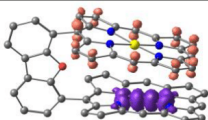
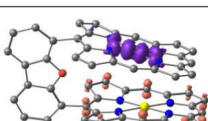
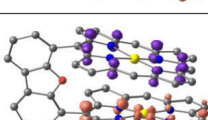
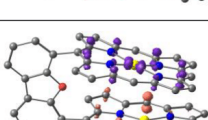
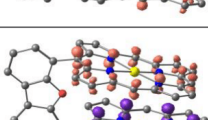
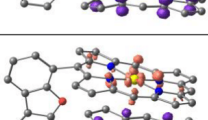
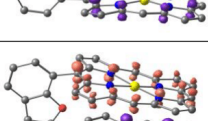
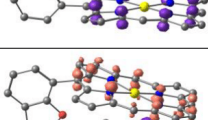
Table S5 TDDFT calculated transitions of $^3[\text{Au}_2(\text{DPD})]_0$.

#	λ / nm (Hypsochromically shifted by 5000 cm^{-1})	f	Difference electron density (purple = electron loss; orange = electron gain). Isosurface value at 0.005 a.u.
1	1113.2	5.068E-6	
2	1049.2	2.7179E-5	
3	995.7	1.1601E-5	
4	988.1	7.3092E-5	
5	830.9	9.888E-5	
6	821.5	0.000399273	
7	816.8	0.001135642	
8	812.9	6.3107E-5	

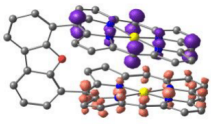
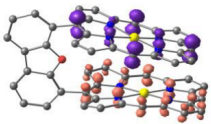
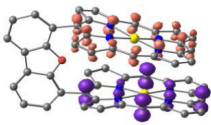
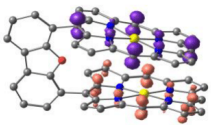
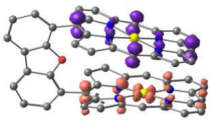
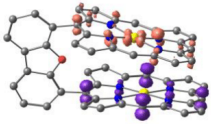
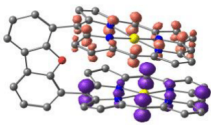
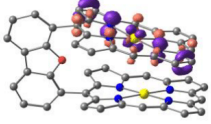
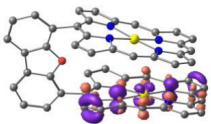
9	503.5	0.004417039	
10	500.5	0.005683903	
11	487.4	0.000813289	
12	482.1	2.3955E-5	
13	478.4	2.6124E-5	
14	477.2	0.000417421	
15	459.6	9.4841E-5	
16	457.4	0.001044318	
17	452.1	0.000571777	

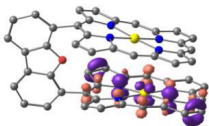
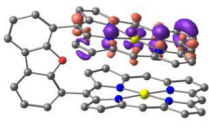
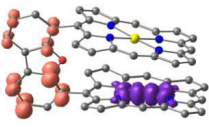
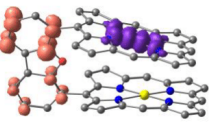
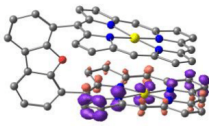
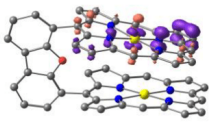
6.2 | Supporting Information to 3.2: Face-to-Face Gold Porphyrins

18	450.8	0.000752841	
19	428.8	0.005370119	
20	424.1	0.001875046	
21	417.2	0.006134964	
22	414.6	0.012985301	
23	412.2	0.019382449	
24	409.4	0.011264582	
25	405.7	0.000534024	
26	405.4	0.002728457	

27	404.5	0.004196505	
28	403.9	0.000463727	
29	401.9	0.003586389	
30	398.5	0.001571312	
31	397.6	0.007496589	
32	396.9	0.000743468	
33	394.7	0.000869042	
34	393.1	0.002713504	
35	386.8	0.007688801	

6.2 | Supporting Information to 3.2: Face-to-Face Gold Porphyrins

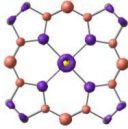
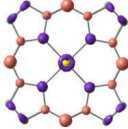
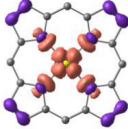
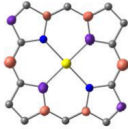
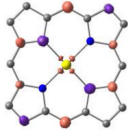
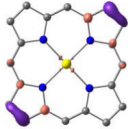
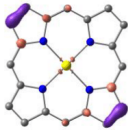
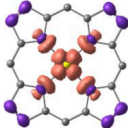
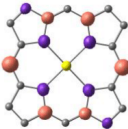
36	385.8	0.000331837	
37	380.7	0.007243711	
38	376.1	0.000289136	
39	375.6	0.005453691	
40	373.2	0.000305324	
41	372.8	0.014965827	
42	370.9	0.000591088	
43	367.7	0.000389492	
44	365.7	1.1978E-5	

45	359.9	1.619E-6	
46	358.0	2.9205E-5	
47	354.6	0.00104644	
48	353.3	0.000159042	
49	349.9	2.8756E-5	
50	349.1	0.000118626	

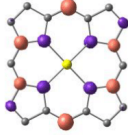
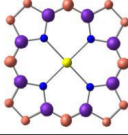
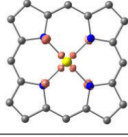
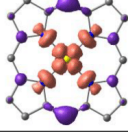
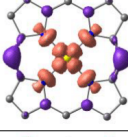
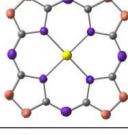
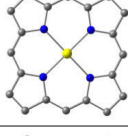
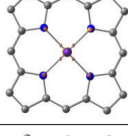
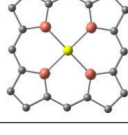
6.2 | Supporting Information to 3.2: Face-to-Face Gold Porphyrins

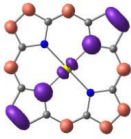
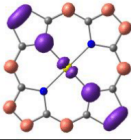
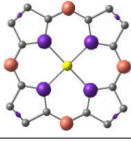
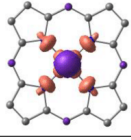
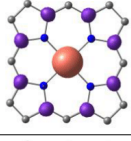
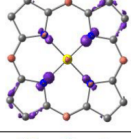
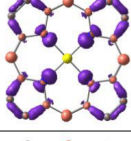
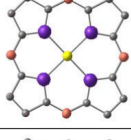
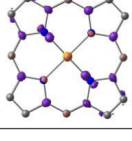
Table S6 TDDFT calculated transitions of $^1[\text{Au}(\text{OEP})]^+$.

	λ / nm	f	Difference electron density (purple = electron loss; orange = electron gain). Isosurface value at 0.004 a.u.
1	544.1	0.000123322	
2	494.8	0.038105813	
3	494.6	0.037929279	
4	468.1	0.000459337	
5	384.2	4.1E-8	
6	384	3.8E-8	
7	374.5	2.1E-8	
8	374	2.1E-8	

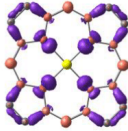
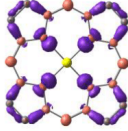
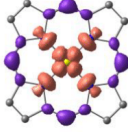
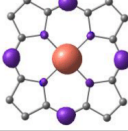
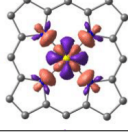
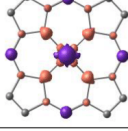
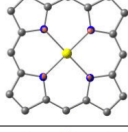
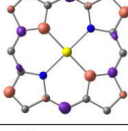
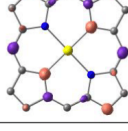
9	361.1	4.4E-8	
10	351.9	1.6E-8	
11	350.7	0.01151767	
12	347.6	0.930943811	
13	347.4	0.934959025	
14	339.8	1.028759728	
15	339.6	1.01425579	
16	323	0.00009274	
17	313.6	0.87302000	

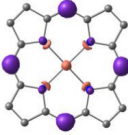
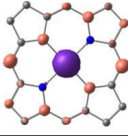
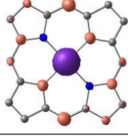
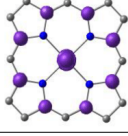
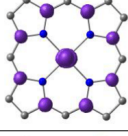
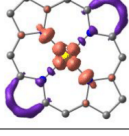
6.2 | Supporting Information to 3.2: Face-to-Face Gold Porphyrins

18	313.5	0.00007745	
19	287.2	2E-9	
20	269.4	1E-9	
21	267.8	0.00000010	
22	267.6	0.00000007	
23	266.4	0.00000000	
24	256.5	0.00000000	
25	246.3	1E-9	
26	242.6	2E-9	

27	236.7	0.08967930	
28	236.7	0.08972400	
29	226.6	5E-9	
30	226.4	4E-9	
31	223.7	0.00000000	
32	216.2	0.00019271	
33	215.7	0.00025028	
34	215.6	0.00000004	
35	215.5	0.00012824	

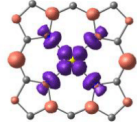
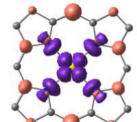
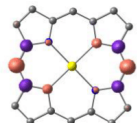
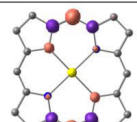
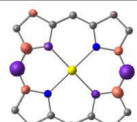
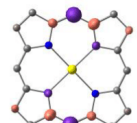
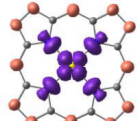
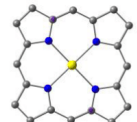
6.2 | Supporting Information to 3.2: Face-to-Face Gold Porphyrins

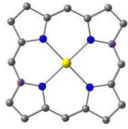
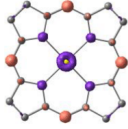
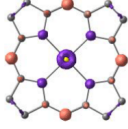
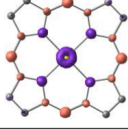
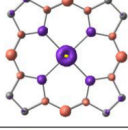
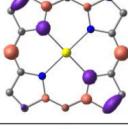
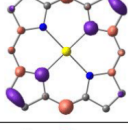
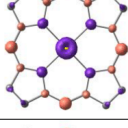
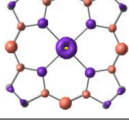
36	214.4	0.00034262	
37	213.3	0.00198051	
38	210.6	0.00000401	
39	210.3	0.00000006	
40	209.6	0.00000032	
41	209.3	0.00000011	
42	208.4	0.00000002	
43	203.9	0.04095048	
44	203.8	0.04196182	

45	203.2	0.01014126	
46	202.5	0.00000076	
47	202.4	0.00000081	
48	202.1	0.00000005	
49	202.1	0.00000011	
50	201.4	1.14039846	

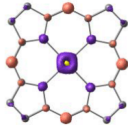
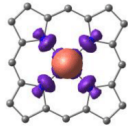
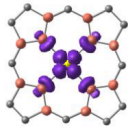
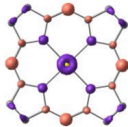
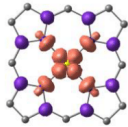
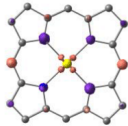
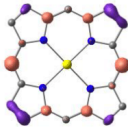
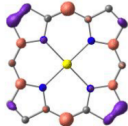
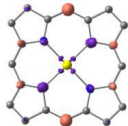
6.2 | Supporting Information to 3.2: Face-to-Face Gold Porphyrins

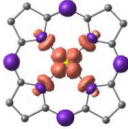
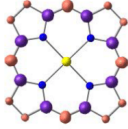
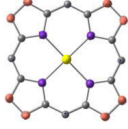
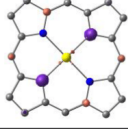
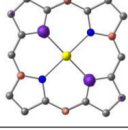
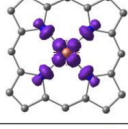
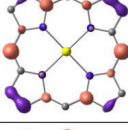
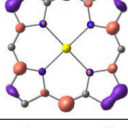
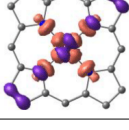
Table S7 TDDFT calculated transitions of $^2[\text{Au}(\text{OEP})]^0$.

#	λ / nm	f	Difference electron density (purple = electron loss; orange = electron gain). Isosurface value at 0.004 a.u.
1	2577.2	1E-09	
2	2552.4	2E-09	
3	630.9		
4	630.4	0.000198369	
5	573.2	4.89E-05	
6	572.9	2.05E-05	
7	550.2	0.000250271	
8	500.3	0.035935239	

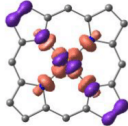
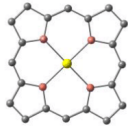
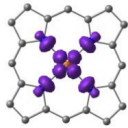
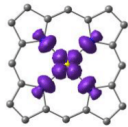
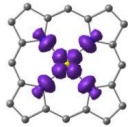
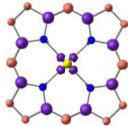
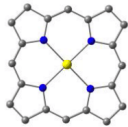
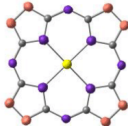
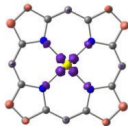
9	500.3	0.036362309	
10	446.1	0	
11	443.6	0	
12	422.5	0	
13	418.5	0	
14	402.0	0.000844813	
15	401.9	0.000889163	
16	391.3	6E-09	
17	389.2	5E-09	

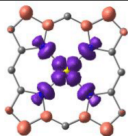
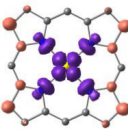
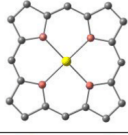
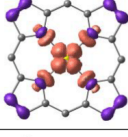
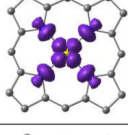
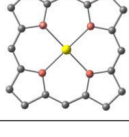
6.2 | Supporting Information to 3.2: Face-to-Face Gold Porphyrins

18	379.8	4E-09	
19	368.7	0.000566833	
20	364.4	0.104290928	
21	364.1	0.00006484	
22	363.5	0.000327271	
23	358.4	0.668245305	
24	358.2	0.005518384	
25	358.0	0.042091256	
26	357.7	0.610844548	

27	353.0	0.010967578	
28	345.8	0	
29	341.8	4.6E-8	
30	338.2	1.068943747	
31	338.1	1.069046786	
32	337.2	1.15E-06	
33	324.0	0.366437774	
34	324.0	0.363293503	
35	316.3	2.15E-03	

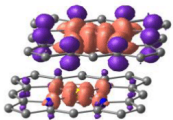
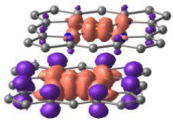
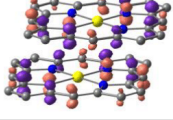
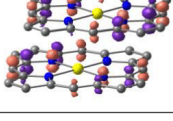
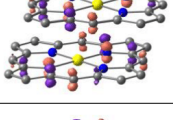
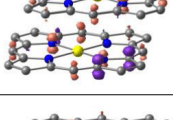
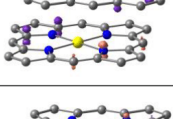
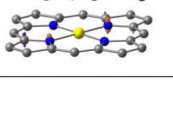
6.2 | Supporting Information to 3.2: Face-to-Face Gold Porphyrins

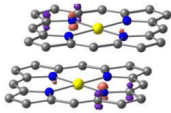
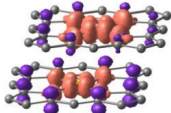
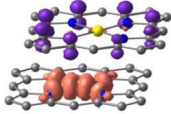
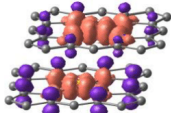
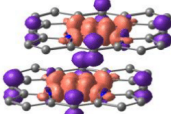
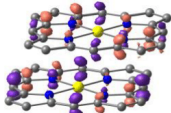
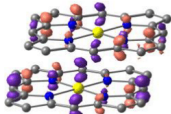
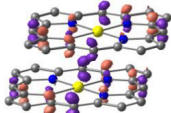
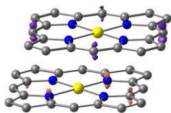
36	316.3	1.8E-7	
37	305.2	0	
38	302.1	8.00E-09	
39	300.1	0.002439402	
40	300.0	0.002418312	
41	297.1	2.00E-08	
42	289.8	0	
43	285.1	6.00E-09	
44	283.6	1.1E-8	

45	282.6	1.26E-7	
46	282.4	8.2E-8	
47	280.0	1E-09	
48	275.3	0.000303148	
49	272.9	1E-09	
50	271.9	2E-09	

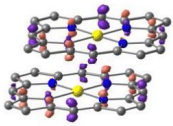
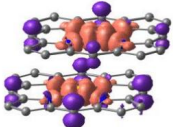
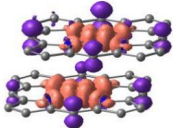
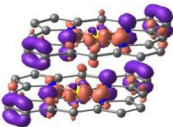
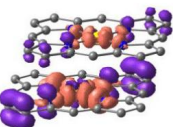
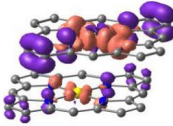
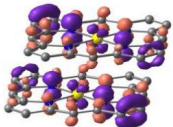
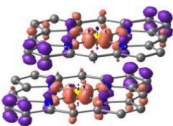
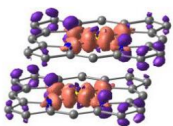
6.2 | Supporting Information to 3.2: Face-to-Face Gold Porphyrins

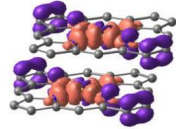
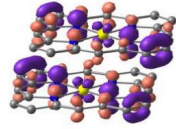
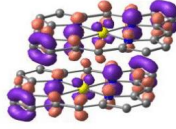
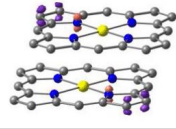
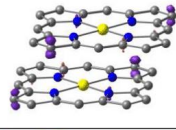
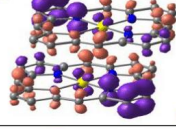
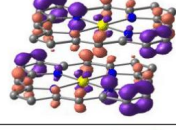
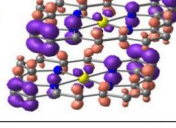
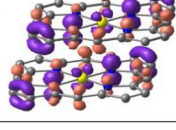
Table S8 TDDFT calculated transitions of $^1\{[\text{Au}(\text{OEP})]_2\}^{2+}$.

#	λ / nm	f	Difference electron density (purple = electron loss; orange = electron gain). Isosurface value at 0.003 a.u.
1	542.2	1.42186E-4	
2	542.0	1.2977E-5	
3	534.8	2.49E-6	
4	518.6	0.02371	
5	518.0	0.02548	
6	515.0	1.88E-05	
7	503.7	3.836E-6	
8	492.2	0.00434	

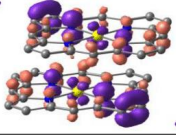
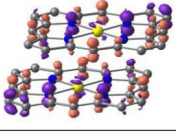
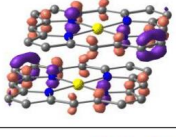
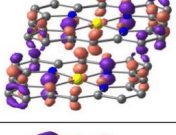
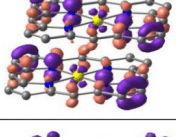
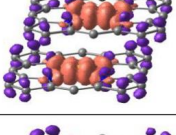
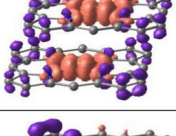
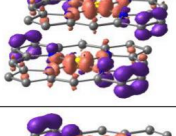
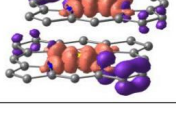
9	484.3	0.01366	
10	480.3	2.803E-6	
11	480.1	1.0104E-5	
12	480.0	1.16186E-4	
13	478.0	3.37583E-4	
14	477.3	2.012E-6	
15	448.7	1.87485E-4	
16	447.7	5.852E-6	
17	446.2	3.32E-7	

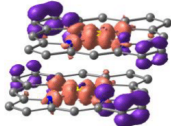
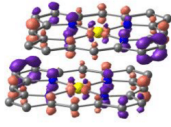
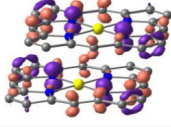
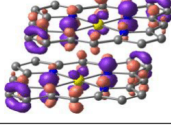
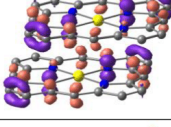
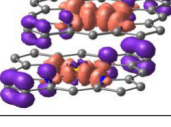
6.2 | Supporting Information to 3.2: Face-to-Face Gold Porphyrins

18	439.0	0.11561	
19	421.2	5.473E-6	
20	420.6	4.95131E-4	
21	389.9	1.043E-6	
22	388.2	1.46709E-4	
23	388.1	1.204E-5	
24	387.0	1.31E-7	
25	385.3	0.00273	
26	384.8	0.00218	

27	384.7	1.39E-7	
28	382.3	0.00172	
29	376.7	1.75286E-4	
30	371.6	6.86E-7	
31	369.5	1.59E-6	
32	368.9	0.00209	
33	365.5	8.55E-7	
34	361.9	7.177E-6	
35	361.4	0.00805	

6.2 | Supporting Information to 3.2: Face-to-Face Gold Porphyrins

36	360.3	0.01619	
37	359.5	2.8329E-5	
38	358.8	9.252E-6	
39	355.6	0.02082	
40	353.8	3.7821E-5	
41	352.9	0.00811	
42	352.8	2.275E-6	
43	352.3	0.01688	
44	351.2	2.962E-6	

45	350.5	0.00947	
46	350.4	3.9983E-5	
47	349.8	0.00952	
48	349.2	6.72E-7	
49	344.0	3.8206E-5	
50	343.8	9.2279E-5	

3 References

- (1) Stoll, S.; Schweiger, A. EasySpin, a comprehensive software package for spectral simulation and analysis in EPR. *J. Magn. Reson.* **2006**, *178*, 42–55. DOI: 10.1016/j.jmr.2005.08.013.
- (2) Neese, F. Software update: The ORCA program system—Version 5.0. *Wiley Interdiscip. Rev. Comput Mol Sci.* **2022**, *12*, e1606. DOI: 10.1002/wcms.1606.
- (3) Becke, A. D. Density-functional thermochemistry. III. The role of exact exchange. *J. Chem. Phys.* **1993**, *98*, 5648–5652. DOI: 10.1063/1.464913.
- (4) Miehlich, B.; Savin, A.; Stoll, H.; Preuss, H. Results obtained with the correlation energy density functionals of Becke and Lee, Yang and Parr. *Chem. Phys. Lett.* **1989**, *157*, 200–206. DOI: 10.1016/0009-2614(89)87234-3.
- (5) Schäfer, A.; Horn, H.; Ahlrichs, R. Fully optimized contracted Gaussian basis sets for atoms Li to Kr. *J. Chem. Phys.* **1992**, *97*, 2571–2577. DOI: 10.1063/1.463096.
- (6) Schäfer, A.; Huber, C.; Ahlrichs, R. Fully optimized contracted Gaussian basis sets of triple zeta valence quality for atoms Li to Kr. *J. Chem. Phys.* **1994**, *100*, 5829–5835. DOI: 10.1063/1.467146.
- (7) Pantazis, D. A.; Chen, X.-Y.; Landis, C. R.; Neese, F. All-Electron Scalar Relativistic Basis Sets for Third-Row Transition Metal Atoms. *J. Chem. Theory Comput.* **2008**, *4*, 908–919. DOI: 10.1021/ct800047t.
- (8) Neese, F.; Wennmohs, F.; Hansen, A.; Becker, U. Efficient, approximate and parallel Hartree–Fock and hybrid DFT calculations. A ‘chain-of-spheres’ algorithm for the Hartree–Fock exchange. *Chem. Phys.* **2009**, *356*, 98–109. DOI: 10.1016/j.chemphys.2008.10.036.
- (9) Miertuš, S.; Scrocco, E.; Tomasi, J. Electrostatic interaction of a solute with a continuum. A direct utilization of AB initio molecular potentials for the prevision of solvent effects. *Chem. Phys.* **1981**, *55*, 117–129. DOI: 10.1016/0301-0104(81)85090-2.
- (10) Grimme, S.; Antony, J.; Ehrlich, S.; Krieg, H. A consistent and accurate ab initio parametrization of density functional dispersion correction (DFT-D) for the 94 elements H–Pu. *J. Chem. Phys.* **2010**, *132*, 154104. DOI: 10.1063/1.3382344.
- (11) Grimme, S.; Ehrlich, S.; Goerigk, L. Effect of the Damping Function in Dispersion Corrected Density Functional Theory. *J. Comput. Chem.* **2011**, *32*, 1456–1465. DOI: 10.1002/jcc.21759.
- (12) Plasser, F. TheoDORE: A toolbox for a detailed and automated analysis of electronic excited state computations. *J. Chem. Phys.* **2020**, *152*, 84108. DOI: 10.1063/1.5143076.
- (13) Mai, S.; Plasser, F.; Dorn, J.; Fumanal, M.; Daniel, C.; González, L. Quantitative wave function analysis for excited states of transition metal complexes. *Coord. Chem. Rev.* **2018**, *361*, 74–97. DOI: 10.1016/j.ccr.2018.01.019.
- (14) Krumsieck, J.; Bröring, M. PorphyStruct: A Digital Tool for the Quantitative Assignment of Non-Planar Distortion Modes in Four-Membered Porphyrinoids. *Chem. Eur. J.* **2021**, *27*, 11580–11588. DOI: 10.1002/chem.202101243.
- (15) Krumsieck, J. *PorphyStruct*, **2023**. <https://github.com/JensKrumsieck/PorphyStruct/releases/tag/v2.0.1>.
- (16) Deng, Y.; Chang, C. J.; Nocera, D. G. Direct Observation of the “Pac-Man” Effect from Dibenzofuran-Bridged Cofacial Bisporphyrins. *J. Am. Chem. Soc.* **2000**, *122*, 410–411. DOI: 10.1021/ja992955r.
- (17) Fleischer, E. B.; Laszlo, A. Synthesis of a Gold Porphyrin. *Inorg. Nucl. Chem. Lett.* **1969**, *5*, 373–376. DOI: 10.1016/0020-1650(69)80083-8.
- (18) Lash, T. D. Porphyrins with Exocyclic rings. Part 10. Synthesis of meso, β -Propanoporphyrins from 4,5,6,7-Tetrahydro-1H-Indoles. *Tetrahedron* **1998**, *54*, 359–374. DOI: 10.1016/S0040-4020(97)10288-5.

- (19) Preiß, S.; Melomedov, J.; Wünsche von Leupoldt, A.; Heinze, K. Gold(III) tetraarylporphyrin amino acid derivatives: ligand or metal centred redox chemistry? *Chem. Sci.* **2016**, *7*, 596–610. DOI: 10.1039/c5sc03429a.
- (20) Bobál, P.; Lightner, D. A. An Improved Coupling Procedure for the Barton-Zard Pyrrole Synthesis. *J. Heterocyclic Chem.* **2001**, *38*, 527–530. DOI: 10.1002/jhet.5570380239.
- (21) Helms, A.; Heiler, D.; McLendon, G. Electron transfer in bis-porphyrin donor-acceptor compounds with polyphenylene spacers shows a weak distance dependence. *J. Am. Chem. Soc.* **1992**, *114*, 6227–6238. DOI: 10.1021/ja00041a047.
- (22) Barton, D. H. R.; Kervagoret, J.; Zard, S. Z. A useful synthesis of pyrroles from nitroolefins. *Tetrahedron* **1990**, *46*, 7587–7598. DOI: 10.1016/S0040-4020(01)89069-4.
- (23) Bolze, F.; Gros, C. P.; Drouin, M.; Espinosa, E.; Harvey, P. D.; Guillard, R. Fine tuning of the photophysical properties of cofacial diporphyrins via the use of different spacers. *J. Organomet. Chem.* **2002**, *643–644*, 89–97. DOI: 10.1016/S0022-328X(01)01346-8.
- (24) Gouterman, M.; Wagniere, G. H. Spectra of Porphyrins. Part II Four Orbital Model. *J. Mol. Spectrosc.* **1963**, *11*, 108–127. DOI: 10.1016/0022-2852(63)90011-0.
- (25) Gouterman, M. Spectra of Porphyrins. *J. Mol. Spectrosc.* **1961**, *6*, 138–163. DOI: 10.1016/0022-2852(61)90236-3.
- (26) Gouterman, M. Study of the Effects of Substitution on the Absorption Spectra of Porphin. *J. Chem. Phys.* **1959**, *30*, 1139–1161. DOI: 10.1063/1.1730148.

6.3 Supporting Information to 3.3: Pushing Molular Orbitals to Higher Energy – A DFT Study on the Spin Distribution in Gold Corrole Complexes

DFT calculations were carried out using the ORCA 5.0.3 program package.^[1] Tight convergence criteria were chosen for all calculations (keywords `tightscf` and `tightopt`). For geometry optimizations and energy calculations, the B3LYP^[2,3] formulation of density functional theory was used employing the ZORA-def2-TZVPP basis set for the corrole macrocycle and Au-SARC-ZORA-def2-TZVPP basis set for the gold centre^[4,5] with the zeroth order regular approximation (keyword: ZORA)^[6], the RIJCOSX approximation.^[7] To account for solvent effects, a conductor-like polarizable continuum model (CPCM, CH₂Cl₂)^[8] modelling dichloromethane was used in all calculations. Grimme's empirical dispersion correction D3BJ^[9,10] was employed. No symmetry constraints were imposed on the molecules. Explicit counterions and/or solvent molecules were not taken into account.

The analyses of *out-of-plane* distortions of the DFT optimized geometries of the porphin scaffolds were conducted using *PorphyStruct* applying the normal-coordinate structure decomposition (NSD) method.^[11,12]

6.3 | Supporting Information to 3.3: Pushing Molular Orbitals to Higher Energy – A DFT Study on the Spin Distribution in Gold Corrole Complexes

Table S1 Absolute normal-coordinate structural decomposition (NSD) analysis of the DFT geometry-optimized structures of 5,10,15-(aryl)-substituted (corrolo)gold complexes in their singlet and doublet ground states.

Compound	B1 (Dom)	A2 (Sad)	B1 (Ruf)	B1 (Wav x)	A2 (Wav y)	A2 (Pro)
[0] ⁰	0.138	0.044	0.062	0.135	0.036	0.000
[0] ⁻	0.099	0.041	0.069	0.185	0.034	0.001
[1] ⁰	0.190	-0.052	0.093	0.165	-0.042	0.002
[1] ⁻	0.132	0.043	0.097	0.187	0.037	-0.001
[2] ⁰	0.175	0.011	0.077	0.162	-0.002	0.002
[2] ⁻	0.117	-0.009	0.079	0.188	0.001	-0.002
[3] ⁰	0.052	-0.058	0.002	0.000	-0.045	0.001
[3] ⁻	0.037	-0.061	-0.001	-0.001	-0.041	-0.001
[4] ⁰	0.132	-0.104	0.043	0.182	-0.047	-0.003
[4] ⁻	0.074	-0.100	0.043	0.181	-0.043	-0.004
[5] ⁰	0.122	0.016	0.037	0.184	-0.001	0.002
[5] ⁻	0.067	-0.013	0.040	0.188	0.002	-0.002
[6] ⁰	0.023	0.068	0.009	0.003	0.049	0.000
[6] ⁻	-0.017	0.067	-0.006	0.000	0.044	0.002
[7] ⁰	0.277	0.022	0.078	0.059	0.026	0.000
[7] ⁻	0.184	0.023	0.072	0.061	0.030	0.001
[8] ⁰	-0.237	0.027	-0.094	-0.048	-0.002	0.004
[8] ⁻	-0.217	0.028	-0.091	-0.042	-0.011	0.003
[9] ⁰	0.023	-0.016	0.002	0.010	-0.013	-0.001
[9] ⁻	0.012	-0.005	0.000	0.011	-0.006	-0.003
[10] ⁰	0.046	0.050	0.013	0.008	-0.053	-0.003
[10] ⁻	0.061	-0.011	0.013	0.003	0.051	0.014
[11] ⁰	-0.148	0.068	-0.065	-0.015	-0.015	0.003
[11] ⁻	-0.115	0.048	-0.062	-0.007	-0.023	-0.005
[12] ⁰	0.037	-0.062	0.008	0.005	-0.047	-0.003
[12] ⁻	0.025	-0.041	0.010	0.008	-0.032	-0.006
[13] ⁰	-0.039	-0.007	0.023	-0.015	0.002	0.000
[13] ⁻	-0.021	-0.006	0.022	-0.027	0.003	0.000
[14] ⁻	-0.052	-0.013	0.017	-0.019	-0.006	0.001
[14] ⁰	-0.038	-0.008	0.014	-0.028	-0.004	0.001
[15] ⁻	0.011	0.004	-0.009	0.003	0.005	-0.001
[15] ⁰	0.011	-0.002	-0.009	0.000	0.004	-0.001
[16] ⁻	-0.285	-0.057	-0.072	-0.267	-0.019	0.000
[16] ⁰	-0.065	0.051	0.005	-0.009	0.014	0.000
[17] ⁻	-0.254	0.027	-0.006	-0.117	0.003	0.001
[17] ⁰	0.106	0.027	0.000	0.028	0.003	0.000
[18] ⁻	-0.047	0.031	0.002	-0.004	0.012	-0.001
[18] ⁰	0.050	0.032	-0.005	0.006	0.013	-0.001
[19] ⁻	1.716	-0.008	-0.214	-0.454	-0.009	-0.001
[19] ⁰	2.668	0.005	-0.486	-0.821	-0.001	0.000
[20] ⁻	0.905	0.003	0.042	0.116	0.006	-0.003
[20] ⁰	0.768	0.005	-0.026	0.167	0.007	-0.002
[21] ⁰	0.045	-0.017	0.003	0.002	-0.017	0.002
[21] ⁻	0.045	-0.015	0.009	-0.001	-0.014	0.002
[22] ⁰	0.456	0.003	-1.852	0.24	0.000	-0.002
[22] ⁻	1.026	-0.047	-1.528	0.569	0.011	-0.001
[23] ⁰	-0.048	-0.007	-0.016	-0.01	-0.007	-0.001
[23] ⁻	-0.040	-0.009	0.009	-0.008	-0.009	0.000
[24] ⁰	0.019	-0.010	0.006	0.011	-0.011	-0.001
[24] ⁻	0.289	-0.001	0.281	-0.132	-0.001	-0.001
[25] ⁰	-0.022	-0.013	0.008	-0.003	0.002	0.001
[25] ⁻	-0.013	-0.108	0.011	-0.002	0.058	0.006
[26] ⁰	0.007	-0.014	-0.007	0.002	-0.008	0.001
[26] ⁻	0.007	-0.018	-0.006	0.002	-0.007	0.001
[27] ⁰	-0.022	-0.003	-0.006	0.000	0.005	0.001
[27] ⁻	0.002	-0.094	-0.003	0.005	0.057	0.006

CHAPTER 6 | Appendix

Table S2 Relative normal-coordinate structural decomposition (NSD) analysis of the DFT geometry-optimized structures of 5,10,15-(aryl)-substituted (corrolato)gold complexes in their singlet and doublet ground states.

Compound	B1 (Dom)	A2 (Sad)	B1 (Ruf)	B1 (Wav x)	A2 (Wav y)	A2 (Pro)
[0] ⁰	0.333	0.106	0.149	0.325	0.087	0.000
[0] ⁻	0.231	0.096	0.161	0.431	0.079	0.002
[1] ⁰	0.349	0.096	0.171	0.303	0.077	0.004
[1] ⁻	0.266	0.087	0.195	0.376	0.074	0.002
[2] ⁰	0.408	0.026	0.179	0.378	0.005	0.005
[2] ⁻	0.295	0.023	0.199	0.475	0.003	0.005
[3] ⁰	0.329	0.367	0.013	0.000	0.285	0.006
[3] ⁻	0.261	0.430	0.007	0.007	0.289	0.007
[4] ⁰	0.258	0.204	0.084	0.356	0.092	0.006
[4] ⁻	0.166	0.225	0.097	0.407	0.097	0.009
[5] ⁰	0.337	0.044	0.102	0.508	0.003	0.006
[5] ⁻	0.215	0.042	0.128	0.603	0.006	0.006
[6] ⁰	0.151	0.447	0.059	0.020	0.322	0.000
[6] ⁻	0.125	0.493	0.044	0.000	0.324	0.015
[7] ⁰	0.600	0.048	0.169	0.128	0.056	0.000
[7] ⁻	0.496	0.062	0.194	0.164	0.081	0.003
[8] ⁰	0.575	0.066	0.228	0.117	0.005	0.010
[8] ⁻	0.554	0.071	0.232	0.107	0.028	0.008
[9] ⁰	0.354	0.246	0.031	0.154	0.200	0.015
[9] ⁻	0.324	0.135	0.000	0.297	0.162	0.081
[10] ⁰	0.266	0.289	0.075	0.046	0.306	0.017
[10] ⁻	0.399	0.072	0.085	0.020	0.333	0.092
[11] ⁰	0.471	0.217	0.207	0.048	0.048	0.010
[11] ⁻	0.442	0.185	0.238	0.027	0.088	0.019
[12] ⁰	0.228	0.383	0.049	0.031	0.290	0.019
[12] ⁻	0.205	0.336	0.082	0.066	0.262	0.049
[13] ⁰	0.453	0.081	0.267	0.174	0.023	0.000
[13] ⁻	0.266	0.076	0.278	0.342	0.038	0.000
[14] ⁻	0.481	0.120	0.157	0.176	0.056	0.009
[14] ⁰	0.409	0.086	0.151	0.301	0.043	0.011
[15] ⁻	0.333	0.121	0.273	0.091	0.152	0.030
[15] ⁰	0.407	0.074	0.333	0.000	0.148	0.037
[16] ⁻	0.407	0.081	0.103	0.381	0.027	0.000
[16] ⁰	0.451	0.354	0.035	0.062	0.097	0.000
[17] ⁻	0.623	0.066	0.015	0.287	0.007	0.002
[17] ⁰	0.646	0.165	0.000	0.171	0.018	0.000
[18] ⁻	0.485	0.320	0.021	0.041	0.124	0.010
[18] ⁰	0.467	0.299	0.047	0.056	0.121	0.009
[19] ⁻	0.714	0.003	0.089	0.189	0.004	0.000
[19] ⁰	0.670	0.001	0.122	0.206	0.000	0.000
[20] ⁻	0.841	0.002	0.039	0.107	0.005	0.002
[20] ⁰	0.787	0.005	0.026	0.171	0.007	0.002
[21] ⁰	0.523	0.197	0.034	0.023	0.197	0.023
[21] ⁻	0.523	0.174	0.104	0.011	0.162	0.023
[22] ⁰	0.178	0.001	0.725	0.094	0.000	0.001
[22] ⁻	0.322	0.014	0.480	0.178	0.003	0.000
[23] ⁰	0.539	0.078	0.179	0.112	0.078	0.011
[23] ⁻	0.533	0.120	0.120	0.106	0.120	0.000
[24] ⁰	0.327	0.172	0.103	0.189	0.189	0.017
[24] ⁻	0.409	0.001	0.398	0.187	0.001	0.001
[25] ⁰	0.449	0.265	0.163	0.061	0.041	0.020
[25] ⁻	0.066	0.545	0.056	0.010	0.293	0.030
[26] ⁰	0.180	0.359	0.180	0.051	0.205	0.026
[26] ⁻	0.171	0.439	0.146	0.049	0.171	0.024
[27] ⁰	0.595	0.081	0.162	0.000	0.135	0.027
[27] ⁻	0.012	0.563	0.018	0.030	0.341	0.036

6.3 | Supporting Information to 3.3: Pushing Molular Orbitals to Higher Energy – A DFT Study on the Spin Distribution in Gold Corrole Complexes

Table S3 Selected metrics of the DFT geometry-optimized structures of 5,10,15-(aryl)-substituted (corolato)gold complexes in their singlet and doublet ground states.

	N1-N3 / Å	N2-N4 / Å	Au-N1 / Å	Au-N2 / Å	Au-N3 / Å	Au-N4 / Å	Au-Mean Plane / Å	Au-N4 Plane / Å	N1-Au-N4 / °	N2-Au-N3 / °
[0] ⁰	3.900	3.901	1.945	1.964	1.963	1.946	-0.054	0.011	80.242	95.046
[0] ⁻	3.919	3.921	1.954	1.974	1.973	1.955	-0.038	0.010	80.633	95.095
[1] ⁰	3.903	3.902	1.947	1.963	1.964	1.946	-0.075	-0.014	80.322	94.998
[1] ⁻	3.920	3.921	1.955	1.974	1.973	1.955	-0.052	0.011	80.623	94.985
[2] ⁰	3.903	3.902	1.946	1.965	1.965	1.945	-0.068	-0.013	80.512	95.491
[2] ⁻	3.921	3.921	1.954	1.975	1.975	1.954	-0.045	0.010	80.790	95.454
[3] ⁰	3.901	3.901	1.946	1.963	1.963	1.946	-0.022	0.005	79.619	94.181
[3] ⁻	3.920	3.920	1.955	1.972	1.972	1.955	-0.015	0.003	79.914	94.086
[4] ⁰	3.903	3.903	1.947	1.964	1.964	1.947	-0.051	-0.010	80.342	95.096
[4] ⁻	3.921	3.920	1.955	1.973	1.974	1.955	-0.029	-0.008	80.566	95.019
[5] ⁰	3.903	3.902	1.946	1.965	1.965	1.946	-0.046	-0.010	80.573	95.623
[5] ⁻	3.920	3.921	1.954	1.975	1.975	1.954	-0.026	-0.008	80.790	95.522
[6] ⁰	3.901	3.901	1.946	1.963	1.963	1.946	-0.01	-0.002	79.597	94.135
[6] ⁻	3.920	3.920	1.955	1.972	1.972	1.955	0.007	-0.001	79.887	94.028
[7] ⁰	3.898	3.899	1.944	1.962	1.961	1.945	-0.092	-0.017	80.111	94.795
[7] ⁻	3.915	3.916	1.952	1.971	1.979	1.953	-0.073	-0.013	80.337	94.659
[8] ⁰	3.899	3.900	1.944	1.964	1.964	1.945	0.109	-0.019	80.295	95.232
[8] ⁻	3.917	3.918	1.952	1.973	1.973	1.953	0.084	-0.013	80.507	95.103
[9] ⁰	3.900	3.900	1.946	1.962	1.962	1.946	-0.011	0.004	79.709	94.275
[9] ⁻	3.919	3.918	1.955	1.971	1.972	1.954	-0.006	0.002	79.998	94.163
[10] ⁰	3.896	3.896	1.944	1.961	1.960	1.944	-0.019	0.003	80.272	94.961
[10] ⁻	3.914	3.914	1.952	1.969	1.969	1.953	-0.025	0.002	80.461	94.787
[11] ⁰	3.897	3.899	1.943	1.963	1.963	1.944	0.060	0.010	80.455	95.441
[11] ⁻	3.915	3.917	1.951	1.972	1.972	1.952	0.045	0.006	80.692	95.279
[12] ⁰	3.900	3.900	1.946	1.962	1.962	1.946	-0.015	0.004	79.705	94.143
[12] ⁻	3.919	3.918	1.955	1.971	1.971	1.955	-0.010	0.002	79.970	94.022
[13] ⁰	3.897	3.897	1.944	1.961	1.961	1.944	0.014	-0.004	80.011	94.662
[13] ⁻	3.916	3.915	1.952	1.971	1.971	1.952	0.008	0.003	80.154	94.411
[14] ⁻	3.899	3.898	1.945	1.962	1.962	1.945	0.020	0.005	80.061	94.885
[14] ⁰	3.917	3.917	1.953	1.971	1.972	1.953	0.015	0.004	80.194	94.651
[15] ⁻	3.900	3.899	1.944	1.963	1.963	1.944	-0.005	-0.001	79.784	94.422
[15] ⁰	3.918	3.918	1.953	1.973	1.973	1.953	-0.005	0.000	80.073	94.301
[16] ⁻	3.908	3.906	1.953	1.960	1.962	1.953	0.111	0.021	80.906	94.684
[16] ⁰	3.915	3.919	1.954	1.971	1.968	1.955	0.025	0.005	80.588	94.682
[17] ⁻	3.902	3.901	1.947	1.962	1.962	1.947	0.101	0.022	80.708	95.250
[17] ⁰	3.918	3.918	1.954	1.972	1.972	1.954	-0.042	0.008	80.830	95.230
[18] ⁻	3.899	3.902	1.946	1.964	1.961	1.946	0.019	0.003	79.669	94.130
[18] ⁰	3.921	3.918	1.955	1.971	1.973	1.955	-0.019	0.003	79.936	93.996
[19] ⁻	3.932	3.933	1.959	1.988	1.987	1.959	-0.629	-0.124	81.28	93.899
[19] ⁰	4.180	4.177	2.105	2.133	2.135	2.105	-1.097	-0.323	78.106	94.533
[20] ⁻	3.860	3.86	1.933	1.940	1.940	1.933	-0.385	0.093	80.913	95.674
[20] ⁰	3.869	3.869	1.931	1.948	1.948	1.931	-0.311	0.070	81.26	95.798
[21] ⁻	3.877	3.877	1.931	1.951	1.951	1.931	-0.0200	-0.005	80.051	92.145
[21] ⁰	3.886	3.886	1.935	1.956	1.957	1.935	-0.019	-0.004	79.975	92.532
[22] ⁻	4.012	4.012	1.993	2.032	2.032	1.993	-0.160	-0.047	78.428	95.648
[22] ⁰	4.237	4.252	2.134	2.137	2.129	2.143	-0.400	0.125	75.482	97.319
[23] ⁻	3.957	3.957	1.974	1.991	1.900	1.974	0.020	-0.004	79.356	93.725
[23] ⁰	3.974	3.975	1.978	2.004	2.003	1.979	0.016	-0.004	79.725	93.732
[24] ⁻	3.936	3.935	1.956	1.991	1.992	1.956	-0.008	-0.002	79.188	97.403
[24] ⁰	3.945	3.946	1.960	1.999	1.998	1.960	-0.103	-0.022	79.214	97.869
[25] ⁰	3.900	3.901	1.944	1.965	1.964	1.944	0.009	-0.002	79.643	94.564
[25] ⁻	3.919	3.920	1.953	1.974	1.974	1.953	0.006	0.001	79.945	94.364
[26] ⁰	3.901	3.901	1.945	1.963	1.964	1.945	-0.004	-0.001	79.855	94.635
[26] ⁻	3.919	3.918	1.954	1.972	1.972	1.954	-0.003	-0.001	80.135	94.561
[27] ⁰	3.901	3.901	1.944	1.966	1.965	1.944	0.010	-0.002	79.566	94.556
[27] ⁻	3.920	3.921	1.953	1.976	1.975	1.953	0.000	0.000	79.925	94.361

Table S4 Gold-Mulliken spin density and energies of frontier molecular orbitals of the DFT geometry-optimized structures of 5,10,15-(aryl)-substituted (corrolato)gold complexes in their singlet and doublet ground states.

	Spin density (Au)	E_{α} (LUMO+2, b_1) / eV	E_{β} (LUMO+2, b_1) / eV	E_{α} (LUMO+1, a_2) / eV	E_{β} (LUMO+1, a_2) / eV	E_{α} (LUMO, a_2) / eV	E_{β} (LUMO, a_2) / eV	E_{α} (HOMO, b_2) / eV	E_{β} (HOMO, b_2) / eV
[0] ⁰		-1.13		-1.93		-2.4		-5.06	
[0] ⁻	0.000	-0.47	-0.45	-1.30	-1.21	-2.72	-1.53	-4.54	-4.20
[1] ⁰		-1.09		-1.87		-2.34		-4.94	
[1] ⁻	0.000	-0.42	-0.40	-1.22	-1.12	-2.65	-1.44	-4.43	-4.11
[2] ⁰		-1.11		-1.85		-2.34	---	-5.01	
[2] ⁻	0.000	-0.43	-0.40	-1.19	-1.09	-2.65	-1.43	-4.48	-4.16
[3] ⁰		-1.11		-1.86		-2.34	---	-5.11	
[3] ⁻	0.000	-0.39	-0.37	-1.16	-1.06	-2.64	-1.37	-4.58	-4.20
[4] ⁰		-1.02		-1.77		-2.24		-4.67	
[4] ⁻	0.000	-0.36	-0.34	-1.14	-1.04	-2.57	-1.36	-4.25	-3.97
[5] ⁰		-1.05		-1.79		-2.27		-4.79	
[5] ⁻	0.000	-0.38	-0.36	-1.14	-1.04	-2.58	-1.36	-4.33	-4.05
[6] ⁰		-1.08		-1.82		-2.31		-4.97	
[6] ⁻	0.000	-0.36	-0.35	-1.13	-1.02	-2.62	-1.35	-4.51	-4.15
[7] ⁰		-1.01		-1.82		-2.28		-5.01	
[7] ⁻	0.000	-0.31	-0.30	-1.17	-1.05	-2.61	-1.33	-4.49	-4.13
[8] ⁰		-1.04		-1.8		-2.3		-5.07	
[8] ⁻	0.000	-0.34	-0.32	-1.12	-1.00	-2.61	-1.34	-4.53	-4.16
[9] ⁰		-1.09		-1.86		-2.32		-4.97	
[9] ⁻	0.000	-0.37	0.35	-1.17	-1.06	-2.62	-1.34	-4.51	-4.15
[10] ⁰		-0.86		-1.65		-2.14		-4.62	
[10] ⁻	0.000	-0.20	-0.18	-1.04	-0.93	-2.48	-1.23	-4.21	-3.91
[11] ⁰		-0.95		-1.70		-2.21		-4.75	
[11] ⁻	0.000	-0.27	-0.25	-1.06	-0.95	-2.54	-1.29	-4.32	-4.01
[12] ⁰		-1.03		-1.79		-2.26		-4.89	
[12] ⁻	0.000	-0.32	-0.30	-1.11	-1.00	-2.56	-1.28	-4.45	-4.12
[13] ⁰		-1.18		-1.87		-2.35		-4.99	
[13] ⁻	0.000	-0.46	-0.44	-1.19	-1.08	-2.65	-1.35	-4.47	-4.09
[14] ⁰		-1.16		-1.86		-2.33		-4.08	
[14] ⁻	0.000	-0.44	-0.42	-1.17	-1.04	-2.63	-1.33	-4.53	-4.17
[15] ⁰		-1.13		-1.87		-2.36		-5.13	
[15] ⁻	0.000	-0.40	-0.39	-1.15	-1.06	-2.65	-1.37	-4.57	-4.18
[16] ⁰		-1.06		-1.79		-2.18		-4.66	
[16] ⁻	0.000	-0.34	-0.33	-1.13	-1.02	-2.62	-1.32	-4.51	-4.13
[17] ⁰		-1.10		-1.81		-2.31		-5.04	
[17] ⁻	0.000	-0.37	-0.35	-1.12	-1.00	-2.62	-1.34	-4.56	-4.17
[18] ⁰		-1.09		-1.85		-2.33		-5.15	
[18] ⁻	0.000	-0.37	-0.35	-1.14	-1.04	-2.62	-1.34	-4.58	-4.21
[19] ⁻		-1.20		1.09		0.24		-4.25	
[19] ²⁻	0.410	-2.89	-0.62	1.39	1.47	1.00	1.01	-3.55	-3.49
[20] ²⁺		-3.22		-4.10		-5.36		-7.49	
[20] ⁺	-0.002	-2.28	-2.27	-5.71	-4.30	-3.35	-3.35	-6.90	-6.61
[21] ⁺		-2.05		-3.23		-3.64		-6.36	
[21] ⁰	0.014	-1.18	-1.15	-2.59	-2.20	-3.90	-2.63	-5.69	-5.46
[22] ⁰		-1.54		0.42		-0.19		-4.30	
[22] ⁻	0.424	-2.95	-0.51	1.20	1.22	0.74	0.77	-3.69	-3.66
[23] ⁰		-3.66		-5.14		-4.09		-7.41	
[23] ⁻	-0.002	-2.88	-2.88	-5.40	-4.14	-3.34	-3.35	-6.86	-6.52
[24] ⁰		-2.47		-3.22		-3.58		-6.33	
[24] ⁻	0.017	-1.66	-1.63	-2.57	-2.23	-3.92	-2.70	-5.68	-5.45
[25] ⁰		-0.85	--	-1.56	--	-2.01		-4.89	
[25] ⁻	0.000	-0.14	-0.12	-0.86	-0.76	-2.33	-1.11	-4.37	-4.04
[26] ⁰		-1.00		-1.62		-2.23		-5.10	
[26] ⁻	0.000	-0.27	-0.25	-0.92	-0.82	-2.51	-1.26	-4.56	-4.19
[27] ⁰		-0.97		-1.79		-2.10		-5.04	
[27] ⁻	0.000	-0.26	-0.24	-1.06	-0.96	-2.43	-1.19	-4.48	-4.11

6.3 | Supporting Information to 3.3: Pushing Molular Orbitals to Higher Energy – A DFT Study on the Spin Distribution in Gold Corrole Complexes

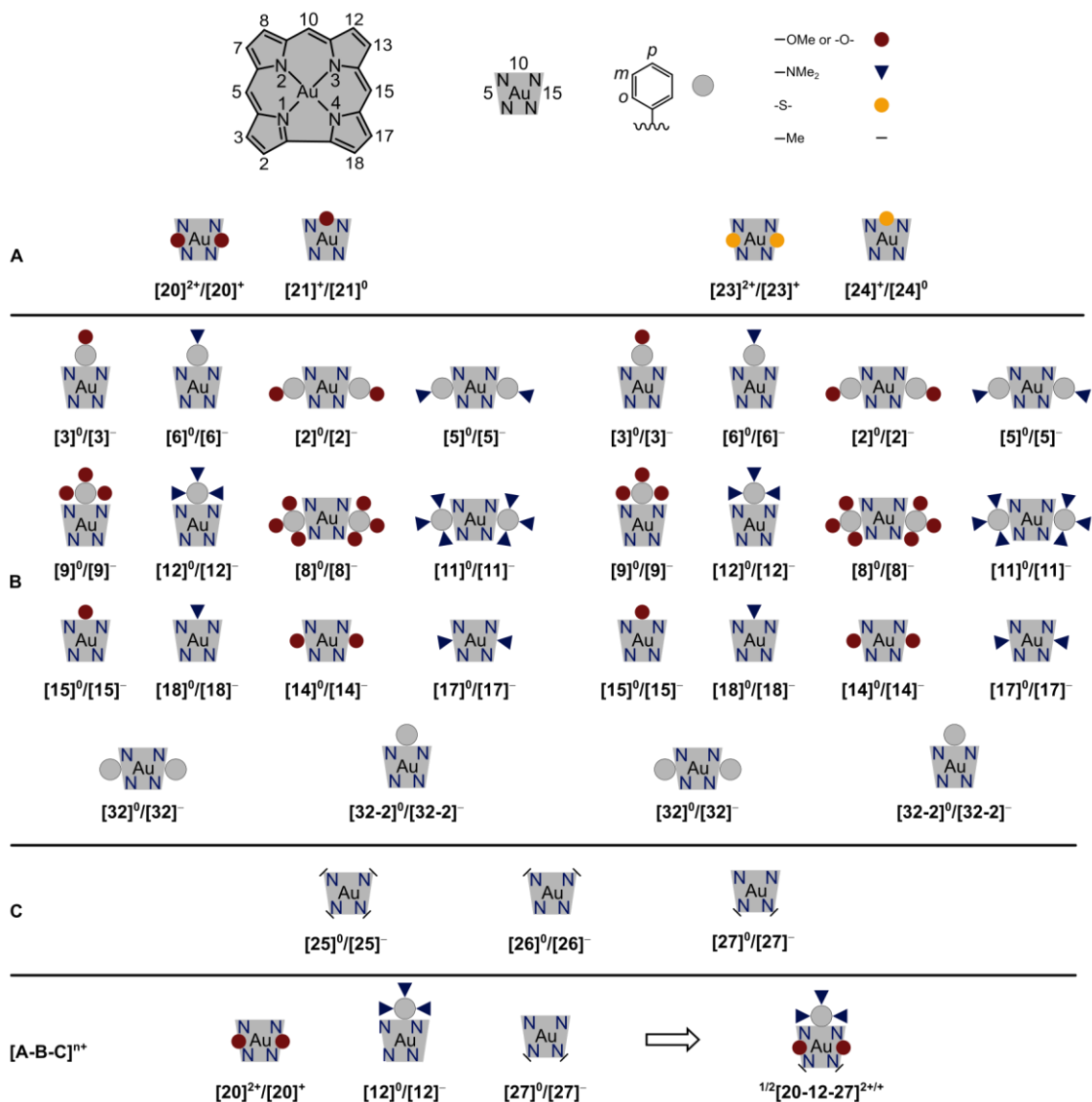


Figure S1 Pictograms of the combined structures of DFT geometry-optimized (corrolato)gold complexes

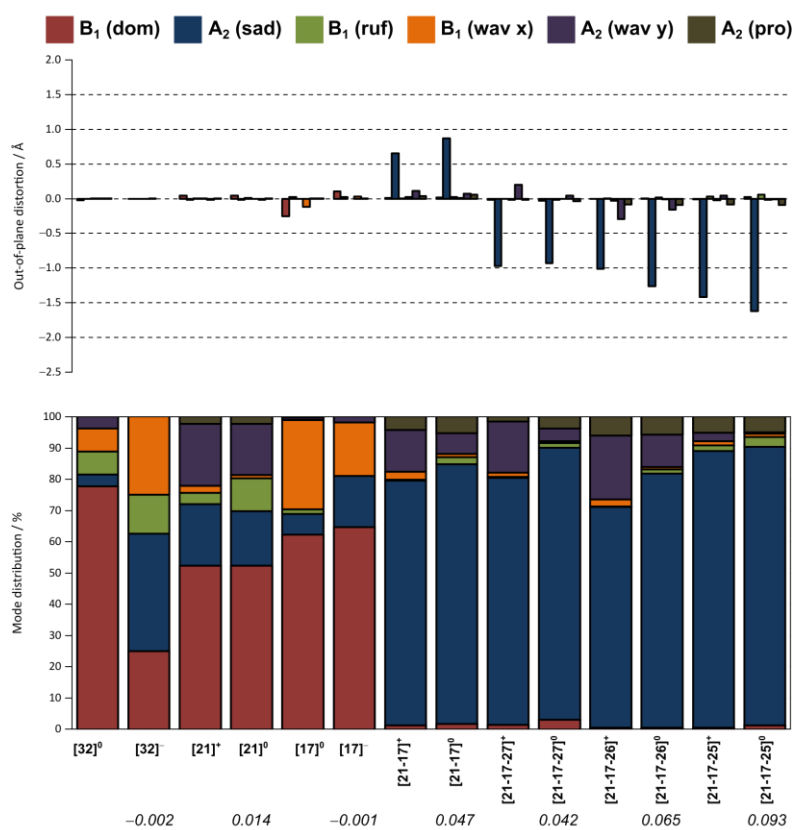


Figure S2 Normal-coordinate structural decomposition (NSD) analysis of the DFT geometry-optimized structures of 5,10,15-trisubstituted (corrolato)gold complexes in their singlet and doublet ground states.

6.3 | Supporting Information to 3.3: Pushing Molular Orbitals to Higher Energy – A DFT Study on the Spin Distribution in Gold Corrole Complexes

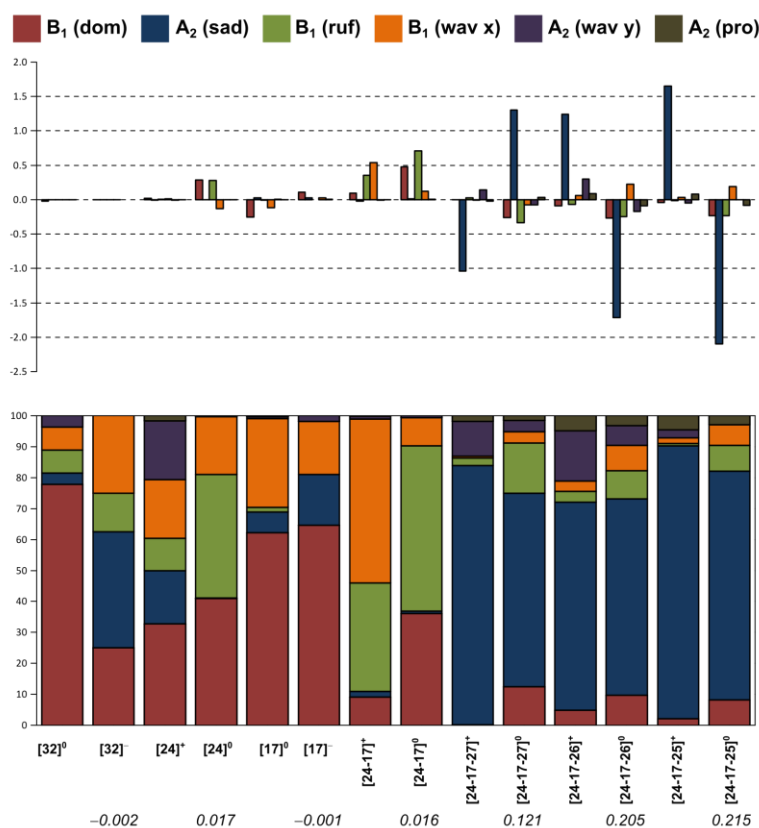


Figure S3 Normal-coordinate structural decomposition (NSD) analysis of the DFT geometry-optimized structures of 5,10,15-trisubstituted (corrolato)gold complexes in their singlet and doublet ground states.

Table S5 Absolute normal-coordinate structural decomposition (NSD) analysis of the DFT geometry-optimized structures of 5,10,15-(aryl)-substituted (corrolato)gold complexes in their singlet and doublet ground states.

Compound	B1 (Dom)	A2 (Sad)	B1 (Ruf)	B1 (Wav x)	A2 (Wav y)	A2 (Pro)
[32] ⁰	-0.021	-0.001	0.002	0.002	0.001	0.000
[32] ⁻	-0.002	-0.003	-0.001	0.002	0.000	0.000
[21] ⁺	0.045	-0.017	0.003	0.002	-0.017	0.002
[21] ⁰	0.045	-0.015	0.009	-0.001	-0.014	0.002
[24] ⁺	0.019	-0.010	0.006	0.011	-0.011	0.001
[24] ⁰	0.289	-0.001	0.281	-0.132	-0.001	-0.001
[17] ⁺	-0.254	0.027	-0.006	-0.117	0.003	0.001
[17] ⁰	0.106	0.027	0.000	0.028	0.003	0.000
[21-17] ⁺	0.010	0.656	0.002	0.022	0.112	0.035
[21-17] ⁰	0.018	0.871	0.023	0.011	0.070	0.055
[24-17] ⁺	0.092	-0.018	0.356	0.536	-0.009	-0.001
[24-17] ⁰	0.478	0.010	0.708	0.121	0.008	0.000
[21-17-27] ⁺	-0.017	-0.968	-0.005	-0.015	0.202	-0.018
[21-17-27] ⁰	-0.032	-0.929	-0.016	-0.005	0.044	-0.040
[21-17-26] ⁺	-0.006	-1.010	0.003	-0.031	-0.292	-0.087
[21-17-26] ⁰	0.007	-1.265	0.020	-0.013	-0.161	-0.089
[21-17-25] ⁺	-0.008	-1.417	0.029	-0.020	0.043	-0.083
[21-17-25] ⁰	0.021	-1.621	0.059	-0.018	-0.009	-0.090
[24-17-27] ⁺	-0.001	-1.037	0.029	-0.007	0.140	-0.022
[24-17-27] ⁰	-0.261	1.304	-0.337	-0.076	-0.076	0.033
[24-17-26] ⁺	-0.089	1.244	-0.066	0.062	0.299	0.090
[24-17-26] ⁰	-0.264	-1.713	-0.244	0.222	-0.170	-0.088
[24-17-25] ⁺	-0.041	1.649	-0.014	0.034	-0.049	0.084
[24-17-25] ⁰	-0.235	-2.099	-0.236	0.192	0.002	-0.080

Table S6 Relative normal-coordinate structural decomposition (NSD) analysis of the DFT geometry-optimized structures of 5,10,15-(aryl)-substituted (corrolato)gold complexes in their singlet and doublet ground states.

Compound	B1 (Dom)	A2 (Sad)	B1 (Ruf)	B1 (Wav x)	A2 (Wav y)	A2 (Pro)
[32] ⁰	0.778	0.037	0.074	0.074	0.037	0.000
[32] ⁻	0.250	0.375	0.125	0.250	0.000	0.000
[21] ⁺	0.523	0.198	0.035	0.023	0.198	0.023
[21] ⁰	0.523	0.174	0.105	0.012	0.163	0.023
[24] ⁺	0.328	0.172	0.103	0.190	0.190	0.017
[24] ⁰	0.410	0.001	0.399	0.187	0.001	0.001
[17] ⁺	0.623	0.066	0.015	0.287	0.007	0.002
[17] ⁰	0.646	0.165	0.000	0.171	0.018	0.000
[21-17] ⁺	0.012	0.784	0.002	0.026	0.134	0.042
[21-17] ⁰	0.017	0.831	0.022	0.010	0.067	0.052
[24-17] ⁺	0.091	0.018	0.352	0.530	0.009	0.001
[24-17] ⁰	0.361	0.008	0.534	0.091	0.006	0.000
[21-17-27] ⁺	0.014	0.790	0.004	0.012	0.165	0.015
[21-17-27] ⁰	0.030	0.871	0.015	0.005	0.041	0.038
[21-17-26] ⁺	0.004	0.707	0.002	0.022	0.204	0.061
[21-17-26] ⁰	0.005	0.814	0.013	0.008	0.104	0.057
[21-17-25] ⁺	0.005	0.886	0.018	0.013	0.027	0.052
[21-17-25] ⁰	0.012	0.892	0.032	0.010	0.005	0.050
[24-17-27] ⁺	0.001	0.839	0.023	0.006	0.113	0.018
[24-17-27] ⁰	0.125	0.625	0.161	0.036	0.036	0.016
[24-17-26] ⁺	0.048	0.672	0.036	0.034	0.162	0.049
[24-17-26] ⁰	0.098	0.634	0.090	0.082	0.063	0.033
[24-17-25] ⁺	0.022	0.881	0.007	0.018	0.026	0.045
[24-17-25] ⁰	0.083	0.738	0.083	0.068	0.001	0.028

Table S7 Selected metrics of the DFT geometry-optimized structures of 5,10,15-(aryl)-substituted (corrolato)gold complexes in their singlet and doublet ground states.

	N1-N3 / Å	N2-N4 / Å	Au-N1 / Å	Au-N2 / Å	Au-N3 / Å	Au-N4 / Å	Au-Mean Plane / Å	Au-N4 Plane / Å	N1-Au- N4 / °	N2-Au- N3 / °
[32] ⁰	3.901	3.901	1.945	1.964	1.964	1.945	0.009	0.002	79.850	94.649
[32] ⁻	3.920	3.920	1.954	1.974	1.973	1.954	0.008	0.001	80.120	94.551
[21] ⁺	3.877	3.877	1.931	1.951	1.951	1.931	-0.020	-0.005	80.051	92.145
[21] ⁰	3.886	3.886	1.935	1.956	1.957	1.935	-0.019	-0.004	79.975	92.533
[24] ⁺	3.936	3.935	1.956	1.991	1.992	1.956	-0.008	-0.002	79.188	97.403
[24] ⁰	3.945	3.946	1.960	1.999	1.998	1.960	-0.103	-0.022	79.214	97.869
[17] ⁺	3.902	3.901	1.947	1.962	1.962	1.947	0.101	0.022	80.708	95.250
[17] ⁰	3.918	3.918	1.954	1.972	1.972	1.954	-0.042	0.008	80.830	95.230
[21-17] ⁺	3.895	3.895	1.944	1.960	1.960	1.943	-0.004	-0.001	82.110	94.374
[21-17] ⁰	3.910	3.908	1.952	1.969	1.969	1.950	-0.006	-0.001	81.497	93.736
[24-17] ⁺	3.963	3.963	1.973	2.000	2.001	1.973	-0.027	0.002	81.443	98.615
[24-17] ⁰	3.955	3.955	1.969	1.997	1.997	1.969	-0.160	-0.026	81.274	98.236
[21-17-27] ⁺	3.900	3.899	1.946	1.964	1.964	1.945	0.005	0.000	81.913	93.976
[21-17-27] ⁰	3.910	3.908	1.950	1.970	1.971	1.949	0.012	-0.002	81.219	93.502
[21-17-26] ⁺	3.900	3.900	1.946	1.964	1.963	1.945	0.003	0.001	81.811	94.188
[21-17-26] ⁰	3.924	3.924	1.958	1.981	1.980	1.958	-0.002	0.000	81.477	94.201
[21-17-25] ⁺	3.908	3.907	1.951	1.970	1.969	1.950	0.003	0.001	81.859	93.929
[21-17-25] ⁰	3.942	3.945	1.970	1.993	1.992	1.972	-0.007	0.000	81.610	94.099
[24-17-27] ⁺	3.957	3.957	1.969	2.003	2.003	1.969	-0.001	-0.001	80.814	98.737
[24-17-27] ⁰	3.994	4.009	1.991	2.028	2.027	2.001	0.088	0.017	80.574	99.172
[24-17-26] ⁺	3.957	3.960	1.970	2.002	2.000	1.971	0.029	0.004	81.119	98.962
[24-17-26] ⁰	4.054	4.032	2.025	2.046	2.054	2.016	0.090	0.016	80.561	100.336
[24-17-25] ⁺	3.966	3.968	1.974	2.009	2.007	1.975	0.013	0.002	81.037	98.870
[24-17-25] ⁰	4.074	4.047	2.037	2.054	2.064	2.024	0.074	0.009	80.605	100.110

6.3 | Supporting Information to 3.3: Pushing Molular Orbitals to Higher Energy – A DFT Study on the Spin Distribution in Gold Corrole Complexes

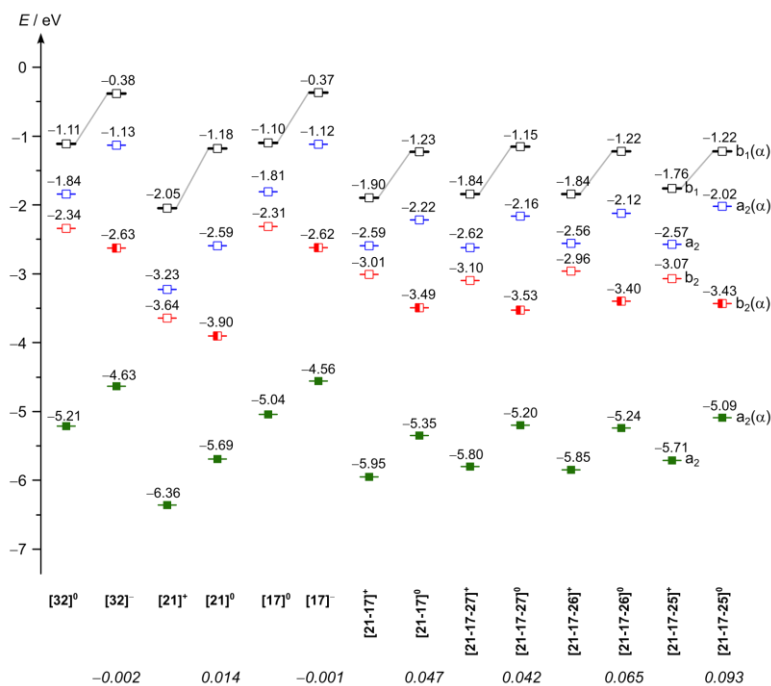


Figure S4 Energies of frontier molecular orbitals of the DFT geometry-optimized of substituted (corrolato)gold complexes in their singlet and doublet (only α energies given) ground states.

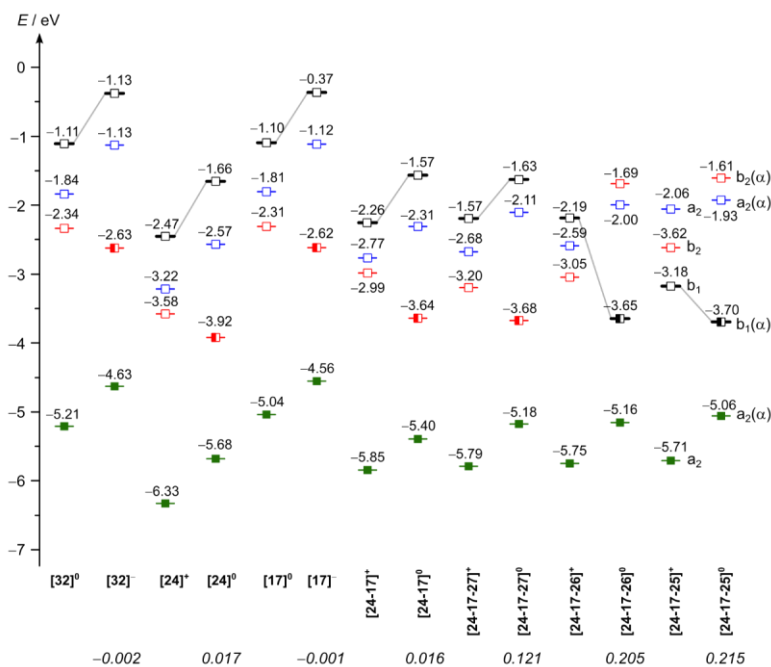
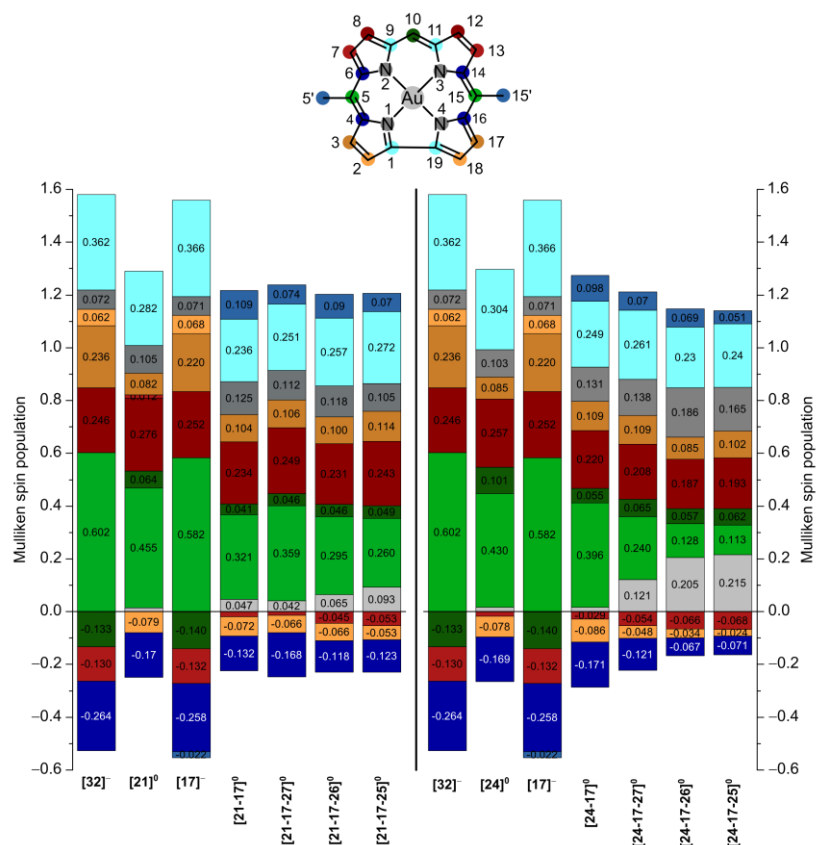


Figure S5 Energies of frontier molecular orbitals of the DFT geometry-optimized of substituted (corrolato)gold complexes in their singlet and doublet (only α energies given) ground states.

Table S8 Gold-Mulliken spin density and energies of frontier molecular orbitals of the DFT geometry-optimized structures of 5,10,15-(aryl)-substituted (corrolato)gold complexes in their singlet and doublet ground states.

	Spin density (Au)	E_{α} (LUMO+2, b_1) / eV	E_{β} (LUMO+2, b_1) / eV	E_{α} (LUMO+1, a_2) / eV	E_{β} (LUMO+1, a_2) / eV	E_{α} (LUMO, a_2) / eV	E_{β} (LUMO, a_2) / eV	E_{α} (HOMO, b_2) / eV	E_{β} (HOMO, b_2) / eV
[32] ⁰		-1.11		-1.84		-2.34		-5.21	
[32] ⁻	0.000	-0.38	-0.37	-2.63	-1.35	-1.13	-1.02	-4.63	-4.25
[21] ⁺		-2.05		-3.23		-3.64		-6.36	
[21] ⁰	0.014	-1.18	-1.15	-2.59	-2.20	-3.9	-2.63	-5.69	-5.46
[24] ⁺		-0.75		-3.22		-3.58		-6.33	
[24] ⁰	0.017	-1.66	-1.63	-2.57	-2.23	-3.92	-2.70	-5.68	-5.45
[17] ⁰		-1.10		-1.81		-2.31		-5.04	
[17] ⁻	-0.001	-0.37	-0.35	-1.12	-1.00	-2.62	-1.34	-4.56	-4.17
[21-17] ⁺		-1.90		-2.59		-3.01		-5.95	
[21-17] ⁰	0.047	-1.23	-1.07	-2.22	-1.79	-3.49	-2.34	-5.35	-5.22
[24-17] ⁺		-2.26		-2.77		-2.99		-5.85	
[24-17] ⁰	0.016	-1.57	-1.54	-2.31	-1.90	-3.64	-2.47	-5.40	-5.22
[21-17-27] ⁺		-1.84		-2.62		-3.1		-5.80	
[21-17-27] ⁰	0.042	-1.15	-1.00	-2.16	-1.77	-3.53	-2.38	-5.20	-5.05
[21-17-26] ⁺		-1.84		-2.56		-2.96		-5.85	
[21-17-26] ⁰	0.065	-1.22	-1.02	-2.12	-1.73	-3.40	-2.26	-5.24	-5.12
[21-17-25] ⁺		-1.76		-2.57		-3.07		-5.71	
[21-17-25] ⁰	0.093	-1.22	-0.96	-2.02	-1.68	-3.43	-2.30	-5.09	-4.96
[24-17-27] ⁺		-2.20		-2.68		-3.20		-5.79	
[24-17-27] ⁰	0.121	-1.63	-1.29	-2.11	-1.84	-3.68	-2.55	-5.18	-5.05
[24-17-26] ⁺		-2.19		-2.59		-3.05		-5.75	
[24-17-26] ⁰	0.205	-3.65	-2.43	-1.69	-1.24	-2.00	-1.78	-5.16	-5.04
[24-17-25] ⁺		-3.18		-2.06		-2.62		-5.71	
[24-17-25] ⁰	0.215	-3.70	-2.48	-1.93	-1.74	-1.61	-1.17	-5.06	-4.96

**Figure S6** Mulliken spin density distribution of DFT geometry optimized structures of substituted (corrolato)gold complexes in their doublet ground state.

6.3 | Supporting Information to 3.3: Pushing Molular Orbitals to Higher Energy – A DFT Study on the Spin Distribution in Gold Corrole Complexes

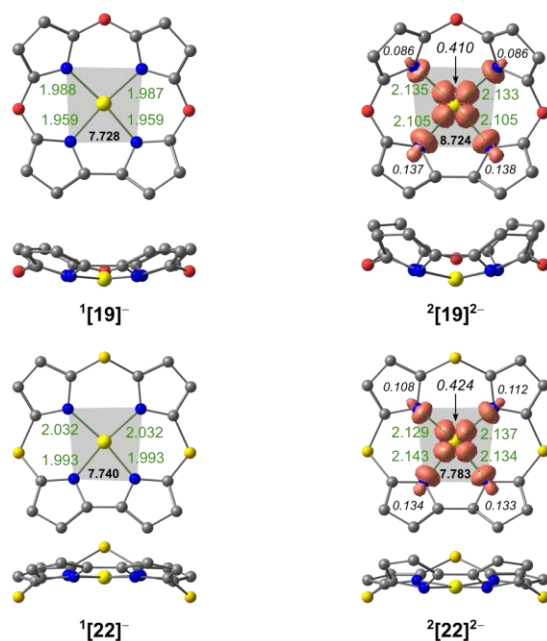


Figure S7 DFT geometry optimized structures of (corrolato)gold complexes in their singlet- and doublet ground states. Mulliken spin density given in italics. Gold-nitrogen distances given in Å. $[AuN_4]$ cavity size given in Å² (bold). Isosurface value at 0.008 a.u. Hydrogen atoms omitted for better visualizations.

Table S9 Absolute normal-coordinate structural decomposition (NSD) analysis of the DFT geometry-optimized structures of 5,10,15-(aryl)-substituted (corrolato)gold complexes in their singlet and doublet ground states.

	B1 (Dom)	A2 (Sad)	B1 (Ruf)	B1 (Wav x)	A2 (Wavy)	A2 (Pro)
[24-32] ⁺	0.142	0.006	0.119	0.185	-0.003	0.001
[24-32] ⁰	0.338	-0.001	0.400	-0.004	0.000	0.001
[24-2] ⁺	0.086	0.242	0.098	0.015	0.017	0.018
[24-2] ⁰	0.375	0.299	0.444	-0.187	0.021	0.009
[24-5] ⁺	0.154	0.014	0.145	0.321	0.000	0.002
[24-5] ⁰	-0.194	-0.036	-0.277	0.447	0.000	-0.003
[24-8] ⁺	-0.134	0.108	-0.100	-0.028	-0.005	0.014
[24-8] ⁰	-0.493	0.034	-0.516	0.142	-0.005	0.007
[24-11] ⁺	-0.078	-0.202	-0.066	-0.022	0.015	-0.014
[24-11] ⁰	-0.362	-0.160	-0.389	0.157	-0.019	-0.002
[24-14] ⁺	-0.102	0.007	0.005	-0.056	-0.017	0.002
[24-14] ⁰	0.303	0.029	0.365	-0.125	0.001	0.004
[24-17] ⁺	0.092	-0.018	0.356	0.536	-0.009	-0.001
[24-17] ⁰	0.478	0.01	0.708	0.121	0.008	0.000
[23-32-2] ²⁺	0.056	0.102	0.020	0.017	0.052	0.001
[23-32-2] ⁺	-0.056	0.104	0.023	-0.014	0.045	0.006
[23-3] ²⁺	0.011	0.191	0.068	0.020	0.090	0.001
[23-3] ⁺	0.002	0.183	0.054	0.018	0.077	0.008
[23-6] ²⁺	0.042	0.284	-0.001	0.007	0.147	0.002
[23-6] ⁺	0.061	0.253	-0.042	0.012	0.119	0.012
[23-9] ²⁺	0.011	0.123	-0.005	-0.005	0.055	-0.004
[23-9] ⁺	0.015	0.035	0.004	0.004	0.011	-0.001
[23-12] ²⁺	-0.004	-0.282	0.004	0.003	-0.144	-0.002
[23-12] ⁺	0.002	-0.223	0.033	-0.003	-0.102	-0.012
[23-15] ²⁺	-0.039	-0.02	0.023	0.030	-0.015	0.000
[23-15] ⁺	-0.050	0.014	0.050	0.027	0.014	0.002
[23-18] ²⁺	0.034	-0.471	-0.043	0.002	-0.234	-0.020
[23-18] ⁺	0.047	0.608	-0.058	-0.001	0.276	0.047

CHAPTER 6 | Appendix

Table S10 Relative normal-coordinate structural decomposition (NSD) analysis of the DFT geometry-optimized structures of substituted (corrolato)gold complexes in their singlet and doublet ground states.

	B1 (Dom)	A2 (Sad)	B1 (Ruf)	B1 (Wav x)	A2 (Wav y)	A2 (Pro)
[24-32] ⁺	0.311	0.013	0.261	0.406	0.007	0.002
[24-32] ⁰	0.454	0.001	0.538	0.005	0.000	0.001
[24-2] ⁺	0.181	0.508	0.206	0.032	0.036	0.038
[24-2] ⁰	0.281	0.224	0.333	0.140	0.016	0.007
[24-5] ⁺	0.242	0.022	0.228	0.505	0.000	0.003
[24-5] ⁰	0.203	0.038	0.289	0.467	0.000	0.003
[24-8] ⁺	0.344	0.278	0.257	0.072	0.013	0.036
[24-8] ⁰	0.412	0.028	0.431	0.119	0.004	0.006
[24-11] ⁺	0.196	0.509	0.166	0.055	0.038	0.035
[24-11] ⁰	0.332	0.147	0.357	0.144	0.017	0.002
[24-14] ⁺	0.540	0.037	0.026	0.296	0.090	0.011
[24-14] ⁰	0.366	0.035	0.441	0.151	0.001	0.005
[24-17] ⁺	0.091	0.018	0.352	0.530	0.009	0.001
[24-17] ⁰	0.361	0.008	0.534	0.091	0.006	0.000
[23-32-2] ²⁺	0.226	0.411	0.081	0.069	0.210	0.004
[23-32-2] ⁺	0.226	0.419	0.093	0.056	0.181	0.024
[23-3] ²⁺	0.029	0.501	0.178	0.052	0.236	0.003
[23-3] ⁺	0.006	0.535	0.158	0.053	0.225	0.023
[23-6] ²⁺	0.087	0.588	0.002	0.014	0.304	0.004
[23-6] ⁺	0.122	0.507	0.084	0.024	0.238	0.024
[23-9] ²⁺	0.054	0.606	0.025	0.025	0.271	0.020
[23-9] ⁺	0.214	0.500	0.057	0.057	0.157	0.014
[23-12] ²⁺	0.009	0.642	0.009	0.007	0.328	0.005
[23-12] ⁺	0.005	0.595	0.088	0.008	0.272	0.032
[23-15] ²⁺	0.307	0.157	0.181	0.236	0.118	0.000
[23-15] ⁺	0.318	0.089	0.318	0.172	0.089	0.013
[23-18] ²⁺	0.042	0.586	0.053	0.002	0.291	0.025
[23-18] ⁺	0.045	0.586	0.056	0.001	0.266	0.045

6.3 | Supporting Information to 3.3: Pushing Molular Orbitals to Higher Energy – A DFT Study on the Spin Distribution in Gold Corrole Complexes

Table S11 Selected metrics of the DFT geometry-optimized structures of substituted (corrolato)gold complexes in their singlet and doublet ground states.

	N1-N3 / Å	N2-N4 / Å	Au-N1 / Å	Au-N2 / Å	Au-N3 / Å	Au-N4 / Å	Au-Mean Plane / Å	Au-N4 Plane / Å	N1-Au- N4 / °	N2-Au- N3 / °
[24-32] ⁺	3.939	3.937	1.957	1.993	1.994	1.957	-0.053	-0.010	79.929	98.303
[24-32] ⁰	3.946	3.945	1.961	1.998	1.999	1.960	-0.118	-0.023	80.005	98.617
[24-2] ⁺	3.939	3.935	1.957	1.993	1.995	1.955	-0.032	-0.004	79.998	98.581
[24-2] ⁰	3.950	3.944	1.963	2.001	2.001	1.958	-0.131	-0.024	80.012	98.954
[24-5] ⁺	3.946	3.946	1.962	1.997	1.997	1.961	-0.055	-0.008	80.311	98.473
[24-5] ⁰	3.948	3.951	1.960	2.004	2.002	1.961	0.065	0.016	79.936	99.217
[24-8] ⁺	3.932	3.935	1.953	1.993	1.992	1.955	0.051	-0.007	79.699	98.195
[24-8] ⁰	3.943	3.946	1.959	1.999	1.997	1.961	0.175	-0.03	79.815	98.371
[24-11] ⁺	3.937	3.934	1.957	1.992	1.993	1.955	0.031	0.004	79.995	98.408
[24-11] ⁰	3.947	3.941	1.961	1.999	1.999	1.958	0.127	0.025	79.929	98.802
[24-14] ⁺	3.936	3.937	1.957	1.991	1.991	1.958	0.037	0.009	79.591	97.739
[24-14] ⁰	3.944	3.944	1.960	1.998	1.998	1.960	-0.105	-0.020	79.496	98.173
[24-17] ⁺	3.963	3.963	1.973	2.000	2.001	1.973	-0.027	0.002	81.443	98.615
[24-17] ⁰	3.955	3.955	1.969	1.997	1.997	1.969	-0.160	-0.026	81.274	98.236
[23-32-2] ²⁺	3.959	3.959	1.977	1.989	1.989	1.977	-0.024	-0.006	79.100	93.119
[23-32-2] ⁺	3.975	3.976	1.981	2.002	2.002	1.981	0.022	0.006	79.472	93.129
[23-3] ²⁺	3.959	3.960	1.978	1.990	1.989	1.978	-0.004	-0.001	79.068	93.057
[23-3] ⁺	3.976	3.976	1.982	2.002	2.001	1.982	0.000	0.000	79.449	93.061
[23-6] ²⁺	3.963	3.964	1.981	1.990	1.990	1.981	-0.019	-0.005	78.969	92.972
[23-6] ⁺	3.979	3.978	1.983	2.002	2.002	1.983	-0.023	-0.006	79.388	92.977
[23-9] ²⁺	3.957	3.957	1.976	1.988	1.989	1.976	-0.005	0.000	79.219	93.182
[23-9] ⁺	3.974	3.974	1.980	2.001	2.001	1.980	-0.005	0.000	79.541	93.153
[23-12] ²⁺	3.962	3.961	1.979	1.990	1.991	1.978	0.001	-0.001	79.129	93.000
[23-12] ⁺	3.976	3.976	1.982	2.000	2.001	1.982	0.000	0.000	79.498	92.991
[23-15] ²⁺	3.958	3.958	1.975	1.990	1.991	1.975	0.013	0.003	79.314	93.439
[23-15] ⁺	3.975	3.975	1.979	2.003	2.003	1.979	0.018	0.005	79.674	93.401
[23-18] ²⁺	3.970	3.970	1.985	1.993	1.993	1.984	-0.016	-0.006	78.761	92.661
[23-18] ⁺	3.987	3.987	1.987	2.006	2.007	1.988	-0.019	-0.006	79.184	92.651

Table S12 Gold-Mulliken spin density and energies of frontier molecular orbitals of the DFT geometry-optimized structures of substituted (corrolato)gold complexes in their singlet and doublet ground states.

	Spin density (Au)	E_a (LUMO +2, b_1) / eV	E_b (LUMO +2, b_1) / eV	E_a (LUMO +1, a_2) / eV	E_b (LUMO +1, a_2) / eV	E_a (LUMO, a_2) / eV	E_b (LUMO, a_2) / eV	E_a (HOMO, b_2) / eV	E_b (HOMO, b_2) / eV
[24-32] ⁺		-2.45		-3.55		-3.21		-2.45	
[24-32] ⁰	0.02	-1.67	-1.65	-2.61	-2.27	-3.91	-2.73	-1.67	-1.65
[24-2] ⁺		-2.40		-3.14		-3.49		-2.39	
[24-2] ⁰	0.02	-1.65	-1.60	-2.57	-2.23	-3.91	-2.73	-1.65	-1.6
[24-5] ⁺		-2.30		-3.01		-3.32		-2.3	
[24-5] ⁰	0.02	-1.58	-1.53	-2.52	-2.18	-3.78	-2.63	-1.58	-1.53
[24-8] ⁺		-2.34		-3.13		-3.48		-2.34	
[24-8] ⁰	0.02	-1.59	-1.56	-2.55	-2.19	-3.92	-2.7	-5.54	-5.35
[24-11] ⁺		-2.21		-2.98		-3.32		-5.33	
[24-11] ⁰	0.02	-1.50	-1.46	-2.44	-2.10	-3.78	-2.59	-5	-4.96
[24-14] ⁺		-2.52		-3.18		-3.51		-6.31	
[24-14] ⁰	0.02	-1.71	-1.68	-2.58	-2.20	-3.90	-2.68	-5.68	-5.49
[24-17] ⁺		-2.26		-2.77		-2.99		-5.85	
[24-17] ⁰	0.02	-1.57	-1.54	-2.31	-1.90	-3.64	-2.47	-5.4	-5.22
[23-32-2] ²⁺		-3.63		-4.06		-5.11		-7.37	
[23-32-2] ⁺	0.00	-2.86	-2.86	-3.34	-3.35	-5.38	-4.13	-6.83	-6.5
[23-3] ²⁺		-3.58		-4.00		-5.08		-6.89	
[23-3] ⁺	0.00	-2.83	-2.83	-3.30	-3.31	-5.36	-4.1	-6.55	-6.47
[23-6] ²⁺		-3.50		-3.88		-5.00		-6.04	
[23-6] ⁺	0.00	-2.78	-2.78	-3.22	-3.23	-5.31	-4.06	-5.67	-5.65
[23-9] ²⁺		-3.55		-3.99		-5.05		-6.61	
[23-9] ⁺	0.00	-2.80	-2.80	-3.27	-3.28	-5.34	-4.09	-6.29	-6.29
[23-12] ²⁺		-3.42		-3.86		-4.92		-5.82	
[23-12] ⁺	0.00	-2.73	-2.73	-3.21	-3.21	-5.23	-4.03	-5.46	-5.45
[23-15] ²⁺		-3.66		-4.03		-5.13		-7.42	
[23-15] ⁺	0.00	-2.89	-2.89	-3.31	-3.32	-5.40	-4.14	-6.87	-6.54
[23-18] ²⁺		-3.42		-3.79		-5.00		-7.02	
[23-18] ⁺	0.00	-2.69	-2.70	-3.13	-3.14	-5.30	-4.03	-6.47	-6.27

6.3 | Supporting Information to 3.3: Pushing Molular Orbitals to Higher Energy – A DFT Study on the Spin Distribution in Gold Corrole Complexes

Table S13 Absolute normal-coordinate structural decomposition (NSD) analysis of the DFT geometry-optimized structures of substituted (corrolato)gold complexes in their singlet and doublet ground states.

	B1 (Dom)	A2 (Sad)	B1 (Ruf)	B1 (Wav x)	A2 (Wav y)	A2 (Pro)
[21-32] ⁺	0.259	-0.009	0.065	0.245	-0.012	0.003
[21-32] ⁰	0.248	0.000	0.099	0.216	-0.009	0.003
[21-2] ⁺	0.045	-0.017	0.003	0.002	-0.017	0.002
[21-2] ⁰	0.281	-0.015	0.124	0.254	0.008	-0.004
[21-5] ⁺	-0.161	0.334	-0.078	-0.003	0.002	0.029
[21-5] ⁰	-0.214	0.295	-0.110	0.010	0.001	0.019
[21-8] ⁺	0.335	0.112	0.084	0.051	0.002	0.012
[21-8] ⁰	-0.469	0.022	-0.177	-0.037	-0.008	0.007
[21-11] ⁺	-0.238	0.166	-0.091	-0.009	-0.038	0.016
[21-11] ⁰	-0.328	0.111	-0.147	-0.014	0.009	0.004
[21-14] ⁺	-0.411	-0.013	0.003	-0.221	-0.007	0.001
[21-14] ⁰	-0.066	-0.013	0.004	0.037	-0.017	0.003
[21-17] ⁺	0.010	0.656	0.002	0.022	0.112	0.035
[21-17] ⁰	0.018	0.871	0.023	0.011	0.070	0.055
[20-32-2] ²⁺	0.836	0.118	0.059	0.172	0.080	0.001
[20-32-2] ⁺	0.717	-0.098	-0.011	0.203	-0.072	-0.005
[20-3] ²⁺	0.772	0.197	0.050	0.181	0.133	0.00
[20-3] ⁺	0.686	0.167	-0.025	0.205	0.115	0.005
[20-6] ²⁺	0.754	0.259	0.085	0.203	0.185	-0.003
[20-6] ⁺	0.678	0.215	-0.007	0.213	0.156	0.005
[20-9] ²⁺	0.754	0.144	0.048	0.153	0.106	-0.006
[20-9] ⁺	0.730	0.034	-0.029	0.174	0.027	-0.002
[20-12] ²⁺	-0.706	-0.259	-0.029	-0.180	-0.185	0.003
[20-12] ⁺	-0.662	-0.139	0.019	-0.200	-0.111	-0.003
[20-15] ²⁺	0.812	-0.019	0.026	0.145	-0.012	-0.001
[20-15] ⁺	0.613	-0.025	-0.029	0.168	-0.018	-0.001
[20-18] ²⁺	0.801	0.381	0.192	0.145	0.249	0.014
[20-18] ⁺	0.592	0.445	0.039	0.199	0.296	0.023

Table S14 Relative normal-coordinate structural decomposition (NSD) analysis of the DFT geometry-optimized structures of substituted (corrolato)gold complexes in their singlet and doublet ground states.

	B1 (Dom)	A2 (Sad)	B1 (Ruf)	B1 (Wav x)	A2 (Wav y)	A2 (Pro)
[21-32] ⁺	0.437	0.015	0.110	0.413	0.020	0.005
[21-32] ⁰	0.431	0.000	0.172	0.376	0.016	0.005
[21-2] ⁺	0.523	0.198	0.035	0.023	0.198	0.023
[21-2] ⁰	0.410	0.022	0.181	0.370	0.012	0.006
[21-5] ⁺	0.265	0.550	0.129	0.005	0.003	0.048
[21-5] ⁰	0.330	0.455	0.169	0.015	0.002	0.029
[21-8] ⁺	0.562	0.188	0.141	0.086	0.003	0.020
[21-8] ⁰	0.651	0.031	0.246	0.051	0.011	0.010
[21-11] ⁺	0.427	0.297	0.163	0.016	0.068	0.029
[21-11] ⁰	0.535	0.181	0.240	0.023	0.015	0.007
[21-14] ⁺	0.627	0.020	0.005	0.337	0.011	0.002
[21-14] ⁰	0.471	0.093	0.029	0.264	0.121	0.021
[21-17] ⁺	0.012	0.784	0.002	0.026	0.134	0.042
[21-17] ⁰	0.017	0.831	0.022	0.011	0.067	0.052
[20-32-2] ²⁺	0.660	0.093	0.047	0.136	0.063	0.001
[20-32-2] ⁺	0.648	0.089	0.010	0.184	0.065	0.005
[20-3] ²⁺	0.579	0.148	0.038	0.136	0.100	0.001
[20-3] ⁺	0.570	0.139	0.021	0.170	0.096	0.004
[20-6] ²⁺	0.507	0.174	0.057	0.137	0.124	0.001
[20-6] ⁺	0.532	0.169	0.005	0.167	0.122	0.004
[20-9] ²⁺	0.623	0.119	0.040	0.126	0.088	0.005
[20-9] ⁺	0.732	0.034	0.029	0.175	0.028	0.002
[20-12] ²⁺	0.518	0.190	0.021	0.132	0.136	0.002
[20-12] ⁺	0.584	0.123	0.017	0.176	0.098	0.003
[20-15] ²⁺	0.800	0.019	0.026	0.143	0.012	0.001
[20-15] ⁺	0.718	0.029	0.034	0.197	0.021	0.001
[20-18] ²⁺	0.449	0.214	0.108	0.081	0.140	0.008
[20-18] ⁺	0.371	0.279	0.024	0.125	0.186	0.014

CHAPTER 6 | Appendix

Table S15 Selected metrics of the DFT geometry-optimized structures of substituted (corrolato)gold complexes in their singlet and doublet ground states.

	N1-N3 / Å	N2-N4 / Å	Au-N1 / Å	Au-N2 / Å	Au-N3 / Å	Au-N4 / Å	Au-Mean Plane / Å	Au-N4 Plane / Å	N1-Au- N4 / °	N2-Au- N3 / °
[21-32] ⁺	3.883	3.882	1.935	1.953	1.954	1.935	-0.107	-0.026	80.837	92.852
[21-32] ⁰	3.891	3.890	1.939	1.957	1.958	1.938	-0.100	0.022	80.734	93.169
[21-2] ⁺	3.887	3.886	1.938	1.955	1.955	1.937	-0.115	0.027	81.033	92.864
[21-2] ⁰	3.892	3.893	1.939	1.959	1.958	1.940	-0.113	0.024	80.858	93.138
[21-5] ⁺	3.880	3.885	1.933	1.955	1.953	1.936	0.067	0.013	81.061	93.375
[21-5] ⁰	3.886	3.892	1.936	1.959	1.958	1.939	0.086	0.017	80.816	93.498
[21-8] ⁺	3.880	3.877	1.933	1.952	1.952	1.931	-0.139	-0.029	80.641	92.760
[21-8] ⁰	3.888	3.891	1.938	1.959	1.957	1.939	0.188	-0.036	80.535	92.832
[21-11] ⁺	3.876	3.881	1.931	1.952	1.952	1.934	0.098	0.019	80.854	82.968
[21-11] ⁰	3.884	3.889	1.935	1.975	1.957	2.938	0.132	0.025	80.636	93.194
[21-14] ⁺	3.886	3.887	1.940	1.953	1.952	1.940	0.166	0.043	80.969	92.219
[21-14] ⁰	3.885	3.885	1.935	1.956	1.956	1.935	0.026	0.006	80.188	82.769
[21-17] ⁺	3.895	3.895	1.944	1.960	1.960	1.943	-0.004	-0.001	82.110	94.374
[21-17] ⁰	3.910	3.908	1.952	1.969	1.969	1.950	-0.006	-0.001	81.497	93.736
[20-32-2] ²⁺	3.861	3.860	1.933	1.938	1.938	1.935	-0.356	-0.080	80.664	95.102
[20-32-2] ⁺	3.869	3.869	1.933	1.946	1.947	1.931	-0.290	-0.066	81.017	95.281
[20-3] ²⁺	3.860	3.859	1.932	1.932	1.938	1.934	-0.325	-0.078	80.571	95.180
[20-3] ⁺	3.868	3.869	1.931	1.947	1.946	1.933	-0.275	-0.061	80.965	95.323
[20-6] ²⁺	3.863	3.864	1.934	1.939	1.939	1.938	-0.319	-0.079	80.486	95.591
[20-6] ⁺	3.871	3.872	1.932	1.947	1.947	1.935	-0.274	-0.062	80.865	95.239
[20-9] ²⁺	3.855	3.856	1.929	1.936	1.937	1.932	-0.320	-0.077	80.641	95.325
[20-9] ⁺	3.867	3.866	1.931	1.946	1.946	1.930	0.296	-0.067	81.092	95.402
[20-12] ²⁺	3.860	3.860	1.933	1.939	1.939	1.929	0.293	0.068	80.626	65.340
[20-12] ⁺	3.866	3.868	1.930	1.945	1.944	1.933	0.266	0.060	81.010	95.328
[20-15] ²⁺	3.857	3.857	1.931	1.939	1.938	1.930	-0.348	0.086	80.770	85.443
[20-15] ⁺	3.863	3.862	1.927	1.945	1.945	1.926	-0.250	0.056	81.056	95.688
[20-18] ²⁺	3.868	3.874	1.938	1.946	1.940	1.942	-0.333	-0.082	80.101	94.632
[20-18] ⁺	3.875	3.879	1.933	1.954	1.950	1.937	-0.237	-0.054	80.400	95.099

6.3 | Supporting Information to 3.3: Pushing Molular Orbitals to Higher Energy – A DFT Study on the Spin Distribution in Gold Corrolo Complexes

Table S16 Gold-Mulliken spin density and energies of frontier molecular orbitals of the DFT geometry-optimized structures of substituted (corrolo)gold complexes in their singlet and doublet ground states.

	Spin density (Au)	E_{α} (LUMO+2, b_1) / eV	E_{β} (LUMO+2, b_1) / eV	E_{α} (LUMO+1, a_2) / eV	E_{β} (LUMO+1, a_2) / eV	E_{α} (LUMO, a_2) / eV	E_{β} (LUMO, a_2) / eV	E_{α} (HOMO, b_2) / eV	E_{β} (HOMO, b_2) / eV
[21-32] ⁺		-2.03		-3.22		-3.59		-6.27	
[21-32] ⁰	0.01	-1.22	-2.19	-2.64	-2.27	-3.88	-2.67	-5.65	-5.45
[21-2] ⁺		-1.99		-3.14		-3.51		-6.14	
[21-2] ⁰	0.01	-1.19	-1.16	-2.58	-2.20	-3.80	-2.61	-5.65	-5.39
[21-5] ⁺		-1.85		-2.99		-3.36		-5.59	
[21-5] ⁰	0.02	-1.12	-1.08	-2.50	-2.11	-3.71	-2.53	-5.21	-5.17
[21-8] ⁺		-1.91		-3.11		-3.49		-6.08	
[21-8] ⁰	0.01	-1.14	-1.12	-2.54	-2.15	-3.84	-2.58	-5.55	-5.35
[21-11] ⁺		-1.77		-2.97		-3.34		-5.35	
[21-11] ⁰	0.01	-1.03	-1.00	-2.54	-2.15	-3.84	-2.58	-5.00	-4.96
[21-14] ⁺		-2.13		-3.14		-3.48		-6.31	
[21-14] ⁰	0.01	-1.22	-1.20	-2.60	-2.17	-3.85	-2.59	-5.69	-5.50
[21-17] ⁺		-1.90		-2.59		-3.01		-5.95	
[21-17] ⁰	0.05	-1.23	-1.07	-2.22	-1.79	-3.49	-2.34	-5.35	-5.22
[20-32-2] ²⁺		-3.16		-4.07		-5.32		-7.44	
[20-32-2] ⁺	0.00	-2.25	-2.23	-3.36	-3.36	-5.69	-4.27	-6.87	-6.59
[20-3] ²⁺		-3.09		-4.00		-5.28		-6.96	
[20-3] ⁺	0.00	-2.21	-2.19	-3.31	-3.31	-5.66	-4.25	-6.60	-6.56
[20-6] ²⁺		-3.00		-3.84		-5.19		-6.14	
[20-6] ⁺	0.02	-2.16	-2.14	-3.20	-3.20	-5.60	-4.19	-5.73	-5.71
[20-9] ²⁺		-3.03		-3.98		-5.26		-6.66	
[20-9] ⁺	0.01	-2.19	-2.18	-3.28	-3.28	-5.65	-4.25	-6.31	-6.31
[20-12] ²⁺		-2.86		-3.84		-5.17		-5.89	
[20-12] ⁺	0.00	-2.10	-2.09	-3.20	-3.20	-5.47	-4.19	-5.49	-5.46
[20-15] ²⁺		-3.19		-4.04		-5.35		-7.51	
[20-15] ⁺	0.00	-2.23	-2.22	-3.32	-3.32	-5.72	-4.29	-6.92	-6.65
[20-18] ²⁺		-3.00		-3.53		-5.16		-7.32	
[20-18] ⁺	0.00	-2.13	-2.11	-2.91	-2.91	-5.57	-4.14	-6.70	-6.55

Table S17 Absolute normal-coordinate structural decomposition (NSD) analysis of the DFT geometry-optimized structures of substituted (corrolo)gold complexes in their singlet and doublet ground states.

	B1 (Dom)	A2 (Sad)	B1 (Ruf)	B1 (Wavx)	A2 (Wavy)	A2 (Pro)
[21-14-25] ⁺	0.355	-0.009	-0.058	0.127	0.025	-0.002
[21-14-25] ⁰	-0.114	0.049	0.075	0.201	-0.022	0.006
[21-14-26] ⁺	-0.383	-0.039	0.001	-0.199	-0.024	0.000
[21-14-26] ⁰	-0.146	0.013	0.011	0.080	-0.017	0.004
[21-14-27] ⁺	-0.187	-0.004	0.017	-0.076	-0.011	0.007
[21-14-27] ⁰	-0.075	0.024	0.038	0.076	-0.027	0.005
[24-14-25] ⁺	-0.098	0.091	0.149	0.061	-0.023	0.003
[24-14-25] ⁰	0.028	0.036	0.618	-0.117	-0.027	0.003
[24-14-26] ⁺	-0.130	-0.032	0.061	-0.039	-0.019	0.000
[24-14-26] ⁰	0.359	-0.026	0.538	-0.146	-0.007	0.002
[24-14-27] ⁺	-0.049	0.041	0.085	0.023	-0.025	0.002
[24-14-27] ⁰	0.243	0.084	0.437	-0.138	-0.014	0.004

Table S18 Absolute normal-coordinate structural decomposition (NSD) analysis of the DFT geometry-optimized structures substituted (corrolato)gold complexes in their singlet and doublet ground states.

	B1 (Dom)	A2 (Sad)	B1 (Ruf)	B1 (Wav x)	A2 (Wavy)	A2 (Pro)
[21-14-25] ⁺	0.616	0.016	0.101	0.220	0.043	0.003
[21-14-25] ⁰	0.244	0.105	0.161	0.430	0.047	0.013
[21-14-26] ⁺	0.593	0.060	0.002	0.308	0.037	0.000
[21-14-26] ⁰	0.539	0.048	0.041	0.295	0.063	0.015
[21-14-27] ⁺	0.619	0.013	0.056	0.252	0.036	0.023
[21-14-27] ⁰	0.306	0.098	0.155	0.310	0.110	0.020
[24-14-25] ⁺	0.231	0.214	0.351	0.144	0.054	0.007
[24-14-25] ⁰	0.033	0.043	0.746	0.141	0.033	0.004
[24-14-26] ⁺	0.463	0.114	0.217	0.139	0.068	0.000
[24-14-26] ⁰	0.333	0.024	0.499	0.135	0.006	0.002
[24-14-27] ⁺	0.218	0.182	0.378	0.102	0.111	0.009
[24-14-27] ⁰	0.264	0.091	0.475	0.150	0.015	0.004

Table S19 Selected metrics of the DFT geometry-optimized structures of substituted (corrolato)gold complexes in their singlet and doublet ground states.

	N1-N3 / Å	N2-N4 / Å	Au-N1 / Å	Au-N2 / Å	Au-N3 / Å	Au-N4 / Å	Au-Mean Plane / Å	Au-N4 Plane / Å	N1-Au-N4 / °	N2-Au-N3 / °
[21-14-25] ⁺	3.884	3.886	1.935	1.956	1.955	1.936	-0.140	0.036	80.671	92.705
[21-14-25] ⁰	3.890	3.890	1.936	1.960	1.960	1.936	0.042	0.012	80.314	93.248
[21-14-26] ⁺	3.900	3.900	1.046	1.964	1.963	1.945	0.003	0.001	81.811	94.188
[21-14-26] ⁰	3.886	3.886	1.933	1.958	1.960	1.934	0.056	0.013	80.257	93.407
[21-14-27] ⁺	3.881	3.881	1.934	1.952	1.952	1.934	0.071	0.016	80.321	91.972
[21-14-27] ⁰	3.887	3.887	1.937	1.956	1.956	1.936	0.029	0.008	80.218	92.551
[24-14-25] ⁺	3.942	3.941	1.957	1.998	1.998	1.957	0.036	0.015	79.556	98.204
[24-14-25] ⁰	3.949	3.946	1.960	2.001	2.002	1.958	-0.088	-0.007	79.604	98.442
[24-14-26] ⁺	3.939	3.939	1.955	1.998	1.998	1.955	0.049	0.014	79.614	98.625
[24-14-26] ⁰	3.946	3.945	1.958	2.001	2.003	1.958	-0.120	-0.018	79.625	98.952
[24-14-27] ⁺	3.938	3.938	1.958	1.992	1.992	1.958	0.018	0.007	79.415	97.288
[24-14-27] ⁰	3.947	3.946	1.961	1.998	1.998	1.960	-0.082	-0.013	79.438	97.702

Table S20 Gold-Mulliken spin density and energies of frontier molecular orbitals of the DFT geometry-optimized structures of substituted (corrolato)gold complexes in their singlet and doublet ground states.

	Spin density (Au)	E _α (LUMO+ 2, b ₁) / eV	E _β (LUMO+ 2, b ₁) / eV	E _α (LUMO+ 1, a ₂) / eV	E _β (LUMO+ 1, a ₂) / eV	E _α (LUMO, a ₂) / eV	E _β (LUMO, a ₂) / eV	E _α (HOMO, b ₂) / eV	E _β (HOMO, b ₂) / eV
[21-14-25] ⁺		-1.84		-2.78		-3.17		-5.89	
[21-14-25] ⁰	0.014	-0.98	-0.96	-2.15	-1.78	-3.53	-2.32	-5.30	-5.08
[21-14-26] ⁺		-1.98		-3.00		-3.23		-6.09	
[21-14-26] ⁰	0.014	-1.11	-1.08	-2.44	-2.02	-3.59	-2.36	-5.47	-5.28
[21-14-27] ⁺		-1.95		-2.94		-3.45		-6.14	
[21-14-27] ⁰	0.014	-1.10	-1.07	-2.27	-1.89	-3.76	-2.51	-5.50	-5.27
[24-14-25] ⁺		-2.28		-2.79		-3.20		-5.90	
[24-14-25] ⁰	0.017	-1.45	-1.42	-2.19	-1.85	-3.66	-2.47	-5.30	-5.09
[24-14-26] ⁺		-2.41		-3.04		-3.27		-6.09	
[24-14-26] ⁰	0.018	-1.59	-1.57	-2.48	-2.09	-3.74	-2.53	-5.47	-5.30
[24-14-27] ⁺		-2.38		-2.90		-3.43		-6.12	
[24-14-27] ⁰	0.017	-1.57	-1.54	-2.28	-1.94	-3.82	-2.61	-5.50	-5.28

6.3 | Supporting Information to 3.3: Pushing Molular Orbitals to Higher Energy – A DFT Study on the Spin Distribution in Gold Corrole Complexes

Table S21 Sum of *out-of-plane* distortions and [AuN₄] cavity size of the DFT geometry-optimized structures of substituted (corrolo)gold complexes in their singlet and doublet ground states obtained from normal-coordinate structural decomposition (NSD) analysis.

Compound	D(oop) / Å	Cavity size / Å ²	Compound	D(oop) / Å	Cavity size / Å ²
[0] ⁰	0.415	7.602	[23-9] ²⁺	0.203	7.814
[0] ⁻	0.429	7.678	[23-9] ⁺	0.070	7.881
[1] ⁰	0.544	7.607	[24-17-27] ⁺	1.236	7.850
[1] ⁻	0.497	7.679	[24-17-27] ⁰	2.087	8.076
[2] ⁰	0.429	7.609	[24-17-26] ⁺	1.850	7.846
[2] ⁻	0.396	7.682	[24-17-26] ⁰	2.701	8.270
[3] ⁰	0.158	7.597	[24-17-25] ⁺	1.871	7.897
[3] ⁻	0.142	7.672	[24-17-25] ⁰	2.844	8.361
[4] ⁰	0.511	7.611	[24-32] ⁺	0.456	7.752
[4] ⁻	0.445	7.680	[24-32] ⁰	0.744	7.784
[5] ⁰	0.362	7.611	[24-2] ⁺	0.476	7.751
[5] ⁻	0.312	7.682	[24-2] ⁰	1.335	7.795
[6] ⁰	0.152	7.599	[24-5] ⁺	0.636	7.785
[6] ⁻	0.136	7.672	[24-5] ⁰	0.957	7.799
[7] ⁰	0.462	7.590	[24-8] ⁺	0.389	7.736
[7] ⁻	0.371	7.659	[24-8] ⁰	1.197	7.779
[8] ⁰	0.412	7.599	[24-11] ⁺	0.397	7.745
[8] ⁻	0.392	7.668	[24-11] ⁰	1.089	7.781
[9] ⁰	0.065	7.594	[24-14] ⁺	0.189	7.746
[9] ⁻	0.037	7.668	[24-14] ⁰	0.827	7.777
[10] ⁰	0.173	7.584	[24-17] ⁺	1.012	7.852
[10] ⁻	0.153	7.653	[24-17] ⁰	1.325	7.819
[11] ⁰	0.314	7.594	[23-32-2] ²⁺	0.248	7.818
[11] ⁻	0.260	7.663	[23-32-2] ⁺	0.248	7.887
[12] ⁰	0.162	7.594	[23-3] ²⁺	0.381	7.822
[12] ⁻	0.122	7.667	[23-3] ⁺	0.342	7.889
[13] ⁰	0.086	7.585	[23-12] ²⁺	0.439	7.830
[13] ⁻	0.079	7.657	[23-12] ⁺	0.375	7.888
[14] ⁻	0.108	7.592	[23-15] ²⁺	0.127	7.817
[14] ⁰	0.093	7.664	[23-15] ⁺	0.157	7.886
[15] ⁻	0.033	7.593	[23-18] ²⁺	0.804	7.860
[15] ⁰	0.027	7.667	[23-18] ⁺	1.037	7.929
[16] ⁻	0.700	7.626	[21-32] ⁺	0.386	7.526
[16] ⁰	0.144	7.664	[21-32] ⁰	0.365	7.556
[17] ⁻	0.295	7.606	[21-2] ⁺	0.461	7.499
[17] ⁰	0.164	7.670	[21-2] ⁰	0.424	7.565
[18] ⁻	0.097	7.595	[21-5] ⁺	0.381	7.532
[18] ⁰	0.107	7.669	[21-5] ⁰	0.382	7.560
[19] ⁻	2.402	7.728	[21-8] ⁺	0.375	7.509
[19] ⁰	3.981	8.724	[21-8] ⁰	0.512	7.552
[20] ⁻	1.075	7.488	[21-11] ⁺	0.31	7.512
[20] ⁰	0.975	7.481	[21-11] ⁰	0.382	7.554
[21] ⁻	0.086	7.499	[21-14] ⁺	0.491	7.541
[21] ⁰	0.086	7.535	[21-14] ⁰	0.074	7.532
[22] ⁻	2.553	8.039	[21-17] ⁺	0.668	7.600
[22] ⁰	3.182	8.992	[21-17] ⁰	0.877	7.676
[23] ⁻	0.089	7.815	[20-32-2] ²⁺	0.890	7.480
[23] ⁰	0.075	7.886	[20-32-2] ⁺	0.779	7.480
[24] ⁻	0.058	7.740	[20-3] ²⁺	0.852	7.444
[24] ⁰	0.705	7.783	[20-3] ⁺	0.768	7.480
[25] ⁰	0.049	7.597	[20-6] ²⁺	0.873	7.460
[25] ⁻	0.198	7.672	[20-6] ⁺	0.783	7.490
[26] ⁰	0.039	7.599	[20-9] ²⁺	0.812	7.430
[26] ⁻	0.041	7.670	[20-9] ⁺	0.773	7.472
[27] ⁰	0.037	7.598	[20-12] ²⁺	0.817	7.446
[27] ⁻	0.167	7.676	[20-12] ⁺	0.738	7.473
[32] ⁰	0.027	7.599	[20-15] ²⁺	0.846	7.435
[32] ⁻	0.008	7.674	[20-15] ⁺	0.657	7.457
[32-1] ⁰	0.310	7.603	[20-18] ²⁺	0.974	7.489

[32-1] ⁻	0.345	7.681	[20-18] ⁺	0.843	7.515
[32-2] ⁰	0.112	7.681	[21-14-25] ⁺	0.576	7.534
[32-2] ⁻	0.111	7.671	[21-14-25] ⁰	0.467	7.555
[21-17] ⁺	0.837	7.600	[21-14-26] ⁺	0.646	7.538
[21-17] ⁰	1.048	7.676	[21-14-26] ⁰	0.271	7.541
[24-17] ⁺	1.012	7.852	[21-14-27] ⁺	0.302	7.515
[24-17] ⁰	1.325	7.819	[21-14-27] ⁰	0.245	7.540
[21-17-27] ⁺	1.225	7.634	[24-14-25] ⁺	0.204	7.766
[21-17-27] ⁰	1.066	7.676	[24-14-25] ⁰	0.690	7.791
[21-17-26] ⁺	1.429	7.624	[24-14-26] ⁺	0.156	7.757
[21-17-26] ⁰	1.555	7.783	[24-14-26] ⁰	0.663	7.783
[21-17-25] ⁺	1.600	7.679	[24-14-27] ⁺	0.109	7.752
[21-17-25] ⁰	1.818	7.876	[24-14-27] ⁰	0.524	7.785
[23-6] ²⁺	0.483	7.835			
[23-6] ⁺	0.499	7.897			

References

- [1] F. Neese, *Wiley Interdiscip. Rev. Comput Mol Sci.* **2022**, 12, 12753.
- [2] A. D. Becke, *J. Chem. Phys.* **1993**, 98, 5648–5652.
- [3] B. Miehlich, A. Savin, H. Stoll, H. Preuss, *Chem. Phys. Lett.* **1989**, 157, 200–206.
- [4] A. Schäfer, H. Horn, R. Ahlrichs, *J. Chem. Phys.* **1992**, 97, 2571–2577.
- [5] A. Schäfer, H. Horn, R. Ahlrichs, *J. Chem. Phys.* **1994**, 100, 5829–5835.
- [6] D. A. Pantazis, X.-Y. Chen, C. R. Landis, F. Neese, *J. Chem. Theory Comput.* **2008**, 4, 908–919.
- [7] F. Neese, F. Wennmohs, A. Hansen, U. Becker, *Chem. Phys.* **2009**, 356, 98–109.
- [8] S. Miertuš, E. Scrocco, J. Tomasi, *Chem. Phys.* **1981**, 55, 117–129.
- [9] S. Grimme, J. Antony, S. Ehrlich, H. Krieg, *J. Chem. Phys.* **2010**, 132, 154104.
- [10] S. Grimme, S. Ehrlich, L. Goerigk, *J. Comput. Chem.* **2011**, 32, 1456–1465.
- [11] J. Krumsieck, M. Bröring, *Chem. Eur. J.* **2021**, 27, 11580–11588.
- [12] J. Krumsieck, *PorphyrStruct*, **2023**.
- <https://github.com/JensKrumsieck/PorphyrStruct/releases/tag/v2.0.1>.

7 Acknowledgements

Zuallererst möchte ich mich bei [REDACTED] bedanken. Dafür, dass Sie mir – schon nach meiner Bachelor- und Masterarbeit – auch die Promotion auf dem gleichen Themengebiet in Ihrem Arbeitskreis ermöglicht haben. Der scheinbar endlose Vorrat an Ideen bei wissenschaftlichen Fragestellungen – sei es im persönlich Gespräch oder auch in den Gruppenseminaren – haben mich immer wieder auf's Neue begeistert und meine eigene Neugier und Begeisterung für die Chemie – auch in weniger ertragreichen Zeiten – neu entfacht. Vielen Dank für alles!

Außerdem bedanke ich mich bei [REDACTED] für die Übernahme der Zweitkorrektur meiner Dissertation.

Bei [REDACTED] bedanke ich mich für die Einführung in die Geheimnisse der Simulation von EPR-Spektren und für die zahlreichen fachlichen Diskussion im Laufe der letzten Jahre.

Ein weiterer Dank geht an die Mitarbeiter und Mitarbeiterinnen der Zentralen Analytik für die Messungen der NMR- und Massenspektren. Im Besonderen [REDACTED] für seine stetig schnelle und kompetente Hilfe bei speziellen Messungen bezüglich NMR-Spektroskopie.

Zudem möchte ich mich bei meinen Modulatoren [REDACTED] und [REDACTED] („Knock-nacnac-knockin' on Heavens door“) sowie bei meinem Bachelorstudenten Matthis Hannes Schäfer bedanken. Es war mir eine Ehre, dich auf deinem Weg zum Bachelorabschluss begleiten zu dürfen. Deine Offenheit, Herzlichkeit und Neugier haben mir imponiert.

Eine weiterer Dank geht an den gesamten [REDACTED]. Zum einen für die zahlreichen fachlichen Ratschläge, Tipps und Diskussionen aber auch für die Freundschaften, die sich über die Jahre aufgebaut haben und es mir jeden Tag – selbst wenn es mal im Labor nicht so gut lief, wer kennt es nicht – leicht gemacht haben, in den AK zu kommen.

Besonders möchte ich mich bei [REDACTED] („Ach [REDACTED], schön war's... und wird es hoffentlich bleiben. Woll!“), [REDACTED] („Pinker Donut verkauft an Kasse 3 von Schäfa“), [REDACTED] („Einfach mal...“ aber „es schaut ja eh keiner“, „Aua! Also wirklich!“) und [REDACTED] („Ich wünsch' dir – wobei: nicht mal das“) bedanken. Ich bin unendlich dankbar dafür, dass ihr mich auf meinem Promotionsweg begleitet habt – ausdrücklich ohne jemandem etwas unterstellen zu wollen.

CHAPTER 7 | Acknowledgements

■■■■ Mehr als nur heiße Luft! Das ein oder andere Mal wurde es auch ziemlich haarig. Ich glaube aber, wir haben den richtigen Riecher bewiesen, als wir Box- und Büronachbarn wurden. Ich danke dir für Alles! Und nun geht es ab in die Weltspitze des Tischtennissports. Jetzt kann ich es ja verraten: Ich bin es. Und ganz wichtig: Die Maus muss aus! Immer dreimal ziehen! Ab auf die Tasten! Bähm!

Ein besonderer Dank geht an ■■■■. Vielen Dank für deine vielen fachlichen und privaten Ratschläge und Gespräche – auch über den großen Teich hinaus – und deinen stetigen Nachschub an Schokobrotchen. Nicht mehr lange, dann hab ich auch dein Rätsel gelöst und stelle dir mal vor, es wären noch mehr Flughäfen.

■■■■, ohne dich wäre die Pumpe immer noch am Laufen und das Gasleck längst nicht gefunden. Vielen Dank für deine fachlichen Ratschläge, dein stetig offenes Ohr und deine schier endlose Zeit, wenn ich dir das Ohr abgekaut habe.

■■■■, bloß jetzt nichts Peinliches...Allez! Aber wir schaffen es ja eh nicht und zuschauen tut auch niemand. ■■■■, lass uns ab sofort jeden Tag zu einem Montag machen. ■■■■, demnächst leider nicht mehr „öfters hier“. ■■■■, 1-1-2 – ich frage direkt nach dir – nur nach dir. ■■■■, bin ab sofort unter Dock. ■■■■, bin doch gerne deine Bleiente. ■■■■, wir halten uns gegenseitig auf dem Laufenden. ■■■■, danke für unsere gemeinsame Freundschaft zum Gold. ■■■■, keep going! Aber nur fünfmal! Auf unsere Blockwerk Zukunft.

■■■■ – meinem Bachelorpapa – danke ich dafür, dass er mich durch seine herausragende Betreuung schon während meiner Bachelorarbeit die Grundlagen für meine Promotion gelegt hat.

Einen weiteren Dank richte ich an meine gewissenhaften Korrekturleser ■■■■, ■■■■ und ■■■■. Warmmachen ist etwas für Amateure. Wir sind direkt auf Betriebstemperatur.

Ein ganz besonderer Dank gilt meiner ■■■■, ■■■■ und meinem ■■■■, dass ihr mich auch immer unterstützt, spontan beherbergt habt, wenn ich mal vorbeigekommen bin und ich mich immer willkommen fühle. Nicht zu vergessen mein ■■■■. Du machst mich zum stolzesten Okel der Welt.

Ein besonderer Dank geht an meine ■■■■ für ihre ununterbrochene und bedingungslose Unterstützung und Hilfe in der Zeit während meines Studiums und der anschließenden Promotion.

■■■■

8 Curriculum Vitae

Lukas Paul Sorge

Address [REDACTED]
Email [REDACTED]
Date of birth 3rd of February 1992
Mobile [REDACTED]
Place of birth Arnsberg, Germany
Nationality German

Research Experience

- 05/2019 – 06/2024 **Doctoral Studies in Chemistry**
Johannes Gutenberg University Mainz, Research group of [REDACTED]
[REDACTED] “Inorganic Chemistry – Sustainable Coordination Chemistry and Photochemistry”
Macrocyclic Tetraaza Gold Complexes – Synthesis, Spectroscopy, Theoretical Studies
- Synthesis of porphyrin ligands and their corresponding gold complexes.
 - Characterization via static absorption- and emission spectroscopy, NMR- and EPR spectroscopy, cyclic- and square wave voltammetry.
 - Quantumchemical calculations for the interpretation of the empirical data.
 - Supervision of students in practical courses and bachelor thesis, teaching analytical methods.
- 04/2017 – 05/2019 **Master of Science in Chemistry**
Johannes Gutenberg University Mainz (overall grade 1.6)
Master’s thesis in the research group of [REDACTED]
Novel Mono- and Binuclear Gold(II) Complexes (grade 1.0)
- 10/2016 – 03/2017 **Research Internship**
Arizona State University, Tempe, Arizona, USA

CHAPTER 8 | Curriculum Vitae

Research group of [REDACTED] “Synthesis, characterization and applications of new inorganic porous materials”

- Exploratory synthesis of nanozeolites through geopolymer chemistry.
- Characterization via powder X-ray diffraction, BET analysis and dynamic light scattering.

04/2012 – 09/2016

Bachelor of Science in Chemistry

Johannes Gutenberg University Mainz (overall grade 1.9)

Bachelor’s thesis in the research group of [REDACTED]

Synthesis of a P-AuP-Dyade for the Study of the Photoinduced Electron Transfer
(grade 1.0)

Educational training

2001 – 2011

High School Degree (grade 1.9)

Gymnasium der Benediktiner Meschede

Skills & Interests

Languages

German (native), English (business fluent)

Software skills

MS Office, Origin, MestRenova, ChemDraw, ChemCraft, Inkscape, MatLab

8.1 List of Publications

- 1) **L. P. Sorge**, Philipp Sikora, K. Heinze, Face-to-face Gold Porphyrins, *Inorg. Chem.* **2024**, *under revision*.
- 2) **L. P. Sorge**, J. Link, K. Heinze, 14-Membered Macrocyclic beta-Diiminato Gold(II) – A New Member for the Gold(II) Complex Family?, *Chem. Eur. J.* **2024**, e202400924.
- 3) S. T. Hauer, P. Kuhn, J. M. Pütz, G. J. Reiss, **L. P. Sorge**, C. Ganter, K. Heinze, T. J. J. Müller, Conformationally Restricted Bis[1]benzothieno[1,4]thiazines - A Rational Design to Enhanced Planarity of Redox-active Fluorophores with Increased Radical Cation Stability, *under revision*.
- 4) J. Moll, R. Naumann, **L. P. Sorge**, C. Förster, N. Gessner, L. Burkhardt, N. Ugur, P. Nuernberger, W. Seidel, C. Ramanan, M. Bauer, K. Heinze, Pseudo-Octahedral Iron(II) Complexes with Near-Degenerate Charge Transfer and Ligand Field States at the Franck-Condon Geometry, *Chem. Eur. J.* **2022**, 28, e202201858.
- 5) Simone T. Hauer, Arno P. Schneeweis, Sven. D. Waniek, **L. P. Sorge**, K. Heinze, Thomas J. J. Müller, Radical cations and dications of bis[1]benzothieno[1,4]thiazine isomers, *Org. Chem. Front* **2021**, 20, 5744–5755.
- 6) S. Chen, W. Zhang, **L. P. Sorge**, D.-K. Seo, Exploratory Synthesis of Low-Silica Nanozeolites through Geopolymer Chemistry, *Cryst. Growth Des.* **2019**, 19, 18804–18811.
- 7) S. Chen, **L. P. Sorge**, D.-K. Seo, Template-free synthesis and structural evolution of discrete hydroxycancrinite zeolite nanorods from high-concentration hydrogels, *Nanoscale* **2017**, 47, 18804–18811.

8.2 Conference Contributions

- 03/2019 **15. Koordinationschemie-Treffen, München, Germany**
Poster presentation
“Novel Gold(II) Complexes”
- 03/2020 **16. Koordinationschemie-Treffen, Freiburg, Germany**
Poster presentation
“Novel Mono- and Binuclear Gold(II) Complexes
- 09/2022 **44th International Conference on Coordination Chemistry, Rimini, Italy**
Poster presentation
“Novel Pacman-Like Gold(II)-Bis(porphyrin)”